

Plasma and related sciences: experimental and theoretical approaches

Edited by

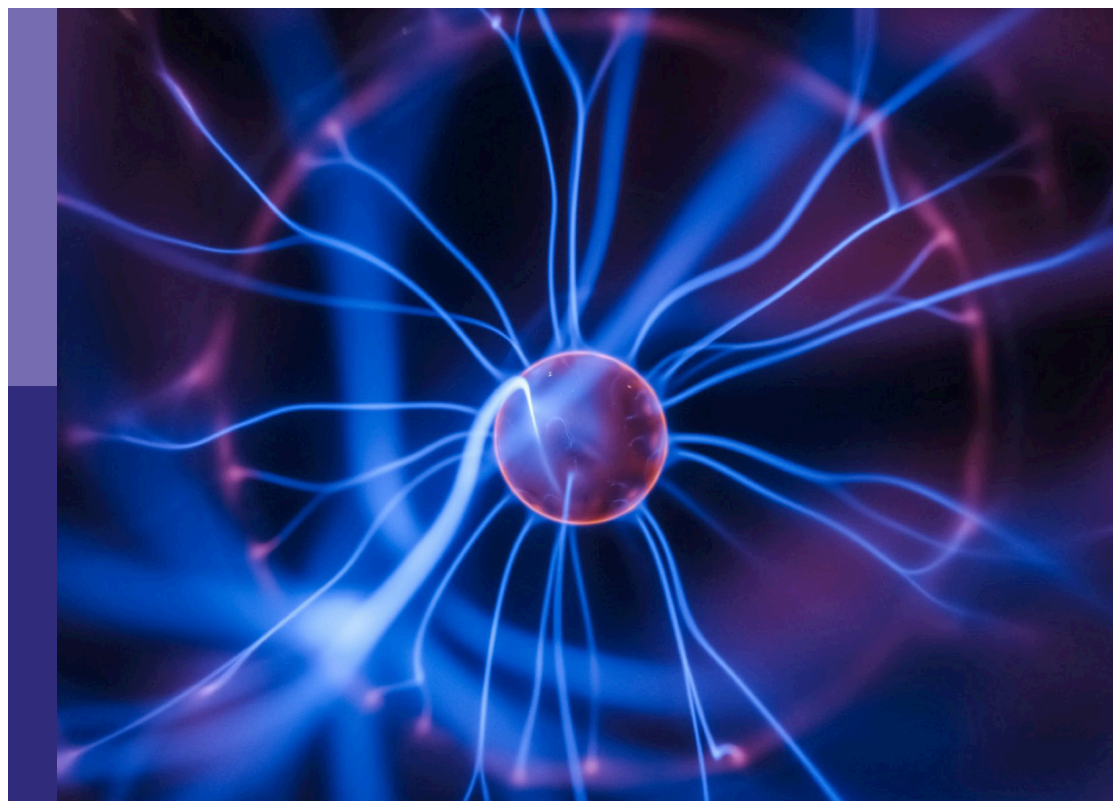
Mohamed Mokhtar Hefny, Paolo Francesco Ambrico,
Amer El-Kalliny, Tarek A. Gad-Allah and Ashraf M. Tawfik

Coordinated by

Hany Mohamed Hamouda

Published in

Frontiers in Physics



FRONTIERS EBOOK COPYRIGHT STATEMENT

The copyright in the text of individual articles in this ebook is the property of their respective authors or their respective institutions or funders. The copyright in graphics and images within each article may be subject to copyright of other parties. In both cases this is subject to a license granted to Frontiers.

The compilation of articles constituting this ebook is the property of Frontiers.

Each article within this ebook, and the ebook itself, are published under the most recent version of the Creative Commons CC-BY licence. The version current at the date of publication of this ebook is CC-BY 4.0. If the CC-BY licence is updated, the licence granted by Frontiers is automatically updated to the new version.

When exercising any right under the CC-BY licence, Frontiers must be attributed as the original publisher of the article or ebook, as applicable.

Authors have the responsibility of ensuring that any graphics or other materials which are the property of others may be included in the CC-BY licence, but this should be checked before relying on the CC-BY licence to reproduce those materials. Any copyright notices relating to those materials must be complied with.

Copyright and source acknowledgement notices may not be removed and must be displayed in any copy, derivative work or partial copy which includes the elements in question.

All copyright, and all rights therein, are protected by national and international copyright laws. The above represents a summary only. For further information please read Frontiers' Conditions for Website Use and Copyright Statement, and the applicable CC-BY licence.

ISSN 1664-8714
ISBN 978-2-8325-5788-4
DOI 10.3389/978-2-8325-5788-4

About Frontiers

Frontiers is more than just an open access publisher of scholarly articles: it is a pioneering approach to the world of academia, radically improving the way scholarly research is managed. The grand vision of Frontiers is a world where all people have an equal opportunity to seek, share and generate knowledge. Frontiers provides immediate and permanent online open access to all its publications, but this alone is not enough to realize our grand goals.

Frontiers journal series

The Frontiers journal series is a multi-tier and interdisciplinary set of open-access, online journals, promising a paradigm shift from the current review, selection and dissemination processes in academic publishing. All Frontiers journals are driven by researchers for researchers; therefore, they constitute a service to the scholarly community. At the same time, the *Frontiers journal series* operates on a revolutionary invention, the tiered publishing system, initially addressing specific communities of scholars, and gradually climbing up to broader public understanding, thus serving the interests of the lay society, too.

Dedication to quality

Each Frontiers article is a landmark of the highest quality, thanks to genuinely collaborative interactions between authors and review editors, who include some of the world's best academicians. Research must be certified by peers before entering a stream of knowledge that may eventually reach the public - and shape society; therefore, Frontiers only applies the most rigorous and unbiased reviews. Frontiers revolutionizes research publishing by freely delivering the most outstanding research, evaluated with no bias from both the academic and social point of view. By applying the most advanced information technologies, Frontiers is catapulting scholarly publishing into a new generation.

What are Frontiers Research Topics?

Frontiers Research Topics are very popular trademarks of the *Frontiers journals series*: they are collections of at least ten articles, all centered on a particular subject. With their unique mix of varied contributions from Original Research to Review Articles, Frontiers Research Topics unify the most influential researchers, the latest key findings and historical advances in a hot research area.

Find out more on how to host your own Frontiers Research Topic or contribute to one as an author by contacting the Frontiers editorial office: frontiersin.org/about/contact

Plasma and related sciences: experimental and theoretical approaches

Topic editors

Mohamed Mokhtar Hefny — Leibniz Institute for Plasma Research and Technology e.V. (INP), Germany

Paolo Francesco Ambrico — Istituto per la Scienza e Tecnologia dei Plasmi - CNR, Italy

Amer El-Kalliny — National Research Centre, Egypt

Tarek A. Gad-Allah — National Research Centre, Egypt

Ashraf M. Tawfik — Mansoura University, Egypt

Topic coordinator

Hany Mohamed Hamouda — Qassim University, Saudi Arabia

Citation

Mokhtar Hefny, M., Ambrico, P. F., El-Kalliny, A., Gad-Allah, T. A., Tawfik, A. M., Hamouda, H. M., eds. (2024). *Plasma and related sciences: experimental and theoretical approaches*. Lausanne: Frontiers Media SA.

doi: 10.3389/978-2-8325-5788-4

Table of contents

- 04 **Editorial: Plasma and related sciences: experimental and theoretical approaches**
Paolo F. Ambrico, Ashraf M. Tawfik, Amer S. El-Kalliny, Tarek A. Gad-Allah and Mohamed Mokhtar Hefny
- 06 **Modeling solar chromospheric spicules with intense lasers**
Jianzhao Wang, Jiayong Zhong, Weiming An, Weimin Zhou, Chen Wang, Bo Zhang, Yongli Ping, Wei Sun, Xiaoxia Yuan, Pengfei Tang, Yapeng Zhang, Qian Zhang, Chunqing Xing, Zhengdong Liu, Jiacheng Yu, Jun Xiong, Shukai He, Roger Hutton, Yuqiu Gu, Gang Zhao and Jie Zhang
- 14 **Research on the influence of gas ionization on pulse forming in linear transformer driver (LTD) electron beam generator**
Qiang Li, Dagang Liu, Fei Xiang, Laqun Liu and Huihui Wang
- 23 **The spark of life: discharge physics as a key aspect of the Miller–Urey experiment**
Savino Longo
- 28 **Evaluating atmospheric pressure cold plasma decontamination techniques for packaging materials: a systematic review and meta-analysis**
Caterina Maccaferri, Matteo Gherardi and Romolo Laurita
- 37 **Assessing plasma activated water irrigation effects on tomato seedlings**
Domenico Aceto, Palma Rosa Rotondo, Carlo Porfido, Benedetta Bottiglione, Costantino Paciolla, Roberto Terzano, Angelantonio Minafra, Marianna Ambrico, Giorgio Dilecce, Beniamino Leoni, Rita Milvia De Miccolis Angelini and Paolo Francesco Ambrico
- 54 **Magnetohydrodynamics simulation of magnetic reconnection process based on the laser-driven Helmholtz capacitor-coil targets**
Chunqing Xing, Yongli Ping, Xu Zhao, Weiming An and Jiayong Zhong
- 63 **LIF measurement in a partially saturated and partially absorbed regime**
Pavel Dvořák, Martina Mrkvičková and Jan Kratzer
- 69 **Air cold plasmas as a new tool for nitrogen fixation in agriculture: underlying mechanisms and current experimental insights**
Domenico Aceto, Paolo F. Ambrico and Fabrizio Esposito
- 76 **Research on the characteristics of the Helium plasma beam in HIT-PSI**
Tao Huang, Qiuyue Nie, Tao Jiang, Cheng Chen, Yang Liu, Jinming Gao, Laizhong Cai, Xu Zhao and Xiaogang Wang



OPEN ACCESS

EDITED AND REVIEWED BY

XinPei Lu,
Huazhong University of Science and
Technology, China

*CORRESPONDENCE

Mohamed Mokhtar Hefny,
✉ mohamed.hefny@inp-greifswald.de,
✉ mmokhtar@fue.edu.eg

RECEIVED 16 November 2024

ACCEPTED 19 November 2024

PUBLISHED 03 December 2024

CITATION

Ambrico PF, Tawfik AM, El-Kalliny AS,
Gad-Allah TA and Mokhtar Hefny M (2024)
Editorial: Plasma and related sciences:
experimental and theoretical approaches.
Front. Phys. 12:1529454.
doi: 10.3389/fphy.2024.1529454

COPYRIGHT

© 2024 Ambrico, Tawfik, El-Kalliny, Gad-Allah
and Mokhtar Hefny. This is an open-access
article distributed under the terms of the
[Creative Commons Attribution License \(CC
BY\)](#). The use, distribution or reproduction in
other forums is permitted, provided the
original author(s) and the copyright owner(s)
are credited and that the original publication
in this journal is cited, in accordance with
accepted academic practice. No use,
distribution or reproduction is permitted
which does not comply with these terms.

Editorial: Plasma and related sciences: experimental and theoretical approaches

Paolo F. Ambrico¹, Ashraf M. Tawfik², Amer S. El-Kalliny³,
Tarek A. Gad-Allah³ and Mohamed Mokhtar Hefny^{4,5*}

¹Istituto per la Scienza e Tecnologia dei Plasmi, Consiglio Nazionale delle Ricerche, Bari, Italy,

²Theoretical Physics Research Group, Physics Department, Faculty of Science, Mansoura University, Mansoura, Egypt, ³Water Pollution Research Department, National Research Centre, Giza, Egypt, ⁴PtX Plasma Development Center, Leibniz Institute for Plasma Science and Technology (INP), Greifswald, Germany, ⁵Engineering Mathematics and Physics Department, Faculty of Engineering and Technology, Future University in Egypt, Cairo, Egypt

KEYWORDS

solar chromospheric spicules, electron beam, pulsed electric field, origin of life, magnetic reconnection, plasma 2 decontamination, plasma agriculture, laser-induced fluorescence

Editorial on the Research Topic

Plasma and related sciences: experimental and theoretical approaches

Plasma physics is one of the most important tools for explaining our universe and is extensively used in engineering, industry, medicine, and agriculture to improve the standard of living. Recently, cold atmospheric plasma (CAP) has attracted significant attention due to its ability to generate a cocktail of reactive oxygen species (ROS), reactive nitrogen species (RNS), UV radiation, and charged particles at atmospheric pressure and room temperature. The investigation of CAP intersects multiple disciplines such as physics, engineering, chemistry, biology, biochemistry, and many others. The goal of this Research Topic, entitled “*Plasma and Related Sciences: Experimental and Theoretical Approaches*,” is to collect high-quality research related to CAP and plasmas, directly or indirectly, through the associated sciences. Our Research Topic comprises a total of nine articles:

In the first article, Wang et al. performed experiments with a high-power laser on a sinusoidal modulated target modeled after solar spicules, revealing structures with alternating polarity magnetic fields. Simulations suggest strong pulses and magnetic reconnection can create and heat spicules. Using one-dimensional sinusoidal modulated synthetic hydrocarbon (C_8H_8 target), researchers observed multipole magnetic fields, consistent with a strong pulse model. This method simulates solar surface density fluctuations and complex magnetic fields. Future studies should examine spicule heating effects, chromospheric bright points, sunspot micro-jets, and intrinsic oscillations, highlighting the roles of Alfvén waves and magnetic reconnection.

In the second article, Li et al. reported that there is currently limited research on how gas ionization affects the pulse formation process in loads driven by pulsed power sources. Therefore, a simulation method using Particle-In-Cell/Moment-Collision Calculation (PIC/MCC) has been proposed to accurately model gas ionization during electron beam generation in Linear Transformer Drivers (LTD.). This method integrates the electromagnetic field and charged particles with circuit modules, providing a clearer

understanding of the impact of gas ionization on pulse shape. Moreover, excessive gas ionization can lead to impedance mismatches and potential load short circuits.

In the third article, [Xing et al.](#) explored the conversion of magnetic energy into plasma kinetic and thermal energy using the FLASH code. Their simulations, which align well with experimental results, reveal significant differences in energy conversion under varying resistivity conditions. This study provides valuable insights into the dynamics of magnetic reconnection, contributing to advancements in laboratory and astrophysical research.

In the fourth article, [Longo](#) discussed the famous Miller–Urey experiment in light of the developments of two fields: computational chemistry and physics of electrical discharges. He showed that the second provides a much more realistic description for understanding the heterodox experiment and presented the role of the energetic electrons produced by the electric field to generate radicals and ions. The suggested role sheds light on biomolecules' formation from elemental chemical components and a better understanding of the origin of life.

In the fifth article, [Maccaferri et al.](#) reported that plasma technologies have garnered significant interest, recently, in the agrifood sector due to their innovative applications. The range of applications spans from direct plasma treatment to indirect methods using plasma-activated media. A key aspect of plasma technology in this sector is its ability to decontaminate surfaces and materials. They systematically compiled studies on the application of CAP for decontaminating packaging materials. Their synthesis of the results indicates that plasma technologies meet the standard requirements typically expected of commercial antiseptics, as the average logarithmic reduction of the pathogen load on the packaging was above 4.

In the sixth article, [Aceto et al.](#) investigated the effectiveness of plasma-activated median agricultural applications. Namely, Plasma-Activated Water (PAW) has been evaluated as an innovative irrigation method to improve growth and defense mechanisms in tomato seedlings, including those infected with the Tomato mottle mosaic virus (ToMMV). The results demonstrated that PAW is a sustainable, chemical-free alternative to traditional fertilizers, promoting plant growth, enhancing stress tolerance, and bolstering resilience against pathogens. These findings underscore the potential of plasma technology as a sustainable agricultural solution, paving the way for advancements in the agri-food industry.

In the seventh article, [Dvořák et al.](#) reported on diagnostic tools essential to understanding the microscopic processes within plasma. Among these tools, laser-induced fluorescence (LIF) is one of the most important methods for detecting various species, offering *in situ* measurements with high sensitivity, versatility, and spatial resolution. This makes the technique a key method for detecting reactive species in plasmas. The authors focused on the challenges of LIF measurements in a partially saturated regime with spatially dependent laser intensity in the sample (caused by absorption). The Rayleigh-calibrated LIF measurements, corrected using the authors' methods, were experimentally validated through LIF of free tellurium atoms in an atmospheric pressure dielectric barrier discharge (DBD) plasma, comparing fluorescence and absorption measurements. The results demonstrate a high reliability of the LIF methods employed.

In the eighth article, [Aceto et al.](#) highlighted cold plasma as a promising tool for enhancing nitrogen fixation processes.

Based on theoretical modeling, they suggest that maintaining non-equilibrium conditions in plasma could allow this technology to surpass the efficiency of the traditional Haber-Bosch process used in industrial nitrogen fixation. The synergy between modelers and experimental physicists is essential to achieve these advancements, leading to refined theoretical models that can guide the development of more efficient plasma systems.

In the ninth article, [Huang et al.](#) reported that the Plasma Surface Interaction device at the Harbin Institute of Technology (HIT-PSI) could serve as an excellent platform for testing the performance of plasma-facing materials and components in extreme irradiation environments such as tokamak devices. To simulate these conditions, preliminary irradiation experiments on tungsten were carried out at HIT-PSI, with a heat flux exceeding 40 MW/m^2 . Moreover, the He plasma beam's emission spectra and heat flux characteristics were measured at different high magnetic field conditions.

In conclusion, our Research Topic presents nine articles that collectively enhance our understanding of plasma physics and its applications. The findings not only contribute to theoretical knowledge but also hold the potential for practical innovations across various sectors. We invite readers to delve into these studies and explore the exciting possibilities that plasma technology offers.

Author contributions

PA: Writing–original draft, Writing–review and editing. AT: Writing–original draft, Writing–review and editing. AE-K: Writing–original draft, Writing–review and editing. TG-A: Writing–original draft, Writing–review and editing. MM: Writing–original draft, Writing–review and editing.

Funding

The author(s) declare that no financial support was received for the research, authorship, and/or publication of this article.

Conflict of interest

The authors declare that the research was conducted in the absence of any commercial or financial relationships that could be construed as a potential conflict of interest.

The author(s) declared that they were an editorial board member of Frontiers, at the time of submission. This had no impact on the peer review process and the final decision.

Publisher's note

All claims expressed in this article are solely those of the authors and do not necessarily represent those of their affiliated organizations, or those of the publisher, the editors and the reviewers. Any product that may be evaluated in this article, or claim that may be made by its manufacturer, is not guaranteed or endorsed by the publisher.



OPEN ACCESS

EDITED BY

Paolo Francesco Ambrico,
Istituto per la Scienza e Tecnologia dei
Plasmi—CNR, Italy

REVIEWED BY

Robertus Erdelyi,
The University of Sheffield,
United Kingdom
Tiago Pereira,
University of Oslo, Norway

*CORRESPONDENCE

Jiayong Zhong,
✉ jyzhong@bnu.edu.cn

RECEIVED 06 August 2023

ACCEPTED 05 September 2023

PUBLISHED 15 September 2023

CITATION

Wang J, Zhong J, An W, Zhou W, Wang C,
Zhang B, Ping Y, Sun W, Yuan X, Tang P,
Zhang Y, Zhang Q, Xing C, Liu Z, Yu J,
Xiong J, He S, Hutton R, Gu Y, Zhao G and
Zhang J (2023), Modeling solar
chromospheric spicules with
intense lasers.
Front. Phys. 11:1273568.
doi: 10.3389/fphy.2023.1273568

COPYRIGHT

© 2023 Wang, Zhong, An, Zhou, Wang,
Zhang, Ping, Sun, Yuan, Tang, Zhang,
Zhang, Xing, Liu, Yu, Xiong, He, Hutton,
Gu, Zhao and Zhang. This is an open-
access article distributed under the terms
of the [Creative Commons Attribution
License \(CC BY\)](https://creativecommons.org/licenses/by/4.0/). The use, distribution or
reproduction in other forums is
permitted, provided the original author(s)
and the copyright owner(s) are credited
and that the original publication in this
journal is cited, in accordance with
accepted academic practice. No use,
distribution or reproduction is permitted
which does not comply with these terms.

Modeling solar chromospheric spicules with intense lasers

Jianzhao Wang¹, Jiayong Zhong^{1,2,3*}, Weiming An^{1,2},
Weimin Zhou⁴, Chen Wang⁵, Bo Zhang⁴, Yongli Ping^{1,2},
Wei Sun^{6,2}, Xiaoxia Yuan¹, Pengfei Tang¹, Yapeng Zhang¹,
Qian Zhang¹, Chunqing Xing¹, Zhengdong Liu¹, Jiacheng Yu¹,
Jun Xiong⁵, Shukai He⁴, Roger Hutton¹, Yuqiu Gu⁴, Gang Zhao⁷
and Jie Zhang^{3,8}

¹Department of Astronomy, Beijing Normal University, Beijing, China, ²Institute for Frontiers in Astronomy and Astrophysics, Beijing Normal University, Beijing, China, ³Key Laboratory for Laser Plasmas, Ministry of Education, School of Physics and Astronomy, Collaborative Innovation Center of IFSA (CICIFSA), Shanghai Jiao Tong University, Shanghai, China, ⁴Science and Technology on Plasma Physics Laboratory, Research Center of Laser Fusion, China Academy of Engineering Physics (CAEP), Mianyang, China, ⁵Shanghai Institute of Laser Plasma, China Academy of Engineering Physics (CAEP), Shanghai, China, ⁶Department of Nuclear Physics, China Institute of Atomic Energy, Beijing, China, ⁷CAS Key Laboratory of Optical Astronomy, National Astronomical Observatories, Chinese Academy of Sciences, Beijing, China, ⁸Key Laboratory for Laser Plasmas, Ministry of Education, School of Physics and Astronomy, Shanghai Jiao Tong University, Shanghai, China

Solar spicules are small-scale jet-like structures in the lower solar atmosphere. Currently, the formation of these widely distributed structures lacks a complete explanation. It is still unclear whether they play an essential role in corona heating. Here, based on the magnetohydrodynamic scaling transformation relation, we perform experiments with the interaction of a high power laser with a one-dimensional sinusoidal modulated target to model solar spicules. We observe several spicule-like structures with alternating polarity magnetic fields around them. Magnetohydrodynamic simulations with similar parameters show the detail information during the spicules' formation. The results suggest that the so-called strong pulse model can lead to the formation of the solar spicules. The magnetic reconnection process may also play a part and lead to additional heating and brightening phenomena.

KEYWORDS

solar spicules, magnetohydrodynamic (MHD), magnetic reconnection, high energy density physics, laboratory astrophysics

1 Introduction

Solar spicules are widely distributed in the lower solar atmosphere (chromosphere). The general length of the Type-I spicules is about 7,000–10,000 km, and most of them have widths of 300–500 km, and lifetimes of 1–10 min or even longer, the upward velocities of about 20–40 km s⁻¹, densities of about $3 \times 10^{-13} \text{ g} \cdot \text{cm}^{-3}$ and temperatures of around 10,000 K, some spicules are heated to more than 100,000 K [1–7]. The spicules can carry 100 times the mass needed to sustain the solar wind [8]. Data from the Solar Dynamics Observatory showed the upper solar atmosphere had been heated subsequently when the spicules moved upwards [9]. There has been no conclusive explanation of the spicules since their discoveries in 1877. Many models have been proposed based on the source of energy driving the ejection of spicules from the chromosphere [10], including the strong pulse model [11,12], the rebound shock model [13], the Alfvén wave model [14–20] and the

magnetic reconnection model [9,21]. Dey et al. discussed the similarities between spicules observed on the Sun and jets produced by polymeric fluids. They found that the nonlinear focusing of quasi-periodic waves in an-isotropic media can generate a forest of jets [22]. The strong pulse model depicts a scenario where a sudden pressure enhancement produces a strong pulse in the photosphere or lower atmosphere at the base of a vertical magnetic flux tube that drives local material into the corona and forms the spicules [11]. In this model, an initial pressure pulse generates a disturbance that nonlinearly steepens into a gas-dynamic shock. This shock can be considered as magnetohydrodynamic (MHD) slow-mode shock for low-beta plasma. This shock interacts with the transition region, thrusting it upward, and the material behind the uplifted transition region is identified as the spicules [2]. Similar to the above model, the rebound shock model has a weaker pulse, although it can explain the distribution of spicule-like structures everywhere in the chromosphere, it cannot account for the periodicity, evolution, and energetic of the spicules [10]. In addition to these hydrodynamic models, the magnetic field may also play an important role in the spicule generation process due to the complex field structure on the solar surface. Many numerical simulations including MHD simulations and two-fluid simulations indicate that Alfvén waves, magneto-sonic waves, and the magnetic reconnection process also contribute to the velocity, length and collimation of the spicules [23–26]. However, it is still uncertain which model is dominant due to the limitations in observational resolution. As an interdisciplinary subject, laboratory astrophysics provides one possible way for us to study solar chromospheric spicules. Current observations are often limited by resolution, atmospheric perturbations, and other factors, while in the laboratory, using the interaction of high energy density lasers with target materials, we can simulate astrophysical phenomena at close range, short timescales (nanosecond), small scales (millimeter) and controlled conditions [22,27,28], and eventually connect laboratory simulations with astrophysical phenomena through scaling laws and dimensionless parameters [29].

Based on the strong pulse model, we perform an experiment using a nanosecond long-pulse laser impinging on a one-dimensional sinusoidal modulated synthetic hydrocarbon (C_8H_8) target to simulate the spicule generation process. Results from nickel-silver-like 13.9 nm soft x-ray self-emission imaging system (SXIS) show several jet-like structures appear behind the target. Proton radiography reveals the magnetic field structure around the spicules, similar to the Biermann self-generated magnetic field. The results of a radiation MHD simulation program ‘FLASH’ show agreement with the experimental results. We reproduce the process of spicules generation through laser-target interaction experiments, and by applying scaling laws, we can show the relevance of the jet-like structures to solar spicules. This is a new approach to studying spicules. It may show great significance for further accurate magnetic field structure studies near the spicules’ footpoints and help the understanding of coronal heating and material transport.

The paper is organized as follows. Section 2 describes the setup of the experiment. In Section 3, we show the experimental results and analyses with the help of three-dimensional MHD simulations and discuss the applications in astrophysics. Section 4 summarizes the results, discusses some remaining problems,

and describes future works concerning about experiments and simulations.

2 Experimental setup

We performed the experiments using the Shenguang-II laser facility (SG-II) firstly [30]. Figure 1 shows the setup of the experiment and the target configuration. The target was made of C_8H_8 , and it was sinusoidally modulated with a period of 55 μm , a length of 2,200 μm , a width of 200 μm , a thickness of $18 \pm 5 \mu\text{m}$, and an amplitude of 3 μm (Figure 1B). A modulated target with varying thickness is used to imitate the tiny density disturbances and alternating magnetic fields in solar chromosphere or lower atmosphere (more details will be discussed in Section 3). The experiment employed a main laser with a wavelength of 527 nm, total energy of about 800 J and a pulse duration of 2 nanoseconds. The target’s modulated side was irradiated with a $450 \mu\text{m} \times 450 \mu\text{m}$ square uniform illumination (with an intensity of $\sim 10^{14} \text{ W} \cdot \text{cm}^{-2}$). The diameter of the laser spot size is 7–8 times larger than the target modulation period. Nickel-silver-like 13.9 nm soft x-ray self-emission imaging technology (SXIS) is a new approach to diagnosing the plasma self-emission intensity profile information. The SXIS system consists of two mirrors (M1 and M2) and an imaging unit (including a shielding cylinder, an aluminum film to shield stray light, and an imaging plane). These mirrors have been coated with multi-layer films that are only sensitive to wavelengths around 13.9 nm. As a result, the self-emission radiation from the plasma is reflected twice off these mirrors and then imaged on the imaging plane (IP), as depicted in Figure 1. The multi-layer spherical mirror M1 and multi-layer spherical imaging mirror M2 can filter out excessive radiation during laser-target interactions, which allow us to obtain clearer structures [31]. We used SXIS to diagnose the plasma self-emission profile after the main laser ablated the target, and we obtained several jet-like structures. However, the magnetic field was not obtained in this experiment, so we redesigned the experiment to investigate the formation of the jet-like structures and the role of the magnetic field in the plasma region.

In order to map the magnetic field structure of the interaction region, a series of new experiments were performed on the Xingguang-III laser facility (XG-III) [32]. The target parameters were the same as before, but we increased the amplitude of the target to 10 microns in order to observe a clearer phenomenon. The experimental setup is shown in Figure 1A. The main laser (wavelength $\lambda = 532 \text{ nm}$, energy about 120 J, pulse duration 2 ns, laser intensity $\sim 10^{14} \text{ W} \cdot \text{cm}^{-2}$) focused on the modulated target with a focal spot diameter of 200 μm . We used proton radiography to diagnose the magnetic field [33]. The proton radiography is a common technique for diagnosing the structures of the magnetic fields. As the protons pass through the plasma, they are deflected by the Lorentz force and eventually imaged on the radiochromic film (RCF) stack. The protons on the RCF stack can form regions of evacuation and accumulation that correspond to regions of strong and weak magnetic fields, respectively [34]. Note that because the proton speed is much larger than the plasma velocity, the electric field has much less effect on the proton radiography. Therefore the deflection of the proton is mainly caused by the magnetic field [35]. In the experiment, we used a short pulse laser to drive a proton target

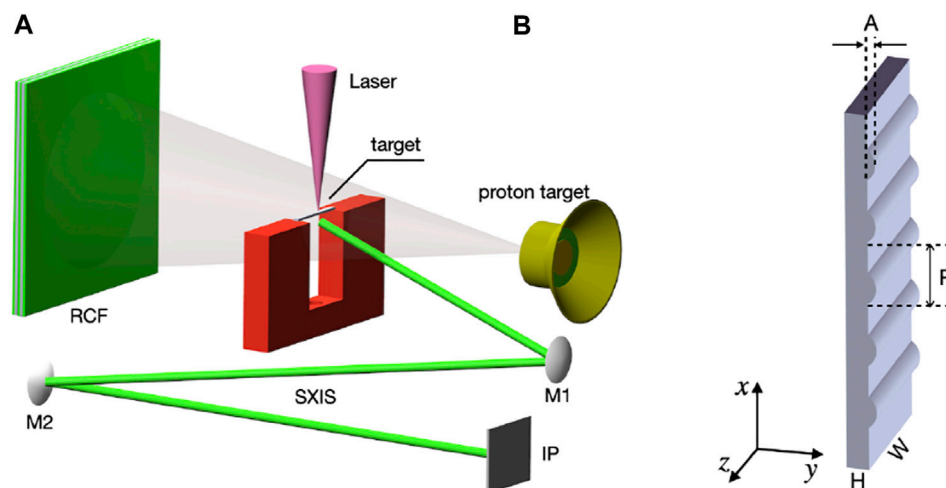


FIGURE 1

Schematic diagram of the experimental setup and sinusoidal modulated target. (A) The C_8H_8 target is located at the target chamber center (TCC). The main laser focuses on the target modulated side from the top, the proton target is located 1 cm to the right of TCC, and the proton detector (RCF) images are recorded at 15 cm to the left of TCC. Soft x-ray self-emission imaging system (SXIS) measures plasma parameters near TCC. (B) Sinusoidal modulated target parameters: width $W = 200 \mu m$, thickness $H = 18 \pm 5 \mu m$, modulation period $p = 55 \mu m$, amplitude $A = 3 \mu m$ or $A = 10 \mu m$, the material is synthetic hydrocarbon C_8H_8 .

to produce a proton beam. The proton target consists of a 10 μm Au foil, a 3 μm Ta foil and a shielding cylinder made of Ni. A picosecond laser (wavelength $\lambda = 1,053 \text{ nm}$, energy about 100 J, pulse duration 0.86 ps, laser intensity $\sim 10^{19} \text{ W} \cdot \text{cm}^{-2}$) is focused on the gold foil as soon as the nanosecond main laser ends ($t = 2 \text{ ns}$), which will produce a beam of protons with an energy greater than 12 MeV. The proton source was 0.8 cm away from the target center. The RCF stack was 12 cm away from the proton target center. The protons passed through the plasma region in the direction of perpendicular to the nanosecond laser incidence direction, and were imaged on the multiple layers RCF stack. The protons with smaller energy will be imaged in the RCF layer closer to the proton target, and those with higher energy will be imaged in the RCF layer further to the proton target. The magnification factor in this experiment was about 15.

3 Results and discussions

Based on the high energy density experimental facilities described above, we use a modulated target to simulate the density fluctuations on the solar surface (or lower atmosphere). The high-power laser is like a sudden pressure enhancement in the photosphere or low chromosphere. When such a strong pulse hits the target, the laser drives a shock, which drives material jets from the opposite surface of the target, due to the interaction of the shocks and the ablative structures, which may mimic the pressure driven spicules on the surface of the sun. The magnetic Reynolds number is around 100 ($Re_M \sim L \text{ (cm)} T \text{ (eV)}^2$), according to the scaling law, if the magnetic Reynolds number in the experiment is at least an order of magnitude higher than 1, the process can be reasonably described by MHD [36,37]. Through a series of experiments and simulations, we can connect the results to the strong pulse model of solar spicules production with scale transformation criteria.

Figures 2A, B show the results of SXIS obtained in the ‘SG-II’ experiment. A $450 \mu m \times 450 \mu m$ square focal spot laser is irradiated on a modulated target and a plain target, respectively. Darker color represents stronger x-ray emission. The modulated target is designed to imitate small density disturbances. A bush of spicules is often produced at the boundary between two adjacent supergranules [38,39]. In each supergranule, there are many granules on a much smaller scale. In the process of granules’ formation, the hot gas from the inner part rises to the surface and slides down again at the edge of a granule cell. As a result, the density will be non-uniform across a single granule cell. Observations also prove that the spicules originate from a small region near the boundary between two adjacent granules [9]. We are concerned about how each spicule in the spicule bush is produced. So we assume that there are some density inhomogeneities in the spicules production region, like ‘granules’ on a much smaller scale. As the distance between two spicules is about several hundred kilometers, we designed a modulated target with a thickness variation period of $55 \mu m$ to imitate the density inhomogeneities. After the scaling transformation, this period corresponds to the distance between two spicules in the solar environment. When the laser ablates the target and produces plasma, the density variation due to the different thicknesses of the target can correspond to the small density disturbances on the solar surface or lower atmosphere. The x-ray emission result (Figure 2A) shows that 10 jet-like structures with an interval of $55 \mu m$ are generated. The separation of those jets is consistent with the period of the modulated target. As shown in Figure 2A, the second to eighth spicules are longer because they are within the laser irradiation range. Their lengths range from $150 \mu m$ to $400 \mu m$. On the other hand, laser irradiation of a plain target only causes the plasma to expand thermally without producing any multiple jet-like structures (Figure 2B). The experimental results verified our hypothesis that the disturbance of density is one of the necessary conditions for the

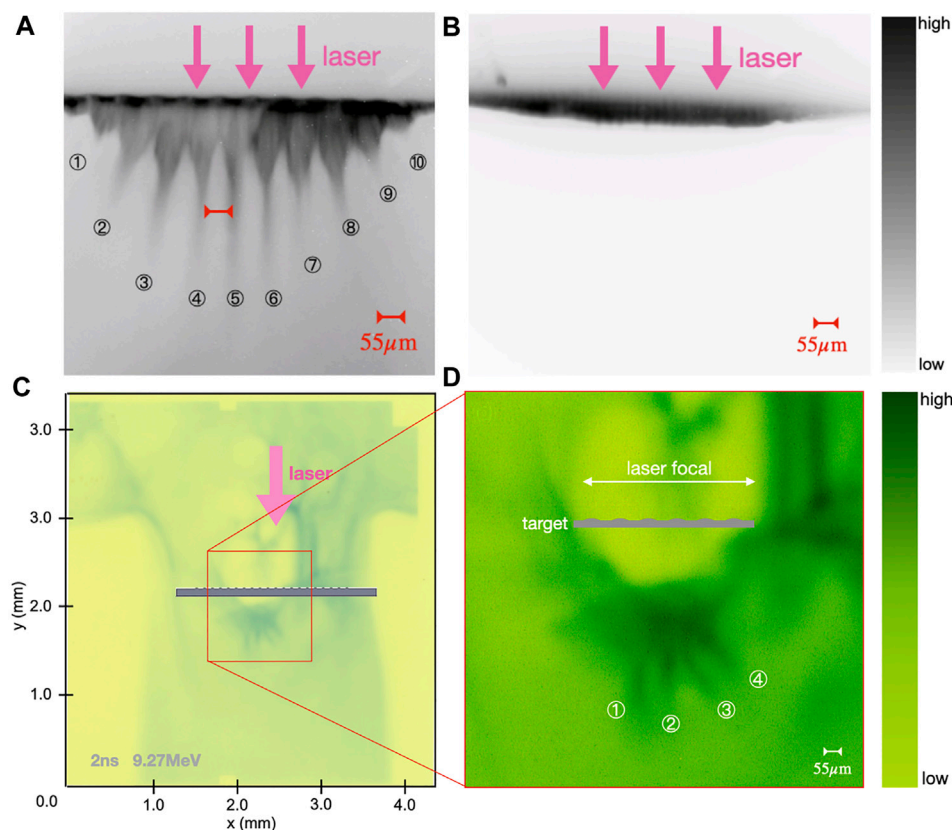


FIGURE 2

Soft x-ray self-emission imaging results in 'SG-II' experiments and proton radiography results obtained with 9.27 MeV protons at 2 ns. (A) Jet-like structures with an interval of 55 μm eject from the modulated target with the irradiation of a 450 μm × 450 μm square focal spot laser. (B) No jet-like structures show up when the laser irradiates the plain target. Darker color represents stronger X-ray emission. (C) Shows the position of the target and the direction of laser incidence; (D) is an enlarged view of the red box section in (C), four jet-like proton accumulation structures are visible. Darker green means more protons are accumulated.

generation of the spicules, while a surface with uniform density cannot produce such structures.

Figure 2C shows one of the proton imaging results (an RCF layer that absorbs protons with a peak energy of 9.27 MeV) that is taken at $t = 2$ ns after the laser focuses on the target. The position of the target and the laser incidence direction are drawn in Figure 2C. The proton evacuation region in the middle is caused by the excessive strength of the laser magnetic field. Darker green means more protons are accumulated. Figure 2D is an enlarged view of the red box shown in Figure 2C, where we can clearly see the multiple jet-like structures. This implies that an alternating strong magnetic field appears behind the target. The separation between the jets is consistent with the period of the target (55 μm). When a thin solid target is ablated by an intense laser, a high-temperature and high-density plasma will be generated. Then the plasma expands forward in the laser direction. The temperature of the plasma is mainly determined by the heat conduction of electrons inside the target rather than the adiabatic expansion of the plasma. Therefore, the direction of the gradient of the plasma temperature is parallel to the target surface, while the gradient of the plasma density is perpendicular to the target surface. Such inconsistency of the temperature and density gradients will generate a thermoelectric potential, which in turn will

induce a thermal current and finally generate a magnetic field. This is the so-called Biermann magnetic field [40–42].

Samanta et al. observed a magnetic network with positive polarity and negative polarity magnetic element around the spicule with a strength of about 10 Gauss [9]. This kind of magnetic field structure is similar to that produced in our experiments and simulations, and the strength of the magnetic field is close to the value scaled to solar spicule (Table 1). In our experiments, due to the periodic thickness variation of the modulated target, several plasma clusters are generated after the laser ablation. An alternating magnetic field is generated around each plasma cluster according to the Biermann battery effect. These alternating magnetic fields at the origin of the spicules are consistent with both the observed and experimentally obtained results. We can also estimate the magnetic field in the experiment by assuming that in the proton radiography the proton is deflected by a uniform magnetic field in the spicule region. The length of the magnetic field region can be considered the same as the thickness of the target. As a result, the magnetic field is around 1.8×10^6 Gauss for a 9.27 MeV proton. According to the time delay and the length of spicule-like structures measured in Figure 2A, we can also estimate the maximum velocity of the jet, which is about 150 km s^{-1} .

TABLE 1 The similarity of solar spicules and laser-driven plasma. The data of solar spicules referenced from [2–7,48,49].

Parameters	Solar spicules	Laser-driven plasma	Scaled to solar spicules
Length (cm)	$\sim 10^8 - 10^9$	$\sim 10^{-2}$	$\sim 10^8$
Time(s)	$\sim 10 - 1000$	$\sim 10^{-9}$	$\sim 10^2$
Pressure (Pa)	$\sim 10^{-3} - 10$	$\sim 10^7$	$\sim 10^{-3}$
Density (cm^{-3})	$\sim 10^{11} - 10^{13}$	$\sim 10^{19} - 10^{21}$	$\sim 10^{11} - 10^{13}$
Velocity (km s^{-1})	$\sim 10 - 1000$	~ 100	$\sim 1 - 100$
Magnetic field(G)	$\sim 10 - 10^2$	$\sim 10^5 - 10^6$	~ 10
Plasma β	≤ 1	~ 1	
Magnetic Reynolds number, Re_M	$10^6 - 10^7$	$> 10^2$	
Mach number, M	2–10	5–15	

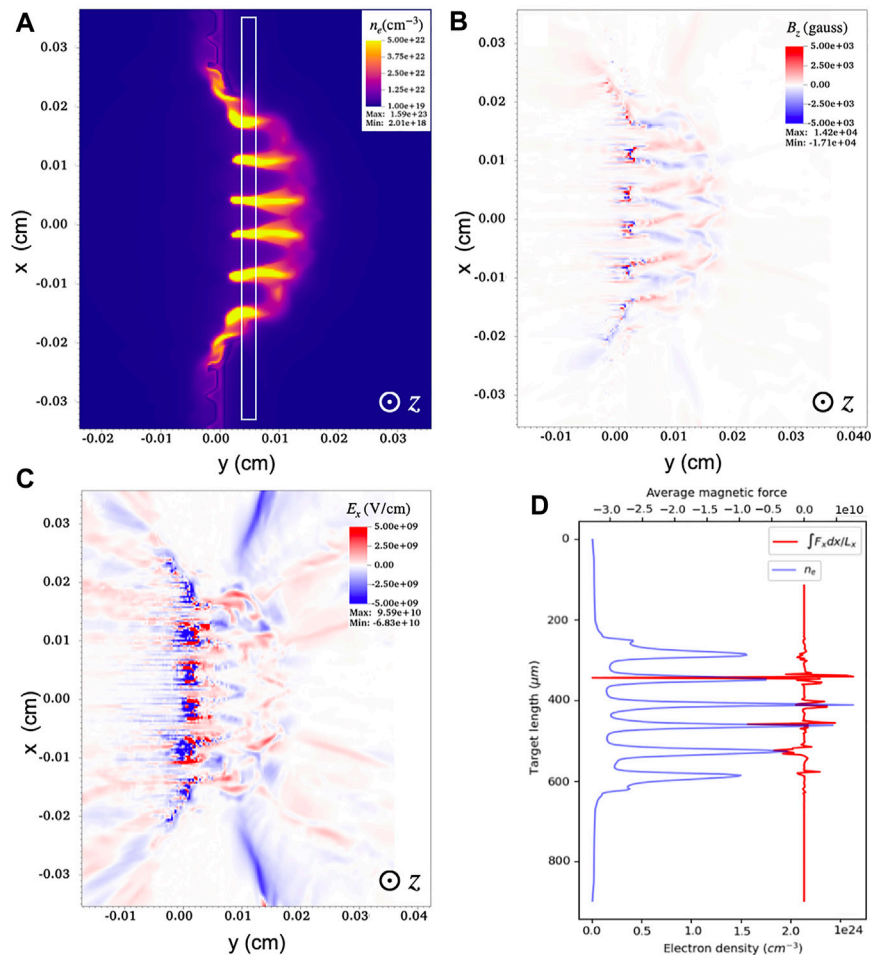


FIGURE 3 MHD simulation results of 'XG-III' experiment at 2 ns. (A) Electron density (cm^{-3}) distribution map, several jet-like structures with an interval of $55 \mu\text{m}$ are found. (B) Magnetic field distribution in z-direction, alternating positive and negative magnetic fields surrounding the jets are found. (C) Electric field distribution in x-direction, the reconnection of reversed magnetic fields between adjacent jets leads to an increase in the local electric field strength. The z-direction is perpendicular to the x-y plane pointing to readers. (D). The red curve and the blue curve show the averaged magnetic force and the electron density along the length of the target, respectively. The data in (D) comes from the rectangle area in (A).

To model the jet-like structures relevant to solar spicules in the laboratory, we should confirm that these two systems share some similar dimensionless parameters. Table 1 shows the comparison of the dimensionless parameters between the solar spicules and the laboratory jets. The Reynolds number ($Re = L\nu/\nu$) and the magnetic Reynolds number ($Re_M \sim L(\text{cm})T(\text{eV})^2$) for two systems are both much larger than 1, where L is the characteristic length, ν is the jet speed, T is the jet temperature and ν is the viscosity. These values show that the viscosity is not important, and the plasma moves along the magnetic field lines. According to $\beta = 4.03 \times 10^{-11} n_e T_e B^{-2}$, we can also obtain that the plasma has $\beta \sim 1$ near the target surface, where $n_e \sim 10^{20} \text{cm}^{-3}$, $T_e \sim 10 \text{eV}$, $B \sim 10^5 \text{G}$. It is similar to the β for the solar spicules generation region. We also calculate another important parameter -the density contrast $\eta_\rho = \rho_j/\rho_a$, where ρ_j and ρ_a represent for the densities of the jet and the surrounding environment. The η_ρ for these two systems are both larger than 1. The Mach numbers of the two systems are also close to each other, which indicates that the two systems are related to a large extent.

A radiation MHD simulation program 'FLASH' is used to help analyze the experimental results [43]. Based on the experimental parameters, we perform a three-dimensional MHD simulation using FLASH. The laser and the target parameters are consistent with 'XG-III' experiment except for the background plasma density, since the simulation requires the addition of a low density background plasma, while in the experiment is a high vacuum chamber. FLASH uses the generalized Ohm's law [44,45] to calculate the magnetic field, which takes advection, diffusion, and Biermann battery terms into account:

$$\frac{\partial \mathbf{B}}{\partial t} = \nabla \times (\mathbf{u} \times \mathbf{B}) - c \nabla \times (\eta \mathbf{j}) + c \frac{\nabla P_e \times \nabla n_e}{en_e^2} \quad (1)$$

where \mathbf{u} is the flow advection velocity, η is the electrical resistivity. Although the dissipation term is considered in our simulations, it can actually be neglected since the magnetic Reynolds number is large enough [37] (> 100).

Figure 3 shows the electron density, magnetic field along z -direction, and electric field along x -direction at 2 ns in the simulation results. The laser ablates the target from left to right. At the moment of the laser ends, it can be clearly seen that the multiple jet-like structures are moving toward the right, which is consistent with the x-ray self-emission result shown in Figure 2A. These jet-like structures have an interval of 55 μm , the maximum electron density of about 10^{23}cm^{-3} , the maximum length of about 120 μm , and the velocity of about 150 km s^{-1} , they are very similar to the parameters in Figure 2A. The full width at half maximum (FWHM) of the laser pulse is about 100 μm , which is 7–8 times larger than the modulation period of the target. With the generation and propagation of the jets, a temperature gradient and a density gradient are generated around each jet, and a magnetic field structure is formed by the Biermann battery effect. The magnetic field along the z -direction is shown in Figure 3B. A toroidal magnetic field surrounds each jet, which has a similar structure to proton radiography results shown in Figure 2D. However, the difference is that the proton accumulation jet-like structures from experiment are more divergent from each other, which may be caused by the power distribution of the laser. The magnetic field is interrupted at $y = 0.012 \text{cm}$ because the continuity of the field is affected by the

propagation of the plasma at the trough of the modulated target. During the propagation of the jet, it also expands laterally, which will cause the reverse magnetic field between the two neighboring jets are becoming closer and closer. From 1.5 ns, the reverse magnetic field annihilates, and the electric field in the vertical direction is significantly enhanced (Figure 3C), which is one of the evidence for the occurrence of magnetic reconnection [46]. We can obtain the averaged Lorentz force based on the simulation results along x -direction from the Maxwell stress tensor,

$$F_x = (\nabla \cdot \mathbf{T})_x = \frac{\partial}{\partial x} \left(\frac{B_x B_x}{4\pi} \right) + \frac{\partial}{\partial y} \left(\frac{B_y B_x}{4\pi} \right) + \frac{\partial}{\partial z} \left(\frac{B_z B_x}{4\pi} \right) - \frac{\partial}{\partial x} \left(\frac{B^2}{8\pi} \right) \quad (2)$$

where $\mathbf{T} = \frac{\mathbf{B}\mathbf{B}}{4\pi} - \frac{|\mathbf{B}|^2}{8\pi} \mathbf{I}$ is the Maxwell stress tensor, where \mathbf{I} is the identity tensor. We calculate the averaged \bar{F}_x (which is $\frac{\int F_x dx}{L_x}$) between $x = 230$ and $x = 250$ (i.e., the white rectangle shown in Figure 3A where the jets start to form). The \bar{F}_x (the red curve shown in Figure 3D) has multiple spikes which have the same locations as those spicules (the blue curve of electron density shown in Figure 3D). It shows that the locations with strong magnetic force are consistent with the locations of the spicules. This indicates the Maxwell stress tensor does have contributions to the process of spicules formation.

According to previous works ([29,37,47]), the two systems can behave as ideal compressible hydrodynamic fluids if the dimensionless numbers are much larger than 1, such as Reynolds number and magnetic Reynolds number. So the ideal MHD equations and the energy equation for the polytropic gas remain invariant when the following transformation conditions are satisfied: $r_2 = ar_1$, $\rho_2 = b\rho_1$, $p_2 = cp_1$, $t_2 = a\sqrt{b}/ct_1$, $v_2 = \sqrt{c/b}v_1$, $B_2 = \sqrt{c}B_1$, where r is the characteristic length, ρ is the number density, p is the pressure, t is the characteristic time, v is the velocity and B is the magnetic field. The subscript 1 represents parameters in the laboratory, and the subscript 2 represents parameters in the solar spicule system. The coefficients a , b , c are arbitrary positive numbers, which can be obtained directly by comparing the parameters from two systems. From our experimental results, we can obtain the transformation coefficients of $a = 10^{10}$, $b = 10^{-8}$, and $c = 10^{-10}$. The scaled parameters (Table 1) are close to the parameters in the experiment, which indicates the experimental results can be applied to explore the formation mechanism of the solar spicules.

4 Conclusion

In this work, we used a high-power laser irradiating a sinusoidally modulated C_8H_8 target with a period of 55 μm and an MHD code 'FLASH' for simulation with similar setup parameters to experiments. We found several spicule-like structures with an interval of 55 μm emitting from the backside of the target and multipole magnetic fields around the spicules. These results are consistent with the description of the strong pulse model, which contributes to the generation of solar spicules. The alternating magnetic fields also correspond to the structures of the magnetic fields near the footpoints of the spicules. Magnetic reconnection between adjacent spicules may also be important for brightening and heating solar spicules.

This is a new way to study solar chromospheric spicules. We can change the amplitude and period of the modulated target to simulate the random density fluctuations on the solar surface, and also apply an external magnetic field to simulate the complex magnetic field on the solar surface. These ideas are easily implemented in the laboratory. In the simulations so far, we have only considered magnetic reconnection with low resistivity, which may underestimate the effect of the magnetic field on the spicules. However, both Alfvén waves and magnetic reconnection may play an important role during spicules' generation and propagation. In the future, we will do more detailed studies regarding the heating effect of the spicules to the corona, the bright points in the chromospheric network, and the formation of micro-jets in the sunspot penumbra region. In addition, intrinsic oscillation is one of the important properties of the spicule. We will also study about this topic in the future.

Data availability statement

The raw data supporting the conclusion of this article will be made available by the authors, without undue reservation.

Author contributions

JW: Writing—original draft. JZ: Supervision, Writing—review and editing. WA: Supervision, Writing—review and editing. WZ: Conceptualization, Writing—review and editing. CW: Formal Analysis, Writing—review and editing. BZ: Data curation, Writing—review and editing. YP: Formal Analysis, Writing—review and editing. WS: Formal Analysis, Writing—review and editing. XY: Formal Analysis, Writing—review and editing. PT: Formal Analysis, Writing—review and editing. YZ: Formal Analysis, Writing—review and editing. QZ: Formal Analysis, Writing—review and editing. CX: Formal Analysis, Writing—review and editing. ZL: Formal Analysis,

Writing—review and editing. JY: Formal Analysis, Writing—review and editing. JX: Formal Analysis, Writing—review and editing. SH: Data curation, Writing—review and editing. RH: Supervision, Writing—review and editing. YG: Supervision, Writing—review and editing. GZ: Funding acquisition, Writing—review and editing. JZ: Funding acquisition, Writing—review and editing.

Funding

The author(s) declare financial support was received for the research, authorship, and/or publication of this article. This work was supported by the National Key R&D Program of China (grant Nos. 2022YFA1603200 and 2022YFA1603203) and the National Natural Science Foundation of China (grant Nos. 12325305, 12175018, 12135001, and 12075030), and the Strategic Priority Research Program of the Chinese Academy of Sciences (grant No. XDA25030700), Youth Interdisciplinary Team (JCTD-2022-05).

Conflict of interest

The authors declare that the research was conducted in the absence of any commercial or financial relationships that could be construed as a potential conflict of interest.

Publisher's note

All claims expressed in this article are solely those of the authors and do not necessarily represent those of their affiliated organizations, or those of the publisher, the editors and the reviewers. Any product that may be evaluated in this article, or claim that may be made by its manufacturer, is not guaranteed or endorsed by the publisher.

References

- Beckers JM. Solar spicules. *Solar Spicules* (1972) 10:73–100. doi:10.1146/annurev.aa.10.090172.000445
- Sterling AC. Solar spicules: A review of recent models and targets for future observations - (invited review). *Solar Phys* (2000) 196:79–111. doi:10.1023/A:1005213923962
- de Pontieu B, McIntosh S, Hansteen VH, Carlsson M, Schrijver CJ, Tarbell TD, et al. A tale of two spicules: The impact of spicules on the magnetic chromosphere. *The Impact Spicules Magn Chromosphere* (2007) 59:S655–2. doi:10.1093/pasj/59.sp3.S655
- Tsiropoula G, Tziotziou K, Kontogiannis I, Madjarska MS, Doyle JG, Suematsu Y. Solar fine-scale structures. I. Spicules and other small-scale, jet-like events at the chromospheric level: Observations and physical parameters. *Observations Phys Parameters* (2012) 169:181–244. doi:10.1007/s11214-012-9920-2
- Pereira TMD, De Pontieu B, Carlsson M. *Quantifying Spicules* (2012) 759:18. doi:10.1088/0004-637X/759/1/18
- Pereira TMD, De Pontieu B, Carlsson M, Hansteen V, Tarbell TD, Lemen J, et al. An interface region imaging spectrograph first view on solar spicules. *AstroPhysical J Lett* (2014) 792:L15. doi:10.1088/2041-8205/792/1/L15
- Skogsrud H, Rouppe van der Voort L, De Pontieu B, Pereira TMD. On the temporal evolution of spicules observed Withiris, Sdo, and hinode. *AstroPhysical J Lett* (2015) 806:170. doi:10.1088/0004-637X/806/2/170
- Withbroe GL. The role of spicules in heating the solar atmosphere Implications of EUV observations. *Astrophys J* (1983) 267:825–36. doi:10.1086/160917
- Samanta T, Tian H, Yurchyshyn V, Peter H, Cao W, Sterling A, et al. Generation of solar spicules and subsequent atmospheric heating. *Science* (2019) 366:890–4. doi:10.1126/science.aaw2796
- De Pontieu B, Erdélyi R, James SP (2004). Solar chromospheric spicules from the leakage of photospheric oscillations and flows. *Nature*, 430, 536–9. doi:10.1038/nature02749
- Suematsu Y, Shibata K, Neshikawa T, Kitai R. Numerical hydrodynamics of the jet phenomena in the solar atmosphere: I. Spicules. *Sol Phys* (1982) 75:99–118. doi:10.1007/BF00153464
- Mackenzie Dover F, Sharma R, Erdélyi R. Magnetohydrodynamic simulations of spicular jet propagation applied to lower solar atmosphere model. *Model* (2021) 913:19. doi:10.3847/1538-4357/abefdl
- Hollweg JV. On the origin of solar spicules. *Astrophys J* (1982) 257:345–53. doi:10.1086/159993
- Cranmer SR, Woolsey LN. Driving solar spicules and jets with magnetohydrodynamic turbulence: Testing a persistent idea. *Astrophys J* (2015) 812:71. doi:10.1088/0004-637X/812/1/71
- Iijima H, Yokoyama T. A three-dimensional magnetohydrodynamic simulation of the formation of solar chromospheric jets with twisted magnetic field lines. *Astrophys J* (2017) 848:38. doi:10.3847/1538-4357/aa8ad1
- Martinez-Sykora J, De Pontieu B, Hansteen VH, Rouppe van der Voort L, Carlsson M, Pereira TMD. On the generation of solar spicules and Alfvénic waves. *Science* (2017) 356:1269–72. doi:10.1126/science.aah5412

17. Liu J, Nelson CJ, Snow B, Wang Y, Erdélyi R. Evidence of ubiquitous Alfvén pulses transporting energy from the photosphere to the upper chromosphere. *Nat Commun* (2019) 10:3504. doi:10.1038/s41467-019-11495-0
18. Oxley W, Scalisi J, Ruderman MS, Erdélyi R. Formation of chromospheric spicules in magnetic bright points: An analytical approach using cartesian slab geometry. *Astrophys J* (2020) 905:168. doi:10.3847/1538-4357/abcafe
19. Scalisi J, Oxley W, Ruderman MS, Erdélyi R. Propagation of torsional alfvén pulses in zero-beta flux tubes. *Astrophys J* (2021) 911:39. doi:10.3847/1538-4357/abe8db
20. Zaqarashvili TV, Lomineishvili S, Leitner P, Hanslmeier A, Gömöry P, Roth M. Kink instability of triangular jets in the solar atmosphere. *Astron Astrophys* (2021) 649: A179. doi:10.1051/0004-6361/202039381
21. Ding JY, Madjarska MS, Doyle JG, Lu QM, Vanninathan K, Huang Z. Magnetic reconnection resulting from flux emergence: Implications for jet formation in the lower solar atmosphere? *Astron Astrophys* (2011) 535:A95. doi:10.1051/0004-6361/201117515
22. Dey S, Chatterjee P, Korsós MB, Liu J, Nelson CJ. Polymeric jets throw light on the origin and nature of the forest of solar spicules. *Nat Phys* (2022) 18:595–600. doi:10.1038/s41567-022-01522-1
23. Heggland L, De Pontieu B, Hansteen VH. Numerical simulations of shock wave-driven chromospheric jets. *Astrophys J* (2007) 666:1277–83. doi:10.1086/518828
24. James SP, Erdélyi R. Spicule formation by ion-neutral damping. *Astron Astrophys* (2002) 393:L11–4. doi:10.1051/0004-6361:20021126
25. James SP, Erdélyi R, De Pontieu B. Can ion-neutral damping help to form spicules? *Astron Astrophys* (2003) 406:715–24. doi:10.1051/0004-6361:20030685
26. Kuźma B, Murawski K, Kayshap P, Wójcik D, Srivastava AK, Dwivedi BN. Two-fluid numerical simulations of solar spicules. *Astrophys J* (2017) 849:78. doi:10.3847/1538-4357/aa8ea1
27. Zhong J, Li Y, Wang X, Wang J, Dong Q, Xiao C, et al. Modelling loop-top X-ray source and reconnection outflows in solar flares with intense lasers. *Nat Phys* (2010) 6: 984–7. doi:10.1038/nphys1790
28. Ping Y, Zhong J, Wang X, Han B, Sun W, Zhang Y, et al. Turbulent magnetic reconnection generated by intense lasers. *Nat Phys* (2023) 19:263–70. doi:10.1038/s41567-022-01855-x
29. Ryutov D, Drake RP, Kane J, Liang E, Remington BA, Wood-Vasey WM. Similarity criteria for the laboratory simulation of supernova hydrodynamics. *Astrophysical J Lett* (1999) 518:821–32. doi:10.1086/307293
30. He XT, Zhang WY. Inertial fusion research in China. *Eur Phys J D* (2007) 44: 227–31. doi:10.1140/epjd/e2007-00005-1
31. Wang C, An H, Jia G, Fang Z, Wang W, Meng X, et al. Diagnosis of high-Z plasma with soft X-ray laser probe. *Acta Physica Sinica* (2014) 63:215203. doi:10.7498/aps.63.215203
32. Zhu Q, Zhou K, Su J, Xie N, Huang X, Zeng X, et al. The xingguang-III laser facility: Precise synchronization with femtosecond, picosecond and nanosecond beams. *Laser Phys Lett* (2018) 15:015301. doi:10.1088/1612-202X/aa94e9
33. Gao L, Ji H, Fiksel G, Fox W, Evans M, Alfonso N. Ultrafast proton radiography of the magnetic fields generated by a laser-driven coil current. *Phys Plasmas* (2016) 23: 043106. doi:10.1063/1.4945643
34. Kasim MF, Bott AFA, Tzeferacos P, Lamb DQ, Gregori G, Vinko SM. Retrieving fields from proton radiography without source profiles. *Phys Rev E* (2019) 100:033208. doi:10.1103/PhysRevE.100.033208
35. Lu Y, Tzeferacos P, Liang E, Follett RK, Gao L, Birkel A, et al. Numerical simulation of magnetized jet creation using a hollow ring of laser beams. *Phys Plasmas* (2019) 26:022902. doi:10.1063/1.5050924
36. Remington BA, Drake RP, Ryutov DD. Experimental astrophysics with high power lasers and Z pinches. *Rev Mod Phys* (2006) 78:755–807. doi:10.1103/RevModPhys.78.755
37. Ryutov DD, Drake RP, Remington BA. Criteria for scaled laboratory simulations of astrophysical MHD phenomena. *Astrophysical MHD Phenomena* (2000) 127:465–8. doi:10.1086/313320
38. Rutten RJ. The quiet-Sun photosphere and chromosphere. *Philosophical Trans R Soc Lond Ser A* (2012) 370:3129–50. doi:10.1098/rsta.2011.0537
39. Goode PR, Yurchyshyn V, Cao W, Abramenko V, Andic A, Ahn K, et al. Highest resolution observations of the quietest Sun. *Astrophysical J Lett* (2010) 714:L31–5. doi:10.1088/2041-8205/714/1/L31
40. Biermann L. Über den Ursprung der Magnetfelder auf Sternen und im interstellaren Raum (miteinem Anhang von A. Schlüter). *Z Naturforschung Teil A* (1950) 5:65.
41. Stamper JA. Review on spontaneous magnetic fields in laser-produced plasmas: Phenomena and measurements. *Laser Part Beams* (1991) 9:841–62. doi:10.1017/S0263034600006595
42. Gao L, Liang E, Lu Y, Follett RK, Sio H, Tzeferacos P, et al. Mega-gauss plasma jet creation using a ring of laser beams. *Mega-Gauss Plasma Jet Creation Using a Ring of Laser Beams* (2019) 873:L11. doi:10.3847/2041-8213/ab07bd
43. Fryxell B, Olson K, Ricker P, Timmes FX, Zingale M, Lamb DQ, et al. FLASH: An adaptive mesh hydrodynamics code for modeling astrophysical thermonuclear flashes. *Astrophysical Thermonuclear Flashes* (2000) 131:273–334. doi:10.1086/317361
44. Epperlein EM. The accuracy of Braginskii's transport coefficients for a Lorentz plasma. *J Phys D Appl Phys* (1984) 17:1823–7. doi:10.1088/0022-3727/17/9/007
45. Epperlein EM, Haines MG. Plasma transport coefficients in a magnetic field by direct numerical solution of the Fokker-Planck equation. *Phys Fluids* (1986) 29: 1029–41. doi:10.1063/1.865901
46. Zhang K, Zhong J, Pei X, Li Y, Sakawa Y, Gang W, et al. Measurement of jet evolution and electron energy spectrum during the process of laser-driven magnetic reconnection. *Acta Physica Sinica* (2015) 64:165201. doi:10.7498/aps.64.165201
47. Yuan D, Wu J, Li Y, Lu X, Zhong J, Yin C, et al. Modeling supersonic-jet deflection in the herbig-haro 110-270 system with high-power lasers. *Astrophys J* (2015) 815:46. doi:10.1088/0004-637X/815/1/46
48. Orozco Suárez D, Asensio Ramos A, Trujillo Bueno J. Height variation of the vector magnetic field in solar spicules. *Astrophysical J Lett* (2015) 803:L18. doi:10.1088/2041-8205/803/2/L18
49. Kriginsky M, Oliver R, Freij N, Kuridze D, Asensio Ramos A, Antolin P. Ubiquitous hundred-Gauss magnetic fields in solar spicules. *Astron Astrophysics* (2020) 642:A61. doi:10.1051/0004-6361/202038546



OPEN ACCESS

EDITED BY

Mohamed Mokhtar Hefny,
Future University in Egypt, Egypt

REVIEWED BY

Mohammed Shihab,
Tanta University, Egypt
Mohamed Abboud,
Faculty of Science, Egypt

*CORRESPONDENCE

Qiang Li,
✉ 1945007625@qq.com

RECEIVED 29 October 2023

ACCEPTED 21 December 2023

PUBLISHED 11 January 2024

CITATION

Li Q, Liu D, Xiang F, Liu L and Wang H (2024),
Research on the influence of gas ionization on
pulse forming in linear transformer driver (LTD)
electron beam generator.
Front. Phys. 11:1329584.
doi: 10.3389/fphy.2023.1329584

COPYRIGHT

© 2024 Li, Liu, Xiang, Liu and Wang. This is an
open-access article distributed under the terms
of the [Creative Commons Attribution License](#)
(CC BY). The use, distribution or reproduction in
other forums is permitted, provided the original
author(s) and the copyright owner(s) are
credited and that the original publication in this
journal is cited, in accordance with accepted
academic practice. No use, distribution or
reproduction is permitted which does not
comply with these terms.

Research on the influence of gas ionization on pulse forming in linear transformer driver (LTD) electron beam generator

Qiang Li^{1*}, Dagang Liu¹, Fei Xiang², Laqun Liu¹ and Huihui Wang¹

¹The School of Electronic Science and Engineering, University of Electronic Science and Technology of China, Chengdu, China, ²The Key Laboratory of High-Power Microwave Technology, Institute of Applied Electronics, China Academy of Engineering Physics (CAEP), Mianyang, China

Currently, there is limited research on the influence of gas ionization on the pulse formation process in pulse power source-driven loads. This paper introduces a road-field-Particle-In-Cell (PIC)/Monte Carlo Collision (MCC) collaborative simulation method that can accurately simulate gas ionization in Linear Transformer Driver (LTD) electron beam generation (EBG). The method couples the electromagnetic field and charged particle simulated through PIC/MCC with the circuit modules, and the load's voltammetry characteristics can real-time feedback to the Blumlein Pulse Forming Network (BPFN) of the LTD. In contrast to prior simulations that used fitted ideal T-shaped pulse input waveforms to model the load, this method provides a clearer depiction of the influence of gas ionization on the pulse shape. Additionally, the paper conducts simulation studies on LTD electron beam generator operating at different argon gas pressures. The findings indicate that introducing gas can effectively increase current while reducing voltage amplitude, thereby lowering the diode impedance. A small amount of gas can slightly enhance peak power, but excessive gas diminishes peak power and significantly shortens voltage pulse width. This is attributed to the beneficial effect of a small amount of gas ionization-produced plasma on the device. However, an excessive amount of gas ionization-generated plasma can lead to impedance mismatch in the device, even resulting in a load short circuit. This phenomenon causes a decrease in pressure drop at the top, consequently shortening the pulse width.

KEYWORDS

road-field-PIC/MCC collaborative simulation method, linear transformer driver (LTD), electron beam generation (EBG), gas ionization, Blumlein pulse forming network (BPFN)

1 Introduction

The linear transformer driver (LTD), first proposed by Russian scientists, is a new pulsed power technology that has been widely used in many fields due to its high voltage and current characteristics, such as Z pinch, ion implantation for material modifications, plasma physics, and so on [1–9]. The principle behind LTD pulse formation involves generating a pulse of the desired shape at low voltage using a linear transformer driver (LTD). Subsequently, voltage multiplication techniques [10–14] are employed to increase its voltage by several orders of magnitude. Ultimately, this voltage, generated by the LTDs, is used to drive various loads such as high-power microwave devices, diodes, thereby exciting high-power microwaves or electron beams. However, current research predominantly employs idealized T-shaped pulse input

waveforms, fitted according to requirements, and then simulates the high-power microwave devices or diodes based on these waveforms. Nevertheless, in the experiments, a pulse power source is needed to drive these devices. This involves complex physical processes, including the generation and propagation of electromagnetic waves, electron emission, and the production of high-power microwaves, among others. Importantly, these processes are interrelated, with the pulse power source influencing the microwave output of high-power microwave devices or diodes, and the structural parameters and voltammetry characteristics of the devices, in turn, affecting the pulse power source. Thus, conducting research solely on high-power microwave devices or diodes is insufficient to comprehensively capture these complex and interconnected physical processes.

Furthermore, current research on high-power microwave devices and diodes is largely conducted under vacuum conditions. However, in practical applications, it is challenging to maintain a perfect vacuum, and small amounts of residual gas often remain. Some studies have indicated that filling an appropriate amount of gas can affect the simulation of high-power microwave devices or diodes [15–20]. This necessitates in-depth research into the performance of high-power microwave devices or diodes in the presence of gases. Additionally, many pulse power applications require pulse signals with a stable voltage plateau, especially in high-power microwave applications. To generate such flat-top pulses, it is necessary to arrange LC components in various configurations to create large-scale pulse forming circuits. However, traditional full three-dimensional electromagnetic PIC/MCC algorithms are insufficient for simulating large-scale circuits. Therefore, there is an urgent need for a self-consistent road-field-PIC/MCC method capable of simulating the aforementioned complex physical processes.

This paper introduces a road-field-PIC/MCC simulation method, wherein the PIC/MCC algorithm is coupled with circuit modules. This coupling facilitates real-time feedback of the load's voltammetry characteristics into the circuit simulation module of the pulse power source, resulting in more precise pulse waveforms. This refinement enhances the overall device simulation's fidelity to practical scenarios. Building upon this foundation, a model is developed for the LTD pulse power generation device. A foil-less diode with ring cathode characteristics is integrated into the pulse power generator. Subsequently, the road-field-PIC/MCC simulation algorithm is employed to comprehensively simulate the entire setup. By introducing argon gas at varying pressures, simulations of the LTD pulse power electron beam generator under different conditions are conducted. This investigation explores the impact of gas ionization on pulse shaping in the LTD electron beam generator and provides an analysis of relevant physical phenomena.

2 Theoretical basic

In order to achieve the road-field-PIC/MCC collaborative simulation method, it is necessary to develop the circuit simulation module and the PIC/MCC simulation module. Subsequently, research on the collaborative coupling methods between circuit module and PIC/MCC module is conducted. The circuit modules are implemented based on the Modified nodal

voltage method [21], as elucidated in detail in our previous work [22]. The subsequent section provides an exhaustive exposition of the implementation process for the PIC/MCC simulation module and the road-field-PIC/MCC collaborative simulation module.

2.1 The fundamental theory of ionization collisions

When the energy of the incident electron is greater than the ionization threshold, the incident electron may ionize the neutral gas molecule. The probability of ionization collision occurring, denoted as P , is given by:

$$P = 1 - e^{-dSn} \quad (1)$$

where d represents the distance traveled by the electron, S denotes the ionization collision cross-section, and n stands for the density of neutral gas molecules. In the ionization process, in addition to providing the threshold energy for ionization, the remaining energy of the incident electron is distributed among the scattered electron and the newly created electrons due to ionization. According to Ref. [23], the energy of the newly created electrons due to ionization is:

$$E_{\text{new}} = B(E_{\text{inc}}) \tan \left[\text{Rarc} \tan \left(\frac{E_{\text{inc}} - E_{\text{ioc}}}{2B(E_{\text{inc}})} \right) \right], \quad (2)$$

where $B(E_{\text{inc}})$ represents a known function [24] (e.g., for argon, $B(E_{\text{inc}}) \cong 10$ eV over a range of 1–70 eV), E_{inc} denotes the incident electron energy, and R is a uniformly distributed random number between 0 and 1. Consequently, the scattered electron energy E_{scat} is given by:

$$E_{\text{scat}} = E_{\text{inc}} - E_{\text{th}} - B(E_{\text{inc}}) \tan \left[\text{Rarc} \tan \left(\frac{E_{\text{inc}} - E_{\text{ioc}}}{2B(E_{\text{inc}})} \right) \right], \quad (3)$$

in Formula 3, E_{th} represents the ionization threshold energy. The velocity direction of the scattered electrons and newly generated electrons after ionization can be determined using an elastic collision model [23], resulting in:

$$\begin{aligned} \frac{\mathbf{v}'}{|\mathbf{v}'|} = & \frac{v_{\text{inc}}}{|v_{\text{inc}}|} \cos \chi + \left(\frac{v_{\text{inc}}}{|v_{\text{inc}}|} \times \mathbf{i} \right) \frac{\sin \chi \sin \phi}{\sin \theta} \\ & + \frac{v_{\text{inc}}}{|v_{\text{inc}}|} \times \left(\mathbf{i} \times \frac{v_{\text{inc}}}{|v_{\text{inc}}|} \right) \frac{\sin \chi \cos \phi}{\sin \theta} \end{aligned} \quad (4)$$

where $\cos \chi = \frac{2+E-2(1+E)^R}{E}$, E represents the electron's energy, ϕ is a uniformly distributed random number between $[0, 2\pi]$, and $\cos \theta = \mathbf{v}_{\text{inc}} \cdot \mathbf{i}$ where \mathbf{i} is the unit vector along the x -axis, v_{inc} , and \mathbf{v}' are the initial and final electron velocities, respectively. If E corresponds to the energy of the scattered electron, then \mathbf{v}' is the velocity of the scattered electron. If E represents the energy of a newly generated ionized electron, then \mathbf{v}' is the velocity of the new electron. Since the mass of ions is much greater than that of electrons, their velocities remain nearly the same as the velocities of the gas molecules before the collision. Consequently, the velocities of newly generated ions follow the Maxwell distribution with respect to gas temperature.

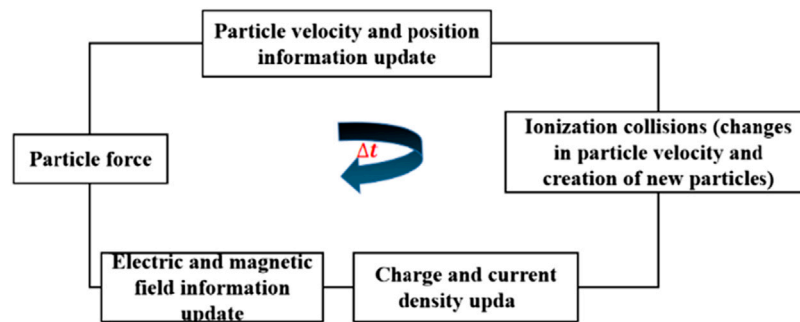


FIGURE 1
PIC/MCC basic algorithm flow chart.

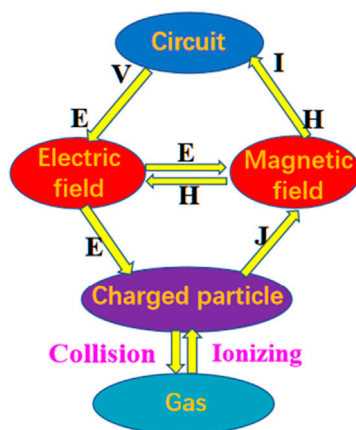


FIGURE 2
Theoretical framework for the fully coupled system of road-field-particle collaborative simulation.

2.2 Road-field-PIC/MCC collaborative method

Figure 1 depicts the fundamental workflow of the fully three-dimensional electromagnetic PIC/MCC algorithm. In the traditional electromagnetic PIC algorithms, the electric and magnetic fields are updated using charge and current density. Subsequently, these fields are used to calculate the forces acting on charged particles, leading to updates in particle velocity and position information. This, in turn, updates the charge and current density, creating a cyclic process. In the electromagnetic PIC/MCC algorithm, an ionization collision module is introduced between the particle velocity and position processing module and the charge and current density processing module. When the particle and gas collision probability given by Formula 1 is satisfied, this module processes the ionization collision process based on Eqs 2–4, generating new particles and further updating particle velocities.

Figure 2 illustrates the theoretical framework for the fully coupled system of road-field-PIC/MCC collaborative simulation. From the diagram, it is evident that the electric and magnetic fields serve as bridges between the circuit module and the charged particle module. In the circuitry, the connection nodes coupled with the PIC/MCC modules are initially determined, and interactive excitation ports are constructed

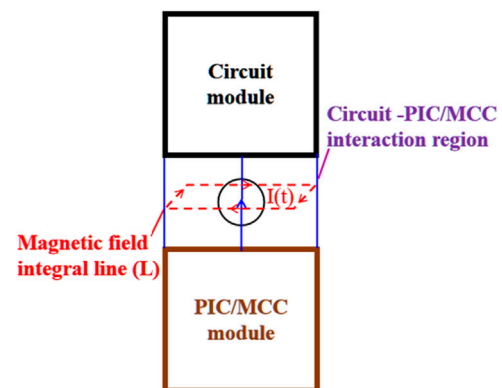


FIGURE 3
Integration approach of the circuit module with PIC/MCC.

within the PIC/MCC modules. At each time step of the collaborative computation, the PIC/MCC module can be regarded as the load for the circuit module, while the circuit module can be seen as the excitation input source for the PIC/MCC module. The voltage V calculated at the circuit module connection nodes serves as the input condition for the corresponding excitation port within the PIC/MCC module. Subsequently, the electric field E is determined based on the electric field distribution at the excitation port and coupled into the electromagnetic field. In contrast to electromagnetic field simulation, the current in the PIC/MCC simulation is influenced not only by the vacuum impedance of the devices but also by the motion of charged particles generated through gas collision ionization. Charged particles are propelled by the electromagnetic field, and conversely, the motion of charged particles also affects the electromagnetic field. This, in turn, impacts the current at the interaction excitation ports. By incorporating this current into the circuit's solution, the road-field-PIC/MCC collaborative simulation can be effectively realized. Referring to Norton's equivalent circuit theory [25], the role of the PIC/MCC grid on circuit devices can be summarized as its effect on the magnetic field around the circuit devices, as depicted in Figure 3. According to Ampere's law, the equivalent current is:

$$I(t) = \int_L \vec{H}(t) \cdot d\vec{L} \quad (5)$$

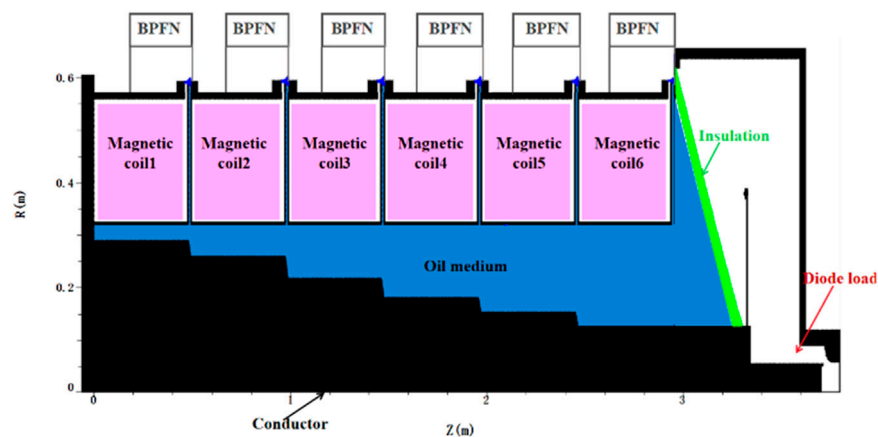


FIGURE 4
Depicts a cross-sectional view of the pulsed particle beam generator.

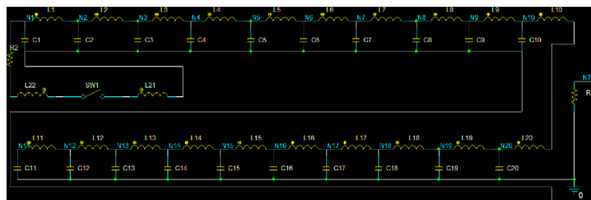


FIGURE 5
Illustrates the equivalent circuit of the Blumlein pulse forming network.

where L represents the perimeter of the grid cross-section surrounding the circuit component.

Generally speaking, the PIC/MCC time step is significantly smaller than the time step of the circuit iteration. Furthermore, for the sake of collaborative simulation, the circuit's iteration time step naturally needs to be the same as the PIC/MCC simulation's time step.

3 Numerical simulation study

In the previous section, the theory and implementation process of the road-field-PIC/MCC collaborative simulation method is described in detail. Now, this methodology will be employed to conduct a simulation study on the gas ionization within the LTD pulsed electron beam generation device.

First, the LTD pulse EBG as shown in Figure 4 was constructed. The device mainly consists of six linear transformer driver (LTD) cavities, an insulator, and a diode load. Each LTD cavity is composed of two Blumlein pulse forming networks (BPFNs) in parallel through the laser-triggered switch, along with corresponding magnetic coils, and oil media. When each BPFN of the LTD cavity was charged to 140 kV, the laser start operating via the control signal, the laser triggered switches is closing, and then, six LTD cavities discharge to the load (such as foil-less diode).

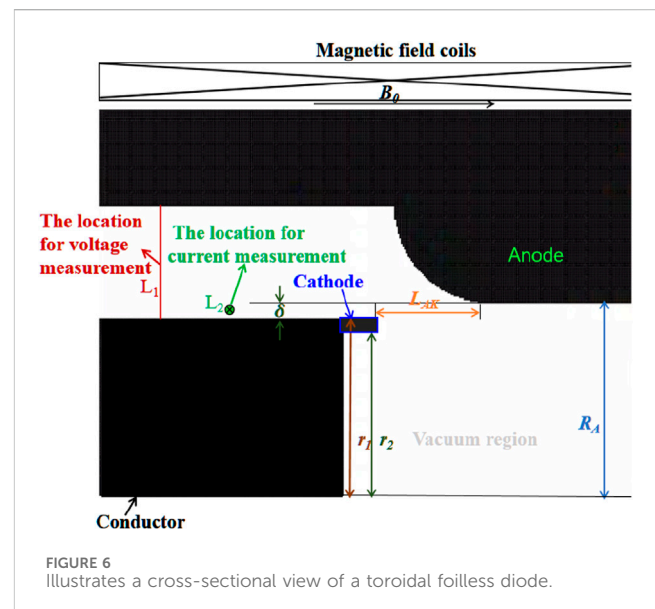


FIGURE 6
Illustrates a cross-sectional view of a toroidal foilless diode.

Figure 5 shows the equivalent circuit of a compact BPFN, each BPFN consists of 20 identical inductors ($L1-L20$) with a value of 84 nH, 20 identical capacitors ($C1-C20$) with a value of 0.85 nF, switch SW1, the load resistance $R1$, and the additional inductance of various wires and switches ($L21-L22$) is 175 nH, $R2$ is the additional resistance of roughly 0.01 Ω .

When utilizing an n -section uniform network, the pulse width τ and impedance Z are, respectively [26]:

$$\tau = 2n\sqrt{LC} \quad (6)$$

$$Z = \sqrt{L/C} \quad (7)$$

where n is the number of stages ($n = 10$ in Figure 5), L is the inductor of each stage, and C is the capacitor of each stage. According to Eq. 7, the load resistance of each BPFN can be calculated as 20 Ω . Each LTD cavity includes two BPFNs connected in parallel, and the effective load resistance of each LTD cavity is 10 Ω . With six

LTDs in series, the entire device has an equivalent load of 60 Ω . Additionally, the magnetic coils are constructed from a magnetic core material with a relative permeability μ_r of 1,000, and the dielectric material has a relative permittivity ϵ_r of 2.5.

Figure 6 shows a schematic of the annular beam foil-less diode. The grid spacing in the PIC/MCC simulation region is 0.5 mm in the z -direction, 0.5 mm in the r -direction, and 1° in the ϕ -direction. According to Ref. [27], the convergence conditions for the FDTD algorithm are as follows:

$$\Delta t \leq \frac{1}{c} \cdot \frac{1}{\sqrt{\frac{1}{\Delta r^2} + \frac{1}{\Delta z^2} + \frac{1}{\Delta \phi^2}}} \quad (8)$$

where c represents the speed of light, Δr denotes the unit length in the R direction for the PIC/MCC algorithm's cell, Δz represents the unit length in the Z direction for the PIC/MCC algorithm's cell, and $\Delta \phi$ signifies the unit arc length in the ϕ direction for the PIC/MCC algorithm's cell. To ensure satisfaction of the convergence conditions for the PIC/MCC algorithm, the time step size must be kept smaller than the maximum value of Δt . According to Formula 8, We can calculate that the maximum value of Δt is approximately 1.1785×10^{-12} s. In simulation computations, to ensure algorithm convergence, it is generally required that the iteration time step does not exceed the maximum value of Δt . In this paper, the total iteration time is 360×10^{-9} s with 433,728 iterations, resulting in an iteration time step of approximately 8.30×10^{-13} s. Consequently, PIC/MCC inherently guarantees the convergence of the algorithm.

In the collaborative simulation of the circuit-field-particle, the time iteration step of the circuit is set to be the same as the PIC/MCC simulation time step to achieve collaborative simulation goals. Therefore, the PIC/MCC simulation time step Δt and the time step h for the circuit module satisfy the condition $\Delta t = h$. Regarding the convergence conditions for the enhanced nodal analysis algorithm, they are outlined in Refs. [28, 29].

$$V^n - V^{n-1} \leq RELTOL \cdot \max(V^{n-1}, V^n) + ABSTOL \quad (9)$$

where n represents the current time iteration step, $n - 1$ denotes the previous time iteration step, $RELTOL$ is the relative error precision in the algorithm's convergence parameters with a default value of 0.005, and $ABSTOL$ is the absolute error precision in the algorithm's convergence parameters with a default value of 1×10^{-6} . In the enhanced nodal analysis algorithm, during the linearization calculation of nonlinear components in the circuit, linearization processing is conducted based on the backward Euler equation [30].

The differential formula for the current and voltage on the capacitor is as follows:

$$I(t) = C \cdot \frac{dV(t)}{dt} \quad (10)$$

where $I(t)$ represents the instantaneous current flowing through the capacitor, C stands for capacitance value, $V(t)$ denotes the instantaneous voltage across the capacitor, and $(dV(t))/dt$ signifies the time derivative of the voltage across the capacitor.

Further linearizing the Formula 10 using the backward Euler method and circuit theory yields:

$$I^n = \left(\frac{C}{h}\right) \cdot V^n - \left(\frac{C}{h}\right) \cdot V^{n-1} \quad (11)$$

where h is the time step, and (C/h) can be considered as the equivalent conductance G_{eq} , Formula 11 can be written as:

$$V^n - V^{n-1} = \left(\frac{h}{C}\right) I^n \quad (12)$$

Substituting Eq. 12 into Eq. 9 yields:

$$\left(\frac{h}{C}\right) I^n \leq 0.005 \cdot \max(V^{n-1}, V^n) + 1 \times 10^{-6} \quad (13)$$

Considering that the capacitance in LTD pulse power devices is typically in the order of nanofarads (nF), as indicated in the manuscript with a capacitance value of 0.85×10^{-9} F, and h represents the time step, set to 8.30×10^{-13} s in this study, substituting these values into the Eq. 13, we obtain:

$$0.00097647 I^n \leq 0.005 \cdot \max(V^{n-1}, V^n) + 1 \times 10^{-6} \quad (14)$$

Taking into account the discharge of capacitors in the circuit, current flow through resistors and loads, there will inevitably be energy losses. In extremely small time iteration steps, the corresponding current is certainly smaller than the corresponding voltage values. As indicated by the Eq. 14, this convergence relationship is guaranteed to be satisfied. Therefore, the overall algorithm convergence is fulfilled, and the algorithm is stable.

In [31, 32], the structure of the cathode and anode determines the electric field distribution inside the diode, as well as its beam characteristics and energy output efficiency of the diode. Taking into account that the diode will generate an annular electron beam, the thickness of the cathode ring cannot exceed the width of the radial gap between the cathode and anode. Therefore, after comprehensive consideration, δ is set to 5 mm, the radius of the anode drift tube R_A was 60 mm, the outer radius of the cathode r_1 was set to 55 mm, the inner radius of the cathode r_2 was set to 51 mm, and the guiding magnetic field B_0 was selected as 1.8 T, L_1 and L_2 represent the locations for voltage and current measurements, respectively. The threshold for cathode explosive emission is set at 150 kV/cm [33].

According to Ref. [22], with the same LTD driving conditions and keeping the other dimensions of the diode unchanged, the horizontal distance L_{AK} between the cathode and anode of the loaded diode is set to 36 mm, the entire device achieves impedance matching, and exhibits higher electron energy output, the overall simulation results closely align with experimental findings. As mentioned earlier, the charging voltage for each stage capacitor is 140 kV, and considering losses, the actual input voltage for the diode is approximately 810 kV. In the background of neutral argon gas, at a gas pressure of 2 Pa, the simulated particle spatial distribution is illustrated in Figure 7.

From Figure 7, it can be observed that, without considering gas ionization breakdown, under the influence of the electric field, the energy of electrons and Ar^+ ions are in the same order of magnitude. However, the mass of Ar^+ ions is much greater than that of electrons, the momentum of Ar^+ ions is significantly greater than that of electrons. This implies that the cyclotron radius of Ar^+ ions is much larger than that of the electron beam. The guiding magnetic field is

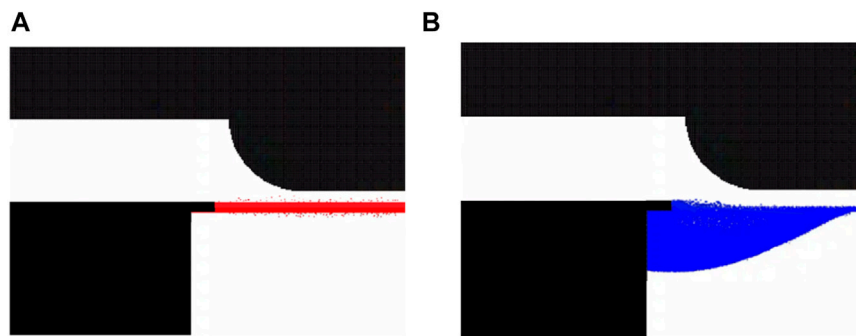


FIGURE 7
Particle spatial distribution chart (A) electrons; (B) Ar^+ .

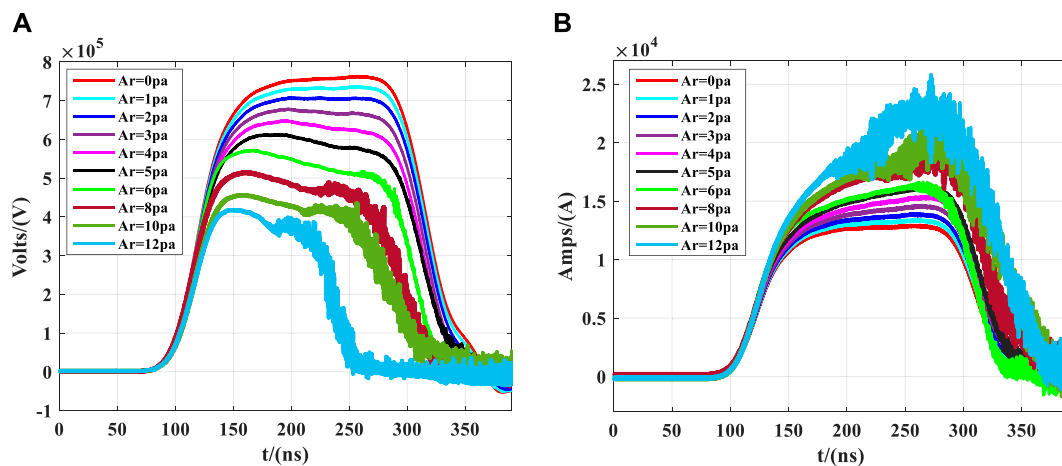


FIGURE 8
Voltage and current with different Argon gas pressures (A) voltage (B) current.

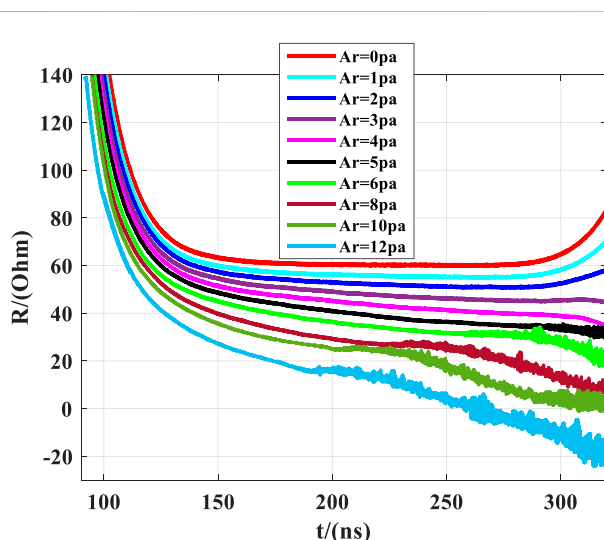


FIGURE 9
Impedance of the diode filled with argon gas at different pressures.

1.8 T, the cyclotron radius of Ar^+ ions is far larger than the thickness of the electron beam. Consequently, the thickness of the Ar^+ ion beam is greater than that of the electron beam, which aligns with Figure 7. Moreover, with increasing gas pressure upon injection, collisions become more intense, leading to a greater extent of particle diffusion. However, the field's constraint on electrons still surpasses that on ions. In the background of argon gas within the range of 0.1–10 Pa, the density varies from $6 \times 10^{16} \text{ m}^{-3}$ to $2 \times 10^{18} \text{ m}^{-3}$. This range aligns with references [34–36], where the density of plasma generated by collisions between relativistic electron beams and background gases falls within a crucial range, changing within the range of $1 \times 10^{15} \text{ m}^{-3}$ to $2 \times 10^{18} \text{ m}^{-3}$. According to reference, plasma within this range has a significant impact on the power output of microwave devices. In the backdrop of neutral argon gas ranging from 0.1 to 10 Pa, the total energy of electrons fluctuates within the range of 4.15 eV to 3 eV, and it diminishes with increasing pressure. The recorded electron energy encompasses both low-energy and high-energy electrons. In the neutral argon gas background ranging from 0.1 to 10 Pa, the ion energy fluctuates within the range of 1.8 eV–0.25 eV, and it decreases as the pressure increases.

TABLE 1 Voltage pulse width under different gas pressures.

Ar/(Pa)	0	1	2	3	4	5	6	8	10	12
Pulse width/(ns)										
Half-pulse width	191.1	189	188.2	186.1	184.9	183.4	182.6	172.4	160	119.5
Pulse peak width	83.0	81.9	80.8	79.6	79.1	78.9	77.5	76.5	60.2	57.4

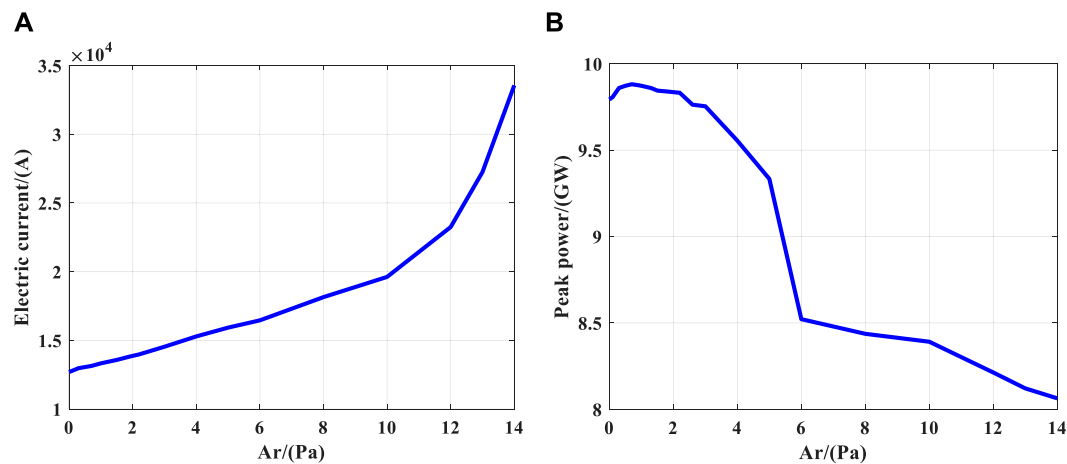


FIGURE 10 Relationship between diode performance and different argon gas pressures (A) beam current, (B) peak power.

Subsequently, simulations were conducted on the pulsed power electron beam generator under varying levels of argon gas infusion, the voltage and current were measured as illustrated in Figure 8. From Figure 8A, the voltage amplitude gradually decreased with the increase of the pressure of filled argon, and the greater the pressure of argon, the more drastic the decline in amplitude. Figure 8B demonstrates that the quality of the current decreases as the pressure increases after argon is filled. Utilizing the measured voltage and current, impedance was computed, as depicted in Figure 9, and in the presence of argon gas at a pressure of 8–12 Pa, there are minor peaks observed. However, due to the influence of the plasma, the pulse width of the output waveform decreases, and the small peaks shift forward, becoming less conspicuous. According to Refs. [15, 37], this is because the quality of the electron beam is contingent upon the quality of the voltage waveform. In previous studies, high-power microwave devices and diodes were typically subjected to fitting ideal and stable voltage output waveforms, neglecting the influence of load characteristics, plasma collisions, and other physical phenomena on the output waveform of the front-end pulse. Figure 8 reiterates that when driving the load with a pulse power source, there is a mutual influence between the load and the pulse generator.

According to Refs. [22, 38], under vacuum conditions, the impedance of the diode is 60 Ω when it is stable, and the entire device is in the impedance matching state. However, upon the introduction of argon gas, the impedance decreases with the increasing gas pressure due to electron collisions with argon atoms, thereby impacting the quality of the electron beam and resulting in a reduction in voltage, as gas infusion continues, the collision-generated charged particles increase, leading to an augmentation in the measured

current, ultimately resulting in a decrease in impedance as the gas pressure increases. This impedance reduction, in turn, leads to an overall impedance mismatch within the system. On one hand, this characteristic of decreased impedance feeds back into the Blumlein pulse forming network (BPFN) within the Linear Transformer Driver (LTD). On the other hand, due to the impedance mismatch, electromagnetic wave reflections occur, with the reflected waves superimposing upon the waveforms generated by the LTD. Consequently, based on these two aspects, the reduced load impedance leads to a decrease in the measured voltage, and the superimposition of reflected waves with the LTD-generated waveforms exacerbates the reduction in voltage amplitude. Furthermore, with the increasing gas pressure infusion, within the range of 2–12 Pa, the voltage waveform exhibits a phenomenon of apex reduction. This phenomenon arises from intensified plasma collisions, exacerbating the impedance mismatch and thereby affecting the stable and smooth apex of the pulse waveform.

According to the literature [26], the pulse width should be calculated based on Formula 6, and it can be seen that the pulse width is only related to the capacitance and inductance values as well as the number of stages in the BPFN pulse network circuit. However, from the voltage waveform and Table 1, it can be observed that both the half-width and full-width of the pulse waveform decrease. Additionally, at higher argon gas pressures, the pulse width decreases more rapidly. This is because collisions between electrons and gas produce charged particles. As simulation time increases, collisions intensify, and the charged particles form a plasma that fills the cavity of the foil-less diode. This plasma has electrical conductivity, causing the diode anode and cathode to enter a conductive state, equivalent to a load approaching a short

circuit. This process leads to a decrease in the measured voltage amplitude, which is the reason for the reduction in pulse width. Furthermore, as the gas pressure increases, for instance, within the range of 2–12 Pa, the voltage waveform exhibits a phenomenon where the top is lowered. This occurs because intensified plasma collisions result in impedance mismatch, thereby affecting the stability and smoothness of the waveform's peak.

In addition, the relationship between the diode electron beam current and peak power with argon gas pressure was also recorded, as shown in Figure 10A the horizontal axis represents the argon gas pressure value. The charged particles generated by electron-ionization of the gas help neutralize the space charge effect of the electron beam, which aids in breaking the constraint imposed by space charge limitations and effectively increases the current magnitude [19]. Figure 10A confirms this phenomenon by showing that the current increases with increasing argon gas pressure, consistent with the experiment in Ref. [20]. Figure 10B illustrates the relationship between peak power and pressure, demonstrating that when a small amount of argon gas is filled, the peak power slightly increases with pressure. This is because the plasma generated by the ionization of a small amount of argon gas can improve both the electron beam quality and current magnitude. However, when an excessive amount of argon gas is filled, intense collisions lead to a decrease in electron beam quality, resulting in a reduction in power. Upon the infusion of argon gas at a pressure range of 6–10 Pa, the diode's peak power gradually diminishes.

4 Conclusion

This study investigated an improved nodal analysis method and a PIC/MCC simulation method, developing a self-consistent simulation approach for gas ionization in pulsed power electron beam generators the Circuit-Field-PIC/MCC simulation method. Using this method, simulations were conducted on a pulsed power electron beam generator under different argon gas pressures. The results revealed that filling the gas could effectively increase the current magnitude while reducing the voltage amplitude, subsequently lowering the impedance of the diode. In addition, a small amount of gas could increase the peak power, but excessive gas led to a decrease in peak power. There was also a noticeable reduction in pulse width, which was related to the plasma formed by particle-gas collisions. As the load impedance decreased, even approaching a short-circuit condition, it reduced the measured voltage amplitude and consequently caused changes in the pulse width. Furthermore, a top voltage drop phenomenon occurred due to the impedance mismatch caused by the plasma generated from particle-gas collisions. These findings provide valuable insights for future comprehensive simulations of high-power microwave devices driven by pulsed power sources.

References

1. Mankowski J, Kristiansen M. A review of short pulse generator technology. *IEEE Trans Plasma Sci* (2000) 28(1):102–8. doi:10.1109/27.842875
2. Schamiloglu E, Barker RJ, Gundersen M, Neuber AA. Modern pulsed power: charlie martin and beyond. *Proceedings of the IEEE* (2004) 92(7):1014–20. doi:10.1109/JPROC.2004.829058
3. Gao S, Moez K. A 2.12-V vpp 11.67-pJ/pulse fully integrated UWB pulse generator in 65-nm CMOS technology. *IEEE Trans Circuits Syst Regular Pap* (2020) 67(3):1058–68. doi:10.1109/TCSI.2019.2955693
4. Weinbrecht EA, McDaniel DH, Bloomquist DD. The Z refurbishment project (ZR) at sandia national laboratories. In: Proceedings of the Digest of Technical Papers. PPC-2003, in 14th IEEE International Pulsed Power Conference (IEEE Cat. No.03CH37472); June 2003; Dallas, TX, USA (2003). p. 157–62. doi:10.1109/PPC.2003.1277682
5. Sato H, Minamitani Y. Output characteristics of bipolar pulse from high-frequency burst pulse generator constructed by nonlinear LC ladders using magnetic switches. *IEEE Trans Plasma Sci* (2020) 48(1):204–11. doi:10.1109/TPS.2019.2957524

Data availability statement

The original contributions presented in the study are included in the article/Supplementary material, further inquiries can be directed to the corresponding author.

Author contributions

QL: Conceptualization, Data curation, Formal Analysis, Investigation, Methodology, Software, Validation, Visualization, Writing—original draft, Writing—review and editing. DL: Methodology, Supervision, Writing—review and editing. FX: Funding acquisition, Supervision, Writing—review and editing. LL: Funding acquisition, Methodology, Project administration, Resources, Supervision, Writing—review and editing. HW: Supervision, Visualization, Writing—review and editing.

Funding

The author(s) declare financial support was received for the research, authorship, and/or publication of this article. This work was supported by Science and Technology on High Power Microwave Laboratory Fund (61426050106-202101), and the National Natural Science Foundation of China (Grant No: 12175216 and 12075051). This study also received financial support from the National Natural Science Foundation of China (Grant No: 12375249).

Conflict of interest

The authors declare that the research was conducted in the absence of any commercial or financial relationships that could be construed as a potential conflict of interest.

Publisher's note

All claims expressed in this article are solely those of the authors and do not necessarily represent those of their affiliated organizations, or those of the publisher, the editors and the reviewers. Any product that may be evaluated in this article, or claim that may be made by its manufacturer, is not guaranteed or endorsed by the publisher.

6. Cook D. Z, ZX, and X-1: a realistic path to high fusion yield, Digest of Technical Papers. In: Proceedings of the 12th IEEE International Pulsed Power Conference. (Cat. No.99CH36358); June 1999; Monterey, CA, USA (1999). p. 33–7. doi:10.1109/PPC.1999.825419
7. Selvakumar D, Madanmohan B. Impact of loading effect from liquid foods on the performance of unipolar and bipolar square pulse generator. *Arab J Sci Eng* (2022) 47: 14315–26. doi:10.1007/s13369-022-06741-5
8. Kumar M, Mishra A. Multiphysics analysis of reversible electroporation and electrodeformation of cervical cells using a nanosecond pulse generator. *IEEE Trans Plasma Sci* (2023) 51(2):534–43. doi:10.1109/TPS.2023.3235373
9. Sinars DB, Sweeney MA, Ampleford DJ, Ao T, Apruzese JP, Armstrong DJ, et al. Review of pulsed power driven high energy density physics research on Z at Sandia. *Phys Plasmas* (2020) 27(7):070501. doi:10.1063/5.0007476
10. Novac BM, Kumar R, Smith IR. A tesla-pulse forming line plasma opening switch pulsed power generator. *Rev Sci Instrum* (2010) 81(10):104704. doi:10.1063/1.3484193
11. Li Z, Yang J, Liu L. A compact repetitive PFN-marx generator. In: Proceedings of the 2015 IEEE International Conference on Plasma Sciences (ICOPS); May 2015; Antalya, Turkey (2015). p. 1. doi:10.1109/PLASMA.2015.7180009
12. Li H, Ryoo H-J, Kim J-S, Rim G-H, Kim Y-B, Deng J. Development of rectangle-pulse Marx generator based on PFN. *IEEE Trans Plasma Sci* (2009) 37(1):190–4. doi:10.1109/tps.2008.2007730
13. Kim AA, Kovalchuk BM, Bastrikov AN, Durakov VG, Volkov SN, Sinebryukhov VA. 100 ns current rise time LTD stage. In: Proceedings of the PPPS-2001 Pulsed Power Plasma Science 2001. 28th IEEE International Conference on Plasma Science and 13th IEEE International Pulsed Power Conference. Digest of Papers (Cat. No.01CH37251); June 2001; Las Vegas, NV, USA (2001). p. 1491–4.
14. Kim AA, Kovalchuk BM, Kumpjak EV, Zoi NV. 0.75 MA, 400 ns rise time LTD stage, Digest of Technical Papers. 12th IEEE International Pulsed Power Conference. (Cat. No.99CH36358). *Proc 12th IEEE Int Pulsed Power Conf* (1999) 2:955–958. doi:10.1109/PPC.1999.823675
15. Kiziridi PP, Ozur GE. Formation of a non-relativistic, high-current electron beam in a gas-filled diode. *Russ Phys J* (2023) 65:1619–24. doi:10.1007/s11182-023-02810-w
16. Arai H, Hotta H. Ionization of gases by a pulsed electron beam as studied by self-focusing. III. He, Ar, and O₂ mixtures. *J Chem Phys* (1981) 75:3876–81. doi:10.1063/1.442544
17. Hammer DA, Kapetanakis CA, Ury M. Formation of ionization channel in high-pressure gas using pulsed relativistic electron beam. *J Appl Phys* (1973) 44:1121–7. doi:10.1063/1.1662316
18. Qian BL, Li CL, Liu YG, Zhang JD, Tan QM, Liu JL, et al. Experiment on the plasma-loaded backward-wave oscillator using a gas-loaded foil-less diode. *J Appl Phys* 1 September (2000) 88(5):3059–63. doi:10.1063/1.1288695
19. Nusinovich GS, Carmel Y, Antonsen TM, Goebel DM, Santoru J. Recent progress in the development of plasma-filled traveling-wave tubes and backward-wave oscillators. *IEEE Trans Plasma Sci* (1998) 26(3):628–45. doi:10.1109/27.700799
20. Thumm MK, Kasperek W. Passive high-power microwave components. *IEEE Trans Plasma Sci* (2002) 30(3):755–86. doi:10.1109/TPS.2002.801653
21. Ho C-W, Ruehli A, Brennan P. The modified nodal approach to network analysis. *IEEE Trans Circuits Syst* (1975) 22(6):504–9. doi:10.1109/TCS.1975.1084079
22. Li Q, Xiang F, Liu D, Liu L, Wang H. Optimization research of pulse power device based on road-field-particle collaborative simulation. *IEEE Trans Plasma Sci* (2023) 51(8):2237–44. doi:10.1109/TPS.2023.3297257
23. Vahedi V, Surendra M. A Monte Carlo collision model for the particle-in-cell method: applications to argon and oxygen discharges. *Comp Phys Commun* (1995) 87(1-2):179–98. doi:10.1016/0010-4655(94)00171-W
24. Opal CB, Peterson WK, Beaty EC. Measurements of secondary-electron spectra produced by electron impact ionization of a number of simple gases. *J Chem Phys* (1971) 55(8):4100–6. doi:10.1063/1.1676707
25. Kuo C-N, Houshmand B, Itoh T. FDTD analysis of active circuits with equivalent current source approach. In: Proceedings of the IEEE Antennas and Propagation Society International Symposium. 1995 Digest; June 1995; Newport Beach, CA, USA (1995). p. 1510–3. doi:10.1109/APS.1995.530863
26. Li H, Ryoo HJ, Kim JS, Rim GH, Kim YB, Deng J. Development of rectangle-pulse marx generator based on PFN. *IEEE Trans Plasma Sci* (2009) 37(1):190–4. doi:10.1109/TPS.2008.2007730
27. Yee K. Numerical solution of initial boundary value problems involving Maxwell's equations in isotropic media. *IEEE Trans Antennas Propag* (1966) AP-14(3):302–7. doi:10.1109/TAP.1966.1138693
28. Shang ZQ. The convergence problem in SPICE. In: Proceedings of the IEE Colloquium on SPICE: Surviving Problems in Circuit Evaluation; June 1993; London, UK (1993). p. 10/1–10/5.
29. McDonald RJ. Convergence in SPICE for advanced IC device modelling. In: Proceedings of the Conference Proceedings '88., IEEE Southeastcon; April 1988; Knoxville, TN, USA (1988). p. 349–52. doi:10.1109/SECON.1988.194875
30. Wilson P, Alan Mantooth H. Chapter 3 - design analysis. In: *Model-based engineering for complex electronic systems*. San Francisco, California: Academia.edu (2013). p. 27–78. doi:10.1016/B978-0-12-385085-0.00003-8
31. Miller RB, Prestwich KR, Poukey JW, Shope SL. Production of annular electron beams by foilless diodes. *J Appl Phys* (1980) 51(7):3506–15. doi:10.1063/1.328203
32. Turchi PJ, Peterkin RE. Modeling of impedance collapse in high-voltage diodes. *IEEE Trans Plasma Sci* (1998) 26(5):1485–91. doi:10.1109/27.736043
33. Rose DV, Welch DR, Oliver BV, Leckbee J, Maenchen J, Johnson D, et al. Numerical analysis of a pulsed compact LTD system for electron beam-driven radiography. *IEEE Trans Plasma Sci* (2006) 34(5):1879–87. doi:10.1109/TPS.2006.881297
34. Carmel Y, Minami K, Kehs R, Destler W, Granatstein V, Abe D, et al. Demonstration of efficiency enhancement in a high-power backward-wave oscillator by plasma injection. *Phys Rev Lett* (1989) 20:2389–392. doi:10.1103/PhysRevLett.62.2389
35. Antonsen TM, Mora P. self-focusing and Raman-scattering of laser-pulses in tenuous plasmas. *Phys Rev Lett* (1992) 15:2204–7. doi:10.1103/PhysRevLett.69.2204
36. Tkach Yu V, Fainberg Yu A, Magda, Igor I, Gaponenko NI, Skachek GV, et al. Microwave emission in the interaction of a high-current relativistic beam with a plasma-filled slow-wave structure. *Physics.Soviet J plasma Phys* (1975) 1:43. <https://api.semanticscholar.org/CorpusID:119041565>.
37. Wang P, Xiang F, Wang G, Tan J, Luo M, Kang Q. Analyzing and improving the output waveform of linear transformer driver cavity. *IEEE Trans Plasma Sci* (2020) 48(11):3950–5. doi:10.1109/TPS.2020.3027884
38. Kiziridi PP, Ozur GE. Production of low-energy, high-current electron beams in a gun with a controlled explosive emission cathode. *Vacuum* (2021) 194(110560):110560. doi:10.1016/j.vacuum.2021.110560



OPEN ACCESS

EDITED BY

Mohamed Mokhtar Hefny,
Future University in Egypt, Egypt

REVIEWED BY

Sergey Macheret,
Purdue University, United States
Richard Van De Sanden,
Dutch Institute for Fundamental Energy
Research, Netherlands

*CORRESPONDENCE

Savino Longo,
✉ savino.longo@uniba.it

RECEIVED 27 February 2024

ACCEPTED 22 March 2024

PUBLISHED 05 April 2024

CITATION

Longo S (2024), The spark of life: discharge
physics as a key aspect of the
Miller–Urey experiment.
Front. Phys. 12:1392578.
doi: 10.3389/fphy.2024.1392578

COPYRIGHT

© 2024 Longo. This is an open-access article
distributed under the terms of the [Creative
Commons Attribution License \(CC BY\)](#). The use,
distribution or reproduction in other forums is
permitted, provided the original author(s) and
the copyright owner(s) are credited and that the
original publication in this journal is cited, in
accordance with accepted academic practice.
No use, distribution or reproduction is
permitted which does not comply with these
terms.

The spark of life: discharge physics as a key aspect of the Miller–Urey experiment

Savino Longo^{1,2*}

¹Dipartimento di Chimica, Università degli Studi di Bari Aldo Moro, Bari, Italy, ²Istituto per la Scienza e Tecnologia dei Plasmi—Consiglio Nazionale delle Ricerche, Bari, Italy

The Miller–Urey experiment demonstrated the possibility of producing biomolecules from the chemical components of the primordial atmosphere, using an electric discharge. It profoundly influenced the development of prebiotic chemistry and astrobiology. The essential aspect of the experiment is the action of the electric field on a gaseous mixture, which produces chemically active species. These last react to ultimately form biomolecules. In this work the hypotheses and methods used to describe the chemical activation of a gas by an electric field, used in computational chemistry and in the physics of electrical discharges, are contrasted, showing that the second provides a much more realistic description of the primary events. A future model should combine the insights of the two communities to bring forth a faithful and insightful description of the experiment, from the primary events to the formation of biomolecules.

KEYWORDS

prebiotic chemistry, Miller–Urey, electric discharge, electric field, modeling, molecular dynamics

1 Introduction

At the beginning of the fifties of the last century, an experiment that combined aspects of chemistry and physics attracted enormous attention, that continues today, and has taken on a paradigmatic role in the research on the origin of life. This is the experiment, or rather the series of experiments conducted by Stanley Miller initially as part of his doctoral thesis under the direction of Harold Urey [1, 2]. It was carried out in an apparatus like a continuous cycle distiller, in which a liquid mixture was brought to the boil in a bottom flask and before being condensed in a water-cooled vapor condenser, was subjected to the action of a pulsed electric discharge, a repeated spark produced by a generator, in an upper flask (Figure 1). The apparatus was filled by a mixture of gases and liquids, based on the hypotheses of the time about the composition of the ancient Earth's atmosphere and strongly influenced by Oparin's work on the origin of life [3]: water, ammonia, hydrogen, and methane. After hundreds of hours of continuous recirculation under the action of the electrical discharge, by performing chemical analysis Miller found that from this chemical mixture some of the basic molecules of life had been formed including amino acids, the constituents of proteins and enzymes.

This experiment, which never fails to be included in a book on the origin of life and astrobiology [4] has produced an immense literature and has even had a great cultural impact. It can be summarized, albeit rather emphatically, as the creation of the molecules of life from the basic molecules of the universe. This experiment has been then repeated, modified, and analyzed from a theoretical point of view with the ideas of chemical kinetics and its methods, more recently with a massive use of computer simulation.

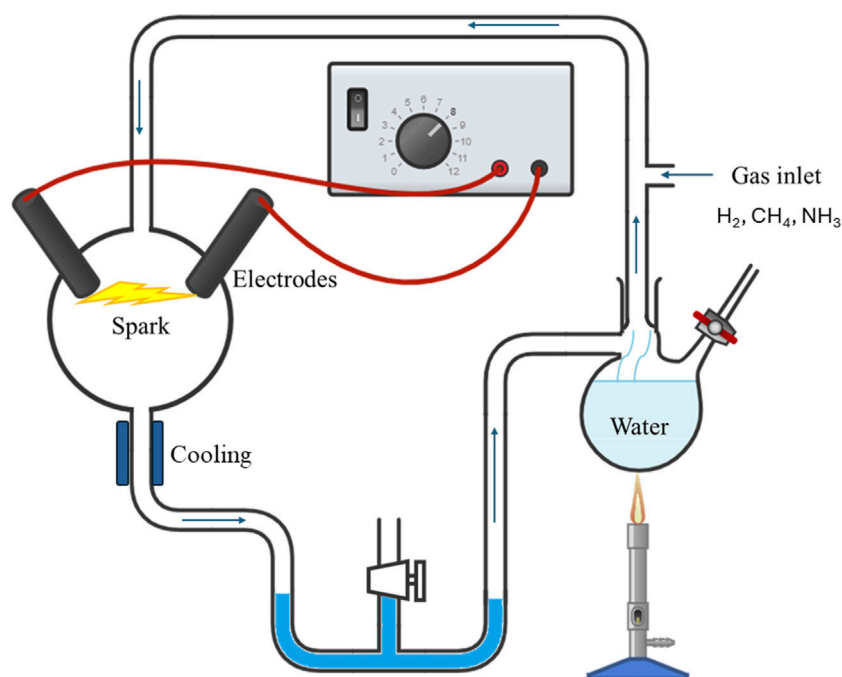


FIGURE 1
Sketch of the Miller-Urey experiment, showing vapor circulation and discharge electrodes. Picture courtesy of Dr. Domenico Aceto, CNR.

2 The role of free electrons

In the Miller-Urey experiment the main source of the events, the cause of the initial chemical activation of the mixture is clearly the population of high energy electrons, in the tens of eV's range, which is produced by the pulsed electric discharge fired in the upper flask. The actual ionization process that occurs in a discharge of this type is a cascade one, in which the electrons are accelerated by the electric field up to kinetic energies sufficient to ionize the neutral species, producing further electrons. Radical formation occurs by several different channels, but all of them are ultimately initiated by the electron impact with a molecule. This phenomenon has been studied by the electrical discharge community for more than a century.

It is known that the fast electrons in an electric discharge are part of the electron energy spectrum, determined by the different collision events and by the electric field [5]. The energy spectrum, also known as electron energy distribution function (EEDF), determines the rate of ionization and dissociation and therefore the formation of radicals. It can be calculated with various numerical methods which have common roots in the Boltzmann transport equation: the celebrated equation formulated 150 years ago, and which provides the very foundation of the kinetic theory of gases [6, 7].

Once the primary processes, those due to electrons, have produced radicals and ions, the chemical reactions downstream can be studied theoretically using the methods of chemical kinetics: the corresponding model is based on a system of coupled differential equations, whose solution is the composition of the gas in function of time [8].

On the other hand, while the description of the primary processes provided by the physics of electrical discharges is rigorous and quantitative, that of chemical kinetics is hindered by the numerous species formed and their complexity, due to the need for data and the complexity of calculation. It has never been attempted for a system of chemical complexity comparable to the Miller-Urey experiment.

3 Computational chemistry's approach to the experiment

In the last two decades, studies of the discharge-induced chemistry based on *ab initio* state-of-the-art methods, in particular molecular dynamics [9], have been very successful in the chemical community [10, 11] and have the potential to adapt to any degree of molecular complexity.

In *ab initio* molecular dynamics, atomic nuclei move according to Newton's equations of motion as classical particles while electrons are described according to quantum mechanics by solving the Schrödinger equation. The advantage of this method over the previously mentioned chemical kinetics is that the individual molecules in the simulation are literally assembled and disassembled at the atomic level, whenever the law of chemistry require so. This way it is no more necessary to predict them at the beginning, to write a scheme like in chemical kinetics, and store their chemical properties in a database.

This approach allows to obtain a theoretical description of chemical reactions based only on the basic law of physics. In principle, future refinements of the methodology and the availability of better computing resources could provide a

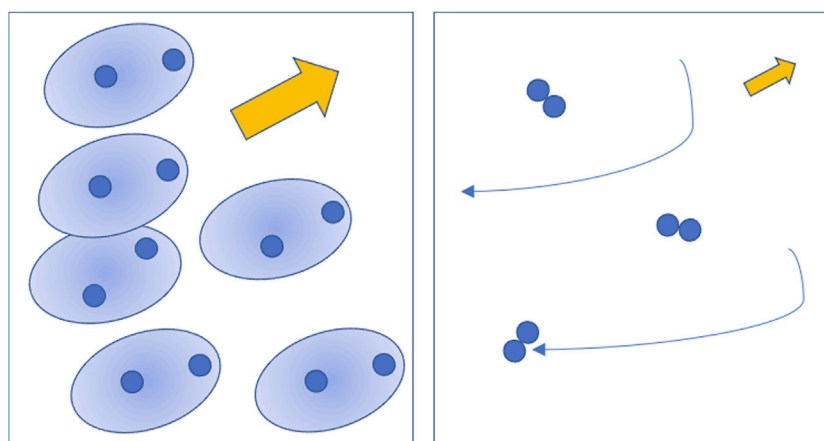


FIGURE 2

Left: sketch of the dissociation process according to the quantum chemical approach, where the electric field alters the molecular wave functions and breaks the chemical bonds. Right: sketch of the dissociation process according to discharge physics, where accelerated free electrons occasionally hit and dissociate molecules. The medium density and the electric field are both about a factor 10^3 lower in the second case compared to the first one. Picture by the author.

complete description of the Miller-Urey experiment using only the initial composition of the gas and an estimate of the electric field applied.

The weak point of this approach is its description of the primary events. Since it does not calculate the energy spectrum of classical electrons, it cannot simulate electron-molecule collisions. Consequently, molecular dynamics simulations of electric-field induced dissociation use *ad hoc* approaches to replace the primary events with others it can describe.

One of such approach is to let the gas molecules dissociate as a direct effect of the electric field. This last modifies the molecular electron charge cloud until molecules break into separated atoms (Figure 2). Quantum calculations show that hydrogen, confined in a space of molecular dimensions, can be ionized by a static field of 0.1 atomic unit, about 5×10^8 V/cm [12] while lower values are required to dissociate molecules. In a well-known *ab initio* simulation of the Miller-Urey experiment [13] the value of the electric field is up to 5×10^7 V/cm, not far from the above estimate and high enough to directly dissociate molecules by breaking polar bonds, like O-H in water.

This description of the initial events is convenient, but the scenario of dielectric breakdown in a gas due to the electron cascade is very different. In a pulsed electric discharge at atmospheric pressure the electric field is close to the dielectric strength [5] of the mixture at standard conditions, whose value is in the range 10^4 V/cm to 10^5 V/cm, three orders of magnitude lower than that assumed in molecular dynamics. The dissociation and ionization of the gas by such a “weak” field is made possible (Figure 2) by the acceleration of free electrons in a medium with a density which is orders of magnitude lower than assumed in molecular dynamics simulations.

These differences are not without consequences: radicals and ions predicted by the two methods are very different, due to *ab initio* models describing the discharge as occurring in the liquid, while in the real experiment it occurs in the vapor [14].

Additionally, the problem with the field remains even assuming that the electric discharge were fired in liquid water: although liquid water density is compatible with molecular dynamics, its dielectric strength is just a little higher than 10^5 V/cm. The reason is that in liquid water the discharge propagates along “streamers”: ionized gas channels produced into the liquid [15, 16].

4 Towards a faithful description of the primary events in the Miller-Urey experiment

The previous sections should have shown that the crux of the problem is the difficulty in describing in a way consistent with physics an electrical discharge in a chemical mixture, which can produce complex molecules. Looking for inspiration, we can look to electrical discharges which provide a radical simplification of the Miller-Urey experiment: those in pure hydrogen, or mixtures of hydrogen with methane.

An extensive literature has been produced in last decades on the models of electric discharges in pure hydrogen and hydrogen/methane, in both cases motivated by the application to the treatment and production of materials. These models calculate the energy spectrum of electrons and in some cases also of ions, based on the transport equation. They include various excited states of the H_2 molecule (vibrational and electronics), the H atom resulting from dissociation, the electrons, typically three kinds of positive ions H^+ , H_2^+ , H_3^+ , of which the last and most complex is often the most abundant, and sometimes also the negative H^- ion. Electrons and ions in these models are subject to tens if not hundreds of different types of collisions with neutrals. For this reason, the models include data for the relevant cross sections, determined by quantum calculations. Among them: ionization, excitation of vibrational and electronic states, direct dissociation, reactions with intermediate electronic excited states [17–19].

The models of discharges in hydrogen-methane mixtures [20–22], the next step toward increasing complexity, add dozens of reactions that describe the production of excited states of CH_4 , of radicals like CH_3 and CH , and of molecular ions such as CH_3^+ which are essential to initiate ionic chemical mechanisms.

This description effort may seem excessive, but it has been demonstrated that in this way it is possible to reproduce very accurately the results of experiments on real electric discharges [23].

The next question is whether it is possible to describe the primary events, and at least the onset of the chemical kinetics, in the complex mixture used by Miller. Indications in this sense have been reported in a recent work [24] where it has been shown that the electron energy spectrum can be determined using state-of-the-art methods for a realistic mixture matching that of the Miller-Urey original experiment and for variants describing less reducing primordial atmospheres. A model including many of the sophistications described above has been developed for lightning in the primordial atmosphere [25]. These works are confirming the specificity and complexity of the scenario produced by the electric discharge: free electrons are essential, the electron distributions are complex and modulate the chemical reactions with different threshold energies; the dissociation and ionization processes involved are numerous and require many cross sections, some of them are poorly known and need new quantum calculations. Another very recent work pointed at the discharge as a key issue in the experiment [26].

However, the problem remains that the formal methods of chemical kinetics employed in the science of electrical discharges are far less versatile than *ab initio* molecular dynamics in describing the formation of complex molecules.

5 Conclusion

The theoretical study of the Miller-Urey experiment has been taken over in recent years by the computational chemistry community, which uses methods able to describe the formation of complex molecules under the effect of an electric field able to dissociate the initial components into more reactive radicals. This created the impression that one could skip interfacing with, and even knowing, the physics of ionized gases, using *ad hoc* solutions to describe the first dissociation events. Unfortunately, this description implies much higher density, stronger field, and faster processes than in the experiment, it ignores the variety of molecular ions, and leads to a deceptive picture of the first chemical events and the environment in which they occur. It must be accepted that much more physics, developed in fields like electric discharges and transport phenomena, is requested to realistically describe the free electrons in the medium and their interaction with the molecules leading to the chemical activation of the mixture.

The type of model that can overcome the difficulties exposed in this work has not yet been created but there are various possibilities in principle. For example, a molecular dynamics simulation could be started based on a description of the gas following primary events, with ions and radicals and excited species, produced by a discharge simulation. One must accept to

pay the computational cost to describe less closely spaced molecules, like in a gas rather than a liquid. Alternatively, one could employ a chemical kinetic description of the kind used in discharge physics, but with the numerous necessary input data provided by molecular dynamics.

The Miller-Urey experiment was a very heterodox experiment right from its initial formulation, joining high voltage components to traditional chemical glassware, and being driven by a vision which is still evocative for researchers and the public. The researchers pursuing an insightful understanding of the Miller-Urey experiment must adopt an interdisciplinary approach. This could bring new kinds of simulation methods, and perhaps new ideas on the birth of biochemistry on our and other planets.

Data availability statement

The original contributions presented in the study are included in the article/Supplementary material, further inquiries can be directed to the corresponding author.

Author contributions

SL: Conceptualization, Formal Analysis, Investigation, Methodology, Resources, Software, Visualization, Writing—original draft, Writing—review and editing.

Funding

The author(s) declare that no financial support was received for the research, authorship, and/or publication of this article.

Acknowledgments

The author thanks Dr. Domenico Aceto, CNR for the realization of Figure 1.

Conflict of interest

The author declares that the research was conducted in the absence of any commercial or financial relationships that could be construed as a potential conflict of interest.

Publisher's note

All claims expressed in this article are solely those of the authors and do not necessarily represent those of their affiliated organizations, or those of the publisher, the editors and the reviewers. Any product that may be evaluated in this article, or claim that may be made by its manufacturer, is not guaranteed or endorsed by the publisher.

References

1. Miller SL. A production of amino acids under possible primitive Earth conditions. *Science* (1953) 117(3046):528–9. doi:10.1126/science.117.3046.528
2. Miller SL, Urey HC. Organic compound synthesis on the primitive Earth. *Science* (1959) 130(3370):245–51. doi:10.1126/science.130.3370.245
3. Oparin AI. *The origin of life on the earth*. 3 (1957).
4. Shaw AM. *Astrochemistry: from astronomy to astrobiology*. New Jersey, United States: John Wiley and Sons (2007).
5. Howatson AM. *An introduction to gas discharges: pergamon international library of science, technology, engineering and social studies*. Amsterdam, Netherlands: Elsevier (1976).
6. Boyle GJ, Stokes PW, Robson RE, White RD. Boltzmann's equation at 150: traditional and modern solution techniques for charged particles in neutral gases. *J Chem Phys* (2023) 159(2):024306. doi:10.1063/5.0153973
7. Vialletto L, Sugawara H, Longo S. Particle propagation and electron transport in gases. *Plasma* (2024) 7(1):121–45. doi:10.3390/plasma7010009
8. Capitelli M, Ferreira CM, Gordiets BF, Osipov AI. *Plasma kinetics in atmospheric gases (Vol. 31)*. Cham: Springer Science and Business Media (2013).
9. Marx D, Hutter J. *Ab initio* molecular dynamics: theory and implementation. *Mod Methods algorithms Quan Chem* (2000) 1(301-449):141.
10. Umari P, Pasquarello A. *Ab initio* molecular dynamics in a finite homogeneous electric field. *Phys Rev Lett* (2002) 89(15):157602. doi:10.1103/physrevlett.89.157602
11. Saitta AM, Saija F, Giaquinta PV. *Ab initio* molecular dynamics study of dissociation of water under an electric field. *Phys Rev Lett* (2012) 108(20):207801. doi:10.1103/physrevlett.108.207801
12. Micca Longo G, Giordano D, Longo S. Static field ionization of the spherically confined hydrogen atom. *Int J Quan Chem* (2024) 124(1):e27249. doi:10.1002/qua.27249
13. Saitta AM, Saija F. Miller experiments in atomistic computer simulations. *PNAS* (2014) 111(38):13768–73. doi:10.1073/pnas.1402894111
14. Bada JL, Cleaves HJ. *Ab initio* simulations and the Miller prebiotic synthesis experiment. *Proc Natl Acad Sci* (2015) 112(4):E342. doi:10.1073/pnas.1420577112
15. Šunka P. Pulse electrical discharges in water and their applications. *Phys Plasmas* (2001) 8(5):2587–94. doi:10.1063/1.1356742
16. Joshi RP, Thagard SM. Streamer-like electrical discharges in water: Part I. Fundamental mechanisms. *Plasma Chem Plasma Process* (2013) 33:1–15. doi:10.1007/s11090-012-9425-5
17. Longo S, Diomede P. Modeling of capacitively coupled RF plasmas in H₂. *Plasma Process Polym* (2009) 6(5):370–9. doi:10.1002/ppap.200800219
18. Capitelli M, Colonna G, Pietanza LD, D'Ammando G. Coupling of radiation, excited states and electron energy distribution function in non-equilibrium hydrogen plasmas. *Spectrochimica Acta B: At Spectrosc* (2013) 83:1–13. doi:10.1016/j.sab.2013.03.004
19. Hjartarson AT, Thorsteinsson EG, Gudmundsson JT. Low pressure hydrogen discharges diluted with argon explored using a global model. *Plasma Sourc Sci Tech* (2010) 19(6):065008. doi:10.1088/0963-0252/19/6/065008
20. Hassouni K, Duten X, Rousseau A, Gicquel A. Investigation of chemical kinetics and energy transfer in a pulsed microwave H₂/CH₄ plasma. *Plasma Sourc Sci Tech* (2001) 10(1):61–75. doi:10.1088/0963-0252/10/1/309
21. Hassouni K, Lombardi G, Duten X, Haagelar G, Silva F, Gicquel A, et al. Overview of the different aspects in modelling moderate pressure H₂ and H₂/CH₄ microwave discharges. *Plasma Sourc Sci Tech* (2006) 15(1):117–25. doi:10.1088/0963-0252/15/1/018
22. Yoon SF, Tan KH, Ahn J. Modeling and analysis of hydrogen–methane plasma in electron cyclotron resonance chemical vapor deposition of diamond-like carbon. *J Appl Phys* (2002) 91(1):40–7.
23. Bruneau B, Lafleur T, Gans T, O'Connell D, Greb A, Korolov I, et al. Effect of gas properties on the dynamics of the electrical slope asymmetry effect in capacitive plasmas: comparison of Ar, H₂ and CF₄. *Plasma Sourc Sci Tech* (2015) 25(1):01LT02. doi:10.1088/0963-0252/25/1/01LT02
24. Micca Longo G, Vialletto L, Diomede P, Longo S, Laporta V. Plasma modeling and prebiotic chemistry: a review of the state-of-the-art and perspectives. *Molecules* (2021) 26(12):3663. doi:10.3390/molecules26123663
25. Köhn C, Chanrion O, Enghoff MB, Dujko S. Streamer discharges in the atmosphere of primordial Earth. *Geophys Res Lett* (2022) 49(5):e2021GL097504. doi:10.1029/2021gl097504
26. Ravanbodshirazi S, Boutfol T, Safaridehkohneh N, Finkler M, Mohammadi-Kambs M, Ott A. The nature of the spark is a pivotal element in the design of a miller–urey experiment. *Life* (2023) 13(11):2201. doi:10.3390/life13112201



OPEN ACCESS

EDITED BY

Paolo Francesco Ambrico,
Istituto per la Scienza e Tecnologia dei
Plasmi—CNR, Italy

REVIEWED BY

Antonella Milella,
University of Bari Aldo Moro, Italy
Anna Maria Coclite,
Graz University of Technology, Austria
Eric Robert,
UMR7344 Groupe de recherches sur
l'énergétique des milieux ionisés (GREMI),
France

*CORRESPONDENCE

Romolo Laurita,
✉ romolo.laurita@unibo.it

RECEIVED 12 March 2024

ACCEPTED 05 April 2024

PUBLISHED 18 April 2024

CITATION

Maccaferri C, Gherardi M and Laurita R (2024),
Evaluating atmospheric pressure cold plasma
decontamination techniques for packaging
materials: a systematic review and meta-
analysis.
Front. Phys. 12:1399720.
doi: 10.3389/fphy.2024.1399720

COPYRIGHT

© 2024 Maccaferri, Gherardi and Laurita. This is
an open-access article distributed under the
terms of the [Creative Commons Attribution
License \(CC BY\)](#). The use, distribution or
reproduction in other forums is permitted,
provided the original author(s) and the
copyright owner(s) are credited and that the
original publication in this journal is cited, in
accordance with accepted academic
practice. No use, distribution or reproduction
is permitted which does not comply with
these terms.

Evaluating atmospheric pressure cold plasma decontamination techniques for packaging materials: a systematic review and meta-analysis

Caterina Maccaferri¹, Matteo Gherardi^{1,2} and Romolo Laurita^{1,3*}

¹Department of Industrial Engineering, Alma Mater Studiorum, Università di Bologna, Bologna, Italy,

²Advanced Mechanics and Materials, Interdepartmental Center for Industrial Research, Università di Bologna, Bologna, Italy, ³Interdepartmental Centre for Industrial Research Health Sciences and Technologies, Alma Mater Studiorum—Università di Bologna, Ozzano dell'Emilia, Italy

Decontaminating food packaging surfaces is a crucial step in the food processing industry to ensure the quality and safety of the product. Decontamination is intended as a procedure aimed to reduce the microbial load present on contaminated packaging to a safe level. Several techniques are traditionally employed, but the industry is seeking innovative methods that could offer economic and environmental benefits. Cold plasma is emerging as a promising solution among the range of possibilities. The present review aims to assess the effectiveness of plasma-assisted systems for decontaminating packaging materials. A systematic collection of inherent records was carried out, and the study outcomes were extracted using the protocol for meta-analysis. The synthesis of the results demonstrates the efficacy of this sanitation technique, since the average logarithmic reduction of the pathogen charge on the packaging was above 4. This outcome is promising since it aligns with standard requirements for traditionally employed antiseptics. Future research should focus on the optimization of processes from the perspective of industrial applications.

KEYWORDS

cold plasma applications, packaging, decontamination (cleaning), microorganisms, plasma decontamination, atmospheric pressure, foodborne pathogens, food industry

1 Introduction

1.1 Foodborne diseases

Foodborne diseases, caused by contaminated food contact or ingestion, pose a significant global health concern. Contamination with bacteria, viruses, parasites, or chemicals can result in various illnesses, with over 200 identified, predominantly affecting the gastrointestinal tract but also leading to neurological, gynecological, and immunological issues [1]. Annually, nearly one in 10 individuals worldwide suffer from foodborne illnesses, resulting in over 420,000 deaths. While foodborne diseases affect all countries, low- and middle-income nations bear a disproportionate burden. Factors such as poverty, international trade, longer food chains, urbanisation, climate change, migration, and increased travel exacerbate these challenges, increasing the risk of contamination and the spread of infections across borders. In the European Union alone, over 5,000 foodborne

outbreaks are reported annually, causing approximately 45,000 cases [2]. In 2022, foodborne outbreaks increased significantly compared to the previous year, highlighting the need for stringent hygiene standards and HACCP (Hazard analysis and critical control points) protocols throughout the food production chain to mitigate contamination risks and safeguard consumers.

1.2 Food packaging

According to the Food Packaging Forum [3], the most used packaging materials and food contact surfaces are:

- Ceramics;
- Glass;
- Metal (mainly aluminum and steel);
- Paper and Board;
- Plastics (in particular polyethylene, High-Density polyethylene, polyethylene terephthalate, polyvinyl chloride, polystyrene, and polycarbonate);
- Wood.

The Codex Alimentarius specifies that the primary requirement for packaging is to avoid being a source of contamination [4]. Established in 1963 by the Food and Agriculture Organization (FAO) and the World Health Organization, the Codex sets international standards, guidelines, and codes of practice for food safety, quality, and fairness in international food trade, encompassing 99% of the global population. Food packaging is pivotal in maintaining food quality and safety by acting as a protective shield against external contaminants, prolonging product shelf life, and preventing spoilage. However, packaging itself can introduce contaminants, jeopardising food safety and integrity. Contaminated food packaging poses health risks, foodborne illnesses, allergic reactions, and economic consequences, such as costly recalls and reputational damage for producers [5, 6]. Preventive measures include stringent quality control throughout the production process, using high-quality packaging materials, adhering to good practices and standards, and implementing rigorous hygiene and health risk analyses, notably through the Hazard Analysis and Critical Control Points (HACCP) method. While not explicitly mandated by legislation, adopting the HACCP methodology is widely recognised and demanded by the national and international market to ensure food safety and prepare for certification schemes. HACCP facilitates both contamination prevention and compliance with industry standards, aligning with market expectations and enhancing consumer confidence in food safety [7].

1.3 Hygiene standards and consolidated decontamination techniques

A crucial yet often overlooked aspect is the biological contamination level of packaging materials, influenced by factors like handling frequency and exposure to air. Different materials exhibit varying propensities for microbial proliferation and require distinct sanitation methods. Production processes vary widely

among packaging materials, presenting opportunities for both contamination and decontamination. Metals, glass, and plastics manufacturing involve temperatures incompatible with microbial survival. Conversely, cellulosic materials present contamination risks due to source contamination, processing in humid environments conducive to microbial growth, and lower processing temperatures that sustain resilient microbial forms. Paper and board production may involve biocidal agents. Post-production contamination risks persist across all materials due to handling, non-sterile air drafts, insect presence, and machine contact. Acceptable hygienic conditions are indicated by cell counts below 10^4 cells/cm², while values exceeding 10^7 cells/cm² denote unsatisfactory conditions [8].

Microbial growth on packaging materials depends on factors like nutrient presence, moisture, and surface biofilm formation. Effective decontamination, typically targeting a 5-log reduction in microbial load, employs various thermal, chemical, and physical methods.

Traditional decontamination approaches include heat treatments, in particular dry heat (>180 °C), hot water and steam (130°C–150°C), and the utilisation of chemicals like hydrogen peroxide, ethylene or propylene oxides [9–11]. A growing interest is directed to more innovative methods like high-pressure processing, high-intensity pulsed electric field treatment, pulsed light, ozone-based treatments and cold-atmospheric plasma, which holds promise for diminishing harmful microorganisms in the context of the food industry more safely and sustainably [12–14].

1.4 Cold plasma technology

Plasma is the fourth state of matter, consisting of charged particles (ions and electrons) and neutral molecules. It can exploit several actions in many different applications, by tuning the different active agents that it includes [15]. These agents are the just-mentioned charged particles, chemically reactive species, such as free radicals, electromagnetic fields, radiations, and heat. For an application of interest, it is possible to control the operating conditions in order to maximise the presence of the active agents of interest. One main characteristic of plasmas (and the most relevant one to choose based on the application) is their macroscopic temperature. Plasmas can be consequently classified into:

- equilibrium (or thermal) plasmas, having the electron temperature in equilibrium with the heavy particles temperature, resulting in a macroscopic temperature higher than 10^4 K;
- non-equilibrium (or cold plasmas), in which only the electron temperature is high, while the heavy particles—mainly influencing the gas temperature—keep values closer to ambient air.

Plasmas can also be classified on the basis of the pressure, which can be atmospheric or lower. Cold plasmas at atmospheric pressure will be hereinafter referred to as CAP (Cold Atmospheric Plasmas). Atmospheric pressure is often preferred in the industrial application perspective, since the arrangement is much simpler and economical. Furthermore, in-line continuous processes are economically

sustainable only at atmospheric pressure, while low-pressure treatments should be carried out as batch processes.

The mechanisms of action related to the microbial inactivation are various. The active chemical components found in CAP demonstrate the ability to deactivate microorganisms on food surfaces due to their antimicrobial characteristics [14]. The primary effective components in the air plasma process include reactive oxygen species (ROS, including ozone, singlet oxygen, superoxide, peroxides, and hydroxyl radical) and reactive nitrogen species (RNS, mainly nitrogen oxides). The antimicrobial properties of these oxidative species can be attributed to lipid peroxidation within cell membranes and the oxidation of proteins and DNA within microbial cells [16]. Keener and Misra [17] have identified potential drivers for implementing this technology in the food industry, including lower energy requirements compared to current technologies, making it more environmentally friendly, reduced operational and maintenance costs due to simple systems with minimal upkeep and sanitation needs, improved chemical safety of foods through plasma inactivation and removal of pesticide and chemical residues, and its status as a green technology promoting environmental sustainability, as it only requires air and electricity to generate effective plasma.

Plasmas can be generated by a wide range of different sources, depending on the high voltage generator characteristics and the configuration of the source electrodes. The most used CAP sources are:

- Corona, in which a pointy electrode locally intensifies the electric field and allows the discharge;
- DBD (Dielectric Barrier Discharge), having two parallel (planar or concentric cylinders) electrodes separated by a dielectric barrier and a gap, in which the discharge takes place;
- Jets, both in the Corona or DBD configuration, presenting a gas flux which creates a plasma plume coming out from a nozzle;
- SDBD (Surface DBD), a particular configuration of DBDs with the ground electrode in the form of a mesh and without a gap, in order to generate plasma in the holes of the mesh.

2 Methods

This report was drafted following the PRISMA 2020 checklist, as described in the PRISMA statement and PRISMA explanation and elaboration [18–20].

A systematic research was carried out on the use of plasma systems for decontamination of surface packaging. The aim was to collect all studies that tested plasma's effectiveness on materials that could potentially or openly be traced back to packaging. The search focused on the years from 2000 to 2023, collecting all articles published in that period that contained terms concerning plasma, packaging materials and possible biological contaminants or decontamination-related terms in the title, abstract or keywords.

The search string used in the Scopus database is reported as [Supplementary Material](#).

Reasons for exclusion from selection could be:

- publication language other than English;

- in-package treatments, i.e., where the plasma is generated inside a closed package;
- antimicrobial action carried out not directly on contaminated packaging, but, e.g., on food or test plates;
- low-pressure treatment of the material, as the analysis is addressed to atmospheric processes (however, studies in which plasma was produced at low pressure but the decontamination takes place at ambient pressure were included);
- removal of chemical contaminants as the analysis is addressed to the antimicrobial action of plasma);
- reviews.

The last search was done in December 2023. In addition to the study selected with this systematic search, other inherent papers in the authors' knowledge were included.

Different categories of information were chosen for the relevant data extraction from reports. First of all, the data about the plasma systems were collected, i.e., the type of plasma source and its dimensions or design characteristics, the operating conditions (voltage, current, frequency, power and power density, type of waveforms), the process gas and eventual other synergic agents such as water vapour, UV, etc. Then, contamination characteristics were summarised in the categories of pathogen strains, initial concentrations, and contamination procedure. Packaging sample material, geometries, and dimensions were reported as well. Finally, the fundamental data item is presented: the maximum inactivation achieved in terms of logarithmic reduction of the initial concentration.

The effect size of the studies, i.e., their outcome, can be presented differently. In this case, Standardised Mean Difference (SMD) was chosen as index. SMD is defined as difference in mean outcomes between groups, as follows:

$$SMD = \text{Mean outcome of treated group} - \text{Mean outcome of control group}$$

In the specific field of decontamination experiments, SMD could be identified as the logarithmic reduction of the pathogen charge (*LogR*), calculated by means of the following formula:

$$\text{LogR} = \text{Log}N_t - \text{Log}N_0$$

where N_t represents the number of colonies in the treated group and N_0 in the control group.

Every individual study included in the quantitative analysis was associated with a *LogR* value for the outcome synthesis.

Averages of logarithmic reductions are also calculated for sub-groups of studies, by differentiating the pathogens in the main categories of: Gram-positive bacteria, Gram-negative bacteria, fungi, and viruses.

3 Results

3.1 Study selection

Subsequently, the flow diagram is presented ([Figure 1](#)). The records were first identified through Scopus database searching, as

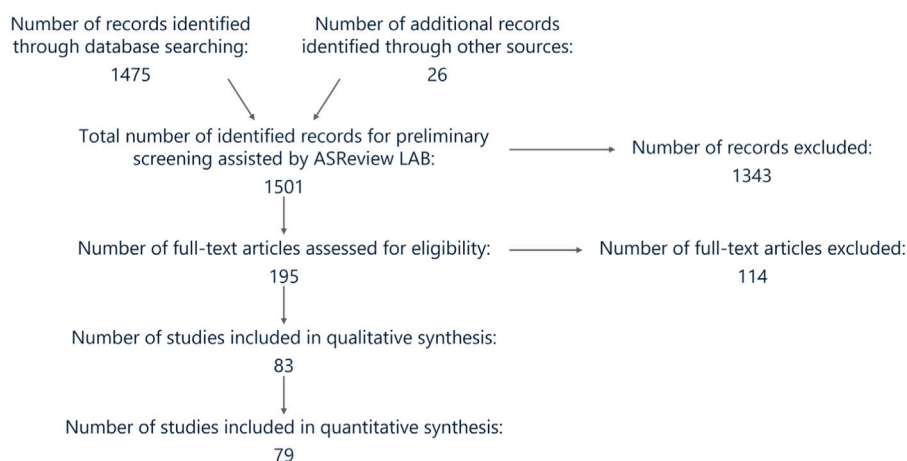


FIGURE 1
Flow diagram of records identification process.

Average outcome of sub-groups

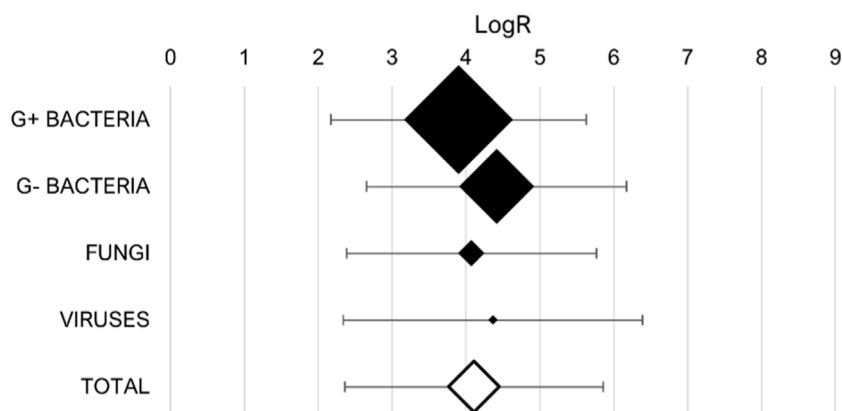


FIGURE 2
Synthesis of study outcomes: averages of sub-groups logarithmic reductions. Marker sizes represent the relative sub-group size.

previously illustrated. A few additional papers known by the authors were included as well. The collection of documents was then subjected to a preliminary screening on the software ASReview LAB (Zenodo, Switzerland), which assisted in the selection of eligible studies employing artificial intelligence tools. An additional amount was excluded by analysing the full-text articles for the above-mentioned reasons. A total number of 83 studies was included in the qualitative synthesis (i.e., the data extraction). Three papers did not present the data item considered to evaluate the outcome, i.e., the logarithmic reduction, and were consequently excluded from the quantitative analysis.

3.2 Summary of data and synthesis of results

The studies outcomes are summarised in the table reported as [Supplementary Material](#). For each study included in the quantitative

analysis, the outcome indicator, chosen as the logarithmic reduction of the contaminant concentration, is reported. The effect estimates of the individual studies are graphically synthesised in the forest plot, with standard deviation if specified. Each different combination of factors (plasma source, type of treatment, pathogen, packaging material) is considered individually and associated with its outcome. The total number of individual cases is 263. Only the most efficient case is considered when different operating conditions were investigated, such as different treatment times, distance between plasma and the substrate, gas flux or generator electrical settings. The averages of these results for groups of similar pathogens are also calculated and reported in [Figure 2](#).

Observing the average reduction rates for the sub-groups, it is evident that Gram-positive bacteria are usually less sensitive than Gram-negative bacteria to plasma treatment since the mean logarithmic reduction is respectively 3.90 ± 1.73 and 4.42 ± 1.76 . This difference is in accordance with the literature and due to their

distinctive structure of cell membrane [21]. The anti-viral effect of plasma on contaminated packaging is a field that needs further investigation, since only 3 studies were included in the quantitative analysis. The mean efficacy against fungi, equal to 4.06 ± 1.76 LogR, reflects the total outcome relative to the whole research. In fact, the total outcome of the meta-analysis is an average of 4.11 ± 1.75 LogR over 256 individual cases, which leads to the conclusion that plasma treatments at atmospheric pressure are effective against foodborne pathogens.

3.2.1 Investigated pathogens

On the basis of the records collection and data extraction, it was possible to identify the most investigated pathogens in the field.

Gram-positive bacteria were the subject of study in 136 cases (51.3% of the total) [22–50] [51–74]; in particular, 32 times the treatment was against endospores [40–42, 44, 46–49, 52, 54, 57, 58, 62, 70] and 5 times against biofilm of *Pseudomonas aeruginosa*, *Staphylococcus aureus*, *Staphylococcus epidermidis* (single-species) [39] and *Streptococci* strains [44]. The most studied Gram-positive bacteria are:

- *Staphylococcus aureus* (50 occurrences, 8 times as *Methicillin-Resistant S. aureus*),
- *Bacillus subtilis* (16 occurrences),
- *Listeria monocytogenes* (11 occurrences),
- *Bacillus atrophaeus* (8 occurrences).

Gram-negative bacteria were the subject of study in 93 cases (35.1% of the total) [24, 25], [28–34], [36–38], [43–45], [48, 50, 51], [61–64], [69, 71] [75–93]; in particular, 7 times in the form of biofilm of *Escherichia coli* (single-species) [78, 90, 94], *Pseudomonas aeruginosa* (single-species) [79, 83, 91] and *Salmonella* strains [88]. The most studied Gram-negative bacteria are:

- *Escherichia coli* (53 occurrences),
- *Staphylococcus typhimurium* (15 occurrences),
- *Pseudomonas aeruginosa* (8 occurrences),
- *Acinetobacter baumannii* (8 occurrences).

Fungi were investigated in 28 cases (10.6%) [23, 26, 31, 32, 45, 68, 73, 89, 95–99], 2 times as biofilm of *Candida albicans* [97, 100]. Among the total number of cases counted as “fungi,” thrice the contaminants were spores [26, 31, 57]. The most studied fungi are:

- *Candida albicans* (10 occurrences),
- *Aspergillus niger* (6 occurrences).

Only 6 experiments considered viruses [52, 62, 101–103]. It is meaningful that 4 out of 5 cited papers were published between 2021 and 2022, suggesting an increasing interest developed after the COVID-19 outbreak. This deduction is corroborated by the fact that the specific contaminant virus was a coronavirus in three studies [101–103]. The contaminant was a bacteriophage in the other two cases [52, 62].

3.2.2 Investigated packaging materials

Polymeric materials were treated in 58% of the cases. The most treated polymeric materials were:

- Polyethylene Terephthalate (36 cases),
- Polypropylene (34 cases),
- Polyethylene (24 cases).

Among the non-polymeric materials (occurred in 42% of the cases), very frequently used substrates were:

- Glass (52 cases),
- Stainless Steel (35 cases),
- Paper (12 cases).

3.2.3 Plasma sources

The following occurrences are referred to a total of 77 specified sources. The most frequently used are:

- DBD (29 times—38%),
- SDBD (18 times—23%),
- Jets (13 times—17%),
- Corona (7 times—9%).

In 3 out of the 84 selected studies, the plasma source was not specified at all, while it was just mentioned as a generic CAP in 5 articles. In 2 papers, 2 different sources were tested in the same paper.

3.2.4 Treatment methods

Different treatment methods are available when CAP are used. Their conventional classification is adopted in this systematic review:

- Direct treatment, in which plasma is in direct contact with the substrate,
- Indirect treatment, in which the anti-microbial action is exerted mainly by the reactive species, since plasma does not occupy the substrate area,
- Plasma-activated water or air, as media carrying the reactive species previously generated by plasma; air or water are subsequently conveyed in contact with the substrate.

Among the selected studies, direct treatment occurred 46 times (56.8%), indirect treatment 31 times (38.3%) and plasma-activated water/air 4 times (4.9%).

A final observation regards the possibility of exploiting synergies with other biocidal agents. Some attempts dealt with the combination of plasma and i) ultraviolet rays [23, 27, 31], ii) hydrogen peroxide [33, 96], iii) water in the form of water vapour [57], water spray [44] or water layer deposited onto the substrate [87].

4 Discussion and conclusion

According to the literature, plasma systems are proven effective in decontaminating packaging materials and food contact surfaces. The antimicrobial efficacy is demonstrated for various operating and environmental conditions, for different plasma source configurations and treatment methods from the direct treatment to the indirect one to the PAW (Plasma-Activated Water) or PPA

(Plasma-Processed Air) exposure. The plasma action inactivated a wide range of different microorganisms. The average inactivation was satisfactory according to European standards for the traditional chemical disinfectants BS EN 13697:2015+A1:2019 and BS EN 14885:2022 [104, 105], which state that the minimum LogR should be at least a 4 LogR for bacteria and at least a 3 LogR for fungi. In practical packaging industry scenarios, it will be crucial to evaluate the impact of initial microbial concentration on the plasma treatment efficacy. Notably, a study conducted by Fernández et al. [106] revealed an inverse relationship between initial concentration and treatment effectiveness since, for high concentrations, significant clumps, and multilayered structures form, potentially offering physical protection against CAP treatment.

In conclusion, future research should consider the proof-of-concept of the process and focus on optimisation, in particular, reducing treatment time and increasing effectiveness. An up-scaling is wished, considering the requirement of industrial facilities as well. In fact, the treatment time is often of the order of minutes, which is not compatible with typical industrial constraints. Furthermore, most of the plasma sources used for the purpose can treat only a limited portion of the surface, of the order of a few square centimeters. Only 3 studies [26, 30, 53] were able to conduct experiments as in-line processes, while all the others were performed statically. The transition from laboratory prototypes to industrial in-line systems should be the main aim of future research in the field.

Author contributions

CM: Writing—original draft, Software, Resources, Methodology, Investigation, Data curation. MG: Writing—review and editing, Funding acquisition, Formal Analysis. RL: Visualization, Supervision, Project administration, Funding acquisition, Conceptualization, Writing—review and editing, Formal Analysis.

Funding

The author(s) declare that financial support was received for the research, authorship, and/or publication of this article. The PhD scholarship of the author CM was funded by the European Union—NextGenerationEU through the Italian Ministry of

University and Research under PNRR—Mission 4 Component 2, Investment 3.3 “Partnerships extended to universities, research centres, companies and funding of basic research projects” D.M. 352/2021—CUP J33C22001330009.

Acknowledgments

The work has been partially supported by COST Action CA19110 - Plasma applications for smart and sustainable agriculture (PLAgri), supported by COST (European Cooperation in Science and Technology) and “ON Foods - Research and innovation network on food and nutrition Sustainability, Safety and Security - Working ON Foods”, funded under the National Recovery and Resilience Plan (NRRP), Mission 4 Component 2 Investment 1.3 funded by the European Union - NextGenerationEU; Project code PE00000003.

Conflict of interest

The authors declare that the research was conducted in the absence of any commercial or financial relationships that could be construed as a potential conflict of interest.

The author(s) declared that they were an editorial board member of Frontiers, at the time of submission. This had no impact on the peer review process and the final decision.

Publisher's note

All claims expressed in this article are solely those of the authors and do not necessarily represent those of their affiliated organizations, or those of the publisher, the editors and the reviewers. Any product that may be evaluated in this article, or claim that may be made by its manufacturer, is not guaranteed or endorsed by the publisher.

Supplementary material

The Supplementary Material for this article can be found online at: <https://www.frontiersin.org/articles/10.3389/fphy.2024.1399720/full#supplementary-material>

References

1. World Health Organization. *Foodborne diseases*. Geneva, Switzerland: World Health Organization (2024).
2. EFSA/European Centre for Disease Prevention and Control ECDC. The European union one health 2022 zoonoses report. *EFSA J* (2023) 21:e8442. doi:10.2903/j.efsa.2023.8442
3. Muncke J. Food packaging materials. *Food Packaging Forum* (2012).
4. European Commission. *Codex Alimentarius*. Brussels: European Commission (2024).
5. Brody AL, Bugusu B, Han JH, Sand CK, McHugh TH. Scientific status summary: innovative food packaging solutions. *J Food Sci* (2008) 73:R107–16. doi:10.1111/j.1750-3841.2008.00933.x
6. Robertson GL. *Food packaging - principles and practice*. Boca Raton, Florida, United States: CRC Press Taylor and Francis Group (2012).
7. Bovee EHG, De Kruijf N, Jetten J, Barendsz AW. HACCP approach to ensure the safety and quality of food packaging. *Food Addit Contam* (1997) 14:721–35. doi:10.1080/02652039709374583
8. Piergiovanni L, Limbo S. *Food packaging*. Milano: Springer (2010). doi:10.1007/978-88-470-1457-2
9. Ansari IA, Datta AK. An overview of sterilization methods for packaging materials used in aseptic packaging systems. *Food Bioprocess Process* (2003) 81:57–65. doi:10.1205/096030803765208670
10. Khadre MA, Yousef AE. Decontamination of a multilaminated aseptic food packaging material and stainless steel by ozone. *J Food Saf* (2001) 21:1–13. doi:10.1111/j.1745-4565.2001.tb00304.x
11. Liao X, Liu D, Xiang Q, Ahn J, Chen S, Ye X, et al. Inactivation mechanisms of non-thermal plasma on microbes: a review. *Food Control* (2017) 75:83–91. doi:10.1016/j.foodcont.2016.12.021
12. Mandal R, Singh A, Pratap Singh A. Recent developments in cold plasma decontamination technology in the food industry. *Trends Food Sci Technol* (2018) 80:93–103. doi:10.1016/j.tifs.2018.07.014

13. Feizollahi E, Misra NN, Roopesh MS. Factors influencing the antimicrobial efficacy of dielectric barrier discharge (DBD) atmospheric cold plasma (ACP) in food processing applications. *Crit Rev Food Sci Nutr* (2021) 61:666–89. doi:10.1080/10408398.2020.1743967
14. Baier M, Görgen M, Ehlbeck J, Knorr D, Herppich WB, Schlüter O. Non-thermal atmospheric pressure plasma: screening for gentle process conditions and antibacterial efficiency on perishable fresh produce. *Innovative Food Sci Emerging Tech* (2014) 22: 147–57. doi:10.1016/j.ifset.2014.01.011
15. Šimončicová J, Kryštofová S, Medvecká V, Ďurišová K, Kaliňáková B. Technical applications of plasma treatments: current state and perspectives. *Appl Microbiol Biotechnol* (2019) 103:5117–29. doi:10.1007/s00253-019-09877-x
16. Muranyi P, Wunderlich J, Heise M. Influence of relative gas humidity on the inactivation efficiency of a low temperature gas plasma. *J Appl Microbiol* (2008) 104: 1659–66. doi:10.1111/j.1365-2672.2007.03691.x
17. Keener KM, Misra NN. Future of cold plasma in food processing. In: *Cold plasma in food and agriculture: fundamentals and applications*. Amsterdam, Netherlands: Elsevier (2016). p. 343–60. doi:10.1016/B978-0-12-801365-6.00014-7
18. Moher D, Liberati A, Tetzlaff J, Altman DG. Preferred reporting items for systematic reviews and meta-analyses: the PRISMA statement. *BMJ (Online)* (2009) 339:b2535–6. doi:10.1136/bmj.b2535
19. Page MJ, McKenzie JE, Bossuyt PM, Boutron I, Hoffmann TC, Mulrow CD, et al. The PRISMA 2020 statement: an updated guideline for reporting systematic reviews. *The BMJ* (2021) 372:n71. doi:10.1136/bmj.n71
20. Page MJ, Moher D, Bossuyt PM, Boutron I, Hoffmann TC, Mulrow CD, et al. PRISMA 2020 explanation and elaboration: updated guidance and exemplars for reporting systematic reviews. *The BMJ* (2021) 372:n160. doi:10.1136/bmj.n160
21. Breijyeh Z, Jubeh B, Karaman R. Resistance of gram-negative bacteria to current antibacterial agents and approaches to resolve it. *Molecules* (2020) 25:1340. doi:10.3390/molecules25061340
22. Maccaferri C, Sainz-García A, Capelli F, Gherardi M, Alba-Elías F, Laurita R. Evaluation of the antimicrobial efficacy of a large-area surface dielectric barrier discharge on food contact surfaces. *Plasma Chem Plasma Process* (2023) 43: 1773–90. doi:10.1007/s11090-023-10410-2
23. Heise M, Neff W, Franken O, Muranyi P, Wunderlich J. Sterilization of polymer foils with dielectric barrier discharges at atmospheric pressure. *Plasma Polym* (2004) 9: 23–33. doi:10.1023/b:papo.0000039814.70172.c0
24. Schnabel U, Schmidt C, Stachowiak J, Bösel A, Andrasch M, Ehlbeck J. Plasma processed air for biological decontamination of PET and fresh plant tissue. *Plasma Process Polym* (2018) 15. doi:10.1002/ppap.201600057
25. Bauer A, Ni Y, Bauer S, Paulsen P, Modic M, Walsh JL, et al. The effects of atmospheric pressure cold plasma treatment on microbiological, physical-chemical and sensory characteristics of vacuum packaged beef loin. *Meat Sci* (2017) 128:77–87. doi:10.1016/j.meatsci.2017.02.003
26. Trompeter FJ, Neff WJ, Franken O, Heise M, Neiger M, Liu S, et al. Reduction of *Bacillus Subtilis* and *Aspergillus Niger* spores using nonthermal atmospheric gas discharges. *IEEE Trans Plasma Sci* (2002) 30:1416–23. doi:10.1109/TPS.2002.804182
27. Muranyi P, Wunderlich J, Langowski HC. Modification of bacterial structures by a low-temperature gas plasma and influence on packaging material. *J Appl Microbiol* (2010) 109:1875–85. doi:10.1111/j.1365-2672.2010.04815.x
28. Puligundla P, Lee T, Mok C. Inactivation effect of dielectric barrier discharge plasma against foodborne pathogens on the surfaces of different packaging materials. *Innovative Food Sci Emerging Tech* (2016) 36:221–7. doi:10.1016/j.ifset.2016.06.027
29. Lee T, Puligundla P, Mok C. Corona discharge plasma jet inactivates food-borne pathogens adsorbed onto packaging material surfaces. *Packaging Tech Sci* (2017) 30: 681–90. doi:10.1002/pts.2311
30. Katsigiannis AS, Hohnik N, Modic M, Bayliss DL, Kovač J, Walsh JL. Continuous in-line decontamination of food-processing surfaces using cold atmospheric pressure air plasma. *Innovative Food Sci Emerging Tech* (2022) 81:103150. doi:10.1016/j.ifset.2022.103150
31. Muranyi P, Wunderlich J, Heise M. Sterilization efficiency of a cascaded dielectric barrier discharge. *J Appl Microbiol* (2007) 103:1535–44. doi:10.1111/j.1365-2672.2007.03385.x
32. Montie TC, Kelly-Wintenberg K, Roth JR. An overview of research using the one atmosphere uniform glow discharge plasma (OAUGDP) for sterilization of surfaces and materials. *IEEE Trans Plasma Sci* (2000) 28:41–50. doi:10.1109/27.842860
33. Imaizumi Y, Takashima K, Katura S, Miiuno A. *Sterilization using OH radical produced by atmospheric discharge plasma*. Boca Raton, Florida, United States: CRC Press (1996).
34. Edelblute CM, Malik MA, Heller LC. Surface-dependent inactivation of model microorganisms with shielded sliding plasma discharges and applied air flow. *Bioelectrochemistry* (2015) 103:22–7. doi:10.1016/j.bioelechem.2014.08.013
35. Edelblute CM, Malik MA, Heller LC. Antibacterial efficacy of a novel plasma reactor without an applied gas flow against methicillin resistant *Staphylococcus aureus* on diverse surfaces. *Bioelectrochemistry* (2016) 112:106–11. doi:10.1016/j.bioelechem.2016.04.001
36. Timmons C, Pai K, Jacob J, Zhang G, Ma LM. Inactivation of *Salmonella enterica*, Shiga toxin-producing *Escherichia coli*, and *Listeria monocytogenes* by a novel surface discharge cold plasma design. *Food Control* (2018) 84:455–62. doi:10.1016/j.foodcont.2017.09.007
37. Dasan BG, Onal-Ulusoy B, Pawlat J, Diatczyk J, Sen Y, Mutlu M. A new and simple approach for decontamination of food contact surfaces with gliding arc discharge atmospheric non-thermal plasma. *Food Bioproc Tech* (2017) 10:650–61. doi:10.1007/s11947-016-1847-2
38. Schnabel U, Andrasch M, Weltmann KD, Ehlbeck J. Inactivation of vegetative microorganisms and bacillus atrophaeus endospores by reactive nitrogen species (RNS). *Plasma Process Polym* (2014) 11:110–6. doi:10.1002/ppap.201300072
39. Tučeková ZK, Vacek L, Krumpolec R, Kelar J, Zemánek M, Černák M, et al. Multi-hollow surface dielectric barrier discharge for bacterial biofilm decontamination. *Molecules* (2021) 26:910. doi:10.3390/molecules26040910
40. Pina-Perez MC, Martinet D, Palacios-Gorba C, Ellert C, Beyrer M. Low-energy short-term cold atmospheric plasma: controlling the inactivation efficacy of bacterial spores in powders. *Food Res Int* (2020) 130:108921. doi:10.1016/j.foodres.2019.108921
41. Dobrynin D, Fridman G, Mukhin YV, Wynosky-Dolfi MA, Rieger J, Rest RF, et al. Cold plasma inactivation of *Bacillus cereus* and *Bacillus anthracis* (anthrax) spores. *IEEE Trans Plasma Sci* (2010) 38:1878–84. doi:10.1109/TPS.2010.2041938
42. Hähnel M, Von Woedtke T, Weltmann KD. Influence of the air humidity on the reduction of *Bacillus* spores in a defined environment at atmospheric pressure using a dielectric barrier surface discharge. *Plasma Process Polym* (2010) 7:244–9. doi:10.1002/ppap.200900076
43. Reece RJ, Sherman DM, Member S, Ben Gadri R, Karakaya F, Chen Z, et al. A remote exposure reactor (RER) for plasma processing and sterilization by plasma active species at one atmosphere. *IEEE Trans Plasma Sci* (2000) 28:56–63. doi:10.1109/27.842864
44. Kovalova Z, Tarabova K, Hensel K, Machala Z. Decontamination of *Streptococci* biofilms and *Bacillus cereus* spores on plastic surfaces with DC and pulsed corona discharges. In: *13th international symposium on High pressure low temperature plasma chemistry*. Cambridge, United Kingdom: Cambridge University Press (2013).
45. Kamgang-Youbi G, Herry JM, Meylheuc T, Laminis S, Naïtali M. Microbial decontamination of stainless steel and polyethylene surfaces using GlidArc plasma activated water without chemical additives. *J Chem Tech Biotechnol* (2018) 93:2544–51. doi:10.1002/jctb.5608
46. Machala Z, Jedlovský I, Chládek L, Pongráč B, Gierl D, Janda M, et al. DC discharges in atmospheric air for bio-decontamination - spectroscopic methods for mechanism identification. *Eur Phys J D* (2009) 54:195–204. doi:10.1140/epjd/e2009-00035-7
47. Kuzminova A, Kretková T, Kylián O, Hanuš J, Khalakhan I, Prukner V, et al. Etching of polymers, proteins and bacterial spores by atmospheric pressure DBD plasma in air. *J Phys D Appl Phys* (2017) 50:135201. doi:10.1088/1361-6463/aa5c21
48. Bugaev SP, Bykov DV, Evdokimov EV, Smajkina SV, Sochugov NS, Sharubin SA. Sterilization on materials in the atmospheric pressure pulse corona discharge plasma. In: *13th International Conference on High-Power Particle Beams*; June, 200; Nagaoka, Japan (2000). p. 946–9.
49. Zš S, MacHala Z. Biodecontamination of plastic and dental surfaces with atmospheric pressure air DC discharges. *IEEE Trans Plasma Sci* (2011) 39:2970–1. doi:10.1109/TPS.2011.2160563
50. Zheng C, Kou Y, Liu Z, Li C, Huang Y, Yan K. Rapid disinfection performance of a touchable pulsed SDBD nonthermal plasma. *IEEE Trans Plasma Sci* (2016) 44:2667–72. doi:10.1109/TPS.2016.2576558
51. Ibis F, Oflaz H, Ercan UK. Biofilm inactivation and prevention on common implant material surfaces by nonthermal DBD plasma treatment. *Plasma Med* (2016) 6: 33–45. doi:10.1615/plasmamed.2016015846
52. Kramer B, Warschat D, Muranyi P. Disinfection of an ambulance using a compact atmospheric plasma device. *J Appl Microbiol* (2022) 133:696–706. doi:10.1111/jam.15599
53. Kim JS, Lee EJ, Choi EH, Kim YJ. Inactivation of *Staphylococcus aureus* on the beef jerky by radio-frequency atmospheric pressure plasma discharge treatment. *Innovative Food Sci Emerging Tech* (2014) 22:124–30. doi:10.1016/j.ifset.2013.12.012
54. Amano I, Tanino M, Fujii N, Tanino Y, Takashima K, Mizuno A. Sterilization using a wide-gap discharge formed by dielectric barrier discharge coupled with surface discharge under atmospheric pressure. In: *2007 IEEE Industry Applications Annual Meeting*; September, 2007; New Orleans, LA, USA (2007). doi:10.1109/07ias.2007.174
55. Bong C, Choi JY, Bae J, Park S, Ko KS, Bak MS, et al. Effectiveness of ozone generated by a dielectric barrier discharge plasma reactor against multidrug-resistant pathogens and *Clostridioides difficile* spores. *Sci Rep* (2022) 12:14118. doi:10.1038/s41598-022-18428-w
56. Cooper M, Fridman G, Staack D, Gutsol AF, Vasilets VN, Anandan S, et al. Decontamination of surfaces from extremophile organisms using nonthermal atmospheric-pressure plasmas. *IEEE Trans Plasma Sci* (2009) 37:866–71. doi:10.1109/TPS.2008.2010618

57. Masaoka S. Plasma sterilization of polyethylene terephthalate bottles by pulsed corona discharge at atmospheric pressure. *Biocontrol Sci* (2007) 12:59–63. doi:10.4265/bio.12.59
58. Klämpfl TG, Isbary G, Shimizu T, Li YF, Zimmermann JL, Stolz W, et al. Cold atmospheric air plasma sterilization against spores and other microorganisms of clinical interest. *Appl Environ Microbiol* (2012) 78:5077–82. doi:10.1128/AEM.00583-12
59. Kramer B, Hasse D, Guist S, Schmitt-John T, Muranyi P. Inactivation of bacterial endospores on surfaces by plasma processed air. *J Appl Microbiol* (2020) 128:920–33. doi:10.1111/jam.14528
60. Deng S, Cheng C, Ni G, Meng Y, Chen H. Bacillus subtilis devitalization mechanism of atmosphere pressure plasma jet. *Curr Appl Phys* (2010) 10:1164–8. doi:10.1016/j.cap.2010.02.004
61. Mizuno A. Destruction of biological particles using non-thermal plasma. *J Clin Biochem Nutr* (2017) 60:12–24. doi:10.3164/jcbs.16-64
62. Ben Gadri R, Reece Roth J, Montie TC, Kelly-Wintenberg K, P-Y Tsai P, Helfritsch DJ, et al. Sterilization and plasma processing of room temperature surfaces with a one atmosphere uniform glow discharge plasma (OAGDP). *Surf Coat Tech* (2000) 131:528–41. doi:10.1016/s0257-8972(00)00803-3
63. Lee H-B, Noh Y-E, Yang H-J, Cheol MS. Inhibition of foodborne pathogens on polystyrene, sausage casings, and smoked salmon using nonthermal plasma treatments. *Sausage Casings, and Smoked Salmon Using Nonthermal Plasma Treatments* (2011) 43:513–7. doi:10.9721/kjfst.2011.43.4.513
64. Kangang-Youbi G, Herry JM, Meylheuc T, Brisset JL, Bellon-Fontaine MN, Doubla A, et al. Microbial inactivation using plasma-activated water obtained by gliding electric discharges. *Lett Appl Microbiol* (2009) 48:13–8. doi:10.1111/j.1472-765X.2008.02476.x
65. Noriega E, Shama G, Laca A, Díaz M, Kong MG. Cold atmospheric gas plasma disinfection of chicken meat and chicken skin contaminated with *Listeria innocua*. *Food Microbiol* (2011) 28:1293–300. doi:10.1016/j.fm.2011.05.007
66. Yun H, Kim B, Jung S, Kruk ZA, Kim DB, Choe W, et al. Inactivation of *Listeria monocytogenes* inoculated on disposable plastic tray, aluminum foil, and paper cup by atmospheric pressure plasma. *Food Control* (2010) 21:1182–6. doi:10.1016/j.foodcont.2010.02.002
67. Govaert M, Smet C, Baka M, Ećimović B, Walsh JL, Van Impe J. Resistance of *L. monocytogenes* and *S. Typhimurium* towards cold atmospheric plasma as function of biofilm age. *Appl Sci (Switzerland)* (2018) 8:2702. doi:10.3390/AP8122702
68. Kvam E, Davis B, Mondello F, Garner AL. Nonthermal atmospheric plasma rapidly disinfects multidrug-resistant microbes by inducing cell surface damage. *Antimicrob Agents Chemother* (2012) 56:2028–36. doi:10.1128/AAC.05642-11
69. Cahill OJ, Claro T, O'Connor N, Cafolla AA, Stevens NT, Daniels S, et al. Cold air plasma to decontaminate inanimate surfaces of the hospital environment. *Appl Environ Microbiol* (2014) 80:2004–10. doi:10.1128/AEM.03480-13
70. Venezia RA, Orrico M, Houston E, Yin S, Naumova YY. Lethal activity of nonthermal plasma sterilization against microorganisms. *Infect Control Hosp Epidemiol* (2008) 29(5):430–6. doi:10.1086/588003
71. Lis KA, Kehrenberg C, Boulaaba A, von Köckritz-Blickwede M, Binder S, Li Y, et al. Inactivation of multidrug-resistant pathogens and *Yersinia enterocolitica* with cold atmospheric-pressure plasma on stainless-steel surfaces. *Int J Antimicrob Agents* (2018) 52:811–8. doi:10.1016/j.ijantimicag.2018.08.023
72. Ma Y, Zhang GJ, Shi XM, Xu GM, Yang Y. Chemical mechanisms of bacterial inactivation using dielectric barrier discharge plasma in atmospheric air. *IEEE Trans Plasma Sci* (2008) 36:1615–20. doi:10.1109/TPS.2008.917165
73. Akan T, Çabuk A. Indirect plasma inactivation by a low temperature atmospheric pressure plasma (LTAPP) system. *J Electrostat* (2014) 72:218–21. doi:10.1016/j.elstat.2014.03.007
74. Schnabel U, Handorf O, Yarova K, Zessin B, Zechlin S, Sydow D, et al. Plasma-treated air and water-assessment of synergistic antimicrobial effects for sanitation of food processing surfaces and environment. *Foods* (2019) 8:55. doi:10.3390/foods8020055
75. Hu M, Guo Y. The effect of air plasma on sterilization of *Escherichia coli* in Dielectric Barrier Discharge. *Plasma Sci Tech* (2012) 14:735–40. doi:10.1088/1009-0630/14/8/10
76. Miao H, Yun G. The sterilization of *Escherichia coli* by dielectric-barrier discharge plasma at atmospheric pressure. *Appl Surf Sci* (2011) 257:7065–70. doi:10.1016/j.apsusc.2011.03.014
77. Tucekova Z, Kovalova Z, Zahoranova A, Machala Z, Cernak M. Inactivation of *Escherichia coli* on PTFE surfaces by diffuse coplanar surface barrier discharge. *Eur Phys J Appl Phys* (2016) 75:24711. doi:10.1051/epjap/2016150590
78. Salgado BAB, Fabbri S, Dickenson A, Hasan MI, Walsh JL. Surface barrier discharges for *Escherichia coli* biofilm inactivation: modes of action and the importance of UV radiation. *PLoS One* (2021) 16:e0247589. doi:10.1371/journal.pone.0247589
79. Lu P, Ziuzina D, Cullen PJ, Bourke P. Inner surface biofilm inactivation by atmospheric pressure helium porous plasma jet. *Plasma Process Polym* (2018) 15. doi:10.1002/ppap.201800055
80. Liu HX, Chen JR. Analysis of surface sterilization and properties of medical poly(tetrafluoroethylene) in remote argon plasma. *IEEE Trans Plasma Sci* (2008) 36(2):230–6. doi:10.1109/TPS.2007.913925
81. Salamitou S, Kirkpatrick MJ, Ly HM, Leblon G, Odic E, DuBow MS. Augmented survival of bacteria within biofilms to exposure to an atmospheric pressure non-thermal plasma source. *Biotechnology* (2009) 8:228–34. doi:10.3923/biotech.2009.228.234
82. Simon A, Dinu OE, Papiu MA, Tudoran CD, Papp J, Anghel SD. A study of 1.74 MHz atmospheric pressure dielectric barrier discharge for non-conventional treatments. *J Electrostat* (2012) 70:235–40. doi:10.1016/j.elstat.2012.03.001
83. Vandervoort KG, Brelles-Mariño G. Plasma-mediated inactivation of *Pseudomonas aeruginosa* biofilms grown on borosilicate surfaces under continuous culture system. *PLoS One* (2014) 9:e108512. doi:10.1371/journal.pone.0108512
84. Zolotukhin D, Burdovitsini V, Oks E, Tyunkov A, Yushkov Y. Sterilization of dielectric containers using a fore-vacuum pressure plasma-cathode electron source. *J Phys Conf Ser* (2015) 652:012044. doi:10.1088/1742-6596/652/1/012044
85. Yu H, Perni S, Shi JJ, Wang DZ, Kong MG, Shama G. Effects of cell surface loading and phase of growth in cold atmospheric gas plasma inactivation of *Escherichia coli* K12. *J Appl Microbiol* (2006) 101:1323–30. doi:10.1111/j.1365-2672.2006.03033.x
86. Gabriel AA, Ugay MCCF, Siringan MAT, Rosario LMD, Tumlos RB, Ramos HJ. Atmospheric pressure plasma jet inactivation of *Pseudomonas aeruginosa* biofilms on stainless steel surfaces. *Innovative Food Sci Emerging Tech* (2016) 36:311–9. doi:10.1016/j.ifset.2016.07.015
87. Aboubakr HA, Nisar M, Nayak G, Nagaraja KV, Collins J, Bruggeman PJ, et al. Bactericidal efficacy of a two-dimensional array of integrated, coaxial, microhollow, dielectric barrier discharge plasma against *Salmonella enterica* serovar heidelberg. *Foodborne Pathog Dis* (2020) 17:157–65. doi:10.1089/fpd.2019.2698
88. Niemira BA, Boyd G, Sites J. Cold plasma rapid decontamination of food contact surfaces contaminated with salmonella biofilms. *J Food Sci* (2014) 79:M917–22. doi:10.1111/1750-3841.12379
89. Heaselgrave W, Shama G, Andrew PW, Kong MG. Inactivation of *Acanthamoeba* spp. and other ocular pathogens by application of cold atmospheric gas plasma. *Appl Environ Microbiol* (2016) 82:3143–8. doi:10.1128/AEM.03863-15
90. Kovalova Z, Leroy M, Kirkpatrick MJ, Odic E, Machala Z. Corona discharges with water electrospray for *Escherichia coli* biofilm eradication on a surface. *Bioelectrochemistry* (2016) 112:91–9. doi:10.1016/j.bioelechem.2016.05.002
91. Zelaya AJ, Stough G, Rad N, Vandervoort K, Brelles-Mariño G. *Pseudomonas aeruginosa* biofilm inactivation: decreased cell culturability, adhesiveness to surfaces, and biofilm thickness upon high-pressure nonthermal plasma treatment. *IEEE Trans Plasma Sci* (2010) 38:3398–403. doi:10.1109/TPS.2010.2082570
92. Pavlovich MJ, Chen Z, Sakiyama Y, Clark DS, Graves DB. Effect of discharge parameters and surface characteristics on ambient-gas plasma disinfection. *Plasma Process Polym* (2013) 10:69–76. doi:10.1002/ppap.201200073
93. Toyokawa Y, Yagyu Y, Misawa T, Sakudo A. A new roller conveyor system of non-thermal gas plasma as a potential control measure of plant pathogenic bacteria in primary food production. *Food Control* (2017) 72:62–72. doi:10.1016/j.foodcont.2016.07.031
94. Cui H, Ma C, Lin L. Synergetic antibacterial efficacy of cold nitrogen plasma and clove oil against *Escherichia coli* O157: H7 biofilms on lettuce. *Food Control* (2016) 66:8–16. doi:10.1016/j.foodcont.2016.01.035
95. Song Y, Wang W, Lu Q, Yang D, Niu J, Liu D. A homogeneous surface inactivation device driven by a pulse high-voltage source. *Plasma Process Polym* (2013) 10:698–705. doi:10.1002/ppap.201300013
96. Kordová T, Scholtz V, Khun J, Soušková H, Hozák P, Čerovský M. Inactivation of microbial food contamination of plastic cups using nonthermal plasma and hydrogen peroxide. *J Food Qual* (2018) 2018:1–7. doi:10.1155/2018/5616437
97. Handorf O, Schnabel U, Bösel A, Weihe T, Bekeschus S, Graf AC, et al. Antimicrobial effects of microwave-induced plasma torch (MiniMIP) treatment on *Candida albicans* biofilms. *Microb Biotechnol* (2019) 12:1034–48. doi:10.1111/1751-7915.13459
98. Šimončicová J, Kaliňáková B, Kováček D, Medvecká V, Lakatoš B, Kryštofová S, et al. Cold plasma treatment triggers antioxidative defense system and induces changes in hyphal surface and subcellular structures of *Aspergillus flavus*. *Appl Microbiol Biotechnol* (2018) 102:6647–58. doi:10.1007/s00253-018-9118-y
99. Schnabel U, Yarova K, Zessin B, Stachowiak J, Ehlbeck J. The combination of plasma-processed air (PPA) and plasma-treated water (PTW) causes synergistic inactivation of *Candida albicans* SC5314. *Appl Sci (Switzerland)* (2020) 10:3303. doi:10.3390/app10093303
100. Fricke K, Koban I, Tresp H, Jablonowski L, Schröder K, Kramer A, et al. Atmospheric pressure plasma: a high-performance tool for the efficient removal of biofilms. *PLoS One* (2012) 7:e42539. doi:10.1371/journal.pone.0042539

101. Capelli F, Tappi S, Gritti T, De Aguiar Saldanha Pinheiro AC, Laurita R, Tylewicz U, et al. Decontamination of food packages from SARS-COV-2 RNA with a cold plasma-assisted system. *Appl Sci (Switzerland)* (2021) 11:4177. doi:10.3390/app11094177
102. Zhang H, Chen M, Huang L, Guo L, Xu S, Zhang J, et al. Using cold atmospheric plasma treated-air for COVID-19 disinfection in cold-chain environment. *J Phys D Appl Phys* (2021) 54:40LT01. doi:10.1088/1361-6463/ac13f7
103. Bhartiya P, Lim JS, Kaushik N, Shaik AM, Shin YO, Kaushik NK, et al. Nonthermal plasma-generated ozone inhibits human coronavirus 229E infectivity on glass surface. *Plasma Process Polym* (2022) 19. doi:10.1002/ppap.202200054
104. BSI. *BSI Standards Publication Chemical disinfectants and antiseptics-Quantitative non-porous surface test for the evaluation of bactericidal and/or fungicidal activity of chemical disinfectants used in food, industrial, domestic and institutional areas-Test method and requirements without mechanical action (phase 2, step 2)* (2020).
105. British Standards Institution. Chemical disinfectants and antiseptics. *Application of European Standards for chemical disinfectants and antiseptics* (n.d.).
106. Fernández A, Shearer N, Wilson DR, Thompson A. Effect of microbial loading on the efficiency of cold atmospheric gas plasma inactivation of *Salmonella enterica* serovar Typhimurium. *Int J Food Microbiol* (2012) 152:175–80. doi:10.1016/j.ijfoodmicro.2011.02.038



OPEN ACCESS

EDITED BY

Eric Robert,
UMR7344 Groupe de recherches sur
l'énergétique des milieux ionisés (GREMI),
France

REVIEWED BY

Pradeep Lamichhane,
University of Warwick, United Kingdom
Sohail Mumtaz,
Kwangwoon University, Republic of Korea

*CORRESPONDENCE

Paolo Francesco Ambrico,
✉ paolofrancesco.ambrico@cnr.it
Rita Milvia De Miccolis Angelini,
✉ ritamilvia.demiccolisangelini@uniba.it

[†]These authors have contributed equally to this work and share last authorship

RECEIVED 12 March 2024

ACCEPTED 09 April 2024

PUBLISHED 06 May 2024

CITATION

Aceto D, Rotondo PR, Porfido C, Bottiglione B, Paciolla C, Terzano R, Minafra A, Ambrico M, Dilecce G, Leoni B, De Miccolis Angelini RM and Ambrico PF (2024), Assessing plasma activated water irrigation effects on tomato seedlings. *Front. Phys.* 12:1399910. doi: 10.3389/fphy.2024.1399910

COPYRIGHT

© 2024 Aceto, Rotondo, Porfido, Bottiglione, Paciolla, Terzano, Minafra, Ambrico, Dilecce, Leoni, De Miccolis Angelini and Ambrico. This is an open-access article distributed under the terms of the [Creative Commons Attribution License \(CC BY\)](https://creativecommons.org/licenses/by/4.0/). The use, distribution or reproduction in other forums is permitted, provided the original author(s) and the copyright owner(s) are credited and that the original publication in this journal is cited, in accordance with accepted academic practice. No use, distribution or reproduction is permitted which does not comply with these terms.

Assessing plasma activated water irrigation effects on tomato seedlings

Domenico Aceto¹, Palma Rosa Rotondo², Carlo Porfido², Benedetta Bottiglione³, Costantino Paciolla³, Roberto Terzano², Angelantonio Minafra⁴, Marianna Ambrico¹, Giorgio Dilecce¹, Beniamino Leoni², Rita Milvia De Miccolis Angelini^{2*†} and Paolo Francesco Ambrico^{1*†}

¹CNR Istituto per la Scienza e Tecnologia dei Plasmi—Sede di Bari—c/o Dipartimento Interateneo di Fisica—Campus Universitario “Ernesto Quagliariello”, Università degli Studi di Bari Aldo Moro, Bari, Italy, ²Dipartimento di Scienze del Suolo, della Pianta e degli Alimenti (Di.S.S.P.A.), Campus Universitario “Ernesto Quagliariello”, Università degli Studi di Bari Aldo Moro, Bari, Italy, ³Dipartimento di Bioscienze, Biotecnologie e Ambiente (DBBA), Campus Universitario “Ernesto Quagliariello”, Università degli Studi di Bari Aldo Moro, Bari, Italy, ⁴CNR Istituto per la Protezione Sostenibile delle Piante—Sede di Bari—c/o Campus Universitario “Ernesto Quagliariello”, Università degli Studi di Bari Aldo Moro, Bari, Italy

Introduction: The study investigates the potential of Plasma Activated Water (PAW) as an innovative irrigation medium to enhance growth and defense responses in tomato seedlings. It explores PAW's utility in both healthy seedlings and those inoculated with *Tomato mottle mosaic virus* (ToMMV).

Methods: PAW, produced through a dielectric barrier volume discharge, serves as a chemical-free alternative to traditional fertilizers. Tomato seedlings were irrigated with PAW or control solutions. The study employs biometric measurements to assess growth and biochemical analysis to evaluate antioxidant levels and pigments. Gene expression analysis was conducted to evaluate the plant response, while the distribution of macro and micronutrients was assessed through micro X-ray fluorescence.

Results and discussion: Results indicate that PAW-irrigated seedlings exhibit significant growth enhancement compared to those receiving conventional fertilization. Increased levels of antioxidant molecules and pigments suggest improved photosynthetic activity and stress tolerance. Gene expression analysis shows up-regulation of defense genes in PAW-treated plants post-viral infection. The up-regulation of defense genes and the restoration of mineral nutrient distribution in PAW-treated, virus-infected plants highlight PAW's role in enhancing plant resilience against pathogens and mitigating nutrient deficiencies. These findings emphasize PAW's potential as a sustainable agricultural solution, promoting plant growth, enhancing defense mechanisms, and reducing biotic stress due to virus infections.

KEYWORDS

PAW, low-temperature-plasma, tomato seedlings, plant growth, gene expression, tomato mottle mosaic virus, micro X-ray fluorescence

1 Introduction

In the last decade, the need for suitable, innovative, and non-chemical strategies for agrifood production and plant protection has given rise to new tools for microbial decontamination, plant resistance induction, and enhancement of growth and nutraceutical properties of products. Low-temperature plasma is proposed as a revolutionary tool in modern agriculture, offering versatile applications that span from seed treatment to soil improvement [1]. This novel approach involves subjecting agricultural systems to non-thermal plasma, generating reactive species such as reactive oxygen species (ROS) and reactive nitrogen species (RNS). These plasma-induced reactive species have shown great potential in influencing various aspects of plant growth, stress response, and overall crop performance [2–4]. However, plasma treatments are mainly confined to the surface of materials, and therefore not able to interact with all plant tissues. Thus, different strategies are required for applications, such as the production and usage of plasma-activated media.

In conjunction with the advancements in low-temperature plasma applications, Plasma Activated Water (PAW) has emerged as a cutting-edge and transformative tool in modern agriculture, offering promising potential to enhance crop productivity and address various challenges faced by the industry. This novel approach involves subjecting water to non-thermal plasma exposing it to ROS and RNS [5] and inducing changes in the physicochemical properties of the liquid. These changes can be tailored for different applications [6,7]. Reactive species in PAW impart beneficial effects on plants inducing physiological and biochemical changes with positive effects on growth and stress tolerance [6]. Thus, PAW can be used for watering crops, soaking seeds, and spraying on foliage, being a sustainable and environmentally friendly alternative to traditional chemical fertilizers and pesticides. Recent research on PAW has shown its potential in agriculture. Studies have found that PAW can enhance seed germination, plant growth, and yield across various crops like wheat, cucumber, and tomato [8,9]. It also improves photosynthetic efficiency, and antioxidant enzyme activities [10], and induces self-defense mechanisms in plants [11,12]. However, further research is needed to fully harness its potential.

In this investigation, we studied the potential of PAW to promote the growth of tomato plants under both normal and virus-induced stress conditions, caused by *Tomato mottle mosaic virus* (ToMMV) infection. This dual-pronged approach allowed us to unravel the biological and physiological mechanisms underlying the multifaceted effects of PAW on the growth of both healthy and virus-inoculated plants.

In the examination of healthy plants, our study employed a comprehensive set of parameters to assess the impact of PAW. We closely monitored the growth of the tomato plants, by measuring parameters such as stem length, diameter and leaf area, and the influence of PAW on key components of the plant's antioxidant defense system, including ascorbate, glutathione, chlorophylls, and carotenoids content. Additionally, the gene expression of four different defense-related genes [phenylalanine ammonia-lyase (PAL), pathogenesis-related protein 1 (PR-1), lipoxygenase (LOX), and catalase (CAT)] was analyzed to explore tomato plant responses after PAW irrigation and ToMMV inoculation. Expanding our focus to plants subjected to ToMMV-induced stress, we implemented a comparative analysis employing micro X-ray fluorescence (μ -XRF) spectroscopy to visualize the changes in the distribution of micro and macro-nutrients in the plant leaves,

unveiling insights into the nuanced responses mechanisms of virus-inoculated plants to PAW treatment.

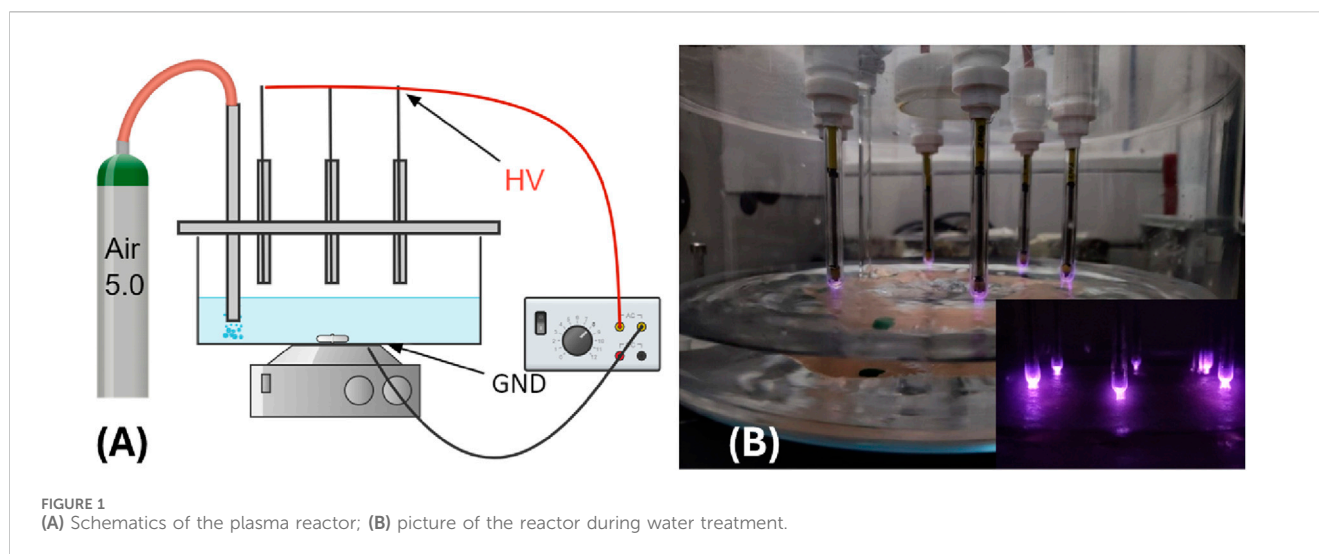
2 Materials and methods

2.1 Plasma activated water production

The plasma reactor employed in this study (Figure 1B) operates on an AC voltage with a frequency of 13 kHz, modulated by a square pulse at a 500 Hz repetition rate with a 38% duty cycle. A schematic of the plasma reactor is shown in Figure 1A. A glass pot is used as the water reservoir and reaction chamber. The pot is closed at the top by a plexiglass cover with holes to house the high-voltage electrodes and the gas inlet tube. The six high-voltage electrodes consist of metal pins enclosed in quartz sleeves. At the bottom of the pot, on its outer face, a copper tape shaped like a hexagon, positioned to have its vertices lining up with the HV electrodes, serves as the grounded electrode. Thus, two dielectric barriers are interposed between the electrodes. When the chamber is filled up with double-distilled water, the liquid itself acts as another dielectric layer and establishes a discharge gap of 5 mm. The double dielectric configuration enhances the reproducibility of the pulsed discharge, ensuring stable plasma activation conditions. A controlled airflow of 2 standard liters per minute (slm) is insufflated directly into the water, providing a complete replacement of the gas in the whole vessel in less than a minute and increasing the water vapor content in the gas mixture, possibly enhancing hydrogen peroxide formation. However, due to the presence of cool walls, the evaporation induced by gas flow and temperature does not reduce the total water volume as vapor condenses on the outer wall of the vessel. Each treatment involves subjecting 500 mL of double-distilled water (RPE Carlo Erba Reagents) to this dynamic process, with continuous stirring to guarantee homogenous exposure. The treatment protocol consists of four 15-min steps, allowing for meticulous control and modulation of the plasma activation parameters. A picture of the setup during the water treatment is reported in Figure 1B.

The discharge voltage-charge and voltage-current characteristics were recorded using a Keysight InfiniiVision MSOX6004A with a bandwidth of 1 GHz and a sampling rate of up to 20 GS/s. To measure the applied voltage, a Tektronix P6015A high voltage probe with a ratio of 1,000:1 at 1 M Ω , a bandwidth of 25 MHz, and a rise time of 4.7 ns was employed. The current was measured using a Magnelab CT-c1.0 Rogowski coil with a rise time of 0.7 ns attached to the ground cable. Additionally, charge measurements were obtained by inserting a 2.4 nF high-voltage capacitor between the induction electrode and the ground. The energy was measured from charge-voltage Lissajous characteristics by integrating them.

The optical diagnostic was performed through a slit in the glass vessel (1.5 mm \times 30 mm) closed by a quartz window. The Plasma Induced Emission (PIE) was collected by an optical fiber designed to adapt to the monochromator slit with a maximum size of 3 mm in width and 5 mm in height. A 30 cm spectrometer (Acton Spectra Pro 2,300) was employed for spectral resolution, featuring a multiple-grating turret (300/600/1200 grooves \times mm $^{-1}$, blazed at 300 nm) and a Princeton Instruments PI-MAX4 1024i CCD (1024 \times 1024 pixel sensor, pixel size 12.8 μ m, active area 13.1 \times 13.1 mm 2). Each CCD image covers a spectral range of approximately 144/65/30 nm for the three gratings. The emission



spectra intensities, detected by the ICCD (Intensified CCD) detector, undergo spectral and intensity correction through calibration and Halogen lamps. These captured spectra are time-resolved with a 50 μ s gate at the start of each high-voltage (HV) half cycle.

2.2 Quantification of reactive nitrogen and oxygen species (RONS) produced in PAW

The PAW was characterized in its chemical composition in terms of the active species identified in the literature as responsible for its biological effects: nitrite and nitrate ions and hydrogen peroxide content. The concentration of the different reactive species was measured using a multiparametric photometer Aqualytic AL400 and Cell Test Lovibond® Water Testing (Tintometer Inc., Germany), according to the manufacturer's instructions for quantification of nitrate ions (Vario Nitra protocol X 535,580, quantification range 0–30 mg L^{-1}), nitrite ions (protocol 512310BT, range 0.01–0.5 mg L^{-1}) and hydrogen peroxide (protocol 512381BT, range 0.03–3 mg L^{-1}). Due to the concentration of active species being higher than the quantification range, in most cases prior to measuring it was necessary to dilute the PAW with the same double-distilled water used to produce it. When the sample was diluted, the results of the tests were multiplied by the corresponding dilution factor.

The pH and oxidation-reduction potential (ORP) values were measured with a HANNA Instruments (USA) pH-meter model HI98191 equipped with a HI72911 pH probe and a HI3131 ORP probe.

2.3 Plant growth and irrigation with PAW

Seeds of tomato (*Solanum lycopersicum* L.) cv. Regina were sown, and the seedlings were then transplanted in a commercial peat moss substrate (BRILL Typical 3, Germany) at the “two true-leaves” stage. Pots ($9 \times 14 \times 5 \text{ cm}^3$) were kept in a thermo-conditioned glasshouse box at $25^\circ\text{C} \pm 2^\circ\text{C}$ and exposed to Osram L36W Cool White lamps with an 18 h photoperiod.

After the transplant, the seedlings were daily irrigated with 5 mL of the appropriate solution according to the irrigation treatment reported

in Table 1. Two positive control solutions, consisting of 1 g L^{-1} ammonium nitrate (YaraTera AMNITRA, Norway), and 0.5 g L^{-1} of the commercial fertilizer (Nitrophoska® Special 12–12–17, NPK-based, EuroChem, Switzerland) were used. Double-distilled water (RPE Carlo Erba Reagents, Italy) was used as the negative control.

Three seedlings per pot represented a single biological replicate. All treatments were performed in three replicates per analysis and the experiments were repeated twice.

2.4 Biometric measurements

The stem length, diameter, and leaf surface area were measured 21 days after the first irrigation time. Biometric measurements were performed by collecting RGB images through a Digital reflex camera with a 50 mm objective (Nikon D5300) of the entire plant and the last three apical leaves of each plant branch. Images were then calibrated with respect to a target of known dimension to extract the pixel/cm conversion constant. The leaf area and stem length were then processed via the freely available Digimizer Image Analysis Software [13]. A total of 18 plants per treatment were analyzed.

2.5 Determination of chlorophyll and carotenoid content, and ascorbate and glutathione pools

The chlorophyll and carotenoid content was determined according to Lichtenthaler [14] with some modifications. Samples of uninoculated seedlings (NTDDW, WNPK, WAN, PAW) were irrigated for 21 days after transplant and subsequently analyzed. In detail, 0.5 g of the aerial part of the seedling were ground with 8 mL of absolute acetone and centrifuged at $20,000 \times g$ for 15 min. The absorbance of the supernatant (total filtrate volume in mL) was spectrophotometrically measured (Beckman DU-800 UV/Vis spectrophotometer, Beckman Coulter, Inc., USA) at 645 nm for chlorophyll *a*, 662 nm for chlorophyll *b*, and 470 nm for carotenoids. Chlorophyll (Chl *a*, *b*, and *a+b*) and carotenoids (Car) contents were calculated using the following equations:

TABLE 1 Summary of the plant growth conditions explored.

Treatment conditions	Sample code
Plants irrigated with double-distilled water	NTDDW
Plants irrigated with tap water added with standard fertilizer (Nitrophoska® Special 12–12–17, NPK-based)	WNPK
Plants irrigated with double-distilled water added with ammonium nitrate (YaraTera AMNITRA)	WAN
Plants irrigated with Plasma Activated Water	PAW
Plants inoculated with ToMMV and irrigated with double-distilled water	I-NTDDW
Plants inoculated with ToMMV and irrigated with Plasma Activated Water	I-PAW

$$\text{Chl } a \text{ } (\mu\text{g/mL}) = 11.24 A_{662} - 2.04 A_{645}$$

$$\text{Chl } b \text{ } (\mu\text{g/mL}) = 20.13 A_{645} - 4.19 A_{662}$$

$$\text{Chls } (a + b) \text{ } (\mu\text{g/mL}) = 7.05 A_{662} + 18.09 A_{645}$$

$$\text{Car } (\mu\text{g/mL}) = (1000 A_{470} - 1.90 \text{Chl } a - 63.14 \text{Chl } b)/214$$

and the values were expressed as μg per g of fresh weight of tissue.

For the ascorbate and glutathione pool content determination, plant samples were homogenized with three volumes of cold 5% (w/v) metaphosphoric acid in a porcelain mortar. The homogenate was centrifuged for 15 min at $20,000 \times g$ and the supernatant was collected for the analysis of ascorbate (AsA), dehydroascorbate (DHA), reduced glutathione (GSH) and oxidized glutathione (GSSG) according to Zhang and Kirkham [15].

2.6 Inoculation with ToMMV

Plants were artificially inoculated at 48 h after transplant and first irrigation. The inoculation was performed mechanically by abrasion with celite and a suspension of ToMMV obtained macerating by mortar and pestle 0.5 g of infected leaves at least 10 days post inoculation (dpi) in 2 mL of 0.1M Tris-HCl buffer pH 8.0. Plants were maintained until the expression of viral symptoms on inoculated plants (about 40 days after transplant).

2.7 RNA extraction and cDNA synthesis

Plant responses to PAW were studied by gene expression analysis carried out on uninoculated tomato plants at 24, 48, and 96 h from the first irrigation, and on uninoculated and ToMMV-inoculated plants at two and seven dpi. Three leaves were sampled from each of the three replicated pots for the untreated control and PAW-irrigated plants. Different seedlings were sampled at each time point to avoid the effects of the wounding stress. Total RNA was extracted from 50 mg of fresh tissues that were macerated in a 1.5 mL tube using a plastic pestle containing CTAB buffer added with 2% 40K-polyvinylpyrrolidone and 2% sodium metabisulfite just before use [16]. After chloroform extraction and isopropanol precipitation, the nucleic acid pellet was resuspended in sterile water and quantified by optical density reading with a NanoPhotometer™ N60 UV/Vis spectrophotometer (Implen, Germany).

Aliquots of 750 ng of the extracts were then reverse transcribed by MMLV-RT (Thermo Fisher Scientific, USA) and random hexanucleotide primers in a 40 μL reaction volume, at 42°C for 1 h, to obtain complementary DNA (cDNA).

2.8 Gene expression analysis

Plant defense-related genes were selected and used for gene expression analysis by quantitative polymerase chain reaction (qPCR). In detail, primer pairs specific for the four target genes (PAL [17], PR-1 [18], LOX [19], and CAT [20]), and for the reference genes elongation factor 1 α (EF-1) and ubiquitin (UBI) [21], were used. qPCR reaction mixture contained $1 \times \text{iQ}^{\text{TM}}$ SYBR® Green Supermix (Bio-Rad, Hercules, CA, United States), 25 μM of each forward and reverse primer, 1 μL of cDNA, and ultrapure water up to 25 μL .

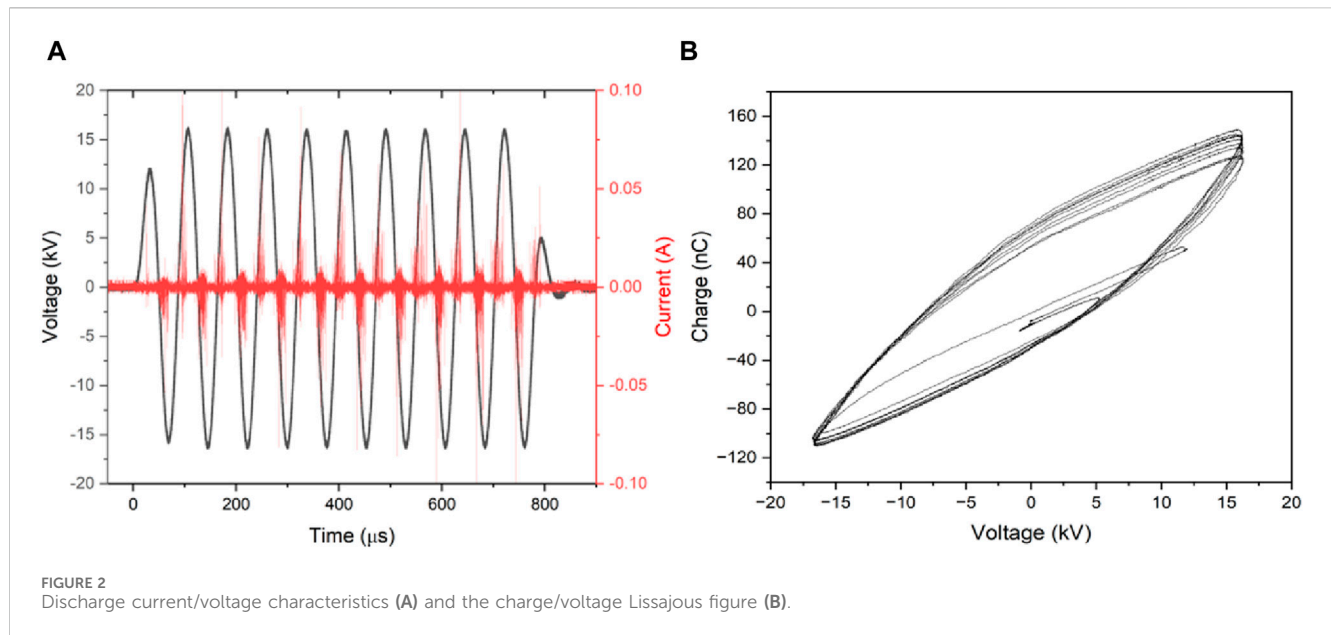
PCR amplification was performed with the following cycling parameters: initial denaturation at 95°C for 3 min, 40 cycles at 95°C for 10 s, and 60°C for 45 s for annealing and extension. Melting curve analysis was performed over the range of 60°C – 95°C . The stability of the two housekeeping genes was verified with BestKeeper® software [22] and the geometrical mean of both genes was used for gene expression analysis. The relative fold change was calculated according to the $2^{-(\Delta\Delta\text{Ct})}$ method [23].

2.9 Virus quantification

For qPCR quantification of ToMMV in tomato plants, the cDNA obtained as previously described and the primer set ToMMV-rtfor (5'-TTGTCATCAGCATGGGCCGACC-3', position 5759 > 5780 on the reference viral genome NC_022230) and ToMMV-rtrev (5'-ACACCTCGCTGAACTGCTGTTG-3', position 5854 > 5875) were used. The amplification mixture consisted of 1X SYBR™ Select Master mix (ThermoFisher Scientific, USA), 0.4 μM of each primer, 1 μL of cDNA, and ultrapure water up to 12.5 μL . A run of 40 cycles was performed with an annealing temperature of 56°C .

2.10 Micro- and macronutrients distribution in seedling leaves

The spatial distribution of several plant macronutrients (Mg, S, P, K, and Ca) and micronutrients (Mn, Fe, Cu, and Zn, data not shown) in tomato leaflets was investigated by collecting micro-focused X-ray



fluorescence elemental maps. For such analysis, tomato leaves were collected from 40-day-old seedlings, the leaflets split and immediately prepared as described by Terzano et al. [24].

The μ -XRF analysis was carried out using a benchtop μ -XRF spectrometer (M4 Tornado, Bruker Nano GmbH, Berlin, Germany) equipped with a micro-focus Rh X-ray source (50 kV, 600 μ A), a polycapillary X-ray optics with a spot-size of 25 μ m and two XflashTM energy dispersive silicon drift detectors (SDD) with 30 mm² sensitive area and an energy resolution of 140 eV @ Mn K α .

In particular, the following treatment conditions (as per Table 1) were analyzed: PAW, I-NTDDW, I-PAW, while WNPk and NTDDW were used as the positive and negative control, respectively. For each of the five sets of leaflets, rectangular areas of approximately 10 \times 15 mm at the middle right of the leaf and including the midrib were imaged by μ -XRF analyses.

All μ -XRF maps were acquired under near-vacuum conditions (20 mbar) using 25 μ m step size and 10 ms per pixel acquisition time. For each sample, the scanning was repeated 3 times, and the relative spectra were averaged to increase the signal-to-noise ratio (S/N). Finally, μ -XRF distribution maps were obtained with the ESPRIT software (Bruker Nano GmbH, Berlin, Germany, version 1.3.0.3273) and presented for each element using relative intensity scales.

2.11 Statistical analysis

The data reported are the average of three replicates from two independent biological experiments. For the investigated analyses, means and standard error (\pm ES) are shown. The Shapiro-Wilk test was run to verify the normality of data distribution. The analysis of variance (one-way ANOVA), followed by Tukey's *post hoc* test, was used to compare the conditions using GraphPad Prism version 9.0.0 for Windows (Boston, Massachusetts USA). Differences were considered statistically significant at a p -value ≤ 0.05 .

3 Results

3.1 Plasma characteristics

Panel A of Figure 2 displays the voltage and current waveforms observed during the PAW production treatment. The filamentary characteristics of the DBD are evident from the current peaks occurring at the onset of each voltage half-cycle. By integrating the obtained Lissajous figures (a typical one is presented in Figure 2B), we were able to estimate the energy dissipated during each voltage burst, resulting in a calculated value of $E_{\text{burst}} = 26$ mJ. Globally, over the course of the treatment, the water is subjected to a total plasma dose of 93.6 J/g_{water}.

3.2 Spectroscopic observation

In Figure 3 the emission spectra collected from the discharge zone above the water surface in air, in the spectral region from 270 to 420 nm, are reported.

They reveal strong bands of the second positive system (SPS) of molecular nitrogen and the first negative system (FNS) of molecular nitrogen ion, together with a clear signature of hydroxyl radical (OH) emission bands in the UV spectral region. In the Vis-NIR region, we observed characteristic sequences of bands of the first positive system (FPS) of molecular nitrogen together with the emission line for atomic oxygen observed at 777 nm (not shown). From the nitrogen SPS(0,0) band the rotational temperature was derived by using the spectroscopic tool Massive OES [25–27]. Figure 4 shows the experimental mean SPS(0,0) band profile, with corresponding standard error, together with synthetic profiles simulated for rotational temperatures of 444, 555, and 600 K respectively for the PIE observed in the corresponding gates. The estimated error from multiple simulations of bands, not shown for the sake of clarity, at different temperatures was on average of the order of 10% of the reported measurements being respectively ± 44 , ± 55 , and ± 60 . By comparing the acquired and simulated spectra, we can

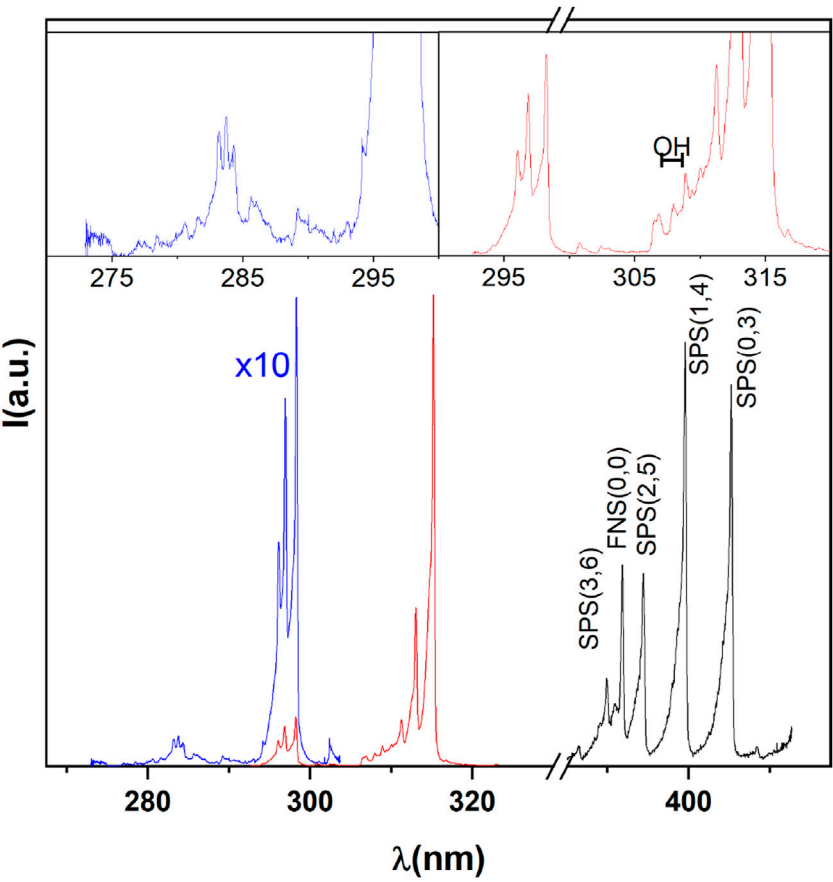


FIGURE 3
Spectral signature of the discharge.

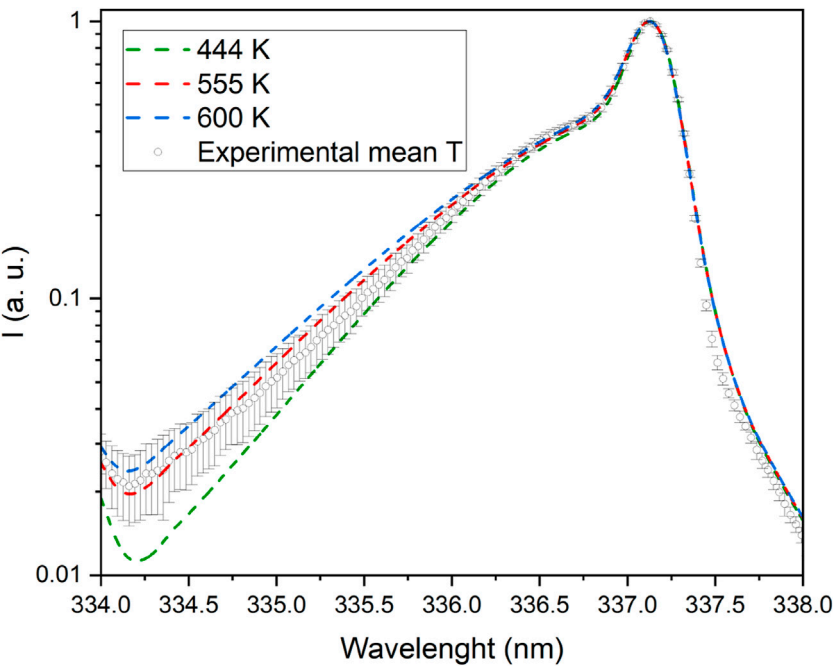


FIGURE 4
SPS(0,0) band signature for plasma temperature measurements.

surmise that the temperature developed in a plasma filament falls indeed in the 444–600 K range. However, it is also important to point out that, due to the filamentary character of the discharge, the temperature measured by optical emission is not representative of the entire volume of the gas inside the chamber but only of the portion of the gas crossed by the streamer. The treated water never reached the boiling point (save for possible local but not detected hot points), and its temperature increased by about 20°C (from 13.5 ± 0.8 to $35.3 \pm 1.4^\circ\text{C}$) in all experiments.

3.3 PAW chemical composition

The chemical composition of PAW in terms of nitrite, nitrate, hydrogen peroxide concentration, pH, and ORP was characterized immediately after plasma treatments of 30 and 60 min. Subsequently, the measurements were repeated on water treated for 60 min 1 week after plasma treatment. This final measurement aimed to assess the chemical evolution of the PAW up to its equilibrium point. Figure 5 reports the analyses as mentioned above, grouped by measured quantity.

During the treatment, H_2O_2 , NO_2^- and NO_3^- were produced, water was acidified and ORP increased. At higher treatment times $[\text{H}_2\text{O}_2]$ increased and NO_2^- was converted into NO_3^- and other RNS.

pH and ORP in the PAW were quite stable after 1 week from the plasma treatment. $[\text{H}_2\text{O}_2]$ and $[\text{NO}_2^-]$ decreased while $[\text{NO}_3^-]$ increased, likely due to a conversion of the first two compounds (i.e., NO_2^- oxidation) and other RNS into the latter.

The energy yield of NO_x production by our DBD setup is $2.7 \text{ g-NO}_x \text{ kWh}^{-1}$. This translates into an energy efficiency of 81.2 MJ/mol NO_x just at the end of a 60-min plasma treatment, i.e. 1309.7 GJ/tN (tN = tons of nitrogen). This value, although somewhat high if compared to other studies focusing on plasma-catalytic nitrogen fixation, falls in ranges typical of NO_x production by DBD plasma without a catalyst [28,29].

3.4 Effects of irrigation with PAW on tomato plants

3.4.1 Biometric characteristics

Biometric parameters of tomato plants irrigated with PAW, in comparison with the other treatment conditions (WAN, WNPk, and NTDDW), were measured after 21 days of treatment. Figure 6 reports a representative example of samples grown in different conditions. Results, reported in Figure 7, show that the PAW treatment performs better in terms of stem length, diameter, and leaf area surface with statistically significant differences with respect to the other cases. No significant differences are obtained among the other cases.

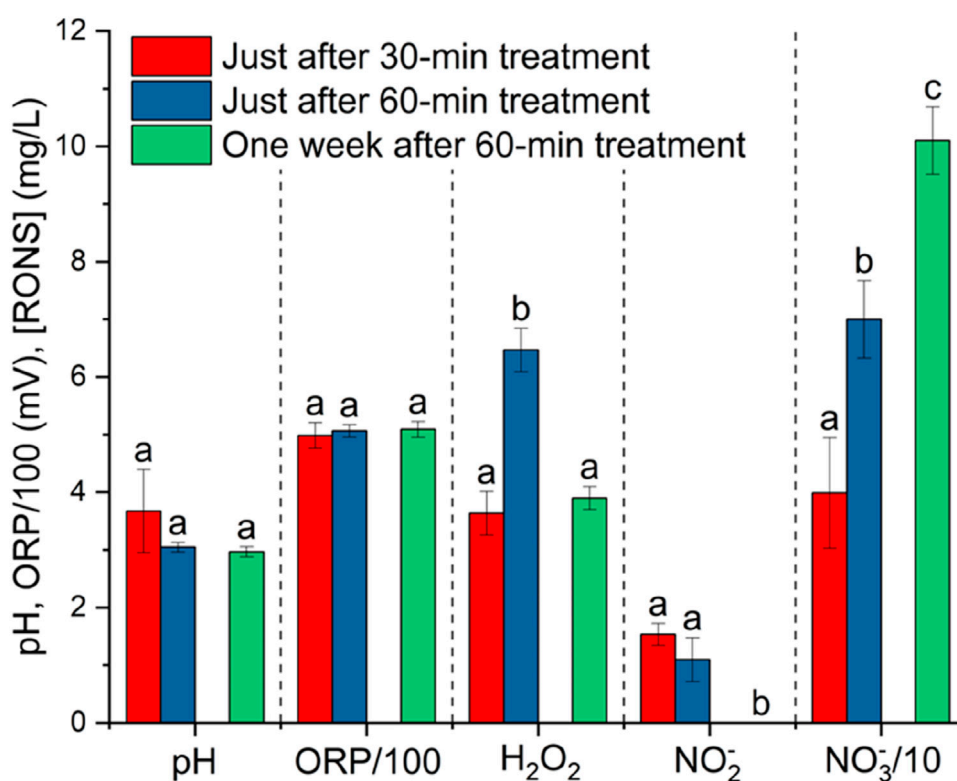


FIGURE 5
pH, ORP, nitrate, nitrite, and hydrogen peroxide content of PAW at two different water-treatment times (30 and 60 min) and 1 week after a 60-min plasma treatment. The 500 mL samples used for this measurements were stored in the dark at room temperature following treatment. Values with the same letter for each parameter are not significantly different by Tukey's HSD test ($p < 0.05$).

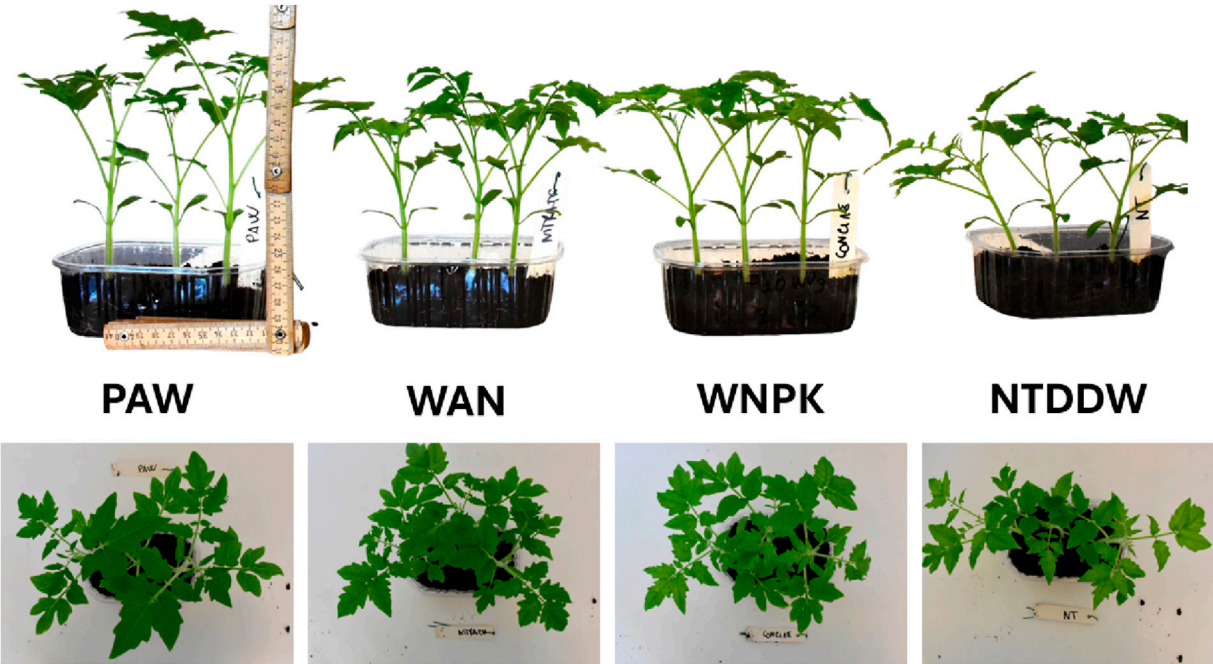


FIGURE 6
Side and top view of a typical tomato seedling after 21 days of irrigation.

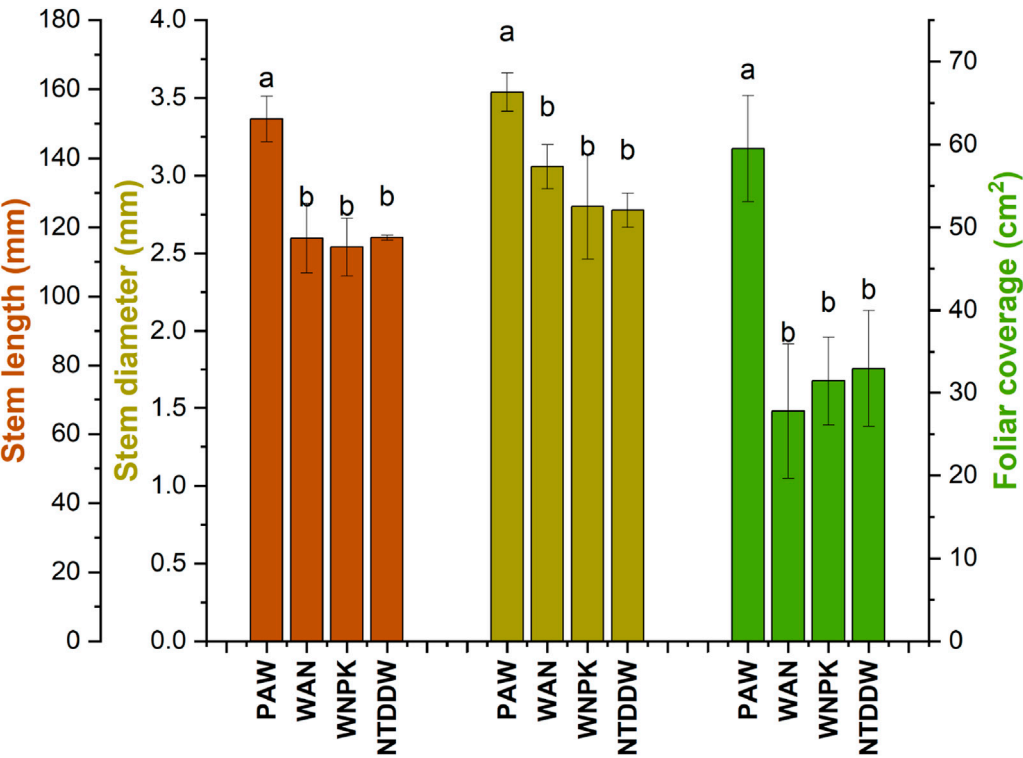


FIGURE 7
Biometric parameters of tomato seedlings at 21 days after the first irrigation. Data are reported as mean values \pm S.E. Values with the same letter for each parameter are not significantly different by Tukey's HSD test ($p < 0.05$).

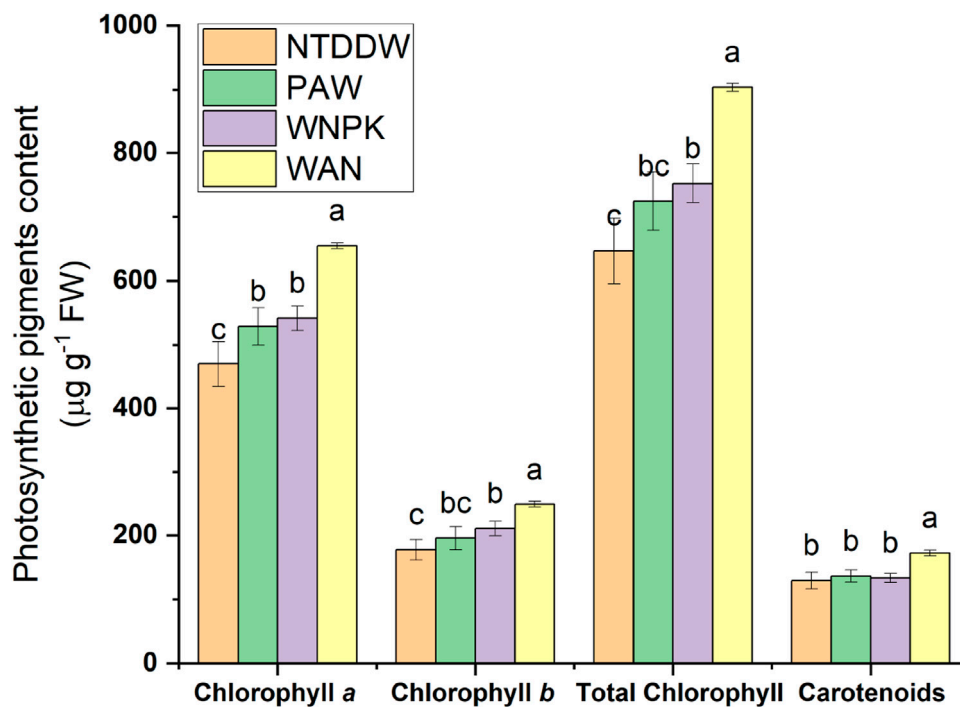


FIGURE 8

Photosynthetic pigments content at 21 days after the first irrigation. Data are reported as mean values \pm S.E. Values with the same letter are not significantly different by Tukey's HSD test ($p < 0.05$).

3.4.2 Effect of different treatments on photosynthetic pigments

In all treatments, a significant increase of chl *a* respect to the control NTDDW was observed (see Figure 8). Chl *b* and total chlorophyll (*a* + *b*) increased in WNPK and more significantly in WAN while no significant changes were observed for the PAW samples with respect to the NTDDW. Carotenoids significantly increased in WAN samples whereas in PAW and WNPK samples, no difference with respect to the control was recorded.

3.4.3 Changes in ascorbate and glutathione pool

The changes in reduced (AsA) and oxidized (DHA) ascorbate forms together with the total pool after treatments are shown in Figure 9A. Tomato seedlings exposed to PAW showed the highest pool content (AsA + DHA) compared to the NTDDW control and other treatments. Particularly, both the reduced and oxidized forms of ascorbic acid were highest ($p < 0.05$) in seedlings treated with PAW. The same levels of AsA total pool and AsA were observed in the WAN sample if compared to the control NTDDW. As regards the WNPK sample, AsA content significantly decreased with respect to NTDDW whereas DHA content did not change with a consequent decrease of AsA total pool. A significant decrease in the AsA/(AsA + DHA) ratio occurred in WAN while no change in the other treatments with respect to the control NTDDW was registered (Figure 9B).

In the seedlings treated with WNPK and WAN, both the reduced (GSH) and oxidized (GSSG) glutathione forms significantly decreased with respect to the control NTDDW, and consequently, a decrease in

glutathione pool was observed (Figure 9C). In the PAW treatment, no difference in GSH and GSSG content was observed, if compared to the control NTDDW. In addition, a decrease in the GSH/(GSH + GSSG) ratio was registered in WNPK and WAN treatments if compared to PAW and NTDDW ones (Figure 9D).

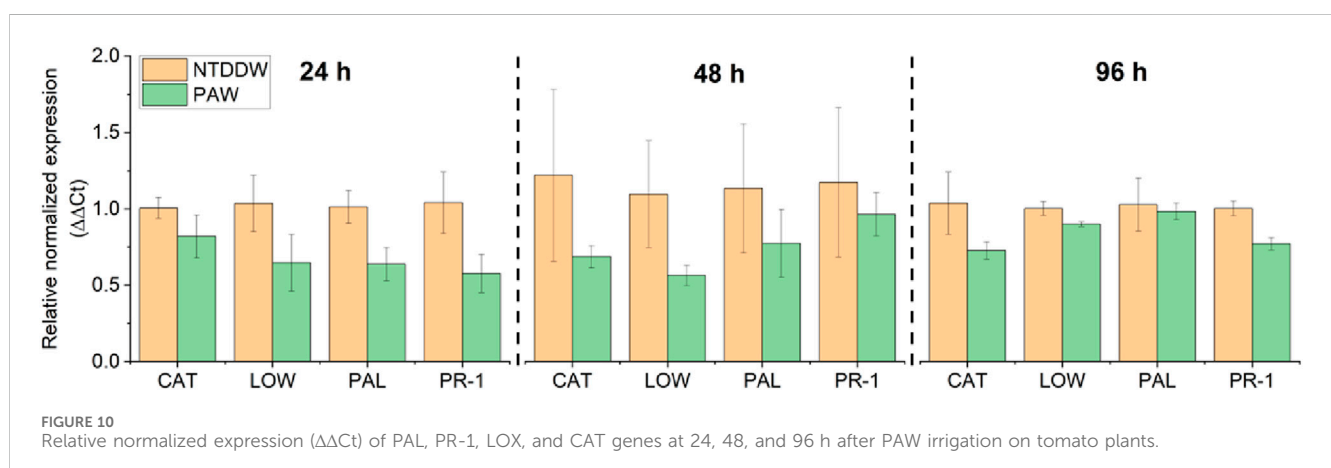
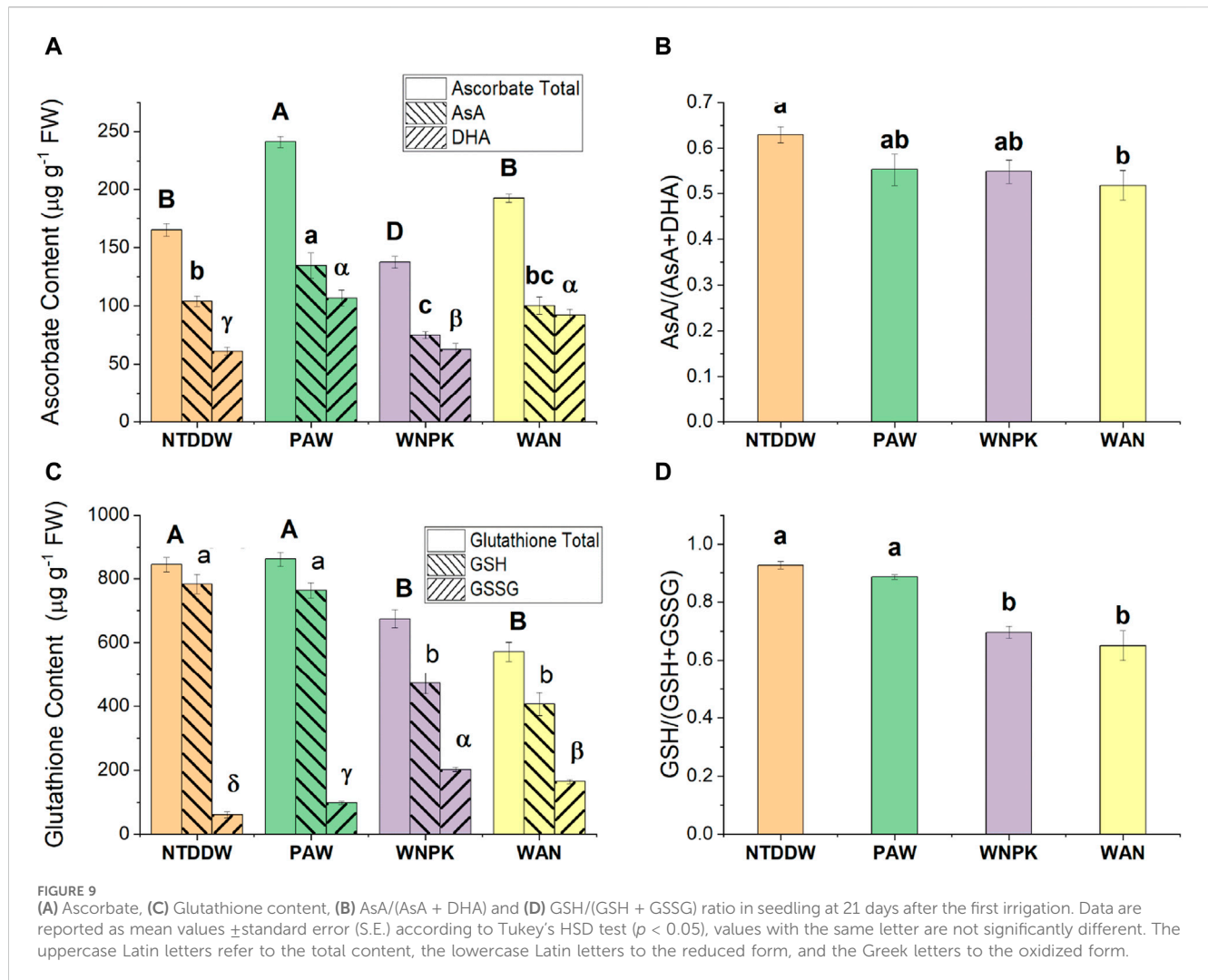
3.4.4 Gene expression analysis in tomato plants irrigated with PAW

To evaluate the possible induction of defense-related genes after irrigation with PAW, the relative normalized expression ($\Delta\Delta C_t$, related to the untreated control) of the PAL, PR-1, LOX, and CAT genes was analyzed.

In un-inoculated plants analyzed at early stages (24, 48, and 96 h) after watering, all four genes were downregulated in the PAW-irrigated plants compared to the control (NTDDW) (Figure 10). Fewer differences in gene expression between the two conditions were generally recorded at 96 h compared to the previous sampling times (Figure 10).

On the contrary, in the ToMMV-inoculated plants analyzed at two and seven dpi, all the genes were upregulated by irrigation with PAW (Figure 11, right panel). In particular, the highest upregulation induced by PAW was recorded for PR-1 and LOX genes at seven dpi, with a mean fold change (FC) of gene expression levels close to two for both genes.

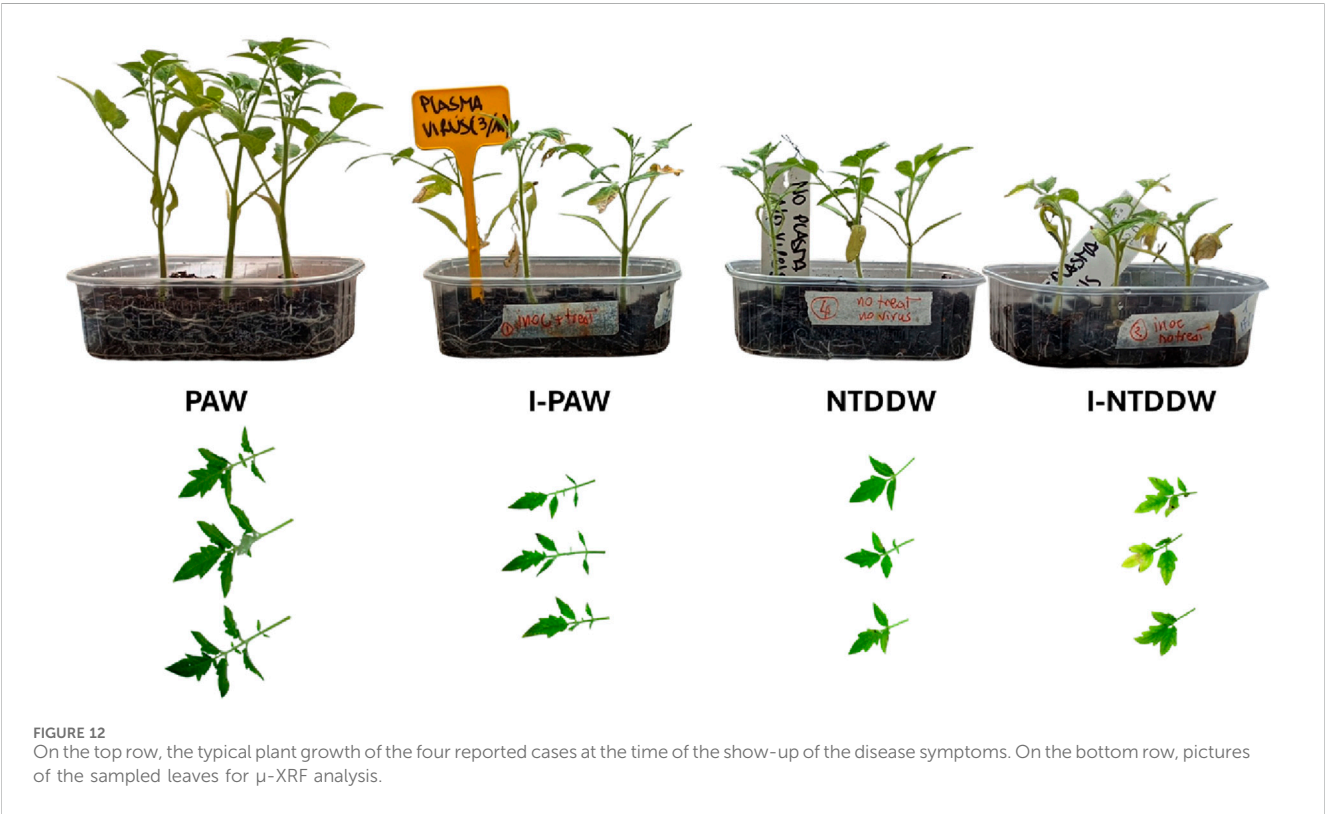
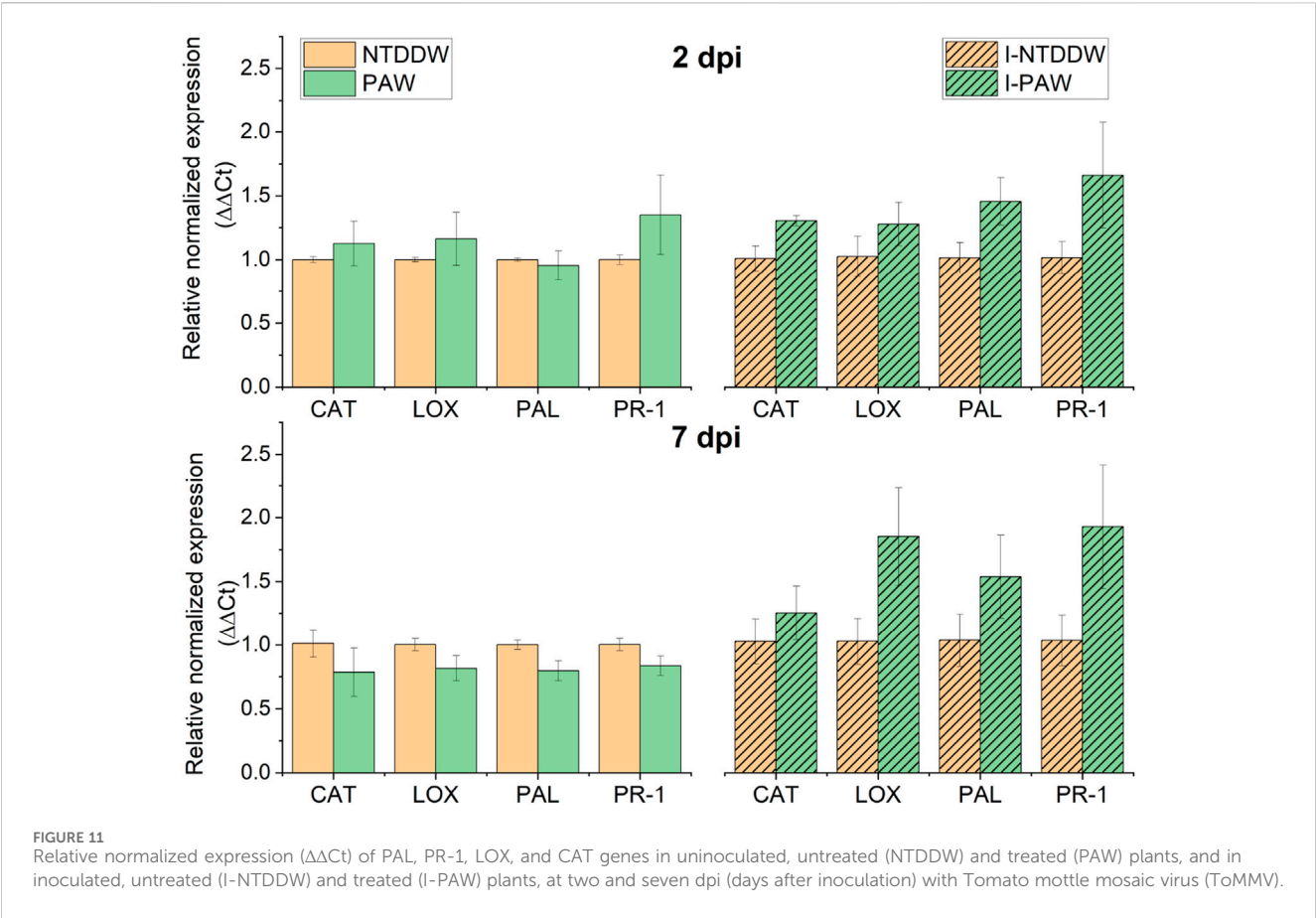
At two dpi, on the uninoculated plants (Figure 11, left panel) the PR-1 gene was upregulated (FC = 1.4), while the other genes were only slightly upregulated (CAT and LOX) or downregulated (PAL) by PAW. At seven dpi, all the genes were slightly downregulated in PAW compared to NTDDW samples.



3.4.5 Virus quantification

Virus concentration in the inoculated plants increased along with the sampling time points because of the viral replication in the infected tissues. Thus, the quantification cycle (C_q) at which the titer started to be visible over the threshold of negative values, decreased

from two dpi to seven dpi in both I-PAW (PAW-treated virus-inoculated) and I-NTDDW (untreated-inoculated) samples. A trend of a slight increase in virus concentration was apparently visible, however, in I-PAW, showing C_q values ranging from 19.97 (2 dpi) to 10.25 (7 dpi), compared to I-NTDDW, with C_q values from



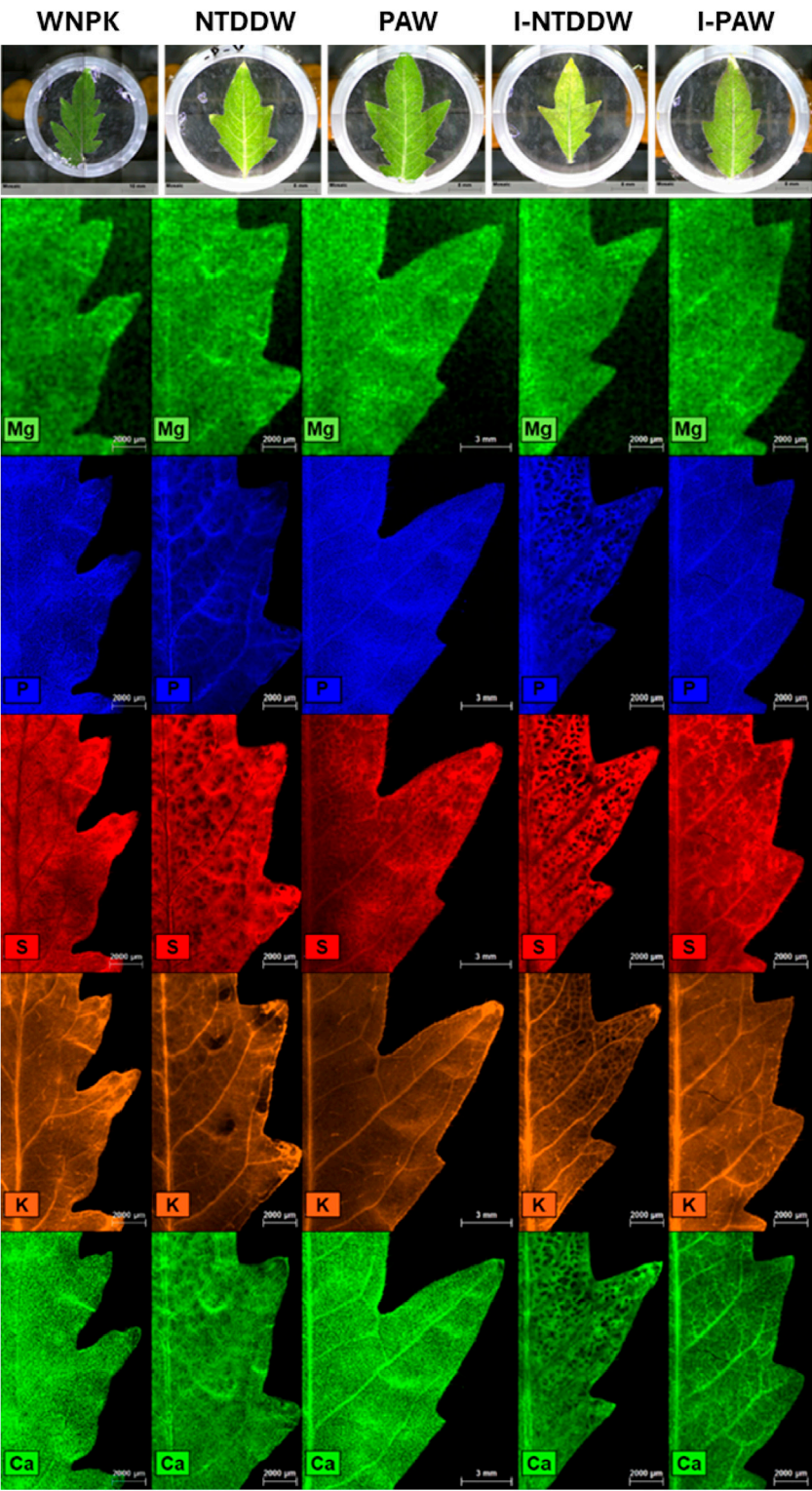


FIGURE 13
Spatial distribution of Mg, P, S, K, and Ca in tomato leaflets, as obtained through μ -XRF analysis.

19.07 to 11.87 at the same time points. No virus infection was detected in uninoculated plants (PAW and NTDDW). The expression of symptoms on inoculated plants (stunting, shoe-stringed and mottled leaves, generalized yellowing of the foliage, etc.) started to be visible after 35–40 dpi because the cultivar Regina (a local variety) used in the trials could be considered quite tolerant to the ToMMV infection [30].

3.4.6 Micro and macronutrients distribution in seedling leaves

In this study, μ -XRF was applied to investigate the possible effects of PAW on element homeostasis at the leaf level, also in the case of ToMMV infection. Figure 12 captures the status of the seedlings at 40 days after transplanting for the PAW, I-PAW, NTDDW, and I-NTDDW cases. Figure 13 shows the spatial distribution of Mg, P, S, K, and Ca in tomato leaflets, as obtained through μ -XRF analysis. For the above-listed elements, the positive control sample (WNPK) shows a rather homogeneous distribution in the different leaf tissues, which in general can be considered indicative of good nutritional and health status [31]. Similar distributions can be observed in PAW samples too, even if some differences occur in the I-PAW leaflet, especially for Ca. Indeed, Ca distribution in I-PAW seems to be partially affected by the ToMMV, with a preferential accumulation of this element in the veins rather than in the leaf lamina. Along with this, in both PAW and I-PAW samples also the S signal increased in the midrib and primary veins with respect to the WNPK. Conversely, in the WNPK and untreated (NTDDW and I-NTDDW) samples, S is not observed in the veins. Besides this, other significant differences were clearly visible in untreated samples (NTDDW and I-NTDDW) when compared to the positive control (WNPK) and the treated ones (PAW, I-PAW). In fact, for all the untreated samples, inhomogeneous element distributions at the leaf level were observed especially for P, S, and Ca, characterized by large dark spots in the distribution maps. Potassium (K) distribution also shows several depletion zones in untreated samples, with fewer but larger dark spots for NTDDW, becoming smaller but more frequent in I-NTDDW. These phenomena appeared more intense for the inoculated samples (Figure 13).

4 Discussion

In this paper, we evaluated Plasma Activated Water (PAW) as a novel irrigation medium to promote growth and defense responses in tomato seedlings, either healthy or inoculated with ToMMV. Plasma-based technologies could pose an interesting and viable alternative to traditional fertilizing methods, by their nature as on/off sources that do not require the employment of chemicals and eliminate the need for stockage [32].

PAW was produced by exposing double-distilled water to a VDBD plasma in a custom-made reactor. The “activation” process involves chemical species that are produced at the onset of the plasma discharge. The main reactants in the gas phase that are exposed to plasma are molecular oxygen and nitrogen, from the supplied air, and water vapor. When the discharge is ignited, these molecules are immediately vibrationally excited, and the energy provided by the plasma breaks them apart and fosters a series of reaction pathways that are not yet fully understood. For example, from the spectroscopic observations we reported, we can infer the formation of NO, atomic oxygen, and hydroxyl radicals near the discharge filaments. These species are then dissolved in the water bulk through the water-gas interface, where they continue to undergo a series of reactions and chemical transformations. As reported by Lukes et al. [33], the transient species produced in the discharge (namely, OH, NO, and NO₂ radicals) are converted into

more stable chemical products once they are dissolved in water, such as H₂O₂, NO₂[−] and NO₃[−], acidifying the produced PAW. At the acidic pH values that are typical of the produced PAW, moreover, a conversion mechanism of H₂O₂ and NO₂[−] into NO₃[−] through the peroxyxynitrite intermediate is established [33], leading to the depletion of hydrogen peroxide and nitrite ion and an increase in the concentration of nitrate ion at longer treatment times. A week after the PAW production, this reaction results in the complete disappearance of NO₂[−], a decrease of the H₂O₂ content in the PAW, and conversely, an increase in NO₃[−]. The acidity (pH 3.0 ± 0.1) after complete treatment of the solution can be attributed mainly to nitric acid. However, the acidic nature of PAW is not a problem when used to water plants grown on soil or a solid substrate since soils and substrates usually have a buffer capacity that prevents substrate acidification or strongly limits pH variations, such as in the case of our study. A proper selection of soil and substrate, as it is usually done in horticulture, is therefore important to get a final pH that is suitable for the growth of the selected crop. In addition, NO₃[−] uptake by plant roots occurs through a symport transport with H⁺ ions which causes an increase of pH of the growth medium [34]. Being nitrogen mainly in the form of NO₃[−] in PAW, such physiological process contributes to balance PAW acidity. Differently, more attention should be paid when PAW is used in hydroponic systems. In this case, the solution should be properly buffered (e.g., by adding other mineral nutrients as base salts or metals with catalytic properties for nitrogen fixation [35,36]) before use.

The measured ORP of 506 ± 11 mV, which suggests an oxidizing character of the PAW, is caused by the presence of all the above-mentioned species, known to possess highly oxidative properties. The typical ORP value of the PAW could prove useful in the decontamination of soils against plant pathogens to prevent and manage soilborne diseases and could also put the plant cell into mild oxidative stress, unlocking new metabolic pathways for growth and defense responses conferring resistance to biotic and abiotic stresses.

Biometric measurements were performed on plants after 21 days of irrigation for the four different treatment conditions. Results showed a statistically different behavior of PAW irrigated samples with respect to other conventional treatments and untreated ones. In particular, the growth of PAW-irrigated seedlings was enhanced by at least 10% for all the measured parameters. Moreover, to evaluate the effect of PAW on the fitness of the seedlings after 21 days of treatment, antioxidant molecules such as ascorbic acid and glutathione and pigments such as chlorophylls and carotenoids were also monitored.

Chlorophylls and carotenoids are pigments that with proteins form the light-harvesting complexes that are part of photosystems, functional units of photosynthesis [37]. Although WNPK and WAN induced an increase in both chl *a* and *b* implying a higher photosynthetic activity, the higher increase of chl *a* than chl *b* in the PAW treatment suggests in the latter an easier translocation of energy from chl *b* to chl *a*. This trend facilitates the irreversible direction in the energy capture process making the energy transfer of light excitation to the reaction center more efficient.

As a consequence, this could lead to higher production of NADPH and ATP in the light-dependent reactions (first stage of the photosynthesis) and their increased availability for the Calvin cycle (second stage of the photosynthesis) with higher production of photosynthates (such as sucrose), necessary for plant growth and

productivity. The sugar sucrose is a source of glucose which is the substrate, in the Smirnoff-Wheeler pathway, for vitamin C biosynthesis in plants [38] that, in our study, increased in PAW-treated seedlings. The presence of ascorbate is associated with preserving the photosynthetic process [39] and limiting ROS-mediated damage and leaf senescence [40]. The decrease in chlorophyll *a* was linked to reductions in AsA content, leading to decreased RuBisCO activity and CO₂ assimilation [40].

It is known that an augmented carotenoid level could be correlated to counteract the damage to the photosynthetic apparatus induced by UV light [41]. The fact that an increase of carotenoid content in PAW was not observed as compared to WAN, could therefore suggest the absence of relevant perturbations in the light-harvesting complex and the energy transfer towards the reaction center [37].

Ascorbate and glutathione are part of the ascorbate-glutathione cycle [42] and are the most abundant low molecular-weight antioxidants in plant cells. They regulate the concentration of the reactive oxygen species in plant cells, particularly hydrogen peroxide [38]; however, they are multifaceted molecules involved in various processes such as plant growth and defense [43]. The higher content of AsA in tomato seedlings irrigated with PAW strongly suggests the role of PAW in promoting the production of this antioxidant compound. On the other hand, the content of reduced glutathione (GSH - another important antioxidant metabolite of the plant) and glutathione pool (GSH + GSSG) remained unchanged in the presence of PAW with respect to the NTDDW control, suggesting a more relevant involvement of AsA rather than GSH in the PAW-modified plant metabolism, confirming the prominent role of ascorbate in the plant defense responses [44,45]. AsA, counteracting the oxidative stress in cells, underlines its key role played in the tolerance to several biotic and abiotic stresses [46]. The decreased GSH content in both WNPK and WAN samples with the contemporaneous higher GSSG production contributed to a shift in the redox state of this metabolite towards the oxidative form with consequent higher oxidized cell status [47] in those seedlings.

The possible induction of genes implicated in plant defense by irrigation of tomato seedlings with PAW was investigated at different time points. Transcript changes of the analyzed genes, including PR-1 and PAL with a key role in defense responses to pathogens, LOX, and the antioxidant enzyme CAT, were compared between treated and untreated control plants. In particular, PR-1 is a molecular marker for the salicylic acid-activated pathway that is rapidly and strongly induced as a response to pathogen infections [48]. All four genes were not activated, in our experiments, during the early stages after plant exposure to PAW. However, the plants irrigated with PAW showed a significant upregulation of the majority of the genes, slightly predominant for PR-1, following inoculation with the virus ToMMV, suggesting an effect of priming of induced defense responses by the treatment [49]. This could suggest that the activation of plant defense responses, possibly primed by reactive species in PAW, should allow the treated plants to be more promptly reactive against pathogens. In the uninoculated condition, downregulation of the same genes in treated vs. untreated samples could be likely due to the activation in treated plants of primary metabolism responsible for plant growth and development instead of that related to defenses [31].

In the cultivar Regina we used for the test, which is a traditional, long-lasting local variety in our region, the symptoms expression appeared very late in the time frame chosen for our experimental plan and, thus, it could be considered tolerant to ToMMV infection. Significant symptoms we observed, such as green mottling, shoe-string leaves, and stunting, started to be visible at least 3 weeks after inoculation. The comparison between I-PAW and I-NTDDW showed indeed a higher virus accumulation rate, with an increase in the former rather than in the latter. It can be hypothesized that the infection of a tobamovirus, having such an active replication and accumulation in the infected tissues, is somehow favored by an overall better nutritional status and nutrient mobilization as promoted by the PAW treatment. It could mean that the plants watered with PAW uptake higher amounts of nutrients (e.g., mineral elements) to support and even enhance the virus replication in well-nourished tissues.

In plants, disorders in element homeostasis at the leaf level are often correlated to nutritional deficiencies, the presence of pathogens (including viruses), environmental stresses, etc. Observing the changes in the spatial distribution of certain macro and/or micronutrients can provide valuable information for understanding the type and the impact of the stressor. For such investigations, μ -XRF is an essential and effective technique [31]. Significant changes in elemental distribution were observed in μ -XRF maps for P, S, Ca, and K in the virus-inoculated sample watered only with distilled water (I-NTDDW) as compared to a nutrient-sufficient uninoculated plant (WNPK), showing several spotted depletion zones. The lack (or lower concentration) of these important macronutrients in many leaf cells provides evidence of the virus infection, resulting in the already mentioned visual symptoms such as stunting, shoe-stringed and mottled leaves, and generalized yellowing of the foliage. Yet, some inhomogeneities in element distribution could be also observed in the plants watered only with double-distilled water (NTDDW), suggesting nutrient deficiencies, as compared to the nutrients-sufficient control (WNPK). However, the virus inoculation appeared to worsen the pre-existing nutritional stress status, with an evident increase in the size and number of nutrients-depleted areas (Figure 13). Such inhomogeneous distributions are not evident in the PAW watered samples, thus suggesting that PAW can provide a sufficient level of nutrients to tomato plants, similar to what happens to the plants irrigated with a solution containing the chemical fertilizer (WNPK). In addition, the irrigation of virus-inoculated plants with PAW (I-PAW) appeared to almost completely restore the mineral nutrients distribution in tomato leaves, becoming more similar to that of the control healthy plant (WNPK).

Finally, the S distribution in PAW-treated plants, either inoculated or uninoculated, showed that S concentration increases in leaf veins, suggesting a mobilization of S-containing compounds (e.g., glutathione) from plant leaves through the phloem. Indeed, S assimilated in leaves is exported via the phloem to sites of protein synthesis (shoot and root apices, and fruits) mainly as glutathione [34] which can also act as a non-enzymatic antioxidant that can be activated to overcome oxidative perturbations [50] like those induced by PAW.

The results of this study regarding the PAW's effects on plant growth and defense responses are in accordance with previous

studies [9–12]. Generally, the results indicate the presence of a better physiological status of the PAW-treated plants to cope with oxidative stress and maintain cellular homeostasis. The augmented chlorophyll *a* content with the increase of antioxidant molecules such as the ascorbate suggests that PAW treatment can potentiate the plant defense and contribute to higher sugar production, necessary for plant growth and productivity. In agreement with our results, an enhancement of plant defense responses induced by PAW treatment has been also reported by several authors [12,51]. Overall, these findings highlight the potential of PAW as a sustainable and innovative irrigation medium for enhancing plant performance and resilience in the face of environmental challenges. However, additional studies regarding the involvement and effect of PAW on other antioxidant systems (such as enzymatic activity, and phenols) and metabolic pathways (such as sugar synthesis) are necessary to better understand the potential of PAW in the plant systems.

5 Conclusion

This thorough exploration, encompassing both healthy and virus-stressed conditions, provides a more detailed understanding of the dynamic interplay between PAW and tomato plant growth. Our findings aim to contribute not only to the growing body of knowledge surrounding the applications of PAW but also to the specific insights into its potential as a stress-alleviating agent in the context of viral infections. Through the examination of plant development, biochemical responses, nutrient dynamics, and gene expression patterns, our research provides further evidence of the role of PAW as a sustainable alternative to conventional chemicals used in agriculture. Furthermore, the over-expression of the defense-related genes of plants irrigated with PAW suggests that the crop resilience to pathogenic challenges could be enhanced potentially reducing crop losses on the field.

Data availability statement

The original contributions presented in the study are included in the article/Supplementary material, further inquiries can be directed to the corresponding author.

Author contributions

DA: Data curation, Investigation, Writing–review and editing, Formal Analysis, Methodology, Validation. PR: Data curation, Formal Analysis, Investigation, Validation, Writing–review and editing, Methodology. CP: Data curation, Investigation, Methodology, Writing–review and editing, Formal Analysis. BB:

Data curation, Investigation, Methodology, Writing–review and editing. CP: Formal Analysis, Methodology, Validation, Writing–review and editing, Resources, Data curation. RT: Data curation, Formal Analysis, Methodology, Validation, Writing–review and editing, Funding acquisition, Resources. AM: Conceptualization, Formal Analysis, Methodology, Writing–review and editing, Funding acquisition, Data curation, Investigation. MA: Data curation, Investigation, Writing–review and editing. GD: Formal Analysis, Methodology, Validation, Writing–review and editing. BL: Investigation, Methodology, Writing–review and editing. RD: Writing–review and editing, Data curation, Formal Analysis, Funding acquisition, Methodology, Resources, Validation, Conceptualization. PA: Conceptualization, Data curation, Funding acquisition, Investigation, Supervision, Writing–original draft, Writing–review and editing, Resources, Validation.

Funding

The author(s) declare that financial support was received for the research, authorship, and/or publication of this article. Open access funding provided by MUR-Fondo Promozione e Sviluppo – DM 737/2021 CUP H99J21017820005 funded by European Union – Next Generation EU PlaTEC. We acknowledge: European Cooperation in Science and Technology, CA19110; Regione Puglia, Riparti - POC PUGLIA FESRT-FSE 2014/2020; Ministero dello Sviluppo Economico, F/050421/01–03/X32 Protection; Ministero dell'Istruzione, dell'Università e della Ricerca, PONa3_00369 SISTEMA; Agritech National Research Center funding from the European Union Next-Generation EU (PIANO NAZIONALE DI RIPRESA E RESILIENZA (PNRR) –MISSIONE 4 COMPONENTE 2, INVESTIMENTO 1.4–D.D. 1032 17/06/2022, CUP H93C22000440007, CN00000022).

Conflict of interest

The authors declare that the research was conducted in the absence of any commercial or financial relationships that could be construed as a potential conflict of interest.

The author(s) declared that they were an editorial board member of Frontiers, at the time of submission. This had no impact on the peer review process and the final decision.

Publisher's note

All claims expressed in this article are solely those of the authors and do not necessarily represent those of their affiliated organizations, or those of the publisher, the editors and the reviewers. Any product that may be evaluated in this article, or claim that may be made by its manufacturer, is not guaranteed or endorsed by the publisher.

References

- Konchev EM, Gusein-zade N, Burmistrov DE, Kolik LV, Dorokhov AS, Izmailov AY, et al. Advancements in plasma agriculture: a review of recent studies. *Int J Mol Sci* (2023) 24:15093. doi:10.3390/ijms242015093
- Ambrico PF, Šimek M, Ambrico M, Morano M, Prukner V, Minafra A, et al. On the air atmospheric pressure plasma treatment effect on the physiology, germination and seedlings of basil seeds. *J Phys D Appl Phys* (2020) 53:104001. doi:10.1088/1361-6463/ab5b1b
- Ambrico PF, Šimek M, Morano M, De Miccolis Angelini RM, Minafra A, Trotti P, et al. Reduction of microbial contamination and improvement of germination of sweet basil (*Ocimum basilicum* L.) seeds via surface dielectric barrier discharge. *J Phys D Appl Phys* (2017) 50:305401. doi:10.1088/1361-6463/aa77c8
- Misra NN, Schlüter O, Cullen PJ. Plasma in food and agriculture. In: *Cold plasma in food and agriculture*. Elsevier (2016). p. 1–16. doi:10.1016/B978-0-12-801365-6.00001-9
- Zhou R, Zhou R, Prasad K, Fang Z, Speight R, Bazaka K, et al. Cold atmospheric plasma activated water as a prospective disinfectant: the crucial role of peroxyxynitrite. *Green Chem* (2018) 20:5276–84. doi:10.1039/c8gc02800a
- Zhou R, Zhou R, Wang P, Xian Y, Mai-Prochnow A, Lu X, et al. Plasma-activated water: generation, origin of reactive species and biological applications. *J Phys D Appl Phys* (2020) 53:303001. doi:10.1088/1361-6463/ab81cf
- Gott RP, Engeling KW, Olson J, Franco C. Plasma activated water: a study of gas type, electrode material, and power supply selection and the impact on the final frontier. *Phys Chem Chem Phys* (2023) 25:5130–45. doi:10.1039/D2CP03489A
- Štěpánová V, Slaviček P, Kelar J, Prášil J, Smékal M, Stupavská M, et al. Atmospheric pressure plasma treatment of agricultural seeds of cucumber (*Cucumis sativus* L.) and pepper (*Capsicum annuum* L.) with effect on reduction of diseases and germination improvement. *Plasma Process Polym* (2018) 15. doi:10.1002/ppap.201700076
- Vichiansan N, Chatmaniwat K, Sungkorn M, Leksakul K, Chaopaisarn P, Boonyawan D. Effect of plasma-activated water generated using plasma jet on tomato (*Solanum lycopersicum* L. Var. cerasiforme) seedling growth. *J Plant Growth Regul* (2023) 42:935–45. doi:10.1007/s00344-022-10603-7
- Kučerová K, Henselová M, Slováková L, Hensel K. Effects of plasma activated water on wheat: germination, growth parameters, photosynthetic pigments, soluble protein content, and antioxidant enzymes activity. *Plasma Process Polym* (2019) 16. doi:10.1002/ppap.201800131
- Adhikari B, Adhikari M, Ghimire B, Park G, Choi EH. Cold atmospheric plasma-activated water irrigation induces defense hormone and gene expression in tomato seedlings. *Sci Rep* (2019) 9:16080. doi:10.1038/s41598-019-52646-z
- Zambon Y, Contaldo N, Laurita R, Várallyay E, Canel A, Gherardi M, et al. Plasma activated water triggers plant defence responses. *Sci Rep* (2020) 10:19211. doi:10.1038/s41598-020-76247-3
- MedCalc Software Ltd. Digimizer image analysis software ver. 6.3.0 (2023). Available at: <https://www.digimizer.com/> (Accessed February 28, 2024).
- Lichtenthaler HK, Chlorophylls and carotenoids: pigments of photosynthetic biomembranes. In: *Methods in enzymology*. Academic Press (1987). p. 350–82. doi:10.1016/0076-6879(87)48036-1
- Zhang J, Kirkham MB. Antioxidant responses to drought in sunflower and sorghum seedlings. *New Phytol* (1996) 132:361–73. doi:10.1111/j.1469-8137.1996.tb01856.x
- Gambino G, Perrone I, Gribaudo I. A Rapid and effective method for RNA extraction from different tissues of grapevine and other woody plants. *Phytochem Anal* (2008) 19:520–5. doi:10.1002/pca.1078
- Abo-Zaid GA, Matar SM, Abdelkhalek A. Induction of plant resistance against tobacco mosaic virus using the biocontrol agent streptomyces cellulosa isolate actino 48. *Agronomy* (2020) 10:1620. doi:10.3390/agronomy10111620
- Molinari S, Fanelli E, Leonetti P. Expression of tomato salicylic acid (SA)-responsive pathogenesis-related genes in *Mi -1-* mediated and SA -induced resistance to root-knot nematodes. *Mol Plant Pathol* (2014) 15:255–64. doi:10.1111/mpp.12085
- Song Y, Chen D, Lu K, Sun Z, Zeng R. Enhanced tomato disease resistance primed by arbuscular mycorrhizal fungus. *Front Plant Sci* (2015) 6:786. doi:10.3389/fpls.2015.00786
- Zhang Z-P, Miao M-M, Wang C-L. Effects of ALA on photosynthesis, antioxidant enzyme activity, and gene expression, and regulation of proline accumulation in tomato seedlings under NaCl stress. *J Plant Growth Regul* (2015) 34:637–50. doi:10.1007/s00344-015-9499-4
- Fuentes A, Ortiz J, Saavedra N, Salazar LA, Meneses C, Arriagada C. Reference gene selection for quantitative real-time PCR in *Solanum lycopersicum* L. inoculated with the mycorrhizal fungus *Rhizophagus irregularis*. *Plant Physiol Biochem* (2016) 101:124–31. doi:10.1016/j.plaphy.2016.01.022
- Pfaffl MW, Tichopad A, Prgomet C, Neuvians TP. Determination of stable housekeeping genes, differentially regulated target genes and sample integrity: BestKeeper – excel-based tool using pair-wise correlations. *Biotechnol Lett* (2004) 26:509–15. doi:10.1023/B:BILE.0000019559.84305.47
- Livak KJ, Schmittgen TD. Analysis of relative gene expression data using real-time quantitative PCR and the 2- $\Delta\Delta C_T$ method. *Methods* (2001) 25:402–8. doi:10.1006/meth.2001.1262
- Terzano R, Alfeld M, Janssens K, Vekemans B, Schoonjans T, Vincze L, et al. Spatially resolved (semi)quantitative determination of iron (Fe) in plants by means of synchrotron micro X-ray fluorescence. *Anal Bioanal Chem* (2013) 405:3341–50. doi:10.1007/s00216-013-6768-6
- Voráč J, Synek P, Procházka V, Hoder T. State-by-state emission spectra fitting for non-equilibrium plasmas: OH spectra of surface barrier discharge at argon/water interface. *J Phys D Appl Phys* (2017) 50:294002. doi:10.1088/1361-6463/aa7570
- Voráč J, Kusýn L, Synek P. Deducing rotational quantum-state distributions from overlapping molecular spectra. *Rev Scientific Instr* (2019) 90:123102. doi:10.1063/1.5128455
- Voráč J, Synek P, Potočnáková L, Hnilica J, Kudrle V. Batch processing of overlapping molecular spectra as a tool for spatio-temporal diagnostics of power modulated microwave plasma jet. *Plasma Sour Sci Technol* (2017) 26:025010. doi:10.1088/1361-6595/aa51f0
- Pei X, Gidon D, Yang YJ, Xiong Z, Graves DB. Reducing energy cost of NOx production in air plasmas. *Chem Eng J* (2019) 362:217–28. doi:10.1016/j.cej.2019.01.011
- Cherkasov N, Ibadon AO, Fitzpatrick P. A review of the existing and alternative methods for greener nitrogen fixation. *Chem Eng Process Process Intensification* (2015) 90:24–33. doi:10.1016/j.ccep.2015.02.004
- Ishibashi K, Kubota K, Kano A, Ishikawa M. Tobamoviruses: old and new threats to tomato cultivation. *J Gen Plant Pathol* (2023) 89:305–21. doi:10.1007/s10327-023-01141-5
- Porfido C, Köpke K, Allegretta I, Bandte M, von Bargen S, Rybak M, et al. Combining micro- and portable-XRF as a tool for fast identification of virus infections in plants: the case study of ASa-Virus in *Fraxinus ornus* L. *Talanta* (2023) 262:124680. doi:10.1016/j.talanta.2023.124680
- Šimek M, Homola T. Plasma-assisted agriculture: history, presence, and prospects—a review. *Eur Phys J D* (2021) 75:210. doi:10.1140/epjd/s10053-021-00206-4
- Lukes P, Dolezalova E, Sisrova I, Clupek M. Aqueous-phase chemistry and bactericidal effects from an air discharge plasma in contact with water: evidence for the formation of peroxyxynitrite through a pseudo-second-order post-discharge reaction of H₂O₂ and HNO₂. *Plasma Sour Sci Technol* (2014) 23:015019. doi:10.1088/0963-0252/23/1/015019
- Taiz L, Zeiger E. *Plant physiology*. San Francisco: Benjamin/Cummings Publishing Company (2015).
- Lamichhane P, Paneru R, Nguyen LN, Lim JS, Bhartiya P, Adhikari BC, et al. Plasma-assisted nitrogen fixation in water with various metals. *React Chem Eng* (2020) 5:2053–7. doi:10.1039/d0re00248h
- Lamichhane P, Veerana M, Lim JS, Mumtaz S, Shrestha B, Kaushik NK, et al. Low-temperature plasma-assisted nitrogen fixation for corn plant growth and development. *Int J Mol Sci* (2021) 22:5360. doi:10.3390/ijms22105360
- Busch A, Hippler M. The structure and function of eukaryotic photosystem I. *Biochim Biophys Acta (Bba) - Bioenerg* (2011) 1807:864–77. doi:10.1016/j.bbabi.2010.09.009
- Paciolla C, Fortunato S, Dipierro N, Paradiso A, De Leonardi S, Mastropasqua L, et al. Vitamin C in plants: from functions to biofortification. *Antioxidants* (2019) 8:519. doi:10.3390/antiox8110519
- Ivanov BN. Role of ascorbic acid in photosynthesis. *Biochemistry (Moscow)* (2014) 79:282–9. doi:10.1134/S0006297914030146
- Barth C, Moeder W, Klessig DF, Conklin PL. The timing of senescence and response to pathogens is altered in the ascorbate-deficient arabidopsis mutant *vitamin c-1*. *Plant Physiol* (2004) 134:1784–92. doi:10.1104/pp.103.032185
- Kacharava N, Chaniashvili S, Badridze G, Chkhubanishvili E, Janukashvili N. Effect of seed irradiation on the content of antioxidants in leaves of Kidney bean. *Cabbage and Beet cultivars* (2009) 137. Available at: https://www.cropl.com/gulnara_3_3_137_145.pdf.
- Foyer CH, Noctor G. Ascorbate and glutathione: the heart of the redox hub. *Plant Physiol* (2011) 155:2–18. doi:10.1104/pp.110.167569
- Foyer CH, Kunert K. The ascorbate–glutathione cycle coming of age. *J Exp Bot* (2024):erae023. doi:10.1093/jxb/erae023
- Foyer CH, Noctor G. Redox homeostasis and antioxidant signaling: a metabolic interface between stress perception and physiological responses. *Plant Cell* (2005) 17:1866–75. doi:10.1105/tpc.105.033589
- Noctor G, Foyer CH. ASCORBATE and glutathione: keeping active oxygen under control. *Annu Rev Plant Physiol Plant Mol Biol* (1998) 49:249–79. doi:10.1146/annurev.arplant.49.1.249
- Höller S, Ueda Y, Wu L, Wang Y, Hajirezaei M-R, Ghaffari M-R, et al. Ascorbate biosynthesis and its involvement in stress tolerance and plant

development in rice (*Oryza sativa* L.). *Plant Mol Biol* (2015) 88:545–60. doi:10.1007/s11103-015-0341-y

47. Sabetta W, Paradiso A, Paciolla C, de Pinto MC. Chemistry, biosynthesis, and antioxidative function of glutathione in plants. In: *Glutathione in plant growth, development, and stress tolerance*. Cham: Springer International Publishing (2017). p. 1–27. doi:10.1007/978-3-319-66682-2_1

48. Glazebrook J. Contrasting mechanisms of defense against biotrophic and necrotrophic pathogens. *Annu Rev Phytopathol* (2005) 43:205–27. doi:10.1146/annurev.phyto.43.040204.135923

49. Conrath U, Chapter 9 priming of induced plant defense responses. *Adv Bot Res* (2009) 51:361–95. doi:10.1016/S0065-2296(09)51009-9

50. Del Buono D, Terzano R, Panfilì I, Bartucca ML, Phytoremediation and detoxification of xenobiotics in plants: herbicide-safeners as a tool to improve plant efficiency in the remediation of polluted environments. A mini-review. *Int J Phytoremediation* (2020) 22:789–803. doi:10.1080/15226514.2019.1710817

51. Perez SM, Biondi E, Laurita R, Proto M, Sarti F, Gherardi M, et al. Plasma activated water as resistance inducer against bacterial leaf spot of tomato. *PLoS One* (2019) 14:e0217788. doi:10.1371/journal.pone.0217788



OPEN ACCESS

EDITED BY

Mohamed Mokhtar Hefny,
Future University in Egypt, Egypt

REVIEWED BY

Mario J. Pinheiro,
University of Lisbon, Portugal
Savino Longo,
University of Bari Aldo Moro, Italy

*CORRESPONDENCE

Jiayong Zhong,
✉ jyzhong@bnu.edu.cn

RECEIVED 02 February 2024

ACCEPTED 09 May 2024

PUBLISHED 28 May 2024

CITATION

Xing C, Ping Y, Zhao X, An W and Zhong J
(2024), Magnetohydrodynamics simulation of
magnetic reconnection process based on the
laser-driven Helmholtz capacitor-coil targets.
Front. Phys. 12:1380844.
doi: 10.3389/fphy.2024.1380844

COPYRIGHT

© 2024 Xing, Ping, Zhao, An and Zhong. This is
an open-access article distributed under the
terms of the [Creative Commons Attribution
License \(CC BY\)](#). The use, distribution or
reproduction in other forums is permitted,
provided the original author(s) and the
copyright owner(s) are credited and that the
original publication in this journal is cited, in
accordance with accepted academic practice.
No use, distribution or reproduction is
permitted which does not comply with these
terms.

Magnetohydrodynamics simulation of magnetic reconnection process based on the laser-driven Helmholtz capacitor-coil targets

Chunqing Xing¹, Yongli Ping^{1,2}, Xu Zhao^{3,4}, Weiming An^{1,2} and
Jiayong Zhong^{1,2*}

¹Department of Astronomy, Beijing Normal University, Beijing, China, ²Institute for Frontiers in
Astronomy and Astrophysics, Beijing Normal University, Beijing, China, ³Key Laboratory for Laser Plasmas
(MoE) and School of Physics and Astronomy, Shanghai Jiao Tong University, Shanghai, China,
⁴Collaborative Innovation Center of IFSA (CICIFSA), Shanghai Jiao Tong University, Shanghai, China

Magnetic reconnection is an important rapid energy release mechanism in astrophysics. Magnetic energy can be effectively converted into plasma kinetic energy, thermal energy, and radiation energy. This study is based on the magnetohydrodynamics simulation method and utilizes the FLASH code to investigate the laser-driven magnetic reconnection physical process of the Helmholtz capacitor-coil target. The simulation model incorporates the laser driving effect, and the external magnetic field consistent with the Helmholtz capacitor-coil target is written in. This approach achieves a magnetic reconnection process that is more consistent with the experiment. By changing the resistivity, subtle differences in energy conversion during the evolution of magnetic reconnection are observed. Under conditions of low resistivity, there is a more pronounced increase in the thermal energy of ions compared to other energy components. In simulations with high resistivity, the increase in electrons thermal energy is more prominent. The simulation gives the evolution trajectory of magnetic reconnection, which is in good agreement with the experimental results. This has important reference value for experimental research on the low- β magnetic reconnection.

KEYWORDS

the magnetohydrodynamics simulation, magnetic reconnection, the Helmholtz capacitor-coil target, plasma physics, energy conversion

1 Introduction

Magnetic reconnection is an important process in astrophysics [1]. The rapid increase of plasma energy can be achieved through the dissipation of magnetic energy. This phenomenon finds extensive application in elucidating solar flares, coronal mass ejections, geomagnetic storms, and other solar-terrestrial space phenomena [2–4]. Extensive magnetic reconnection data has been acquired through observations by the Magnetospheric Multiscale spacecraft [5–7]. Magnetic reconnection has also been used to explain the high-energy-density astrophysical systems, such as gamma-ray bursts [8, 9], black hole accretion disks [10, 11], and pulsar [12]. Magnetic reconnection increases electron heat energy in the inertial confinement fusion experiment and destroys the uniformity of fusion materials, which has always been an

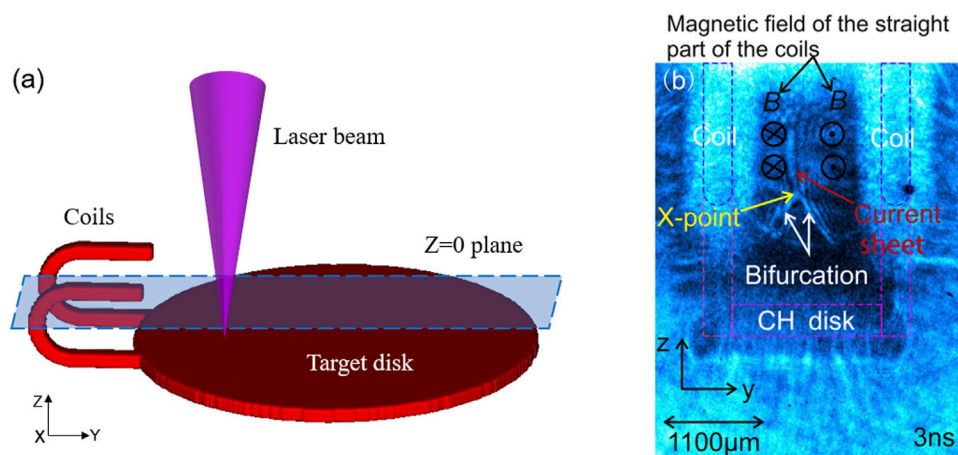


FIGURE 1 (A) The diagram of the FLASH simulation setup; (B) The shadow image collected in the laboratory from Yuan et al. [29].

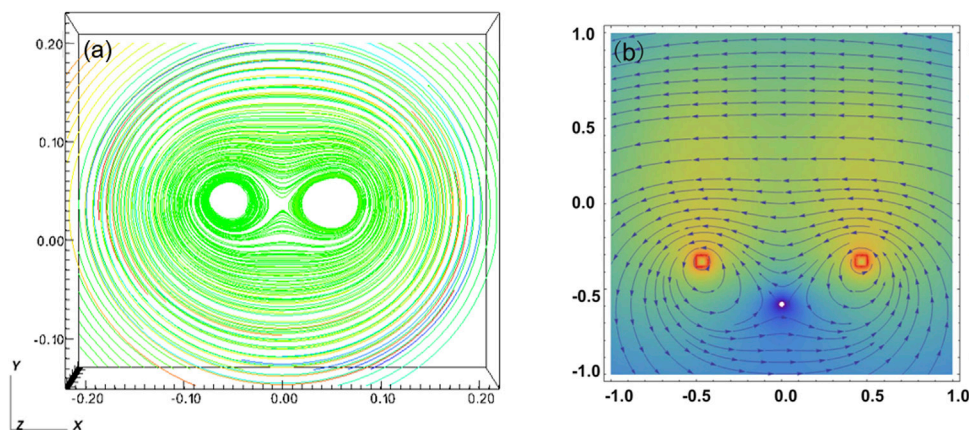


FIGURE 2 (A) The coils magnetic force lines that was written at the end time of the laser in the FLASH simulation, (B) The structure of the coils magnetic force lines from the Radia simulation.

important issue [13, 14]. In recent years, laboratory research on magnetic reconnection has made a lot of progress, complementing astronomical observational research. High-power laser devices reproduced the loop-top X-ray source [15], affirming the pivotal role of magnetic reconnection in solar-terrestrial space phenomena. In the magnetic reconnection experiment (MRX), the length of the current sheet was given as a few ion skin depth [16] and the experiments indicated that magnetic reconnection mechanisms were divided into forced magnetic reconnection and pulled magnetic reconnection [17]. In the experiment of Pei et al. [18], it was the first time to use the Helmholtz capacitor-coil target to reproduce the low- β magnetic reconnection process on a traditional laser device. This kind of target was used to further study the particle acceleration by the magnetic reconnection in many experiments. Shu et al. [19] pointed that the ion acoustic and electron acoustic bursts can lead to electron heating and bulk acceleration. Abraham et al. [20] reported the out-of-plane reconnection electric field had the direct capability to accelerate electrons.

The capacitor-coil target can effectively generate strong magnetic fields in laser-driven experiments. It consists of two parallel upper and lower target disks that connected by a coil. Featuring an upper target disk with a laser injection hole, the lasers are precisely focused into the lower target disk through this aperture. The lower target disk is ablated by the laser and generates a substantial population of electrons. Due to their light mass, these electrons can reach the upper target disk faster than the ions, leading to a potential difference between the upper and lower target disks. The potential difference drives the electrons back to the lower target disk along the connecting coil, initiating a current and inducing the magnetic field. The intensity of the induced magnetic field will gradually increase with the laser injection process, reaching the strongest at the end of the laser pulse [21]. In 1986, Daido et al. [22] employed a B-dot probe to measure the magnetic field of the capacitive-coil target. The laser power was approximately $1.3 \times 10^{14} \text{ W cm}^{-2}$, and the experiment confirmed that the magnetic field intensity up to 60T. This result has been confirmed many times in subsequent studies [23, 24], and Proton deflectometry can obtain two-dimensional magnetic

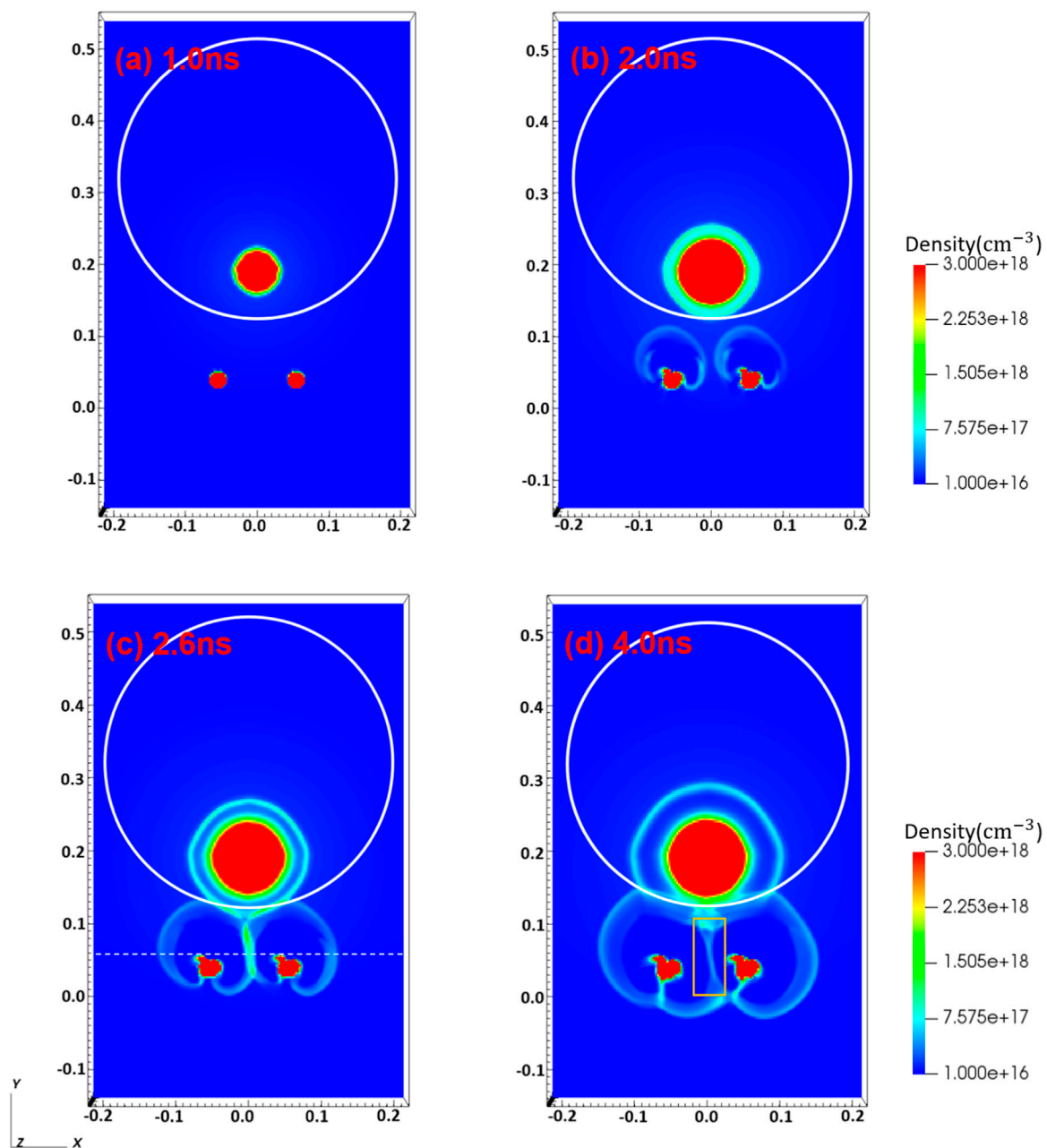


FIGURE 3

The results of electron number density under the condition of low resistivity in FLASH simulation at (A) 1.0 ns, (B) 2.0 ns, (C) 2.6 ns and (D) 4.0 ns, taking the x-y plane section view of $z = 0.0$. The two red spots at $y = 0.03$ indicate the position of the top of the coil, and the white frame line indicates the position of the target plate. The coordinate unit is centimeters.

field structure [25–27]. In 2013, Fujioka et al. [28] repeated this experiment on the high-power laser GEKKO-XII and employed the Faraday effect to measure the magnetic field. The obtained magnetic field intensity could reach approximately 1.5 kT. The presence of a smaller reverse magnetic field area between the double coils of the Helmholtz capacitive-coil target was attributed to the consistent direction of the current. This configuration aligns with the typical topological features was observed in magnetic reconnection. Yuan et al. [29] used the Helmholtz capacitive-coil target to produce a parallel reverse magnetic field structure, exhibiting a strength of approximately 38.5T. They successfully replicated the magnetic reconnection process

on the XG-III laser. However, among the many current experiments, the systematic and comprehensive magnetohydrodynamic simulation for these experiments are scarce. Recently, Xu et al. [30] used magnetohydrodynamic simulation to confirm that the accumulated of the experimental plasma comes from magnetic reconnection.

In recent years, there are many simulation methods of magnetic reconnection. Egedal et al. [31] obtain the important role of parallel electric field in particle acceleration by using kinetic simulation method. Fox et al. [32] used PIC simulation and found that the fermi acceleration process plays an important part in reconnection acceleration. These simulations revolve around the magnetic reconnection process, and we

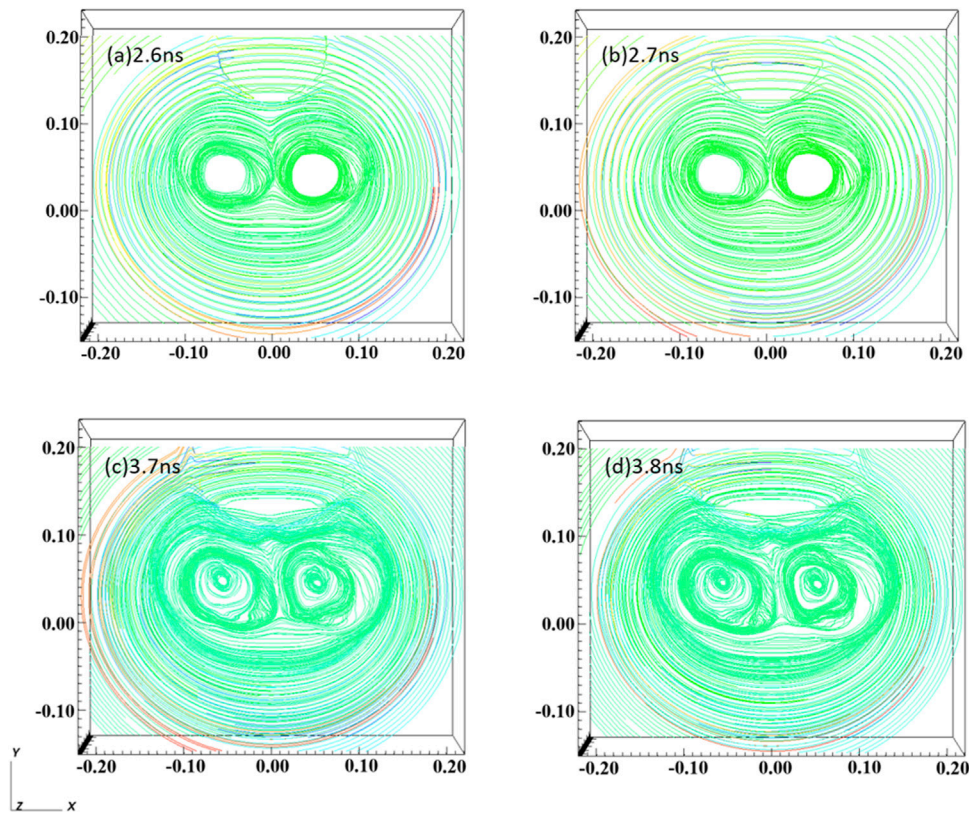


FIGURE 4

The structure of the magnetic lines of force of the coils before [(A) 2.6 ns and (B) 2.7 ns] and after [(C) 3.7 ns and (D) 3.8 ns] the moment of magnetic reconnection. The coordinate unit is centimeters.

want to simulate the whole experimental process. PIC simulation can introduce laser parameters, but the computing power is limited to the picosecond level. In order to introduce lasers in nanosecond level, we will utilize the FLASH radiation magnetohydrodynamic code to simulate the magnetic reconnection experiment on three-dimension. The energy conversion of magnetic reconnection is very complex, and the whole process is mixed with many factors such as the electric field, waves, and turbulence. The most fundamental reason is the issue of resistivity. The magnetic diffusion term introduced by resistivity is the key to whether magnetic reconnection can occur. Observational data indicate the existence of anomalous resistivity in astronomical environments [33–35], but the origin of the anomalous resistivity still require extensive research. Different resistivity values were applied in the simulation to confirm the impact of resistivity on the occurrence rate of magnetic reconnection and the energy distribution following magnetic energy conversion. The structure of this paper is delineated as follows. Section 2 introduces the simulation setup, Section 3 displays and analyzes the simulation results, and Section 4 provides the conclusion.

2 The simulation setup

This investigation uses the FLASH simulation code to simulate and study the laser-driven Helmholtz capacitor-coil target magnetic reconnection experiment. FLASH, a radiation

magnetohydrodynamics simulation code, was developed by the University of Chicago [36]. It possesses the capability to track the motion patterns of plasma by solving the magnetohydrodynamics equations. The dimensionless magnetohydrodynamics equations are as Eqs 1–6:

$$\frac{\partial \rho}{\partial t} + \nabla \cdot (\rho \vec{v}) = 0, \quad (1)$$

$$\frac{\partial \rho \vec{v}}{\partial t} + \nabla (\rho \vec{v} \vec{v} - \vec{B} \vec{B}) + \nabla p_* = 0, \quad (2)$$

$$\frac{\partial \rho E}{\partial t} + \nabla \cdot (\vec{v} (\rho E + p_*) - \vec{B} (\vec{v} \cdot \vec{B})) = \nabla \cdot (\vec{B} \times (\eta \nabla \times \vec{B})), \quad (3)$$

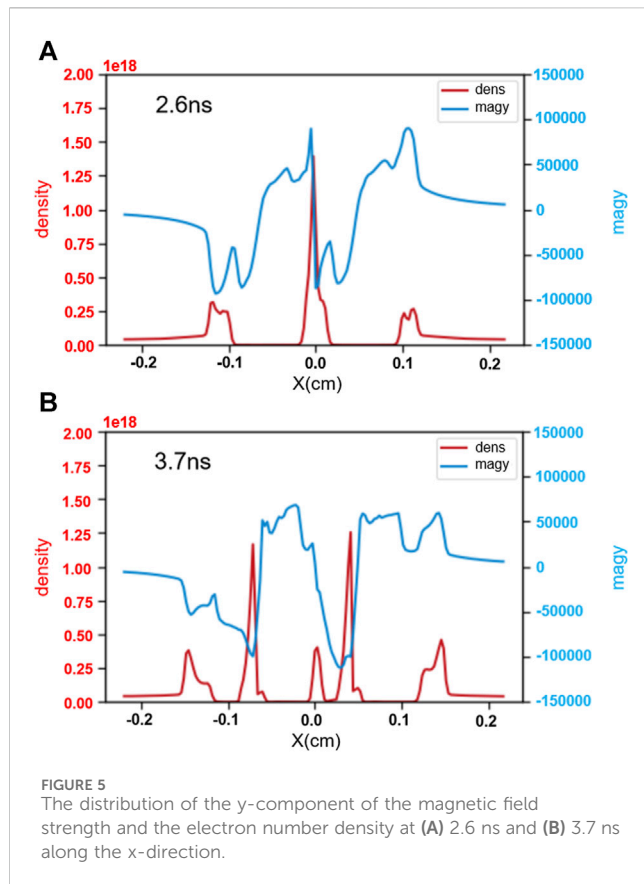
$$\frac{\partial \vec{B}}{\partial t} + \nabla \cdot (\vec{v} \vec{B} - \vec{B} \vec{v}) = -\nabla \times (\eta \nabla \times \vec{B}), \quad (4)$$

Where,

$$p_* = P + \frac{B^2}{2}, \quad (5)$$

$$E = \frac{1}{2} v^2 + \epsilon + \frac{B^2}{2\rho}. \quad (6)$$

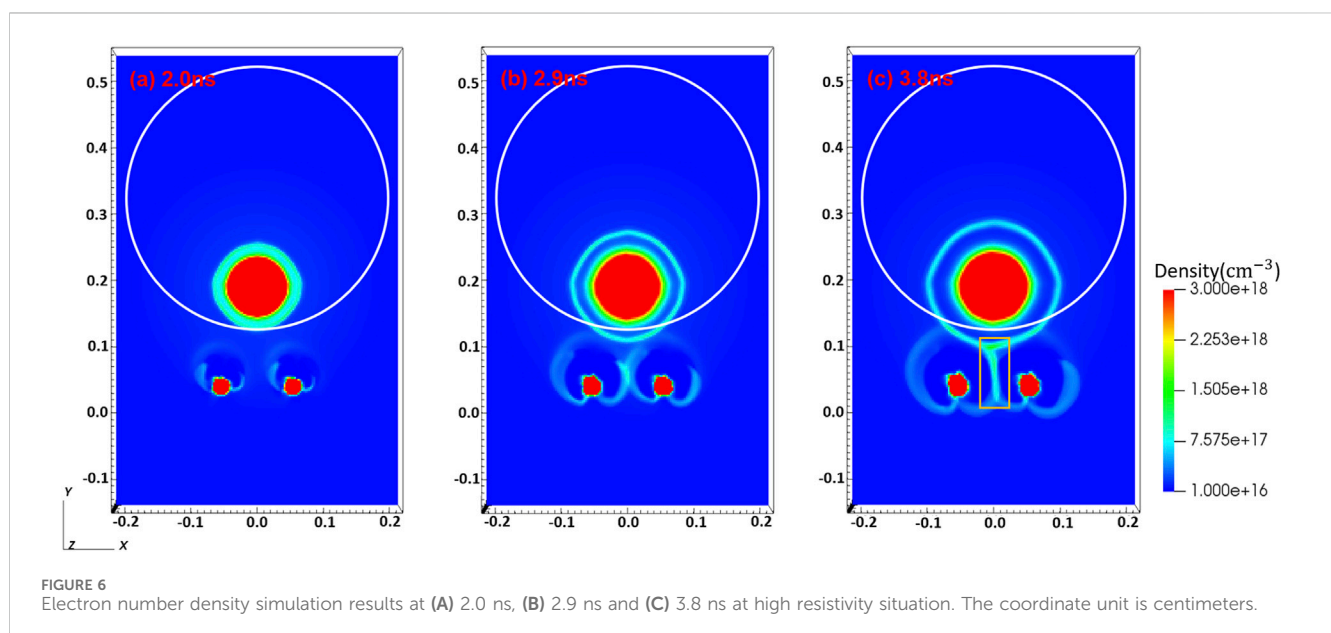
In the expression, ρ represents the density, \vec{v} represents the velocity, p represents the thermal pressure, T represents the temperature, \vec{B} represents the magnetic field strength, E represents the total specific energy, ϵ represents the specific internal energy, and η represents the resistivity. The FLASH code

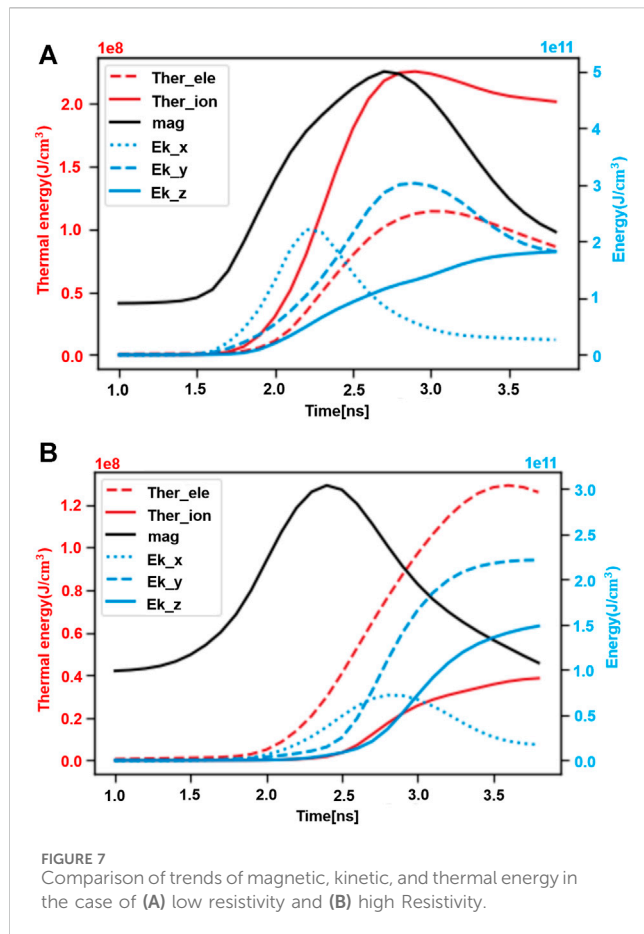


is a single-fluid simulation, therefore the capacity to replicate the coil current generation process and the naturally induced magnetic field structure. In our simulation, we wrote a magnetic field module to realize the simulation study of magnetic reconnection. The initial structure of the written magnetic field is consistent with the Radia static magnetic field simulation [37], ensuring the correctness.

The FLASH code contains the laser Energy deposition unit, which allow adding the laser parameters to the simulation. Compared with the general hydrodynamics simulation, it can better reproduce the real situation in the experiment. The FLASH code contains magnetic field modules such as Biermann magnetic field and Hall magnetic field. The special magnetic field structure can be written as the initial condition in the Simulation_initBlock.F90 file. However, the magnetic field written in this way cannot be reused or adjusted in the subsequent plasma evolution process. The magnetic field intensity generated by the target will increase with the injection of the laser and reach the maximum strength at the end of the laser. Consequently, it is imperative to ensure that the simulated magnetic field intensity at the conclusion of the laser pulse is indeed at its maximum value. We add an additional code module to write the magnetic field within the main program file hy_uhd_unsplit.F90 of FLASH. To avoid the writing of an external magnetic field from interfering with other modules of the main program, the magnetic field is added following the writing method of the Biermann magnetic field module that treated as a source item. The magnetic field is written using the magnetic vector potential method, defined as $\vec{B} = \nabla \times \vec{A}$, which satisfies $\nabla \cdot \vec{B} = 0$. This method effectively maintains the divergence of the simulated grid magnetic field at zero, ensuring the accuracy of the magnetohydrodynamics simulations.

The target parameters and laser parameters in the simulation are established based on the experiment of Yuan et al. [29]. The simulation is written in a cartesian coordinate system. The simulation range in the x, y, and z directions is $(-2200, 2200) \times (-1500, 5500) \times (-500, 500) \mu\text{m}$. The number of simulation grids is $160 \times 256 \times 64$. The outflow boundary conditions are employed. The magnetic field is introduced into the simulation at approximately 1.0 ns. The magnetic field intensity added inside the coil area ranges from $\sim 50\text{T}$, and the maximum value is slightly higher than the experimental measurement value of 38.5T . In order to avoid the influence of boundary effects in the simulation, the coil target structure is simplified. Only the lower target disk and coil area





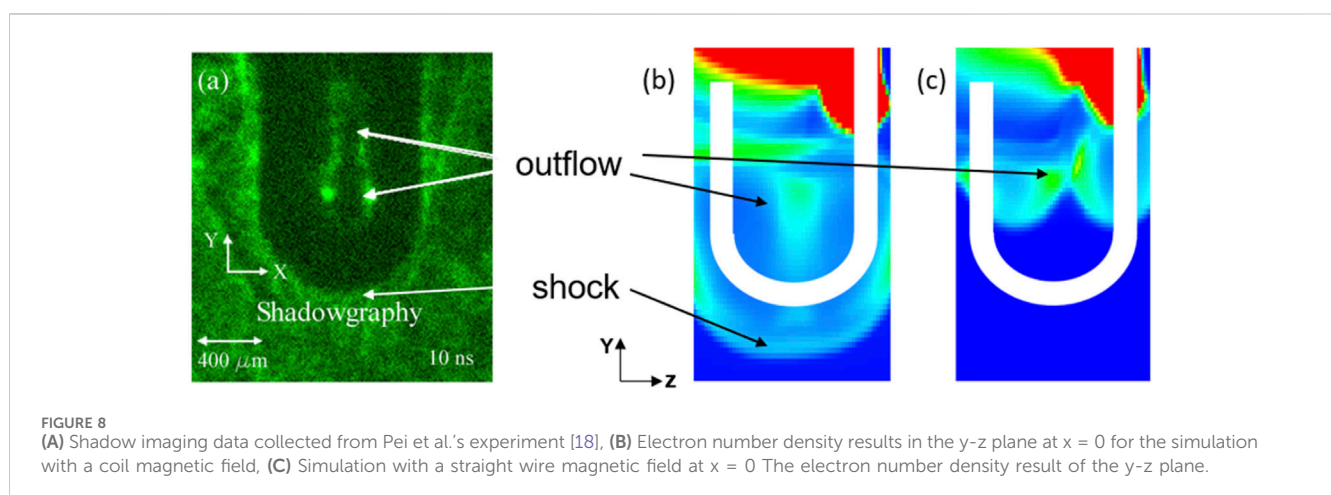
are retained, while the upper target disk is removed (as shown in Figure 1A). For stability purposes, the magnetic field is split and the magnetic field of the semi-circular arc coil is written. After the magnetic field is initialized, it undergoes free evolution with the plasma. The accuracy of the written magnetic field is ensured by comparing the written magnetic field structure with the Radia simulation results (as shown in Figure 2). The laser energy is set at 130J, the pulse width is 1.0 ns, and the focal spot radius is 200 μm , which are basically consistent with the experimental parameters.

The laser radiation position is set to (0, 1900, -300) μm , which is about 300 μm from the boundary of the lower target disk.

The FLASH code contains the Spitzer highZ resistivity module that designed for reasonably calculate the resistivity value of each grid. However, this work wanted to study the conversion of magnetic energy under different resistivities, so we chose to use constant resistivity for calculations.

3 Simulation results

Figures 3A–D show the electron number density results in the case of low resistivity ($\eta = 0.716 \text{ cm}^2 \text{ s}^{-1}$, data was taken from $z = 0$ plane marked by the blue frame line in Figure 1A). The white circle in Figure 3 denotes the position of the target disk. The high-density region within the circle corresponds to the plasma generated by the target disk after laser irradiation. Two high-density areas outside the white circle represent the vertex position of the two coils. At 1.0 ns, the laser pulse ends and the magnetic field completes writing. The plasma begins to be constrained by the magnetic field to move around the coils (as shown in Figure 3B). Magnetic reconnection occurs at approximately 2.6 ns ($\sim 46.8 \tau_A$). Magnetic reconnection is still ongoing at the end of the simulation. Note that the 4.0 ns in the simulation corresponds to the 3.0 ns after the laser ended in Yuan et al.'s experiment [29]. The simulated electron number density results exhibit concordance with the experimental shadow imaging results (as shown in Figures 1B, 3D). The current sheet size obtained from the simulation results can estimate the reconnection rate of magnetic reconnection, which is approximately 0.04 ± 0.05 at 4.0 ns ($\sim 72.0 \tau_A$). In the simulation, the opening angle of the magnetic reconnection outflow region is approximately $55^\circ \pm 5^\circ$, which is basically consistent with the experimental result of $60^\circ \pm 5^\circ$. The simulation shows that the electron number density in the magnetic reconnection region is less than 10^{19} cm^{-3} , and the magnetic reconnection process cannot be observed in the range above 10^{19} cm^{-3} . The electron temperature in the magnetic reconnection region is approximately $2.56 \times 10^6 \text{ K}$. The simulation parameters are consistent with the experimental data. The plasma β value in the simulation is lower than the



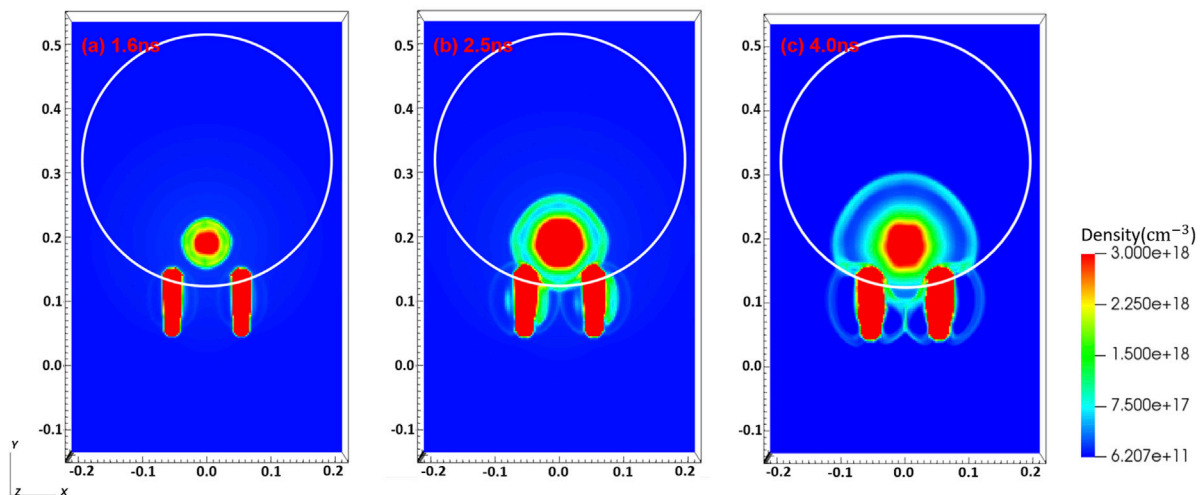


FIGURE 9
The electron number density at (A) 1.6 ns, (B) 2.5 ns, and (C) 4.0 ns by adding a straight wire magnetic field, intercepting the x-y plane of $z = 0.035$, which is beneficial to observing the plasma moving around the coil. The coordinate unit is centimeters.

predicted 0.016 from the experiment, that is approximately 0.007. This indicates that the magnetic reconnection process dominated by magnetic pressure.

Figure 4 illustrates the evolution of magnetic field. In the simulation, from the start of magnetic reconnection at 2.6 ns ($\sim 46.8 \tau_A$) to the end of the simulation at 4.0 ns ($\sim 72.0 \tau_A$), the changes in magnetic field topology continue to occur. The position of the x point of magnetic reconnection is shifted in the x direction, and the shape of the magnetic field lines in the magnetic reconnection area is tilted at 3.7 ns ($\sim 66.7 \tau_A$). To exam the two instances of magnetic field topology changes (2.6 ns and 3.7 ns), the electron number density and magnetic field (y-direction component) changes along the x direction are shown in Figure 5. The magnetic field shows obvious positive and negative alternation at the x point. Plasma accumulates in the current sheet area, and the width of the magnetic reconnection current sheet at 2.6 ns is slightly larger than that at 3.7 ns, approximately 2.8 times.

Figures 6A–C depict the simulated electron number density results with high resistivity ($\eta = 71.6 \text{ cm}^2\text{s}^{-1}$). The magnetic reconnection occurs (as shown in Figure 6B) and gradually characterized by a long current sheet (as shown in Figure 6C). The moment of magnetic reconnection initiation under high resistivity is basically the same as that under low resistivity. The magnetic energy begins to dissipate rapidly from $\sim 2.5 \text{ ns}$ ($\sim 45.0 \tau_A$), as shown in Figure 7B. The estimated reconnection rate is approximately 0.10 ± 0.03 , that is higher than the reconnection rate at 4.0 ns in the low resistivity simulation.

The variations in magnetic energy, kinetic energy and thermal energy within the magnetic reconnection region in low resistivity simulation are shown in Figure 7A (statistics the orange square area of Figure 3D). It can be seen that the magnetic energy is significantly dissipated after about 2.6 ns, which confirms the occurrence of magnetic reconnection. And the thermal energy and kinetic energy of the plasma increase significantly. In Figure 7, the red solid line represents the change of ion thermal energy, and the red dotted line represents the change of electron thermal energy. The increase in ion

thermal energy is higher than that of electrons, $\Delta E_{\text{ion}}/\Delta E_{\text{ele}} \sim 2.5$. The blue dotted line, dotted line, and solid line represent the plasma kinetic energy in the x, y, and z directions respectively. The increase in plasma kinetic energy is mainly observed in the y and z directions. The y direction corresponds to the outflow direction of magnetic reconnection, and the z direction corresponds to the out-of-plane direction of magnetic reconnection. The increase of the kinetic energy in the two directions is roughly equivalent. In addition, at the end of the simulation, the plasma kinetic energy in the y and z direction is basically at the same intensity as the electron thermal energy. It can be seen from the energy changes that the dissipation of magnetic energy in magnetic reconnection can be effectively converted into thermal energy and kinetic energy of the plasma. In the case of high resistivity, the energy distribution is different from the low resistivity case, as shown in Figure 7B. The thermal energy and kinetic energy of the plasma are still effectively increased. The electron thermal energy exhibits a stronger increase compared to the ion thermal energy, which is different with the result in the low resistivity case, with $\Delta E_{\text{ele}}/\Delta E_{\text{ion}} \sim 3.1$. In our simulation, ohmic heating dominates the energy distribution. In the case of high resistivity, the electrons obtain more thermal energy than ions. The increase of kinetic energy in the outflow direction is more severe than that of kinetic energy in the out-plane direction.

Additionally, opposite magnetic field structures in the straight-wire region can also cause magnetic reconnection. The experiments of Pei et al. [18] mainly focused on discussing the magnetic reconnection process within the magnetic field of the straight-wire region. They observed plasma accumulated of magnetic reconnection in the x-y plane (corresponding to the y-z plane in the simulation, as shown in Figures 8A–C). The outflow direction of magnetic reconnection in the straight-line region is mainly in the z direction perpendicular to the x-y plane. The dark region between the two bright lines in Figure 8A corresponds to the high-density plasma outflow generated by magnetic reconnection. Only the straight-wire magnetic field was added to the simulation, and the

simulation results were compared with the simulation results of adding the semi-circular arc coil magnetic field. The same current value was set in the two simulations. The evolution of the electron number density simulation results in the x-y plane with only the partial magnetic field of the straight wire added is shown in Figure 9. The plasma is bound by the magnetic field to move around the straight wire, and reconnection begins at 2.5 ns and continues to 4.0 ns (as shown in Figure 9). At the location where the coil magnetic field was added, an obvious high-density plasma accumulation area also appears inside the coil (as shown in Figure 8B). The plasma is the outflow in the y direction generated by the magnetic reconnection of the coil magnetic field. The accumulation of magnetic reconnection outflows in the two different regions inside the coil is in good agreement with the experimental results of Pei et al. [18]. It can be seen that the magnetic reconnection of straight wires and half-arc coils overlap significantly, so experimental research on magnetic reconnection needs to be more cautious. Besides, we find that the laser power intensity has great influence on the experiment, but the target material and coil geometry parameters have little influence on the experiment.

4 Results and discussion

The magnetic reconnection experiments of using Helmholtz capacitor-coil targets are simulated and investigated through the FLASH radiation magnetohydrodynamics simulation code. The simulation replicates the evolution process of magnetic reconnection and is in good agreement with the experimental results of Yuan et al. [29]. Different from previous steady-state models [38] (the Harris layer model), We have not artificially interfered with the plasma properties and magnetic field in the simulation, and can obtain more realistic information on the development of magnetic reconnection. In the simulation, the magnetic energy is effectively converted into the thermal energy and kinetic energy of the plasma. The main reason for the increase in kinetic energy is the electric field of the magnetic reconnection, so it increases significantly in both the outflow direction and the out-of-plane direction. In the case of low resistivity ($\eta = 0.716 \text{ cm}^2 \text{ s}^{-1}$), the thermal energy of ions increases more significantly compared to other energy components. The kinetic energy in the magnetic reconnection outflow direction increases significantly. Ohmic heating dominates the energy conversion, in the high resistivity ($\eta = 71.6 \text{ cm}^2 \text{ s}^{-1}$) simulation, so the increase in electron thermal energy is more prominent. Similar to low-resistivity case, the kinetic energy in the magnetic reconnection outflow direction and the out-plane direction increases significantly. The distribution of plasma

energy is discrete compared to the low-resistivity situation. And the reconnection rate increases significantly.

Data availability statement

The original contributions presented in the study are included in the article/Supplementary material, further inquiries can be directed to the corresponding author.

Author contributions

CX: Writing—original draft. YP: Writing—review and editing. XZ: Writing—review and editing. WA: Writing—review and editing. JZ: Writing—review and editing.

Funding

The author(s) declare that financial support was received for the research, authorship, and/or publication of this article. This Project supported by the National Program on Key Basic Research Project (Grant No. 2022YFA1603203), the National Natural Science Foundation of China (Grant Nos 12325305, 12175018, 12135001, and 1207503), and the Strategic Priority Research Program of the Chinese Academy of Sciences (Grant No. XDA25030700). The software used in this work was developed in part by the DOE NNSA- and DOE Office of Science supported Flash Center for Computational Science at the University of Chicago and the University of Rochester.

Conflict of interest

The authors declare that the research was conducted in the absence of any commercial or financial relationships that could be construed as a potential conflict of interest.

Publisher's note

All claims expressed in this article are solely those of the authors and do not necessarily represent those of their affiliated organizations, or those of the publisher, the editors and the reviewers. Any product that may be evaluated in this article, or claim that may be made by its manufacturer, is not guaranteed or endorsed by the publisher.

References

1. Yamada M, Kulsrud R, Ji H Magnetic reconnection. *Rev Mod Phys* (2010) 82(1): 603–64. doi:10.1103/revmodphys.82.603
2. Masuda S, Kosugi T, Hara H, Tsuneta S, Ogawara Y. The solar optical telescope for the hinode mission: an overview. *Nature* (1994) 371(6497):495–7. doi:10.1038/371495a0
3. Bhattacharjee A Impulsive magnetic reconnection in the earth's magnetotail and the solar corona *Annu Rev Astron Astrophys* (2004) 42:365–84. doi:10.1146/annurev.astro.42.053102.134039
4. Gosling JT Magnetic reconnection in the solar wind. *Space Sci Rev* (2012) 172: 187–200. doi:10.1007/s11214-011-9747-2
5. Ergun RE, Goodrich KA, Wilder FD, Holmes JC, Stawarz JE, Eriksson S, et al. Magnetospheric Multiscale satellites observations of parallel electric fields associated with magnetic reconnection. *Phys Rev Lett* (2016) 116(23):235102. doi:10.1103/physrevlett.116.235102
6. Burch JL, Torbert RB, Phan TD, Chen LJ, Moore TE, Ergun RE, et al. Electron-scale measurements of magnetic reconnection in space. *Science* (2016) 352(6290):aaf2939. doi:10.1126/science.aaf2939
7. Stawarz JE, Eastwood JP, Phan TD, Gingell IL, Pyakurel PS, Shay MA, et al. Turbulence-driven magnetic reconnection and the magnetic correlation length:

observations from Magnetospheric Multiscale in Earth's magnetosheath. *Phys Plasmas* (2022) 29(1). doi:10.1063/5.0071106

8. Zhang B, Yan H THE INTERNAL-COLLISION-INDUCED MAGNETIC RECONNECTION AND TURBULENCE (ICMART) MODEL OF GAMMA-RAY BURSTS. *Astrophysical J* (2010) 726(2):90. doi:10.1088/0004-637x/726/2/90

9. Schoeffler KM, Grismayer T, Uzdensky D, Fonseca RA, Silva LO Bright gamma-ray flares powered by magnetic reconnection in QED-strength magnetic fields. *Astrophysical J* (2019) 870(1):49. doi:10.3847/1538-4357/aaf1b9

10. Singh CB, Dal Pino EDG, Kadowaki LHS *Astrophysical J Lett* (2015) 799(2):L20. doi:10.1088/2041-8205/799/2/L20

11. Ripperda B, Bacchini F, Philippov AA Magnetic reconnection and hot spot formation in black hole accretion disks. *Astrophysical J* (2020) 900(2):100. doi:10.3847/1538-4357/ababab

12. Contopoulos I. The role of reconnection in the pulsar magnetosphere. *Astron Astrophys* (2007) 466(1):301–7. doi:10.1051/0004-6361:20065973

13. Joglekar AS, Thomas AGR, Fox W, Bhattacharjee A. Magnetic reconnection in plasma under inertial confinement fusion conditions driven by heat flux effects in ohm's law. *Phys Rev Lett* (2014) 112(10):105004. doi:10.1103/physrevlett.112.105004

14. Hohenberger M, Chang PY, Fiksel G, Knauer JP, Betti R, Marshall FJ, et al. Inertial confinement fusion implosions with imposed magnetic field compression using the OMEGA Laser. *Phys Plasmas* (2012) 19(5). doi:10.1063/1.3696032

15. Zhong J, Li Y, Wang X, Wang J, Dong Q, Xiao C, et al. Modelling loop-top X-ray source and reconnection outflows in solar flares with intense lasers. *Nat Phys* (2010) 6(12):984–7. doi:10.1038/nphys1790

16. Yamada M, Yoo J, Jara-Almonte J, Ji H, Kulsrud RM, Myers CE. Conversion of magnetic energy in the magnetic reconnection layer of a laboratory plasma. *Nat Commun* (2014) 5:4774. doi:10.1038/ncomms5774

17. Yamada M, Ji H, Hsu S, Carter T, Kulsrud R, Bretz N, et al. Study of driven magnetic reconnection in a laboratory plasma. *Phys Plasmas* (1997) 4(5):1936–44. doi:10.1063/1.872336

18. Pei XX, Zhong JY, Sakawa Y, Zhang Z, Zhang K, Wei HG, et al. Magnetic reconnection driven by Gekko XII lasers with a Helmholtz capacitor-coil target. *Phys Plasmas* (2016) 23:032125. doi:10.1063/1.4944928

19. Zhang S, Chien A, Gao L, Ji H, Eric GB, et al. Ion and electron acoustic bursts during anti-parallel magnetic reconnection driven by lasers. *Nat Phys* (2023) 19:909–16. doi:10.1038/s41567-023-01972-1

20. Chien A, Gao L, Zhang S, Ji H, Eric GB, William D, et al. (2023). Non-thermal electron acceleration from magnetically driven reconnection in a laboratory plasma *Nat Phys* 19:254–62. doi:10.1038/s41567-022-01839-x

21. Fiksel G, Fox W, Gao L, Ji H A simple model for estimating a magnetic field in laser-driven coils. *Appl Phys Lett* (2016) 109:134103. doi:10.1063/1.4963763

22. Daido H, Miki F, Mima K, Fujita M, Sawai K, Fujita H, et al. Generation of a strong magnetic field by an intense CO₂ laser pulse. *Phys Rev Lett* (1986) 56(8):846–9. doi:10.1103/physrevlett.56.846

23. Courtois C, Ash AD, Chambers DM, Grundy RAD, Woolsey NC Creation of a uniform high magnetic-field strength environment for laser-driven experiments. *J Appl Phys* (2005) 98:054913. doi:10.1063/1.2035896

24. Fujioka S, Zhang Z, Yamamoto N, Ohira S, Fujii Y, Ishihara K, et al. High-energy-density plasmas generation on GEKKO-LFEX laser facility for fast-ignition laser fusion studies and laboratory astrophysics. *Plasma Phys Controlled Fusion* (2012) 54(12):124042. doi:10.1088/0741-3335/54/12/124042

25. Gao L, Ji H, Fiksel G, Fox W, Evans M, Alfonso N Ultrafast proton radiography of the magnetic fields generated by a laser-driven coil current. *Phys Plasmas* (2016) 23:043106. doi:10.1063/1.4945643

26. Bradford P, Read MP, Ehret M, Antonelli L, Khan M, Booth N, et al. Proton deflectometry of a capacitor coil target along two axes *High Power Laser Sci Eng*, 8 (2020). p. e11. doi:10.1017/hpl.2020.9

27. Wang W, Shan L, Zhang F, Yuan Z, Liu D, Tian C, et al. Pulsed magnetic fields of over 100 T produced by relativistic intensity laser pulse irradiating no-hole capacitor-coil target. *Phys Plasmas* (2023) 30(7). doi:10.1063/5.0120697

28. Fujioka S, Zhang Z, Ishihara K, Shigemori K, Hironaka Y, Johzaki T, et al. *Scientific Rep* (2013) 3(1):1–7. doi:10.1038/srep01170

29. Yuan X, Zhong J, Zhang Z, Zhou W, Teng J, Li Y, et al. Low- β magnetic reconnection driven by the intense lasers with a double-turn capacitor-coil. *Plasma Phys Controlled Fusion* (2018) 60(6):065009. doi:10.1088/1361-6587/aabaa9

30. Shan-Shan X, Zhi-Xing M, Jia-Yong Z, Jun LIN. *Chin Astron Astrophys* (2021) 45(2):131–46. doi:10.1016/j.chinastron.2021.05.001

31. Egedal J, Daughton W, Le A, et al. Large-scale electron acceleration by parallel electric fields during magnetic reconnection. *Nat Phys* (2012) 8(4):321–4. doi:10.1038/nphys2249

32. Fox W, Park J, Deng W, Fiksel G, Spitkovsky A, Bhattacharjee A. Astrophysical particle acceleration mechanisms in colliding magnetized laser-produced plasmas. *Phys Plasmas* (2017) 24:092901. doi:10.1063/1.4993204

33. Eastwood JP, Phan TD, Bale SD, Tjulin A Observations of turbulence generated by magnetic reconnection. *Phys Rev Lett* (2009) 102(3):035001. doi:10.1103/physrevlett.102.035001

34. Torbert RB, Burch JL, Giles BL, Gershman D, Pollock CJ, Dorelli J, et al. Estimates of terms in Ohm's law during an encounter with an electron diffusion region. *Geophys Res Lett* (2016) 43(12):5918–25. doi:10.1002/2016GL069553

35. Graham DB, Khotyaintsev YV, André M, Vaivads A, Divin A, Drake JF, et al. Direct observations of anomalous resistivity and diffusion in collisionless plasma. *Nat Commun* (2022) 13(1):2954. doi:10.1038/s41467-022-30561-8

36. Lee D New high-order methods using Gaussian processes for computational fluid dynamics simulations. *J Comput Phys* (2013) 243:269–92. doi:10.1088/1742-6596/837/1/012018

37. Elleaume P, Chubar O, Chavanne J. Computing 3D magnetic field from insertion devices. *Accel Conf* (2008) 3:3509–11. doi:10.1109/PAC.1997.753258

38. Potter MA, Browning PK, Gordovskyy M Forced magnetic reconnection and plasmoid coalescence: I. Magnetohydrodynamic simulations. *Astron Astrophys* (2019) 623:A15. doi:10.1051/0004-6361/201833565



OPEN ACCESS

EDITED BY

Paolo Francesco Ambrico,
Istituto per la Scienza e Tecnologia dei
Plasmi—CNR, Italy

REVIEWED BY

Luca Matteo Martini,
University of Trento, Italy
Kristaq Gazeli,
UPR3407 Laboratoire des Sciences des
Procédés et des Matériaux (LSPM), France

*CORRESPONDENCE

Pavel Dvořák,
✉ pdvorak@physics.muni.cz

RECEIVED 27 March 2024

ACCEPTED 03 June 2024

PUBLISHED 10 July 2024

CITATION

Dvořák P, Mrkvičková M and Kratzer J (2024), LIF
measurement in a partially saturated and
partially absorbed regime.
Front. Phys. 12:1408078.
doi: 10.3389/fphy.2024.1408078

COPYRIGHT

© 2024 Dvořák, Mrkvičková and Kratzer. This is
an open-access article distributed under the
terms of the [Creative Commons Attribution
License \(CC BY\)](#). The use, distribution or
reproduction in other forums is permitted,
provided the original author(s) and the
copyright owner(s) are credited and that the
original publication in this journal is cited, in
accordance with accepted academic practice.
No use, distribution or reproduction is
permitted which does not comply with these
terms.

LIF measurement in a partially saturated and partially absorbed regime

Pavel Dvořák^{1*}, Martina Mrkvičková¹ and Jan Kratzer²

¹Department of Plasma Physics and Technology, Faculty of Science, Masaryk University, Brno, Czechia,

²The Czech Academy of Sciences, Institute of Analytical Chemistry, Brno, Czechia

The problems of laser-induced fluorescence (LIF) measurements in a partially saturated regime with spatially dependent laser intensity in the sample (caused by absorption) are analyzed. The obtained equations are tested by means of LIF of free tellurium atoms in a plasma of an atmospheric pressure dielectric barrier discharge (DBD) by comparing fluorescence and absorption measurements. The results show a high reliability of LIF measurements.

KEYWORDS

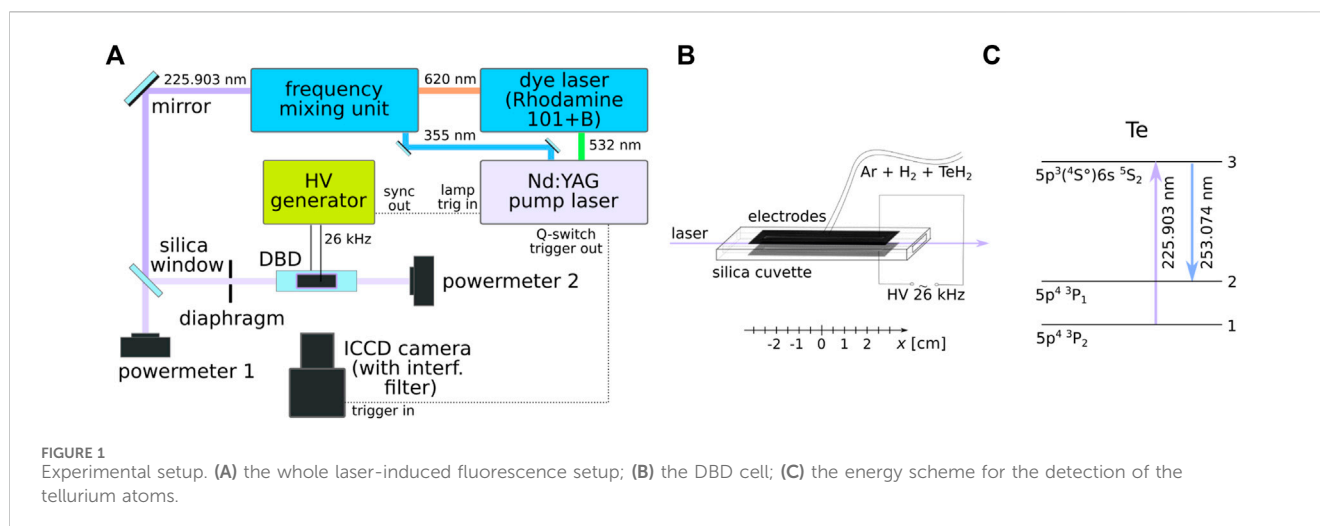
fluorescence, laser-induced fluorescence, absorption, dielectric barrier discharge, plasma

1 Introduction

Fluorescence, frequently realized as laser-induced fluorescence (LIF), is one of the most important methods for detection of various species in numerous scientific fields [1–3]. It offers *in situ* measurements with high sensitivity (going to single-molecule detection [4]), versatility, and spatial resolution. Due to these advantages, it is a key method for detection of reactive species in plasmas [5–9], including free atoms, molecular radicals, complete molecules, and ions.

Unfortunately, the phenomena occurring during the fluorescence process can be relatively complicated due to collisions of the excited state [10], laser induced photodissociation [11, 12], invasivity of the method [13, 14], or necessity of calibration of the detection system [5–7]. As a result, the absolute concentrations obtained by LIF sometimes exhibit high uncertainty [15]. Therefore, any validation of the results of the LIF method is valuable. Moreover, the fluorescence process can be complicated by partial saturation, i.e., by deviation of the fluorescence signal from its linear dependence on the energy of laser pulses, which is caused by evident depletion of the investigated ground state, stimulated emission, and eventually by photoionization of the excited state. Therefore, LIF saturation was studied by several works [16–18]. Another complication is that the laser beam may be fully or partially absorbed in the studied sample, which leads to spatially variable energy of laser pulses. In addition, the absorption can be partially saturated from the same reasons which cause the saturation of the fluorescence.

The abovementioned complications were the motivation to derive equations that can be used for evaluation of LIF and that take into account the absorption of the laser beam in the sample (in this case in plasma) and the saturation of both LIF and absorption. This study also aimed to validate the concentration values gained from LIF measurements by absorption. These intentions were realized in atmospheric pressure plasma of a dielectric barrier discharge (DBD) ignited in a so-called atomizer, i.e., in a device that is used for dissociation (atomization) of volatile species in the field of trace element analysis to determine metal concentrations by atomic spectrometry. Particularly, the presented



measurement was realized on LIF of free tellurium atoms that were supplied to the plasma in the form of tellurium hydride (TeH_2), which was atomized in the plasma to produce the free Te atoms.

2 Experimental

A volume DBD was ignited inside a DBD atomizer consisting of two parts—an optical and an inlet arm. The DBD was ignited in the optical arm—a 75-mm-long silica vessel with 7 mm \times 3 mm internal rectangular cross-section. Two planar copper electrodes (50 mm long, 5 mm wide) were placed on the outer surfaces of the upper and lower bases of the vessel and supplied with a sinusoidal voltage of 26 kHz frequency and 9 kV amplitude. An inlet arm—a silica tube with internal diameter 2 mm—was sealed to the centre of the optical arm and served as the inlet for the working gas mixture from the hydride generator unit. This compartment served for almost quantitative ($93\% \pm 5\%$) conversion of the Te standard solution (50 ng/mL Te) by chemical reaction, reduction by NaBH_4 to TeH_2 . Ar (75 sccm) served as the carrier gas, while 50 sccm H_2 is produced as a by-product of the chemical reaction. After passing through the atomizer, the gases escaped freely through its open ends into the surrounding atmosphere.

The scheme of the whole laser-induced fluorescence setup is shown in Figure 1. Figure 1C shows the energy scheme for the detection of the tellurium atoms. The ground state $5p^4 3P_2$ atoms were excited to the $5p^3 6s \ ^5S_2$ state by absorbing laser photons of wavelength 225.903 nm. The resulting fluorescence photons of wavelength 253.074 nm were emitted while the atoms were depopulated to the $5p^4 3P_1$ state. The excitation laser beam was generated by a system consisting of a Q-switched pump laser (Spectra-Physics, Quanta-Ray PRO-270-30), a dye laser (Sirah, PrecisionScan PRSC-D-24-EG with Rhodamine 101/B), and a frequency conversion unit. The output beam with a wavelength of 225.903 nm, spectral width of 0.4 pm, single-pulse duration of 8 ns, and repetition frequency of 30 Hz was divided into two branches by a silica window acting as a beam splitter, which decreased the energy of the laser beam entering the DBD in order to reduce the strong fluorescence saturation. The laser beam was circular with a diameter of approx. 3 mm. Before entering the DBD, a part of its spatial wings was cut by a

rectangular (5 \times 2 mm) diaphragm so that it could pass through the center of the optical arm of the atomizer without touching the silica walls. The beam was localized at the axis of the optical arm. The energy of both beams was monitored by pyroelectric power meters (Ophir, Vega PE9), providing the information on the laser energy before entering the discharge and after the absorption on tellurium atoms (the ratio between the energy measured by the first power meter and the real energy at the DBD input was obtained from measurements realized when there was no plasma and no absorption in the atomizer). The fluorescence signal was detected perpendicular to the laser beam by using an ICCD camera (Princeton Instruments, PI-MAX). The spatial resolution of the measurements was 0.08 mm. An interference filter (AHF 257/12 BrightLine HC) was mounted on the camera lens to separate the fluorescence signal from the ambient radiation. The signal was temporally integrated over 100 ns, covering the entire laser pulse and the fluorescence decay (only for measurements of the fluorescence decay rate, discussed in Section 4, the signal was integrated only over 0.64 ns, and the delay between the laser pulse and the signal detection was gradually increased by a step 0.5 ns). In order to increase the signal-to-noise ratio, the fluorescence image was accumulated on the ICCD camera chip from typically 300 of laser shots.

3 Theory

For calculating the LIF signal, we will use the simple three-level model, where atoms or molecules are excited by a laser photon from their ground state (denoted as the level 1) to a higher excited state (level 3). The excitation is followed by a spontaneous radiative decay to a lower excited state (level 2), which is accompanied by emission of a fluorescence photon—this fluorescence radiation is detected, and its intensity is used for determination of the concentration of studied atoms or molecules. Alternatively, the excited atom in the third level can undergo radiative transition to another lower lying state, or its excitation can be non-radiatively quenched by a number of collisional processes. The rate of the desired fluorescence transition to level 2 is described by the Einstein coefficient of spontaneous emission (A_{32}), whereas the total depopulation rate of level 3 can be described by the reciprocal value of

the lifetime of the excited level 3 ($1/\tau$). The product $A_{32} \tau$ gives the quantum efficiency of the fluorescence.

In the standard LIF measurement in the linear regime, where the fluorescence signal is directly proportional to the energy of laser pulses, the measured fluorescence signal can be calculated according to [10].

$$M_f = a_f A_{32} \tau \frac{\kappa B_{13}}{c} n E_f \iiint_V D_f \frac{\Omega}{4\pi} s dV, \quad (1)$$

where n is the concentration of studied atoms, E_f is the mean energy of laser pulses, B_{13} is the Einstein coefficient for excitation from the ground level to the excited level 3, and κ describes the overlap between the spectral profiles of the laser line and the absorption line [19] (for the narrow laser line, κ is simply equal to the ratio between the maximum and integral intensities of the absorption line. M_f in Eq. 1 is the fluorescence signal integrated temporally over the whole fluorescence duration and spectrally over the whole fluorescence transition; it is not spectrally integrated over the excitation line—if it was spectrally integrated also over the excitation line, the factor κ should be left out from the equation). c is the speed of light, and a_f is the number of accumulations used during the collection of the fluorescence signal. D_f is the detector sensitivity for the fluorescence wavelength—this constant includes the quantum efficiency of the ICCD camera (η_f) and the transmission of the used interference filter (T). Ω is the solid angle for detection of fluorescence photons covered by the detector. Finally, s describes the spatial distribution of laser beam energy normalized to 1 (i.e., the surface integral of s over the plane perpendicular to the beam axis is equal to 1). In practice, it is problematic to predict the value of the integral $\iiint_V D_f \frac{\Omega}{4\pi} s dV$. Therefore, the LIF measurement is often calibrated by Rayleigh scattering, which gives the signal

$$M_r = a_r \frac{d\sigma_r}{d\Omega} \frac{p_r}{kT_r} \frac{E_r}{h\nu_r} \iiint_V D_r \Omega s dV, \quad (2)$$

where $d\sigma_r/d\Omega$ is the differential cross-section for Rayleigh scattering on the gas used for calibration; p_r and T_r are the pressure and temperature of the calibration gas, respectively (the gas concentration is equal to $n_r = p_r/kT_r$); and k is the Boltzmann constant. E_r is the mean energy of laser pulses used for Rayleigh scattering, ν_r is the frequency of laser light, and h is the Planck constant. D_r is the detector sensitivity for Rayleigh wavelength, and this quantity is proportional to the ICCD quantum efficiency η_r . The combination of Eqs 1, 2 enables to calculate the concentration of studied atoms by

$$n_0 = 4\pi \frac{a_r \eta_r}{a_f \eta_f T} \frac{n_r E_r}{M_r h\nu_r} \frac{d\sigma_r}{d\Omega} \frac{c M_f}{A_{32} \tau \kappa B_{13} E_f}. \quad (3)$$

When the partially saturated LIF regime is used, the ratio M_f/E_f in Eq. 3 must be replaced by the term $M_f \beta / \ln(1 + \beta E_f)$ [17], which takes into account the partial saturation of the LIF process quantified by the saturation constant β . In addition, if an appreciable part of the laser beam is absorbed during the measurement, the spatial dependence of the laser pulse energy should be taken into account:

$$n(x) = 4\pi \frac{a_r \eta_r}{a_f \eta_f T} \frac{n_r E_r}{M_r h\nu_r} \frac{d\sigma_r}{d\Omega} \frac{c M_f(x) \beta}{A_{32} \tau \kappa B_{13} \ln[1 + \beta E_f(x)]}. \quad (4)$$

This equation must be supplemented by another equation that describes the spatial variation of the laser pulse energy along the

direction of the laser beam propagation (x). With no saturation, the variation would be described by $\frac{dE_f}{dx} = -n(x) \kappa \sigma_a E_f(x)$, where the absorption cross-section $\sigma_a = A_{31} \frac{\lambda_{13}^2}{8\pi} \frac{g_3}{g_1}$. A_{31} is the Einstein coefficient for spontaneous emission from directly excited level 3 to ground level 1, which is connected to the Einstein coefficient for excitation by the relation $B_{13} = A_{31} \frac{\lambda_{13}^3}{8\pi h} \frac{g_3}{g_1}$, where g_1 and g_3 are the degenerations of the ground and excited state, respectively. If we take into account the saturation effects (the depletion of the ground state and stimulated emission), we will find that the number of photons lost from the laser pulse is proportional to

$$\mathcal{A} = \int_0^\infty [n_1(t) \kappa B_{13} - n_3(t) \kappa B_{31}] I(t) dt, \quad (5)$$

where n_1 and n_3 are the concentrations of the ground and directly excited states, respectively; B_{31} is the Einstein coefficient for stimulated emission; and I is the laser intensity. The first term describes excitation, and the second term is the creation of new laser photons by stimulated emission (when laser intensity is small, i.e., in the linear regime, $n_3 \ll n_1$ and $n_1 \approx \text{const.}$, which simplifies the integral to $\mathcal{A} \approx n_1 \kappa B_{13} \int_0^\infty I(t) dt$). From the rate equation analysis of a partially saturated fluorescence process, it follows [15, 17] that the number of fluorescence photons is also proportional to the integral \mathcal{A} , defined in Eq. 5. Consequently, saturation of both the absorption and fluorescence can be described by the same formula, and the equation for the spatial variation of the laser pulse energy can be rewritten to

$$\frac{dE_f}{dx} = -n(x) \kappa \sigma_a \frac{\ln[1 + \beta E_f(x)]}{\beta}. \quad (6)$$

The term $\ln[1 + \beta E_f(x)]/\beta$ in Eq. 6 takes into account the partial saturation of the absorption. For low laser energies, $\ln[1 + \beta E_f(x)]/\beta \approx E_f(x)$, which is the limit of the linear regime. Of course, in non-homogeneous environments, β (and also the decay time τ) may also depend on the position. When saturation and absorption are strong or when the concentration of measured species strongly varies in the direction perpendicular to x , β may vary along the laser beam (in the x direction) also due to different absorption in various parts of the beam, resulting in changes of the beam profile. It should be noted that fluorescence and absorption processes are characterised by identical saturation constants (β) only if ground state depletion and emission stimulated by laser photons dominate to the saturation mechanisms. In rare situations, when other saturation mechanisms (photoionization of the excited state; emission stimulated by fluorescence photons) play an important role, the saturation constants for absorption and fluorescence may differ.

4 Results

In our study, we applied the equations obtained in Section 3 on the LIF of free Te atoms generated by a DBD. First, let us assess the non-linearity or saturation of the LIF process. Saturation can be revealed when a straight line is fitted to the dependence $\ln M_f$ on $\ln E_f$ because the slope of the fitted line is equal to 1 for linear LIF and

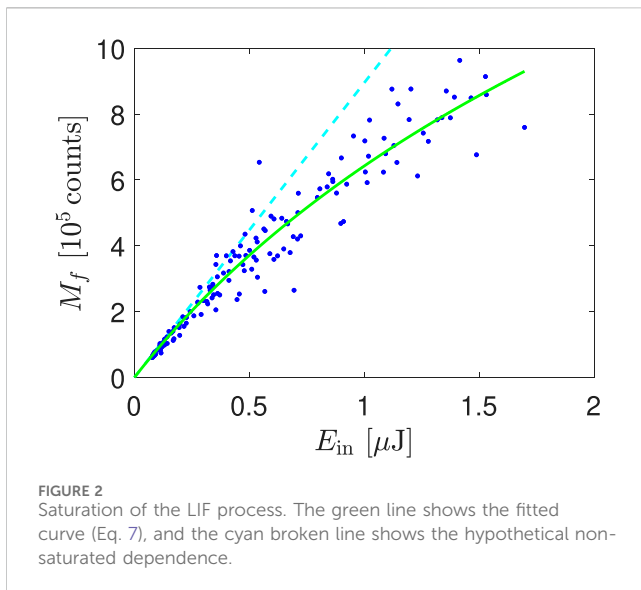


FIGURE 2
Saturation of the LIF process. The green line shows the fitted curve (Eq. 7), and the cyan broken line shows the hypothetical non-saturated dependence.

smaller than 1 for saturated LIF, whereas slope higher than 1 indicates some photodissociation ignited by the laser [12]. In our measurement, the slope had the value (0.88 ± 0.01) , indicating a weak saturation (according to [17] caused mainly by the ground state depletion). Therefore, the dependence of the measured fluorescence signal on the energy of laser pulses was fitted by the equation

$$M_f = \frac{\alpha}{\beta} \ln(1 + \beta E_f), \quad (7)$$

derived in [17] for Gaussian beams, where β is the above mentioned saturation constant and αE_f gives the hypothetical signal that would be measured if no saturation occurred. Both the data and the fit (with $\beta = (8.8 \pm 0.2) \cdot 10^5 \text{ J}^{-1}$) are shown in Figure 2, which demonstrates the deviation of the real fluorescence signal from the hypothetical linear dependence shown by the broken cyan line.

Not only fluorescence but also absorption can be affected by saturation processes. Therefore, Eq. 6 should be used instead of the traditional equation $\frac{dE_f}{dx} = -n\kappa\sigma_a E_f$ for strong laser intensities. The fact that absorption in our measurements was partially saturated can be demonstrated by Figure 3, which shows the ratio between the energy of laser pulses that enter and leave the DBD reactor. The fact that this ratio is not constant, but it is a slightly decreasing function of the laser pulse energy, is an evidence of the saturation of absorption.

In order to characterize the fluorescence process, it is necessary to measure the fluorescence decay time (i.e., the lifetime of the excited state) and the spectral profile of the excitation line. The decay time was measured by variation of the delay between the laser pulse and the interval when the ICCD camera collects the fluorescence radiation. In our case, the decay time was significantly shorter than the laser pulse duration, and a weak tail of the laser pulse disturbed the decay process. Consequently, it would not be correct to fit a single exponential through the measured data, and the fluorescence decay was fitted by the convolution $\int_0^t L(t') e^{-(t-t')/\tau} dt'$, where the temporal shape of the laser pulse tail intensity L (strictly speaking, L is the convolution of the temporal profile of the laser pulse and the temporal response of the camera) was determined from the temporally resolved measurement of Rayleigh-scattered laser photons. This procedure led to the value

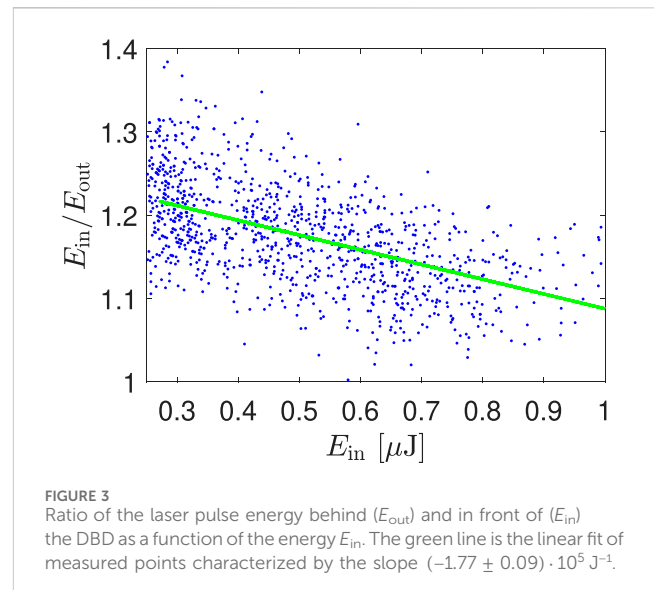
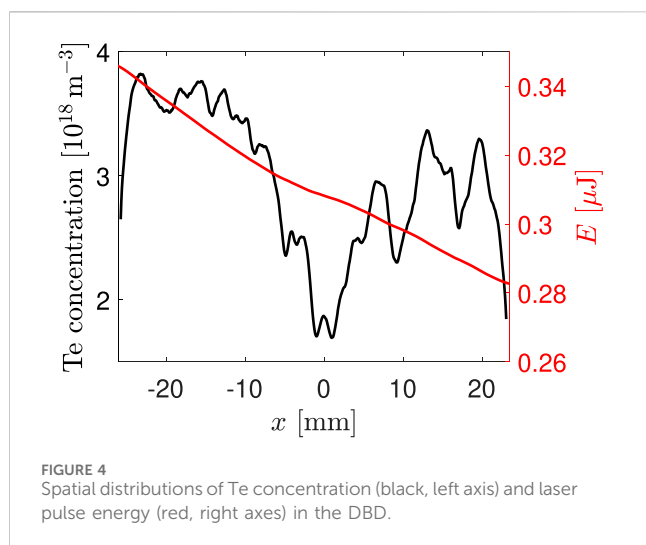


FIGURE 3
Ratio of the laser pulse energy behind (E_{out}) and in front of (E_{in}) the DBD as a function of the energy E_{in} . The green line is the linear fit of measured points characterized by the slope $(-1.77 \pm 0.09) \cdot 10^5 \text{ J}^{-1}$.

$\tau = (1.7 \pm 0.2) \text{ ns}$. In our case, the fluorescence quantum yield $A_{32} \tau = 1.6 \cdot 10^{-3}$ was low because the chosen fluorescence line was a triplet–quintet transition, and it was weak. The remaining characteristics, the excitation line profile, were measured by the variation of laser wavelength. The measured shape agreed with the Voigt profile with the Gauss parameter $\sigma \approx 1 \cdot 10^9 \text{ Hz}$ and Lorentz parameter $\gamma \approx 5 \cdot 10^9 \text{ Hz}$ and with the ratio between maximum and spectrally integrated signals $\kappa = (5.6 \pm 0.3) \text{ Hz}^{-1}$. Due to the narrow laser linewidth and small Doppler broadening of the relatively heavy atoms in the plasma with a low gas temperature around 550 K [20], the spectral profile of the excitation line is controlled by broadening mechanisms connected with the atmospheric pressure (collisional broadening, van der Waals broadening, event. resonance broadening) [21]. In addition, Stark broadening may play a role in the DBD.

Finally, we can proceed to the calculation of the concentration of free Te atoms realized by Eqs 4, 6. At the beginning of the solution, Eq. 4 is used for the calculation of the Te concentration in one of the discharge edges. When the concentration is known, Eq. 6 is used for the calculation of laser pulse energy in the neighboring point and the alternating use of both these equations continues until the Te concentration and the laser pulse energy are known along the whole beam path in the plasma. The obtained concentration profile for the measurement, where TeH_2 was generated from a solution with Te concentration $50 \mu\text{g/L}$, is shown by the black curve in Figure 4 (it should be noted that the wavy structures in the right half of the DBD reactor were caused by an uneven surface of the front silica wall of the atomizer, which deflected part of the fluorescence radiation). The consequences of the concentration profile for the understanding of the TeH_2 atomization are described elsewhere [22]; here, we will only summarize that the presence of free Te atoms in the whole discharge region and the high Te concentration demonstrate a good performance of the DBD in atomization of the hydride. The mean concentration in the left part (not affected by the uneven surface) of the atomizer $3.5 \cdot 10^{18} \text{ m}^{-3}$ is in good agreement with the expected value between $3.45 \cdot 10^{18} \text{ m}^{-3}$ and $3.83 \cdot 10^{18} \text{ m}^{-3}$ (calculated from the TeH_2 supply rate from the hydride generator to the DBD assuming full hydride atomization), indicating reliability of the used measurement and evaluation procedure.



There are several sources of uncertainty of the concentration values: the first is the variability of the measured intensities, which was, in our case, approximately 8%. The second was the uncertainty of LIF parameters, namely, of τ , κ , and β . In our case, the uncertainty of κ and β was only few percent, but the uncertainty of the decay time τ was approximately 10%. All the above listed sources together led in our measurements to an uncertainty below 20%. The third source can be the uncertainty of the Einstein coefficients A_{32} and B_{13} . Our values were taken from [23]. Unfortunately, we did not find the uncertainty of the used Einstein coefficient in the cited work and in the references therein.

At last, when solving the pair of Eqs 4, 6, one of the results is the spatial development of laser pulse energy. One example of this curve is shown in Figure 4 by the red curve. From such a curve, it is possible to obtain the ratio of the energy of laser pulses at the input and at the output of the DBD reactor, which can be simply compared with the measured value of this ratio. In other words, our experiment enabled comparing the results of fluorescence and absorption measurements. In our experiment, the ratio of laser pulse energies predicted from the intensity of the fluorescence signal by means of Eqs 4, 6 had the value 1.34, whereas the directly measured value was 1.25. The results of the fluorescence and absorption measurements differed only by 7%, which could be attributed to losses caused by the reflection of the fluorescence radiation on the front atomizer wall, which shows a very good agreement.

5 Conclusion

The equations for the evaluation of Rayleigh-calibrated LIF measurements in a partially saturated regime when a detectable

part of laser photons is absorbed in the sample, in other words of partially saturated fluorescence measurement with spatially dependent intensity of the excitation radiation, were summarized. LIF measurement evaluated by these equations was tested on free tellurium atoms present in an atmospheric pressure DBD. The results were in a good agreement with both the expected Te concentration and with the measured absorption of laser in the DBD, demonstrating a high reliability of absolute LIF measurements.

Data availability statement

The original contributions presented in the study are included in the article/Supplementary material, further inquiries can be directed to the corresponding author.

Author contributions

PD: writing–review and editing and writing–original draft. MM: writing–review and editing and writing–original draft. JK: writing–review and editing and writing–original draft.

Funding

The author(s) declare that financial support was received for the research, authorship, and/or publication of this article. This research has been supported by the Czech Science Foundation (Contract 23-05974K), Institute of Analytical Chemistry of the Czech Academy of Sciences (RVO: 68081715), and by the Project LM2023039 funded by the Ministry of Education, Youth and Sports of the Czech Republic.

Conflict of interest

The authors declare that the research was conducted in the absence of any commercial or financial relationships that could be construed as a potential conflict of interest.

Publisher's note

All claims expressed in this article are solely those of the authors and do not necessarily represent those of their affiliated organizations, or those of the publisher, the editors, and the reviewers. Any product that may be evaluated in this article, or claim that may be made by its manufacturer, is not guaranteed or endorsed by the publisher.

References

- Geddes CD, Lakowicz JR. *Reviews in fluorescence* 2016. Cham, Switzerland: Springer (2017).
- Birch DJS, Chen Y, Rolinski OJ. *Photonics: biomedical photonics, spectroscopy, and microscopy*. John Wiley and Sons (2015). p. 1–58. chap. fluorescence.
- Stchur P, Yang KX, Hou X, Sun T, G MR. Laser excited atomic fluorescence spectrometry — a review. *Spectrochimica Acta B* (2001) 56:1565–92. doi:10.1016/s0584-8547(01)00265-8
- Shashkova S, Leak MC. Single-molecule fluorescence microscopy review: shedding new light on old problems. *Biosci Rep* (2017) 37:BSR20170031. doi:10.1042/bsr20170031
- Amorim J, Baravian G, Jolly J. Laser-induced resonance fluorescence as a diagnostic technique in non-thermal equilibrium plasmas. *J Phys D: Appl Phys* (2000) 33:R51–65. doi:10.1088/0022-3727/33/9/201

6. Niemi K, von der Gathen VS, Döbele H. Absolute calibration of atomic density measurements by laser-induced fluorescence spectroscopy with two-photon excitation. *J Phys D: Appl Phys* (2001) 34:2330–5. doi:10.1088/0022-3727/34/15/312
7. Döbele HF, Mosbach T, Niemi K, Schulz-von der Gathen V. Laser-induced fluorescence measurements of absolute atomic densities: concepts and limitations. *Plasma Sourc Sci. Technol.* (2005) 14:S31–41. doi:10.1088/0963-0252/14/2/s05
8. Freearge TGM, Hancock G. 23RD international conference on phenomena in ionized *J Phys IV France* (1997) 7:C4. doi:10.1051/jp4:1997403
9. Dilecce G, Martini L, Tosi S, Scotoni M, De Benedictis S. Laser induced fluorescence in atmospheric pressure discharges. *Plasma Sourc Sci. Technol.* (2015) 18:034007. doi:10.1088/0963-0252/24/3/034007
10. Voráč J, Dvořák P, Mrkvíčková M. Laser induced fluorescence of hydroxyl (OH) radical in cold atmospheric discharges. In: Britun N., Nikiforov A., editors *Photon counting*. Rijeka, Croatia. IntechOpen (2017).
11. Kulatilaka WD, Frank JH, Patterson BD, Settersten TB. Analysis of 205-nm photolytic production of atomic hydrogen in methane flames. *Appl Phys B* (2009) 97:227–42. doi:10.1007/s00340-009-3474-3
12. Dvořák P, Procházka V, Krumpolec R, Zemánek M. Solution to the perturbation of LIF measurements via photodissociation, OH measurement in atmospheric-pressure multihollow DBD. *Plasma Process Polym* (2020) 17:202000020. doi:10.1002/ppap.202000020
13. Ambrico PF, Ambrico M, Šimek M, Colaianni A, Dilecce G, De Benedictis S. Laser triggered single streamer in a pin-to-pin coplanar dielectric barrier discharge. *Appl Phys Lett* (2009) 94:231501. doi:10.1063/1.3152284
14. Mrkvíčková M, Ráhel J, Dvořák P, Trunec D, Morávek T. Fluorescence (TALIF) measurement of atomic hydrogen concentration in a coplanar surface dielectric barrier discharge. *Plasma Sourc Sci. Technol.* (2016) 25:055015. doi:10.1088/0963-0252/25/5/055015
15. Verreycken T, Mensink R, van der Horst R, Sadeghi N, Bruggeman PJ. Absolute OH density measurements in the effluent of a cold atmospheric-pressure Ar–H₂O RF plasma jet in air. *Plasma Sourc Sci. Technol.* (2013) 22:055014. doi:10.1088/0963-0252/22/5/055014
16. Daily JW. Laser induced fluorescence spectroscopy in flames. *Prog Energ Combust. Sci.* (1997) 23:133–99. doi:10.1016/s0360-1285(97)00008-7
17. Mrkvíčková M, Dvořák P, Svoboda M, Kratzer J, Voráč J, Dědina J. Dealing with saturation of the laser-induced fluorescence signal: an application to lead atoms. *Combustion and Flame* (2022) 241:112100. doi:10.1016/j.combustflame.2022.112100
18. Voráč J, Dvořák P, Procházka V, Morávek T, Ráhel J. Dependence of laser-induced fluorescence on exciting-laser power: partial saturation and laser – plasma interaction. *Eur Phys J Appl Phys* (2015) 71:20812. doi:10.1051/epjap/2015150022
19. Voráč J, Dvořák P, Procházka V, Ehlbeck J, Reuter S. Measurement of hydroxyl radical (OH) concentration in an argon RF plasma jet by laser-induced fluorescence. *Plasma Sourc Sci. Technol.* (2013) 22:025016. doi:10.1088/0963-0252/22/2/025016
20. Dvořák P, Talába M, Obrušník A, Kratzer J, Dědina J. Concentration of atomic hydrogen in a dielectric barrier discharge measured by two-photon absorption fluorescence. *Plasma Sourc Sci. Technol.* (2017) 26:085002. doi:10.1088/1361-6595/aa76f7
21. Konjević N. Plasma broadening and shifting of non-hydrogenic spectral lines: present status and applications *Phys Rep* (1999) 316:339. doi:10.1016/S0370-1573(98)00132-X
22. Buřková K, Musil S, Kratzer J, Dvořák P, Mrkvíčková M, Voráč J, et al. Generation of tellurium hydride and its atomization in a dielectric barrier discharge for atomic absorption spectrometry. *Spectrochimica Acta Part B* (2020) 171:105947. doi:10.1016/j.sab.2020.105947
23. Kramida A, Ralchenko Y, Reader JNIST ASD Team. *NIST atomic spectra database (ver. 5.11)*. Gaithersburg, MD: National Institute of Standards and Technology (2023). Available from: <https://physics.nist.gov/asd> (Accessed May 22, 2024).



OPEN ACCESS

EDITED BY

Mario J. Pinheiro,
University of Lisbon, Portugal

REVIEWED BY

Biswajit Sahu,
West Bengal State University, India

*CORRESPONDENCE

Paolo F. Ambrico,
✉ paolofrancesco.ambrico@cnr.it

RECEIVED 26 June 2024

ACCEPTED 13 September 2024

PUBLISHED 09 October 2024

CITATION

Aceto D, Ambrico PF and Esposito F (2024) Air cold plasmas as a new tool for nitrogen fixation in agriculture: underlying mechanisms and current experimental insights.
Front. Phys. 12:1455481.
doi: 10.3389/fphy.2024.1455481

COPYRIGHT

© 2024 Aceto, Ambrico and Esposito. This is an open-access article distributed under the terms of the [Creative Commons Attribution License \(CC BY\)](#). The use, distribution or reproduction in other forums is permitted, provided the original author(s) and the copyright owner(s) are credited and that the original publication in this journal is cited, in accordance with accepted academic practice. No use, distribution or reproduction is permitted which does not comply with these terms.

Air cold plasmas as a new tool for nitrogen fixation in agriculture: underlying mechanisms and current experimental insights

Domenico Aceto, Paolo F. Ambrico* and Fabrizio Esposito

CNR Istituto per la Scienza e Tecnologia dei Plasmi, Bari, Italy

Nitrogen fixation is crucial for plant growth and global agriculture, especially with the projected population growth requiring a significant increase in food production. Traditional nitrogen fixation relies on the Haber-Bosch (H-B) process, which is energy-intensive and environmentally harmful due to greenhouse gas emissions. Emerging technologies, such as cold plasma, offer promising alternatives with lower energy consumption. Cold plasma facilitates reactive nitrogen species generation under ambient conditions, potentially improving the production efficiency of nitrogen oxides (NO_x). However, optimizing cold plasma nitrogen fixation requires a synergy between experimental and theoretical approaches. Accurate input data are essential for refining theoretical models, which can then guide the design of more efficient processes. This integrated approach can leverage renewable energy, operate on smaller scales, and minimize environmental impacts, making cold plasma a sustainable solution for future nitrogen fixation needs.

KEYWORDS

nitrogen fixation, air plasma, atmospheric pressure cold plasmas, Zel'dovich reaction, modelling

1 Introduction

Nitrogen (N) is essential for plant development, as it is needed for synthesizing proteins and nucleic acids. Nitrogen fixation is a crucial process for providing these compounds. This is a big issue considering an expected population of nine billion people by 2050 that would require an expansion of global agricultural output by 70%–100% [1].

The established synthesis technology for N fertilizers relies strongly on the Haber-Bosch (H-B) process, to convert N_2 gas into biologically available ammonia (NH_3). The current industrial production of reactive N (RNS) is 120 teragrams per year (Tg yr^{-1}), twice the amount from all-natural land processes (63 Tg yr^{-1} [2]). Fertilizer production consumes about 80% of this RNS [3], and is essential for sustaining half of the global human population [4]. However, the efficiency of RNS utilization is poor, with 50%–70% lost to the

Abbreviations: DBD, Dielectric Barrier Discharge; EC, Energy Consumption; e-M, electron-Molecules collisions; FHO, forced harmonic oscillator; GA, Gliding Arc; H-B, Haber Bosch; MJ/mol N, MegaJoules consumed per mole of Nitrogen (fixed) produced; N, nitrogen atoms; NO_x , Nitric Oxides; PAW, Plasma Activated Water; QCT, quasi-classical modeling methods; RNS, Reactive Nitrogen Species; ROS, Reactive Oxygen Species; SC, semiclassical modeling methods; Tg yr^{-1} , Tera grams per year; VT, Vibration-to-Translation energy transfer; VV, Vibration-to-Vibration energy transfer.

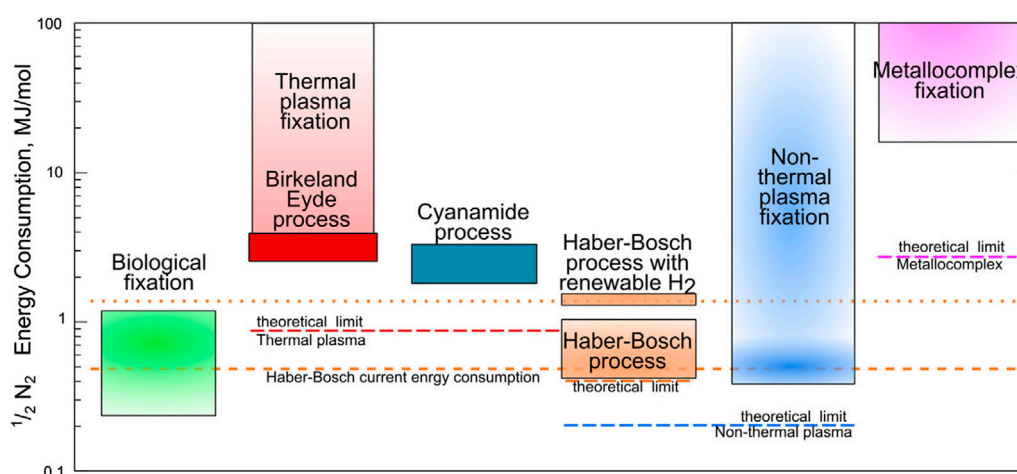


FIGURE 1
Comparison of the energy consumption for nitrogen fixation with different methods (Reprinted from [15] with permission of Elsevier B.V.).

environment [5, 6]. The accumulation of excess RNS, such as NH_3 , nitrous oxide (N_2O), and nitrate (NO_3^-), in the atmosphere and ecosystems leads to serious environmental and climate issues [2, 3, 7, 8]. These issues encompass alterations in ecosystem productivity and biodiversity [9, 10], the eutrophication and nitrate pollution of freshwater [10, 11], the deterioration of ozone and air quality [11, 12], and the exacerbation of climate change due to greenhouse gases [3, 7].

At the beginning of the 20th century, the fertilizers produced by H-B substituted the non-renewable mineral ones. Nowadays, the H-B process drains more than 1% of the globally produced energy, releasing more than 3×10^{11} kg year⁻¹ of CO_2 , and requiring about 2% of the global natural gas production, to synthesize the needed hydrogen for NH_3 synthesis [13–15]. Therefore, while H-B processes should be made more sustainable [16], greener strategies in nitrogen fixation should also be pursued. In Figure 1 the energy consumption in terms of MJ consumed per N mole of various processes is represented together with the calculated theoretical limits. Among the explored processes for nitrogen fixation, the most efficient is still the H-B, surpassed only by biological nitrogen fixation. Other industrial-scale processes adopted in the past like the thermal plasma-based Birkeland-Eyde, or the Frank-Caro process leading to calcium cyanamide are far more energy-consuming. Metallo-complexes fixation currently has poor efficiency and a theoretical limit far from the H-B.

Since the 1970s, plasma technologies have been pointed to as a possible alternative for large-scale NH_3 production, in the presence of a catalyst or not. Different plasma sources have been proposed for ammonia synthesis, such as glow discharge, gliding arc, microwave, radio frequency, pulsed discharges, and dielectric barrier discharges. The current reported energy yield for the plasma and catalytic materials process is ranging from 1.71–58.8 MJ/mol N [17–33]. Best performances are achieved by pulsed discharge systems and dielectric barrier discharge reactors at atmospheric pressure that facilitates the integration of catalytic materials.

Novel approaches based on Cold Plasma are currently being extensively investigated and promise versatile applications. These innovative methods entail subjecting agricultural systems to non-

thermal plasma, generating reactive species such as reactive oxygen species (ROS) and reactive nitrogen species (RNS) [34, 35]. One crucial allure of these technologies is the achievement of lower energy consumption (EC) than the H-B process, according to theoretical calculations [36]. It is our opinion, that the main advantage of cold plasma technology is related to their intrinsic non-thermal nature and the energy transfer processes involved in reactive species productions. We will try to give our opinion on the elementary processes leading to nitrogen oxide production and their potential impact on the agrifood industry of this technology reporting briefly on the current status of the ongoing research.

2 Plasma nitrogen fixation in dry air

Direct, efficient production of NO_x from air, at variance with current indirect production by NH_3 synthesis, using H-B process, would open plenty of possibilities in recycling. NO_x allows the direct synthesis of nitric acid (HNO_3) [37], which can be used for chemical fertilizers production, but also the fast maturation of natural fertilizers from livestock slurry, an environment-friendly process, which is currently being developed [38].

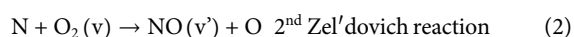
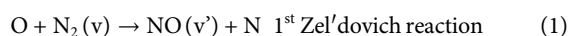
2.1 Plasma production of NO_x from air: the mechanism

Plasma production of NO_x from air, such as in lightning, by a thermal plasma was industrially realized by the Birkeland-Eyde process. The NO_x production efficiency of a few percent limits its application to a handful of special uses thus making the process not competitive with current industrial processes.

An energy analysis [15, 36] on the use of cold plasma can however envisage a completely different development, with a theoretical maximum limit of 35% efficiency [36], exceeding the current total efficiency of industrial NO_x production [37].

Cold plasma behavior is complex and influenced by numerous parameters and conditions. For instance, electron temperatures

might reach 10000 K while gas remains at 400 K and molecular vibrational temperature at 3000 K [39]. To properly study the kinetics of a cold plasma, therefore we need to know vibrational *state-to-state* processes involving, at least, electron-molecule (e-M) and molecule-molecule collisions. e-M processes transfer electron energy from the discharge to the internal energy, mostly vibrational, of air molecular species. Then, by molecular collisions and vibration-to-vibration (VV) exchange processes, as in $N_2(v_1) + N_2(v_2) \rightarrow N_2(v_1-1) + N_2(v_2+1)$, a significant fraction of molecules increases its vibrational energy [36, 40], provided low-lying levels are continuously replenished by e-M processes. When vibrational energy reaches oxygen dissociation energy ($\approx 5\text{eV}$), O atoms can initiate the Zel'dovich chain (Equations 1, 2), while N_2 remains mostly undissociated.



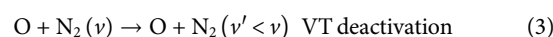
This is favorable for energy efficiency because it is more efficient to make N_2 react rather than obtaining N atoms from dissociation. For the same reasons processes involving excited electronic states of N_2 and O_2 should be avoided. The ideal Zel'dovich reaction path of Equations 1, 2 is thought to be the most efficient one [36, 40]. However, many other concurrent collision processes take place, such as, for example, vibration-to-translation (VT) deactivation processes (as in $N + O_2(v) \rightarrow N + O_2(v-1)$); the reverse of the Zel'dovich (Equation 1) reaction; plasma-walls vibrational deactivation collision; NO dissociation/reaction by collisions with other air species.

2.2 Cold plasma production of NOx from air: coupling modeling with experiment issue

The non-equilibrium nature of cold plasmas requires a guiding model to design experiments to investigate the possible reaction pathways occurring in the discharge systems. Therefore, chemical kinetics modelling is crucial in this context, provided the data used as input for this modelling is accurate and detailed. Up to now, no one has been able to replicate the predictions reported in Ref. [36] (except for [41]) by detailed modelling. Indeed, the main problem for modelling is the extremely approximate data taken as input. For example, the first Zel'dovich reaction Equation 1, i.e., the core of the NO production mechanism from air, has been known for many years only by empirical models. The model of Gordiets [42] considered the possibility of reaction once the reaction threshold has been reached, which occurs, at room temperature, when N_2 is at least in $v = 12$ state. More recent studies [43–46] contemplating the adiabatic path to reaction on the triplet potential energy surfaces (PES), showed a much more complex situation. In [45] a complete compilation of vibrationally detailed data (i.e., considering the whole vibrational ladder of reagents and products) concerning the adiabatic path has been calculated, with an excellent agreement with the experimental thermal rate. The differences in results obtained from the simple models adopted in the past and still used in the literature are huge (orders of magnitude, see [45, 47]), particularly in the energy region between vibrational levels $v = 12$ –30 where most of the reaction occurs. Another aspect of great

impact is the determination of the final NO vibration in reaction (Equation 1). In [48] a comparison of a kinetic scheme in air is presented using the same set of rate coefficients calculated in [45, 46, 49, 50], but considering state-to-state or only initially state-selected rate coefficients in (1). The results of N and NO production are qualitatively different, stressing the importance of accurate and detailed molecular dynamics calculations as input of the kinetics.

With a higher probability than reaction (Equation 1), the VT deactivation:

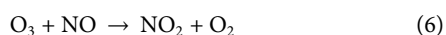
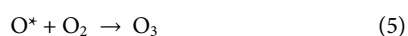


can take place starting from the same collision. This is a big issue for nitrogen fixation because it depletes the N_2 vibrational population essential for good efficiency in Equation 1. In fact, in cold plasmas, the strongly endothermic reaction (Equation 1) should be preferentially activated by vibrational pumping of molecular species involved rather than by heating, in order to keep the rate of VT processes like (Equation 3) low. However, the accurate rate value of the process (Equation 3) for $v > 1$ has remained unknown for decades, with only the $v = 1$ to $v' = 0$ rate coefficient known experimentally. The only known result, however, was also dramatically different (even 20 orders of magnitude at 300 K) from theoretical results obtained by quasi-classical (QCT), semiclassical (SC), and quantum methods [45, 51, 52]. Only in very recent years the problem has been solved [52, 53], by recognizing the fundamental role of vibronic transitions of the collisional system and calculating other transitions from $v \neq 1$. Indeed, process (Equation 3) shows even other issues when studied theoretically. The methods used for studying molecular collisions of heavy particles can be QCT, SC, or quantum methods on a scale of increasing accuracy and computational cost. In studies on air species aiming to create vibrationally detailed databases, using accurate quantum methods is simply unfeasible. While these methods are essential for establishing benchmarks (as demonstrated in [44]), they are unsuitable for the comprehensive calculations necessary for kinetic modeling. Semiclassical and, first, QCT must be used instead, requiring huge computational resources. However, some processes are difficult to treat even with these simpler methods, due to their specific limitations. In particular, the process in Equation 3 cannot be reproduced theoretically by QCT at low total energy [54]. However, at collision energy values comparable to or higher than the reaction (Equation 1) threshold, QCT becomes suitable for accurate results for the inelastic process (Equation 3). Deactivation processes are surely present in all collision processes of interest in air plasmas. Most of the VT data used in current kinetic models of air plasmas have been calculated by methods based on a forced harmonic oscillator (FHO) semiclassical model [55] or by QCT [56, 57]. However, FHO is designed to treat non-reactive cases at not very high total energy, while QCT tends to be more accurate at higher energy, especially over the threshold for reactions originating from the collisions considered [46]. Merging of different semi- and quasi-classical methods for cold plasma modeling input data calculation is therefore desirable. This merging of methods could be successfully applied potentially to *all* collisional systems involving air species of interest in this context, such as N_2 - O_2 , from which O atoms production depends, and research is active in this sense [39, 46, 54].

Another important collisional system is of course the second Zel'dovich reaction. Even in this case, recent results in [49] are quite complete, accurate, and more suited for nitrogen fixation studies than older studies on this topic [58].

2.3 Current experimental approaches for nitrogen fixation

In most air plasmas, the Zel'dovich reactions (Equations 1, 2) leading to NO productions can further proceed towards NO₂, resulting in a gas-phase mixture of nitrogen oxides referred to as NO_x. These reactions involve ozone or oxygen radicals oxidizing NO (Equations 4–6):



Following earlier studies on thermal plasma (i.e., electric arc exploiting the Birkeland-Eyde reaction), other plasma types and reactors have been examined for NO_x production. This has led to an overabundance of possible sources, making any comparison between different methodologies quite complicated, as no standard reactors or even measurements techniques for different parameters are widely accepted. Energy consumption, for example, is dependent on power and NO_x concentration. NO_x concentrations can be determined via a plethora of methods: Fourier-transform infrared spectroscopy, mass spectroscopy, chemiluminescence, ion chromatography, as well as a nondispersive infra-red sensor with an ultra-violet sensor through a gas analyzer, *in situ* laser induced fluorescence, laser Raman spectroscopy, optical absorption. Power can be calculated by the Lissajous method [59, 60], numerically integrating the product of the voltage and current and multiplying by the frequency, or by calorimetric methods by multiplying air density, gas temperature, heat capacity of the air, and volume [61]. Moreover, for a real industrial application, the total power should include all the energy consumption in the production pipeline, such as gas flow system and storage, power sources absorption, etc., that are not always considered.

A great number of plasma sources have been investigated in the context of nitrogen fixation into NO_x. Gliding arc (GA) reactors are promising for gas conversion, achieving efficient NO_x production with reduced energy. GA plasmas feature a reduced electric field of less than 100 Td and electron energies around 1 eV, ideal for the vibrational excitation of gas molecules. Reactor optimizations, including controlling pressure, specific energy input, and reactor designs, enhance NO_x yield and energy efficiency across various setups (EC 0.67–4.8 MJ/mol N) [62–69].

NO_x generation in transient spark discharge, which involves non-thermal and thermal plasma phases, has also been achieved. Although a limited volume, which means that only a portion of the N₂ gas is exposed to the plasma, innovations like floating electrodes could improve NO_x yield and efficiency, reducing energy needs (EC 1.9–40 MJ/mol N) [62, 70–74].

Dielectric Barrier Discharge (DBD) systems could be of great interest for the great versatility they offer in reactor design and for the possibility to operate them at atmospheric pressure. For

example, other than simple cylindrical, plug-flow-like reactors, it is possible to incorporate water (for nitrogen fixation into NO₃) or other materials in the interelectronic gap. Packed-bed DBD reactors with various catalysts improve NO_x yield, resulting in higher energy costs. Promising catalytic materials include γ-Al₂O₃ and Al₂O₃-supported metallic nanoparticles (EC 17–33 MJ/mol N) [62, 75–77].

Low-pressure microwave plasmas achieved the best energy consumption and NO yield. However, past claims (EC = 0.28 MJ/mol N [41]) are unconfirmed. Energy use excludes reactor cooling and vacuum needs, that eventually add up and make total consumption higher (EC 0.84–3.76 MJ/mol N) [78, 79].

NO_x formation by plasma jets in air or N₂ reacting with water results in NO₂ and NO₃ due to oxygen presence. Key factors affecting NO_x production include gas composition, flow rate, and temperature. Studies show reducing the flow rate and increasing oxygen content boosts NO_x concentration, while lower gas temperature and electric field enhance production efficiency (EC 0.42–3.6 MJ/mol N) [80–89].

From the existing literature, it can be concluded that efficient NO_x production in plasma systems relies on optimizing reduced electric fields to favor vibrational excitation (enhancing Zel'dovich reactions), controlling gas temperature to prevent NO reconversion, and utilizing appropriate catalysts. Key parameters include voltage, electric field strength, gas composition and flow rates, and reactor design.

All the reported results show that the current technology is still far from theoretical limits, but is closing the gap between H-B processes.

3 Future perspective

In countries where agriculture is significant, environmentally sustainable HNO₃ production could serve as an important power-to-chemicals channel, accumulating excess renewable power into valuable chemicals using cold plasma reactors operating at room temperature and atmospheric pressure, thus requiring lower investments than an H-B plant [37]: this would be vital to boosting agriculture in low-income countries. Moreover, a diffused grid energy/fertilizer production usage would be more resilient to natural disasters and armed conflicts than centralized power production and fertilizer import, avoiding direct and indirect related import, transportation, and distribution costs. In our opinion the most viable possible solutions are currently two: production of hybrid fertilizer from slurry and plasma-activated water.

3.1 Hybrid fertilizers

Efficient air plasma production of NO_x offers significant advantages for the fertilizer industry, allowing direct synthesis of nitric acid (HNO₃) [37], for chemical and hybrid fertilizers. Acidification of livestock slurry process has been used in agriculture [90] since 2003, but the novelty is the easy-to-manage *direct* fertilizer production by air plasma [38]. The latter process facilitates easy production of fertilizers from slurry and air, with benefits including recycling livestock wastewater, eliminating

inorganic feedstock, preserving natural manure components, shorter organic fertilizer production times, avoiding stocking dangerous acids, reducing greenhouse gases (i.e., N_2O and CH_4), and preventing ammonia emissions. It supports precision agriculture [91], minimizes environmental losses, and can also be applied in principle to human wastewater. Preliminary experiments in the fields show that this “hybrid” (artificial/natural) manure can be extremely effective [92].

3.2 Plasma-activated water

Concurrently, alongside advancements in low-temperature plasma applications, plasma-activated water (PAW) has surfaced as a cutting-edge tool in modern agriculture, with the potential to enhance crop productivity and mitigate industry challenges [93–98]. PAW production involves subjecting water to non-thermal plasma, generating reactive species such as ROS and RNS. The physicochemical alterations induced by plasma treatment on water can be tailored for diverse applications [99]. PAW reactive species elicit beneficial effects on plants, inducing physiological and biochemical changes conducive to growth and stress tolerance [97, 98, 100]. PAW offers a sustainable and eco-friendly alternative to conventional chemical fertilizers and pesticides, applicable in watering crops, seed soaking, and foliage spraying.

4 Conclusion

Concerning future developments in nitrogen fixation, cold plasma seems to be the only promising and industrially scalable method because its use could further lower the EC of the process, based on thermodynamic calculations. The highest energy efficiency is expected when vibrationally excited nitrogen molecules are formed in sufficient quantities, the temperature of the resulting gases is not high enough to decompose the reaction products, and the reaction is channeled into a particular reaction pathway. Atmospheric pressure cold plasma nitrogen fixation has many environmental advantages as it requires only electricity, air, and, depending on the application, wastewater (hybrid fertilizers) or water (PAW) as feedstock. Contrary to large-scale high-pressure ammonia synthesis plants, plasma nitrogen fixation may be performed on a much smaller scale, locally producing the fertilizers and eliminating the problems associated with fertilizers' transportation and storage. Moreover, such plants can be ideally powered by renewable energy sources, further reducing the environmental impact of fertilizer production.

However, detailed modeling tools are needed to maximize cold plasma nitrogen fixation efficiency. An essential step is establishing

an efficient dialogue between practical and theoretical experiments: accurate data sets should be fed to models so that they could shed light on the mechanism pathways that should be preferred to optimize the reaction.

Data availability statement

The original contributions presented in the study are included in the article/supplementary material, further inquiries can be directed to the corresponding author.

Author contributions

DA: Data curation, Writing - review and editing, Writing - original draft, Validation, Conceptualization. PA: Funding acquisition, Data curation, Writing - review and editing, Writing - original draft, Validation, Supervision, Conceptualization. FE: Writing - review and editing, Writing - original draft, Validation, Supervision, Conceptualization.

Funding

The author(s) declare that financial support was received for the research, authorship, and/or publication of this article. European Cooperation in Science and Technology, CA19110; Regione Puglia, Riparti - POC PUGLIA FESRT-FSE 2014/2020.

Conflict of interest

The authors declare that the research was conducted in the absence of any commercial or financial relationships that could be construed as a potential conflict of interest.

The author(s) declared that they were an editorial board member of Frontiers, at the time of submission. This had no impact on the peer review process and the final decision.

Publisher's note

All claims expressed in this article are solely those of the authors and do not necessarily represent those of their affiliated organizations, or those of the publisher, the editors and the reviewers. Any product that may be evaluated in this article, or claim that may be made by its manufacturer, is not guaranteed or endorsed by the publisher.

References

1. Godfray HCJ, Beddington JR, Crute IR, Haddad L, Lawrence D, Muir AF, et al. Food security: the challenge of feeding 9 billion people. *Science* (1979) (2010) 327: 812–818. doi:10.1126/science.1185383
2. Fowler D, Coyle M, Skiba U, Sutton MA, Cape JN, Reis S, et al. The global nitrogen cycle in the twenty-first century. *Phil Trans R Soc B: Biol Sci* (2013) 368:20130164. doi:10.1098/rstb.2013.0164
3. Galloway JN, Townsend AR, Erisman JW, Bekunda M, Cai Z, Freney JR, et al. Transformation of the nitrogen cycle: recent trends, questions, and potential solutions. *Science* (1979) 2008:889–92. doi:10.1126/science.1136674
4. Erisman JW, Sutton MA, Galloway J, Klimont Z, Winiwarter W. How a century of ammonia synthesis changed the world. *Nat Geosci* (2008) 1:636–9. doi:10.1038/ngeo325

5. Cassman KG, Dobermann A, Walters DT. Agroecosystems, nitrogen-use efficiency, and nitrogen management. *Ambio* (2002) 31:132–40. doi:10.1579/0044-7447-31.2.132
6. Ladha JK, Pathak H, Krupnik TJ, Six J, van Kessel C. Efficiency of fertilizer nitrogen in cereal production: retrospects and prospects. *Adv Agron* (2005) 87. doi:10.1016/S0065-2113(05)87003-8
7. Erisman JW, Galloway J, Seitzinger S, Bleeker A, Butterbach-Bahl K. Reactive nitrogen in the environment and its effect on climate change. *Curr Opin Environ Sustain* (2011) 3:281–90. doi:10.1016/j.cosust.2011.08.012
8. Schlesinger WH. On the fate of anthropogenic nitrogen. *Proc Natl Acad Sci U S A* (2009) 106:203–8. doi:10.1073/pnas.0810193105
9. Tilman D, Isbell F. Biodiversity: recovery as nitrogen declines. *Nature* (2015) 528. doi:10.1038/nature16320
10. Vitousek PM, Aber JD, Howarth RW, Likens GE, Matson PA, Schindler DW, et al. Human alteration of the global nitrogen cycle: sources and consequences. *Ecol Appl* (1997) 7:737–50. doi:10.1890/1051-0761(1997)007[0737:HAOTGN]2.0.CO;2
11. Townsend AR, Howarth RW, Bazzaz FA, Booth MS, Cleveland CC, Collinge SK, et al. Human health effects of a changing global nitrogen cycle. *Front Ecol Environ* (2003) 1:240–6. doi:10.1890/1540-9295(2003)001[0240:hheoac]2.0.co;2
12. Ravishankara AR, Daniel JS, Portmann RW. Nitrous oxide (N₂O): the dominant ozone-depleting substance emitted in the 21st century. *Science* (1979) 209:123–5. doi:10.1126/science.1176985
13. Van Der Ham CJM, Koper MTM, Hetterscheid DGH. Challenges in reduction of dinitrogen by proton and electron transfer. *Chem Soc Rev* (2014) 43:5183–91. doi:10.1039/c4cs00085d
14. Tanabe Y, Nishibayashi Y. Developing more sustainable processes for ammonia synthesis. *Coord Chem Rev* (2013) 257:2551–64. doi:10.1016/j.ccr.2013.02.010
15. Cherkasov N, Ibadon AO, Fitzpatrick P. A review of the existing and alternative methods for greener nitrogen fixation. *Chem Eng Process Process Intensification* (2015) 90:24–33. doi:10.1016/j.cep.2015.02.004
16. Smith C, Hill AK, Torrente-Murciano L. Current and future role of Haber-Bosch ammonia in a carbon-free energy landscape. *Energy Environ Sci* (2020) 13:331–44. doi:10.1039/c9ee02873k
17. Shah J, Wu T, Lucero J, Carreon MA, Carreon ML. Nonthermal plasma synthesis of ammonia over Ni-MOF-74. *ACS Sustain Chem Eng* (2019) 7:377–83. doi:10.1021/acssuschemeng.8b03705
18. Shah JR, Harrison JM, Carreon ML. Ammonia plasma-catalytic synthesis using low melting point alloys. *Catalysts* (2018) 8:437. doi:10.3390/catal8100437
19. Hu J, Wildfire C, Stiegman AE, Dagle RA, Shekhawat D, Abdelsayed V, et al. Microwave-driven heterogeneous catalysis for activation of dinitrogen to ammonia under atmospheric pressure. *Chem Eng J* (2020) 397:125388. doi:10.1016/j.cej.2020.125388
20. Brandenburg R, Bogaerts A, Bongers W, Fridman A, Fridman G, Locke BR, et al. White paper on the future of plasma science in environment, for gas conversion and agriculture. *Plasma Process Polym* (2019) 16. doi:10.1002/ppap.201700238
21. Kim M, Biswas S, Nava G, Wong BM, Mangolini L. Reduced energy cost of ammonia synthesis via RF plasma pulsing. *ACS Sustain Chem Eng* (2022) 10:15135–47. doi:10.1021/acssuschemeng.2c04593
22. Peng P, Chen P, Addy M, Cheng Y, Anderson E, Zhou N, et al. Atmospheric plasma-assisted ammonia synthesis enhanced via synergistic catalytic absorption. *ACS Sustain Chem Eng* (2019) 7:100–4. doi:10.1021/acssuschemeng.8b03887
23. Hong J, Prawer S, Murphy AB. Plasma catalysis as an alternative route for ammonia production: status, mechanisms, and prospects for progress. *ACS Sustain Chem Eng* (2018) 6:15–31. doi:10.1021/acssuschemeng.7b02381
24. Iwamoto M, Akiyama M, Aihara K, Deguchi T. Ammonia synthesis on wool-like Au, Pt, Pd, Ag, or Cu electrode catalysts in nonthermal atmospheric-pressure plasma of N₂ and H₂. *ACS Catal* (2017) 7:6924–9. doi:10.1021/acscatal.7b01624
25. Peng P, Li Y, Cheng Y, Deng S, Chen P, Ruan R. Atmospheric pressure ammonia synthesis using non-thermal plasma assisted catalysis. *Plasma Chem Plasma Process* (2016) 36:1201–10. doi:10.1007/s11090-016-9713-6
26. Peng P, Cheng Y, Hatzebeller R, Addy M, Zhou N, Schiappacase C, et al. Ru-based multifunctional mesoporous catalyst for low-pressure and non-thermal plasma synthesis of ammonia. *Int J Hydrogen Energ* (2017) 42:19056–66. doi:10.1016/j.ijhydene.2017.06.118
27. Li S, van Raak T, Gallucci F. Investigating the operation parameters for ammonia synthesis in dielectric barrier discharge reactors. *J Phys D Appl Phys* (2020) 53:014008. doi:10.1088/1361-6463/ab4b37
28. Zhu X, Hu X, Wu X, Cai Y, Zhang H, Tu X. Ammonia synthesis over γ -Al₂O₃ pellets in a packed-bed dielectric barrier discharge reactor. *J Phys D Appl Phys* (2020) 53:164002. doi:10.1088/1361-6463/ab6cd1
29. Xie Q, Zhuge S, Song X, Lu M, Yu F, Ruan R, et al. Non-thermal atmospheric plasma synthesis of ammonia in a DBD reactor packed with various catalysts. *J Phys D Appl Phys* (2020) 53:064002. doi:10.1088/1361-6463/ab57e5
30. Liu C, Brown NMD, Meenan BJ. Uniformity analysis of dielectric barrier discharge (DBD) processed polyethylene terephthalate (PET) surface. *Appl Surf Sci* (2006) 252:2297–310. doi:10.1016/j.apsusc.2005.04.016
31. Zeng X, Zhang S, Liu Y, Hu X, Ostrikov KK, Shao T. Energy-efficient pathways for pulsed-plasma-activated sustainable ammonia synthesis. *ACS Sustain Chem Eng* (2023) 11:1110–20. doi:10.1021/acssuschemeng.2c06259
32. Bai M, Zhang Z, Bai M, Bai X, Gao H. Synthesis of ammonia using CH₄/N₂ plasmas based on micro-gap discharge under environmentally friendly condition. *Plasma Chem Plasma Process* (2008) 28:405–14. doi:10.1007/s11090-008-9132-4
33. Ma Y, Tian Y, Zeng Y, Tu X. Plasma synthesis of ammonia in a tangled wire dielectric barrier discharge reactor: effect of electrode materials. *J Energy Inst* (2021) 99:137–44. doi:10.1016/j.joei.2021.09.002
34. Ambrico PF, Šimek M, Morano M, De Miccolis Angelini RM, Minafra A, Trotti P, et al. Reduction of microbial contamination and improvement of germination of sweet basil (*Ocimum basilicum* L.) seeds via surface dielectric barrier discharge. *J Phys D Appl Phys* (2017) 50:305401. doi:10.1088/1361-6463/aa77c8
35. Ambrico PF, Šimek M, Ambrico M, Morano M, Prukner V, Minafra A, et al. On the air atmospheric pressure plasma treatment effect on the physiology, germination and seedlings of basil seeds. *J Phys D Appl Phys* (2020) 53:104001. doi:10.1088/1361-6463/ab5b1b
36. Rusanov VD, Fridman AA, Sholin GV. The physics of a chemically active plasma with nonequilibrium vibrational excitation of molecules. *Soviet Phys Uspekhi* (1981) 24:447–74. doi:10.1070/PU1981v024n06ABEH004884
37. Rouwenhorst KHR, Jaldari F, Bogaerts A, Lefferts L. From the Birkeland–Eyde process towards energy-efficient plasma-based NO_x synthesis: a techno-economic analysis. *Energy Environ Sci* (2021) 14:2520–34. doi:10.1039/D0EE03763J
38. Ingels R, Graves DB. Improving the efficiency of organic fertilizer and nitrogen use via air plasma and distributed renewable energy. *Plasma Med* (2015) 5:257–70. doi:10.1615/PlasmaMed.2016015763
39. Capitelli M, Celiberto R, Colonna G, Esposito F, Gorse C, Hassouni K, et al. *Fundamental aspects of plasma chemical physics*. New York, NY: Springer New York (2016). doi:10.1007/978-1-4419-8185-1
40. Fridman A. *Plasma chemistry*. Cambridge: Cambridge University Press (2008). doi:10.1017/CBO9780511546075
41. Azizov R, Zhivotov V, Krotov M, Rusanov V, Tarasov Y, Fridman A. Synthesis of nitrogen oxides in a nonequilibrium microwave discharge under electron-cyclotron resonance conditions. *Khimiya Vysok Energii* (1980) 14:366–8.
42. Gordiets BF, Ferreira CM, Guerra VL, Loureiro JMAH, Nahorny J, Pagnon D, et al. Kinetic model of a low-pressure N₂–O₂ flowing glow discharge. *IEEE Trans Plasma Sci* (1995) 23:750–68. doi:10.1109/27.467998
43. Gamallo P, González M, Sayós R. *Ab initio* derived analytical fits of the two lowest triplet potential energy surfaces and theoretical rate constants for the N(4S)+NO(X 2Π) system. *J Chem Phys* (2003) 119:2545–56. doi:10.1063/1.1586251
44. Akpınar S, Armenise I, Defazio P, Esposito F, Gamallo P, Petrongolo C, et al. Quantum mechanical and quasiclassical Born–Oppenheimer dynamics of the reaction N₂ on the N₂O and surfaces. *Chem Phys* (2012) 398:81–9. doi:10.1016/j.chemphys.2011.05.005
45. Esposito F, Armenise I. Reactive, inelastic, and dissociation processes in collisions of atomic oxygen with molecular nitrogen. *J Phys Chem A* (2017) 121:6211–9. doi:10.1021/acs.jpca.7b04442
46. Esposito F. On the relevance of accurate input data for vibrational kinetics in air cold plasmas: the case of nitrogen fixation. *Plasma Sour Sci Technol* (2022) 31:094010. doi:10.1088/1361-6595/ac9082
47. Armenise I, Esposito F. N₂, O₂, NO state-to-state vibrational kinetics in hypersonic boundary layers: the problem of rescaling rate coefficients to uniform vibrational ladders. *Chem Phys* (2015) 446:30–46. doi:10.1016/j.chemphys.2014.11.004
48. Armenise I. Low temperature state-to-state vibrational kinetics of O + N₂(v) and N + O₂(v) collisions. *Chem Phys* (2023) 571:111937. doi:10.1016/j.chemphys.2023.111937
49. Esposito F, Armenise I. Reactive, inelastic, and dissociation processes in collisions of atomic nitrogen with molecular oxygen. *J Phys Chem A* (2021) 125:3953–64. doi:10.1021/acs.jpca.0c09999
50. Armenise I, Esposito F. N + O₂(v) collisions: reactive, inelastic and dissociation rates for state-to-state vibrational kinetic models. *Chem Phys* (2021) 551:111325. doi:10.1016/j.chemphys.2021.111325
51. Ivanov MV, Schinke R, Mcbane GC. Theoretical investigation of vibrational relaxation of NO⁺(²Π), O, and N in collisions with O⁺(³P). *Mol Phys* (2007) 105:1183–91. doi:10.1080/00268970701288087
52. Hong Q, Bartolomei M, Esposito F, Coletti C, Sun Q, Pirani F. Reconciling experimental and theoretical vibrational deactivation in low-energy O + N₂ collisions. *Phys Chem Chem Phys* (2021) 23:15475–9. doi:10.1039/D1CP01976G
53. Hong Q, Bartolomei M, Pirani F, Esposito F, Sun Q, Coletti C. Vibrational deactivation in O⁺(³P) + N₂ collisions: from an old problem towards its solution. *Plasma Sour Sci Technol* (2022) 31:084008. doi:10.1088/1361-6595/ac86f3
54. Esposito F. Reactivity, relaxation and dissociation of vibrationally excited molecules in low-temperature plasma modeling. *Rend Lincei Sci Fis Nat* (2019) 30:57–66. doi:10.1007/s12210-019-00778-9

55. Lino da Silva M, Loureiro J, Guerra V. A multiquantum dataset for vibrational excitation and dissociation in high-temperature O₂-O₂ collisions. *Chem Phys Lett* (2012) 531:28–33. doi:10.1016/j.cplett.2012.01.074
56. Esposito F, Armenise I, Capitelli M. N–N₂ state to state vibrational-relaxation and dissociation rates based on quasiclassical calculations. *Chem Phys* (2006) 331:1–8. doi:10.1016/j.chemphys.2006.09.035
57. Esposito F, Armenise I, Capitta G, Capitelli M. O–O₂ state-to-state vibrational relaxation and dissociation rates based on quasiclassical calculations. *Chem Phys* (2008) 351:91–8. doi:10.1016/j.chemphys.2008.04.004
58. Bose D, Candler GV. Thermal rate constants of the O₂+N→NO+O reaction based on the A₂' and A₄' potential-energy surfaces. *J Chem Phys* (1997) 107:6136–45. doi:10.1063/1.475132
59. Pipa AV, Koskulics J, Brandenburg R, Hoder T. The simplest equivalent circuit of a pulsed dielectric barrier discharge and the determination of the gas gap charge transfer. *Rev Scientific Instr* (2012) 83:115112. doi:10.1063/1.4767637
60. Pipa AV, Koskulics J, Brandenburg R, Hoder T. Erratum: “The simplest equivalent circuit of a pulsed dielectric barrier discharge and the determination of the gas gap charge transfer”. *Rev Sci Instrum* (2012) 83:115112. doi:10.1063/1.4767637
61. Archambault-Caron M, Gagnon H, Nisol B, Piyakis K, Wertheimer MR. Precise energy and temperature measurements in dielectric barrier discharges at atmospheric pressure. *Plasma Sour Sci Technol* (2015) 24:045004. doi:10.1088/0963-0252/24/4/045004
62. Pei X, Gidon D, Yang YJ, Xiong Z, Graves DB. Reducing energy cost of NO_x production in air plasmas. *Chem Eng J* (2019) 362:217–28. doi:10.1016/j.cej.2019.01.011
63. Vervloessem E, Aghaei M, Jaldali F, Hafezkhiani B, Bogaerts A. Plasma-based N₂ fixation into NO_x: insights from modeling toward optimum yields and energy costs in a Gliding Arc plasmatron. *ACS Sustain Chem Eng* (2020) 8:9711–20. doi:10.1021/acssuschemeng.0c01815
64. Patil BS, Peeters FJJ, van Rooij GJ, Medrano JA, Gallucci F, Lang J, et al. Plasma assisted nitrogen oxide production from air: using pulsed powered gliding arc reactor for a containerized plant. *AIChE J* (2018) 64:526–37. doi:10.1002/aic.15922
65. Wang W, Patil B, Heijkers S, Hessel V, Bogaerts A. Nitrogen fixation by Gliding Arc plasma: better insight by chemical kinetics modelling. *ChemSusChem* (2017) 10:2145–57. doi:10.1002/cssc.201700095
66. Tsonev I, O'Modhrain C, Bogaerts A, Gorbanev Y. Nitrogen fixation by an arc plasma at elevated pressure to increase the energy efficiency and production rate of NO_x. *ACS Sustain Chem Eng* (2023) 11:1888–97. doi:10.1021/acssuschemeng.2c06357
67. Muzammil I, Lee DH, Dinh DK, Kang H, Roh SA, Kim Y-N, et al. A novel energy efficient path for nitrogen fixation using a non-thermal arc. *RSC Adv* (2021) 11:12729–38. doi:10.1039/D1RA01357B
68. Chen H, Wu A, Mathieu S, Gao P, Li X, Xu BZ, et al. Highly efficient nitrogen fixation enabled by an atmospheric pressure rotating gliding arc. *Plasma Process Polym* (2021) 18:18. doi:10.1002/ppap.202000200
69. Van Alphen S, Ahmadi Eshtehardi H, O'Modhrain C, Bogaerts J, Van Poyer H, Creel J, et al. Effusion nozzle for energy-efficient NO_x production in a rotating gliding arc plasma reactor. *Chem Eng J* (2022) 443:136529. doi:10.1016/j.cej.2022.136529
70. Rehbein N, Cooray V. NO production in spark and corona discharges. *J Electrostat* (2001) 51–52:333–9. doi:10.1016/S0304-3886(01)00115-2
71. Janda M, Martišovič V, Hensel K, Machala Z. Generation of antimicrobial NO_x by atmospheric air transient spark discharge. *Plasma Chem Plasma Process* (2016) 36:767–81. doi:10.1007/s11090-016-9694-5
72. Pavlovich MJ, Ono T, Galleher C, Curtis B, Clark DS, Machala Z, et al. Air spark-like plasma source for antimicrobial NO_x generation. *J Phys D Appl Phys* (2014) 47:505202. doi:10.1088/0022-3727/47/50/505202
73. Abdelaziz AA, Teramoto Y, Nozaki T, Kim H-H. Toward reducing the energy cost of NO_x formation in a spark discharge reactor through pinpointing its mechanism. *ACS Sustain Chem Eng* (2023) 11:4106–18. doi:10.1021/acssuschemeng.2c06535
74. Zhang S, Zong L, Zeng X, Zhou R, Liu Y, Zhang C, et al. Sustainable nitrogen fixation with nanosecond pulsed spark discharges: insights into free-radical-chain reactions. *Green Chem* (2022) 24:1534–44. doi:10.1039/D1GC03859A
75. Patil BS, Cherkasov N, Lang J, Ibadon AO, Hessel V, Wang Q. Low temperature plasma-catalytic NO_x synthesis in a packed DBD reactor: effect of support materials and supported active metal oxides. *Appl Catal B* (2016) 194:123–33. doi:10.1016/j.apcatb.2016.04.055
76. Roy NC, Maira N, Pattyn C, Remy A, Delplancke M-P, Reniers F. Mechanisms of reducing energy costs for nitrogen fixation using air-based atmospheric DBD plasmas over water in contact with the electrode. *Chem Eng J* (2023) 461:141844. doi:10.1016/j.cej.2023.141844
77. Li Y, Qin L, Wang H-L, Li S-S, Yuan H, Yang D-Z. High efficiency NO_x synthesis and regulation using dielectric barrier discharge in the needle array packed bed reactor. *Chem Eng J* (2023) 461:141922. doi:10.1016/j.cej.2023.141922
78. Mutel B, Dessaux O, Goudmand P. Energy cost improvement of the nitrogen oxides synthesis in a low pressure plasma. *Revue de Physique Appliquée* (1984) 19:461–4. doi:10.1051/rphysap:01984001906046100
79. Kim T, Song S, Kim J, Iwasaki R. Formation of NO_x from air and N₂O₂ mixtures using a nonthermal microwave plasma system. *Jpn J Appl Phys* (2010) 49:126201. doi:10.1143/JJAP.49.126201
80. Peng P, Chen P, Addy M, Cheng Y, Zhang Y, Anderson E, et al. *In situ* plasma-assisted atmospheric nitrogen fixation using water and spray-type jet plasma. *Chem Commun* (2018) 54:2886–9. doi:10.1039/c8cc00697k
81. Gorbanev Y, Vervloessem E, Nikiforov A, Bogaerts A. Nitrogen fixation with water vapor by nonequilibrium plasma: toward sustainable ammonia production. *ACS Sustain Chem Eng* (2020) 8:2996–3004. doi:10.1021/acssuschemeng.9b07849
82. Toth JR, Abuyazid NH, Lacks DJ, Renner JN, Sankaran RM. A plasma-water droplet reactor for process-intensified, continuous nitrogen fixation at atmospheric pressure. *ACS Sustain Chem Eng* (2020) 8:14845–54. doi:10.1021/acssuschemeng.0c04432
83. Peng P, Schiappacasse C, Zhou N, Addy M, Cheng Y, Zhang Y, et al. Plasma *in situ* gas-liquid nitrogen fixation using concentrated high-intensity electric field. *J Phys D Appl Phys* (2019) 52:494001. doi:10.1088/1361-6463/ab3ea6
84. Kumari S, Pishgar S, Schwarting ME, Paxton WF, Spurgeon JM. Synergistic plasma-assisted electrochemical reduction of nitrogen to ammonia. *Chem Commun* (2018) 54:13347–50. doi:10.1039/C8CC07869F
85. Hawtof R, Ghosh S, Guarr E, Xu C, Mohan Sankaran R, Renner JN. Catalyst-free, highly selective synthesis of ammonia from nitrogen and water by a plasma electrolytic system. *Sci Adv* (2019) 5:eaat5778. doi:10.1126/sciadv.aat5778
86. Sakakura T, Uemura S, Hino M, Kiyomatsu S, Takatsui Y, Yamasaki R, et al. Excitation of H₂O at the plasma/water interface by UV irradiation for the elevation of ammonia production. *Green Chem* (2018) 20:627–33. doi:10.1039/C7GC03007J
87. Sakakura T, Murakami N, Takatsui Y, Haruyama T. Nitrogen fixation in a plasma/liquid interfacial reaction and its switching between reduction and oxidation. *The J Phys Chem C* (2020) 124:9401–8. doi:10.1021/acs.jpcc.0c02392
88. Sakakura T, Murakami N, Takatsui Y, Morimoto M, Haruyama T. Contribution of discharge excited atomic N, N²*, and N²+ to a plasma/liquid interfacial reaction as suggested by quantitative analysis. *ChemPhysChem* (2019) 20:1467–74. doi:10.1002/cphc.201900212
89. Haruyama T, Namise T, Shimoshimizu N, Uemura S, Takatsui Y, Hino M, et al. Non-catalyzed one-step synthesis of ammonia from atmospheric air and water. *Green Chem* (2016) 18:4536–41. doi:10.1039/C6GC01560C
90. Fangueiro D, Hjorth M, Gioelli F. Acidification of animal slurry– a review. *J Environ Manage* (2015) 149:46–56. doi:10.1016/j.jenvman.2014.10.001
91. Sutton MA, Bleeker A, Howard CM, Erisman JW, Abrol YP, Bekunda M, et al. Our nutrient world: the challenge to produce more food and energy with less pollution. *Centre Ecol and Hydrol behalf Glob Partnership Nutrient Manag (Gpnm) Int Nitrogen Initiat (Ini)* (2013).
92. Graves DB, Bakken LB, Jensen MB, Ingels R. Plasma activated organic fertilizer. *Plasma Chem Plasma Process* (2019) 39:1–19. doi:10.1007/s11090-018-9944-9
93. Zhang S, Rousseau A, Dufour T. Promoting lentil germination and stem growth by plasma activated tap water, demineralized water and liquid fertilizer. *RSC Adv* (2017) 7:31244–51. doi:10.1039/c7ra04663d
94. Cortese E, Settimi AG, Pattenuzzo S, Cappellin L, Galenda A, Famengo A, et al. Plasma-activated water triggers rapid and sustained cytosolic Ca²⁺ elevations in arabidopsis thaliana. *Plants* (2021) 10:2516. doi:10.3390/plants10112516
95. Adhikari B, Adhikari M, Ghimire B, Park G, Choi EH. Cold atmospheric plasma-activated water irrigation induces defense hormone and gene expression in tomato seedlings. *Sci Rep* (2019) 9:16080. doi:10.1038/s41598-019-52646-z
96. Vichiansan N, Chatmaniwat K, Sungkorn M, Leksakul K, Chaopaisarn P, Boonyawan D. Effect of plasma-activated water generated using plasma jet on tomato (*Solanum lycopersicum* L. Var. cerasiforme) seedling growth. *J Plant Growth Regul* (2023) 42:935–45. doi:10.1007/s00344-022-10603-7
97. Aceto D, Rotondo PR, Porfido C, Bottiglione B, Paciolla C, Terzano R, et al. Assessing plasma activated water irrigation effects on tomato seedlings. *Front Phys* (2024) 12. doi:10.3389/fphy.2024.1399910
98. Zambon Y, Contaldo N, Laurita R, Várallyay E, Canel A, Gherardi M, et al. Plasma activated water triggers plant defence responses. *Sci Rep* (2020) 10:19211. doi:10.1038/s41598-020-76247-3
99. Thirumdas R, Kothakota A, Annappure U, Siliveru K, Blundell R, Gatt R, et al. Plasma activated water (PAW): chemistry, physico-chemical properties, applications in food and agriculture. *Trends Food Sci Technol* (2018) 77:21–31. doi:10.1016/j.tifs.2018.05.007
100. Zhao YM, Patange A, Sun DW, Tiwari B. Plasma-activated water: physicochemical properties, microbial inactivation mechanisms, factors influencing antimicrobial effectiveness, and applications in the food industry. *Compr Rev Food Sci Food Saf* (2020) 19:3951–79. doi:10.1111/1541-4337.12644



OPEN ACCESS

EDITED BY

Paolo Francesco Ambrico,
Istituto per la Scienza e Tecnologia dei Plasmi -
CNR, Italy

REVIEWED BY

Ralf Schneider,
University of Greifswald, Germany
Guido Van Oost,
Ghent University, Belgium

*CORRESPONDENCE

Qiuyue Nie,
✉ nieqiuyue@hit.edu.cn

RECEIVED 02 September 2024

ACCEPTED 07 October 2024

PUBLISHED 23 October 2024

CITATION

Huang T, Nie Q, Jiang T, Chen C, Liu Y, Gao J,
Cai L, Zhao X and Wang X (2024) Research on
the characteristics of the Helium plasma beam
in HIT-PSI.


Front. Phys. 12:1489880.

doi: 10.3389/fphy.2024.1489880

COPYRIGHT

© 2024 Huang, Nie, Jiang, Chen, Liu, Gao, Cai,
Zhao and Wang. This is an open-access article
distributed under the terms of the [Creative
Commons Attribution License \(CC BY\)](#). The use,
distribution or reproduction in other forums is
permitted, provided the original author(s) and
the copyright owner(s) are credited and that the
original publication in this journal is cited, in
accordance with accepted academic practice.
No use, distribution or reproduction is
permitted which does not comply with these
terms.

Research on the characteristics of the Helium plasma beam in HIT-PSI

Tao Huang¹, Qiuyue Nie ^{2,3*}, Tao Jiang², Cheng Chen¹,
Yang Liu¹, Jinming Gao⁴, Laizhong Cai⁴, Xu Zhao¹ and
Xiaogang Wang^{1,3}

¹School of Physics, Harbin Institute of Technology, Harbin, China, ²School of Electrical Engineering and Automation, Harbin Institute of Technology, Harbin, China, ³Laboratory for Space Environment and Physical Science, Harbin Institute of Technology, Harbin, China, ⁴Southwestern Institute of Physics, Chengdu, China

As a high heat flux linear plasma device designed for studying divertor materials in future fusion reactors, HIT-PSI (Plasma Surface Interaction device at Harbin Institute of Technology) has been successfully constructed and has maintained stable operation since its completion. The characteristics of He plasma beams in HIT-PSI are investigated by emission spectroscopy and an infrared camera, with preliminary irradiation experiments conducted by bombarding tungsten with the beam. For relatively conservative discharge parameters, HIT-PSI achieved a steady-state heat flux capacity of ~ 40 MW/m² using infrared measurements, with the full width at half maximum (FWHM) of the heat flux beam reaching 4 mm. These characteristics make HIT-PSI an advanced platform for testing divertor materials and plasma-facing components, providing essential experimental supports for research and development of high-performance divertor materials.

KEYWORDS

linear plasma device, high heat flux, plasma-surface interaction, plasma facing components, divertor plasma environment

1 Introduction

The performance of materials for the tokamak divertor target and other plasma-facing components (PFCs) is critical to determining their reliability [1–5]. As fusion devices advance towards reactor parameter regimes, the expected high heat flux will exceed 10 MW/m² in divertor regions [6], accompanied by highly high particle flux. Nevertheless, most existing divertors of fusion devices, generally operate with short discharge pulses and relatively low heat flux on their target plates, significantly below the requirement for future fusion reactors [7–10].

To further evaluate and optimize the performance of PFC materials, various linear plasma devices (LPDs) have been developed as test platforms to experimentally simulate plasma surface interactions (PSIs) in future fusion reactors [11–18], mainly focusing on the study of tungsten [19, 20]. Characterized by a simple structure and low cost, enable flexible magnetic field configurations by various plasma sources to simulate plasma temperatures and densities similar to those in fusion reactor boundary regions, LPDs have been widely used in research areas of plasma physics and applications, particularly for simulating significant physical processes in divertor/scrape-off-layer (D-SOL) environments. For instance, Pilot-PSI [21, 22] employs a cascaded arc plasma source capable of generating

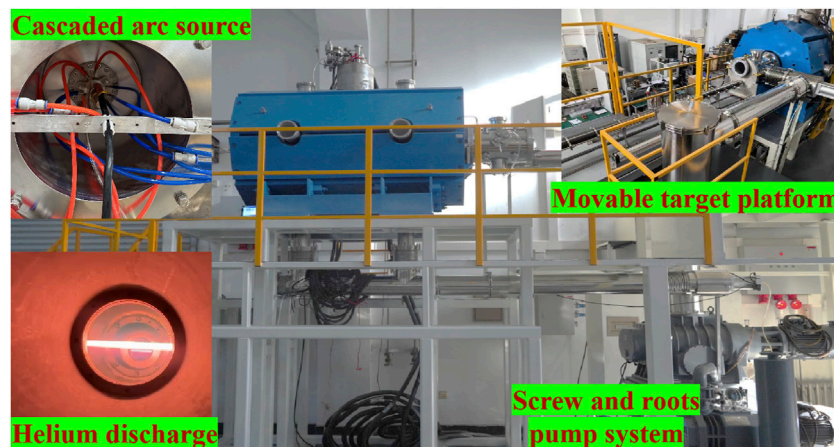


FIGURE 1
A photograph of the HIT-PSI device.

high magnetic fields in short pulses, up to 1.6 T for a few seconds, to produce hydrogen plasma beams with electron density of $5 \times 10^{21} \text{ m}^{-3}$ and electron temperature of 3 eV. The next-generation LPD, Magnum-PSI [23–26], designed and constructed based on the experience from Pilot-PSI, achieves steady-state particle flux $>10^{25} \text{ m}^{-2}\text{s}^{-1}$ and heat flux $>50 \text{ MW/m}^2$ [26]. At Oak Ridge National Laboratory (ORNL), MEPX uses a helicon source in a confinement magnetic field of $\sim 1.4 \text{ T}$ and with additional heating methods, e.g., ECRH and ICRH, for a designed power of $\sim 1 \text{ MW}$ [27, 28]. Recently, another high heat flux simulation facility for PSIs known as HIT-PSI [29] at Harbin Institute of Technology (HIT) has been designed and is now in operation. As illustrated in Figure 1, this facility utilizes a cascaded arc plasma source in a high magnetic field exceeding 2 T generated by superconducting magnets to simulate characteristics of extreme heat and particle flux in divertor region.

Supported by these devices, the physical simulation of LPDs, such as that in HIT-PSI and other devices, allows for a more intuitive understanding transport characteristics in the D-SOL region, and particularly provides crucial support for the studies on high heat load effects. First, the similarity between the LPDs (such as HIT-PSI and other similar devices) and the D-SOL region of tokamaks makes it an appreciated platform for studying edge physics in fusion plasmas [30, 31]. In an open magnetic field environment similar to that in the D-SOL region of tokamaks, the LPD can effectively simulate feature transport processes of D-SOL plasmas [31–33]. Nevertheless, the toroidal geometry feature of tokamaks other than that in LPDs may cause the notable drift effect on transport, leading to limitations in LPD physical simulations [34]. For HIT-PSI, the plasma beta is designed and experimentally estimated 10^{-5} – 10^{-4} , in the range of D-SOL plasmas of existing tokamaks and future reactors (e.g., $\sim 10^{-5}$ for ITER [35]). Also, the normalized collision rate (by the electron gyro-frequency) in HIT-PSI is 10^{-3} – 10^{-2} , much higher than that for tokamak D-SOL plasmas (e.g., 10^{-5} – 10^{-4} for ITER [35]). To present the divertor target property, the ratio of Debye length, which features the target sheath thickness, to the electron gyroradius is 10^{-1} – 10^0 , also in the same range as for ITER ($\sim 10^0$) [35]. Additionally, the electron temperature in LPDs is typically lower (ranging from a few eV to tens of eV [26, 36]),

allowing for detached state research. Most prominently, HIT-PSI can achieve a parameter range much higher than that of existing tokamak devices but of the future reactor regime, in steady-state operations. Particularly, HIT-PSI is capable to generate a high heat flux density of $\geq 20 \text{ MW/m}^2$, close to that on the divertor of fusion reactors [37, 38], which is a crucial parameter for studies of high heat load effects on target materials. On the other hand, one however needs to aware the noteworthy electron temperature difference between the LPD and the tokamak SOL region (usually $>100 \text{ eV}$ [37]), which complicates the interpretation of simulation results. Nevertheless, by adjusting the operating parameters, one may can yield the LPD experimental environments closer to tokamak divertor conditions. Furthermore, the linear device enables detailed investigations on PSIs between various ions (such as hydrogen, helium, as well as argon, etc.) and materials across different parameter ranges as well as boundary processes. However, it is difficult for HIT-PSI to achieve the effects of multiple particles working together (the particle composition in the D-SOL region is not only complex, but also with significant differences in temperatures of particles) [37]. Additionally, by adjusting the working gases and operation conditions of LPDs, one can further explore atomic-molecular processes of different particles, such as ionization, excitation, as well as molecular activation recombination (MAR) and electron-ion recombination (EIR), etc [39, 40]. Such processes provide crucial insights into energy and particle transports characteristics of the plasma, especially for energy loss mechanism in detachment. Generally, these capabilities mentioned above make the linear device an indispensable experimental tool in the future of fusion research and materials science.

This study focused on the characterization of helium plasma beams generated in HIT-PSI with high magnetic fields. Optical emission spectroscopy was then employed to measure the plasma's spectral characteristics beam at different magnetic field strengths and gas flow conditions and excitation temperatures were calculated. An infrared camera was used to evaluate the heat flux capacity of the device. Irradiation experiments were also conducted for pure tungsten samples. In steady-state operations of HIT-PSI, even for

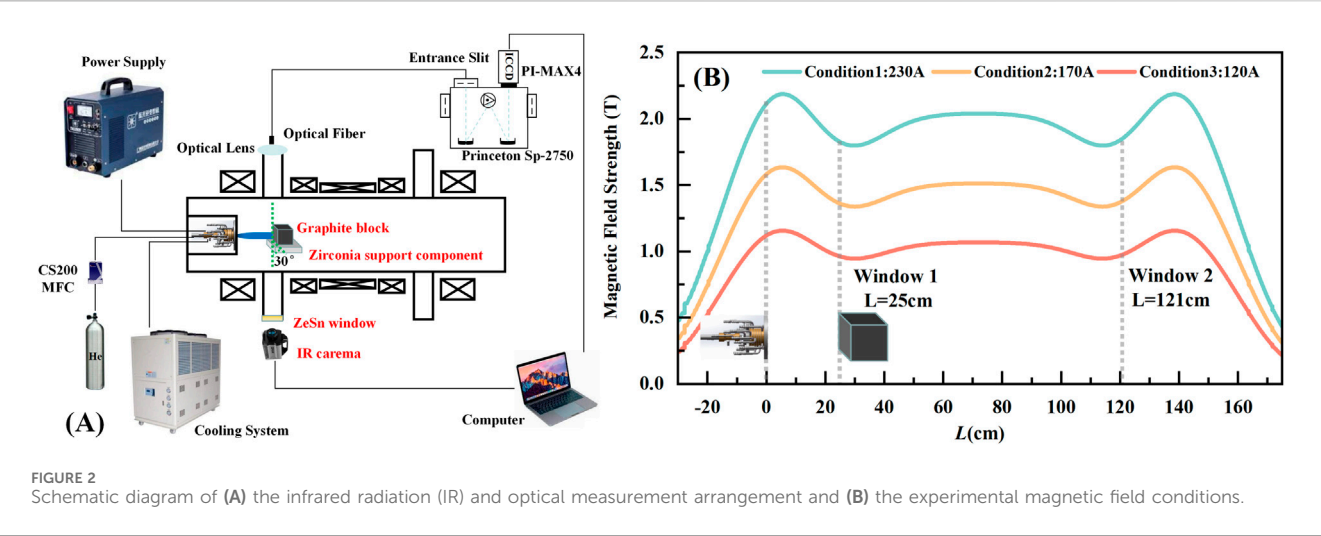


TABLE 1 Thermodynamic parameters of the graphite block used.

	Thermal conductivity (W/mK)	Density (kg/m ³)	Specific heat (J/kgK)
graphite	<i>k</i>	1,880	700

relatively conservative discharge parameters, the heat flux of helium plasma beams can reach up to 40 MW/m², demonstrating the experimental capability to simulate processes equivalent to those in the divertor environment.

The arrangement of this paper is as follows: Section 2 introduces the experimental setups. The results and analysis of emission spectroscopy, infrared diagnostics, and tungsten irradiation are presented in Section 3. The final section provides a conclusion.

2 Experiment setup

The HIT-PSI device (Figure 1) is operated in a 2 m long chamber by superconducting magnets, capable of reaching a magnetic field of up to 2.5 T, with a uniform magnetic field region >1 m and 8 radial boreholes to allow for flexible configuration of the vacuum system and diagnostic equipment. The plasma is generated by a cascaded arc source to generate a steady-state high-density plasma beam. The pumping system, consisting of screw and root pumps, achieves a pumping speed of 2500 L/s, maintaining a background pressure of 0.01 Pa. The movable target platform allows for changing the irradiation platform position axially.

A schematic diagram of the experimental setup is presented in Figure 2A. The discharge gas used in experiments is pure helium (He), with gas flow rates controlled at 1.4 slm, 1.7 slm, and 2.1 slm, respectively, corresponding to vacuum chamber pressures of 3.0 Pa, 3.5 Pa, and 4.0 Pa measured by an INFICON capacitance diaphragm gauge (Model CDG025). The collection point for emission spectroscopy and the infrared camera are both at Window 1, 25 cm from the plasma source outlet. Three axial magnetic fields are applied, corresponding to coil currents of 120 A, 170 A, and 230 A, producing field intensities of approximately 2.0 T (C1), 1.5 T (C2), and 1.0 T (C3), as shown in Figure 2B.

Optical emission spectra are collected with a Princeton Instruments (PI) SP-2750 spectrometer and a MAX4 1024i ICCD. Two diffraction gratings are utilized, one with a groove density of 300 g/mm and the other with 2,400 g/mm. Optical transmission is achieved through a UV-VIS fiber bundle (Model LG-455-020-3). The focusing optics consists of a fused silica plano-convex lens, 50.8 mm in diameter and 200 mm in focal length. Wavelength calibration is carried out by an AvaLight-HAL-CAL-Mini, while intensity calibration is performed with a PI intensity lamp in conjunction with the IntelliCal[®] system.

For heat flux measurement, real-time surface temperature changes of the graphite block under plasma beam bombardment are captured and recorded by the infrared camera. Then, a three-dimensional heat conduction equation was applied to calculate the heat flux of the plasma beam. A graphite cube with an 80 mm edge length is placed at Window 1, resting on a zirconia ceramic plate with a significantly lower thermal conductivity than graphite to ensure adiabatic conditions for the graphite during irradiation. The FLIR A700sc infrared camera, operating within the 7.5–14.0 μm wavelength range, is positioned at Window 1, perpendicular to the beam transmission direction. The Plasma Beam Facing Surface (PBFS) of the graphite cube is tilted 30° to the chamber symmetric axis to facilitate the observation of temperature changes on the surface with the infrared camera. The observation window is made of optical-grade ZnSe with a special coating, ensuring an infrared transmission rate of over 95% in a 6–14 μm wavelength range. The acquisition frequency is fixed at 30 Hz. Before experimental measurements, the infrared camera is placed behind the ZnSe window and calibrated by a standard heat source, with the infrared emissivity of the graphite cube surface measured at the same 30-degree angle setting. The thermal conductivity of the graphite is measured by a laser flash method and fitted to an exponential function as.

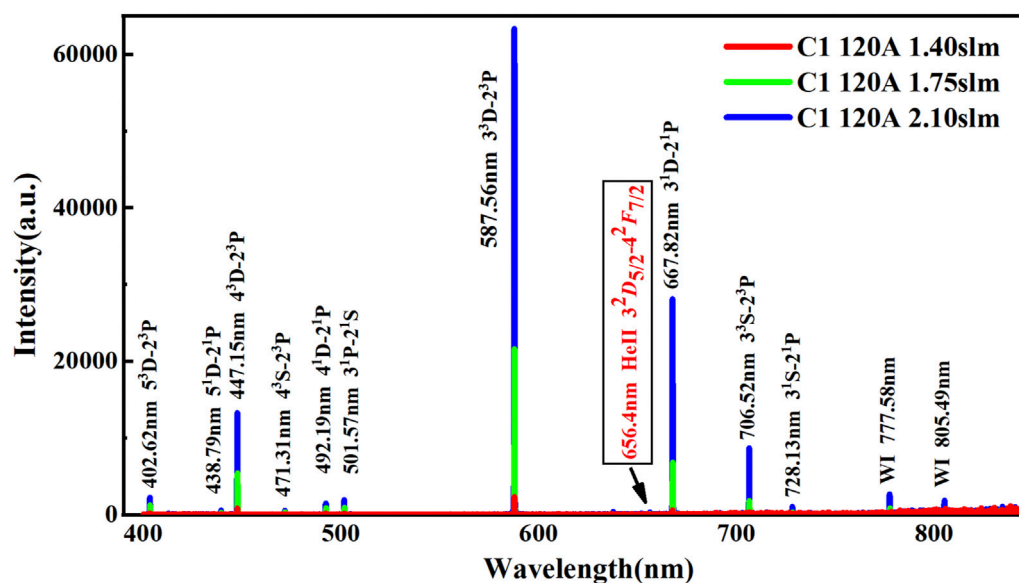


FIGURE 3
Typical spectra of the He plasma beam at different gas flow rates at C1 and a discharge current of 120 A.

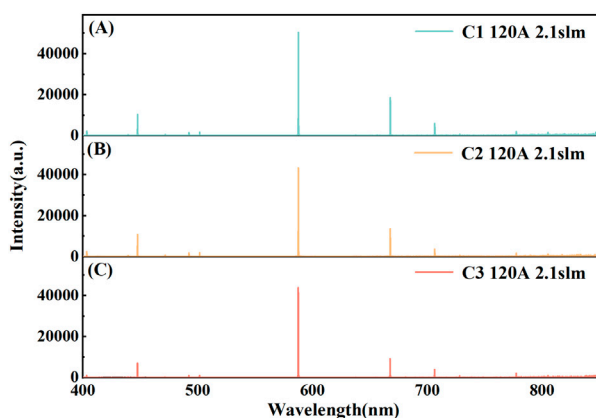


FIGURE 4
Typical spectra of He plasma beams at C1(A), C1(B) and C1(C) with a discharge current of 120 A and a gas flow rate of 2.1 slm.

$$k = 39.3532 + 62.6777 \times e^{-0.0015(T-273.15)}$$

where T is the temperature in Kelvin (K), and other parameters are listed in Table 1.

The irradiated sample is a circular pure tungsten disk with a diameter of 30 mm and a thickness of 4 mm. The irradiation location is also at Window 1, with the sample fixed onto a water-cooled target plate. The back of the sample remains in contact with a water-cooled copper plate, facilitating the cooling process by heat conduction during irradiation. To easily observe the practical interaction between the sample and the plasma, the entire target is positioned on a movable platform, and the samples undergo irradiation experiments under two conditions: without an applied bias and with a bias of -80 V. After finishing the irradiation, the sample is first cooled and then

exposed to atmospheric pressure, followed by Scanning Electron Microscope analysis.

3 Results and discussion

In this section, Section 3.1 will introduce the measurement and analysis of the spectral characteristics of the He plasma beam using emission spectroscopy under different magnetic fields, while Section 3.2 will present the measurement results of the heat flux of the HIT-PSI device using an infrared (IR) camera. Section 3.3 provides preliminary results of the irradiation of pure tungsten target plates with the He plasma beam.

3.1 Emission spectral characteristics of He plasma in strong magnetic fields

Figure 3 presents a comparison of the spectral intensities as the gas flow rate increases from 1.4 slm to 2.1 slm and the pressure rises from 3.0 Pa to 4.0 Pa at C1, and Figure 5A gives the intensity ratios of the main He I spectral lines. The substantial enhancement in line intensity indicates a significant increase in the density of excited atoms due to increased gas flow. This increase in gas flow can simultaneously raise the electron temperature and density to some extent, as demonstrated in experiments conducted on other experimental setups [41, 42].

Figure 4 compares the spectra in different magnetic fields (C1, C2, and C3) at a discharge current of 120 A and a gas flow rate of 2.1 slm. The differences in spectral lines of various cases are minimal. The simple and stable energy level structure of helium atoms results in a high probability of spontaneous emission for strong He I lines during transitions from excited states to the ground state. The plasma produced by the cascaded arc source has a

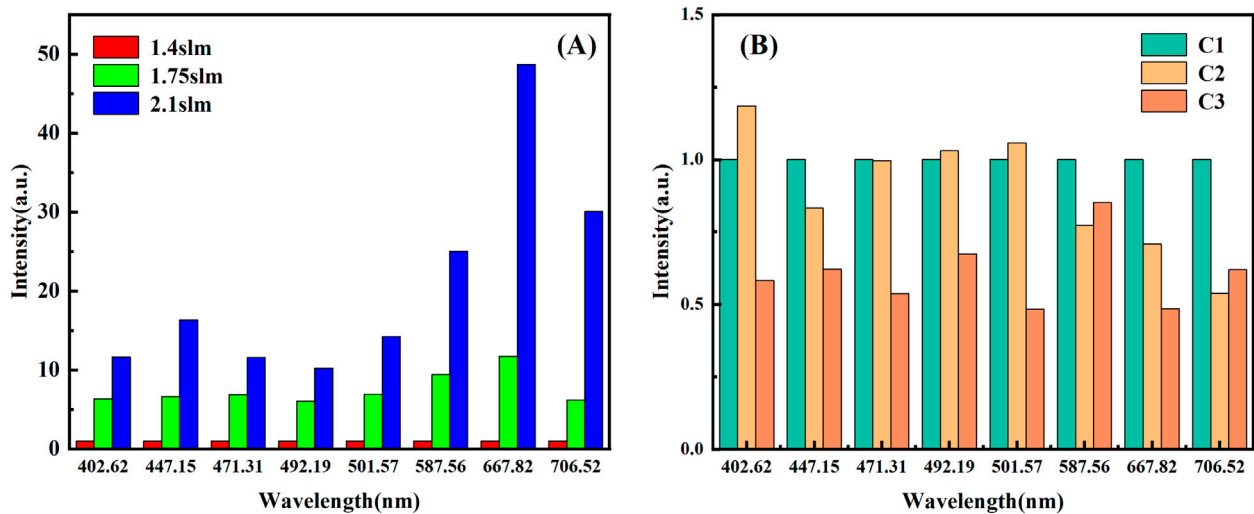


FIGURE 5

(A) Intensity ratios of the main He I spectral lines at different gas flow rates at C1 and a discharge current of 120 A, with normalization to the spectral intensity at C1. (B) Intensity ratios of the main He I spectral lines at different magnetic field conditions at a gas flow rate of 1.4 slm and a discharge current of 120 A, with normalization to the spectral intensity at C1.

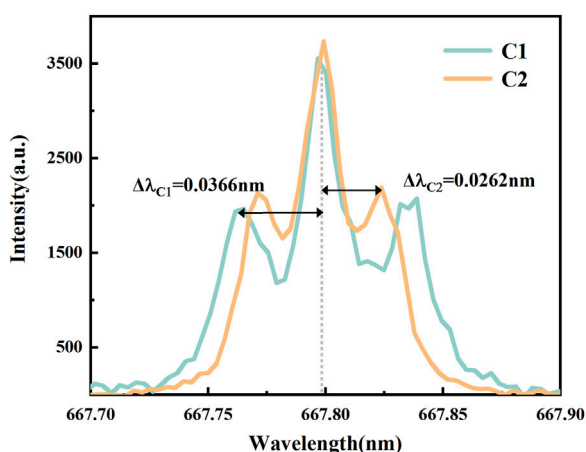


FIGURE 6

Zeeman splitting of He I 667.8 nm spectrum at C1.

relatively low electron temperature (~ 5 eV) [23, 43–45], challenging to excite a transition to higher energy levels. Thus, the transitions mainly concentrated on a few strong lines at lower energy levels. Such factors together lead to main spectral profiles without significant differences in the three magnetic field conditions.

Figure 5B presents the intensity ratios of the main He I spectral lines at different magnetic field conditions, with all lines normalized by that of C1. The results indicate that as the magnetic field strengthens, the line intensity increases, particularly as comparing the lines for C1 and C3 with the more pronounced magnetic field difference. The presence of a strong magnetic field induces a noticeable Zeeman effect, resulting in broader spectra and much more apparent intensity differences. The excitation of helium atoms primarily occurs by collision and recombination excitations (including radiative and three-body

recombinations). Near the exit of the plasma source, the electron temperature is relatively high [46], which makes collisional ionization and excitation the dominant processes, with electron collisions to ground-state helium atoms being the primary excitation mechanism. At stronger magnetic fields, the beam is better confined, radial diffusion, and the density is better maintained. Additionally, the power supply voltage for the plasma source increases from 107.0 V at C3 to 119.8 V at C2, and to 126.5 V at C1, indicating that more energy is coupled into the plasma as the magnetic field strengthens, leading to an increase in electron temperature. Furthermore, a weak He II 656.4 nm line appears in the spectrum, indicating an increase in the number of high-energy electrons. Consequently, the spectral intensity is higher at stronger magnetic fields.

At high magnetic fields, the spectral lines exhibit significant Zeeman splitting, which complicates the calculation of parameters with broadening. Figure 6 shows the Zeeman splitting of He I 667.8 nm line ($2^1\text{P}-3^1\text{D}$), clearly observed at C1 and C2. However, this splitting can be used to calculate the magnetic field accurately. The splitting caused by the Zeeman effect can be written [47].

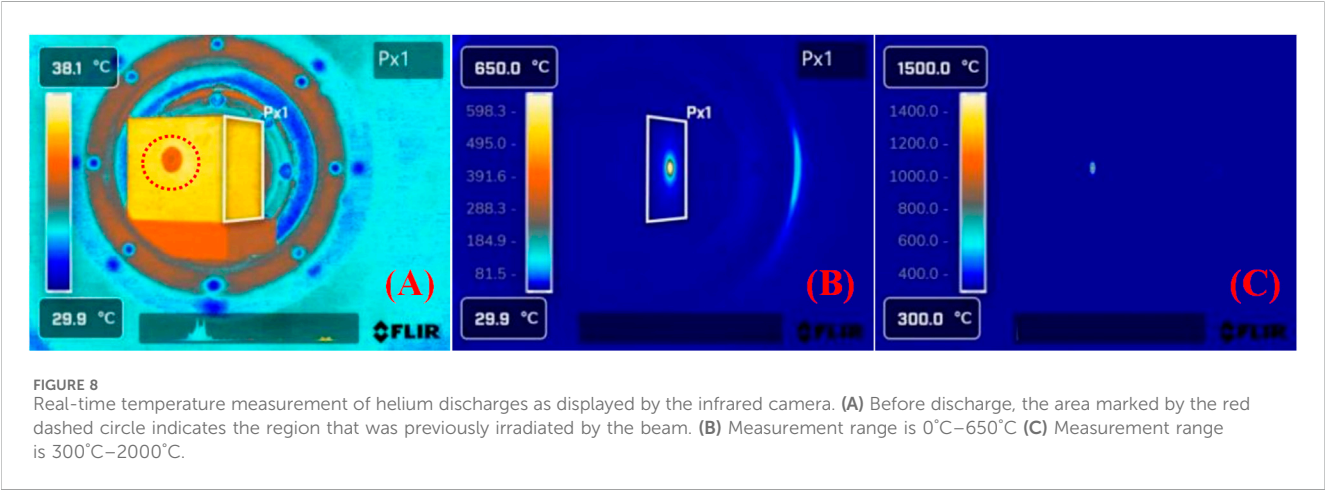
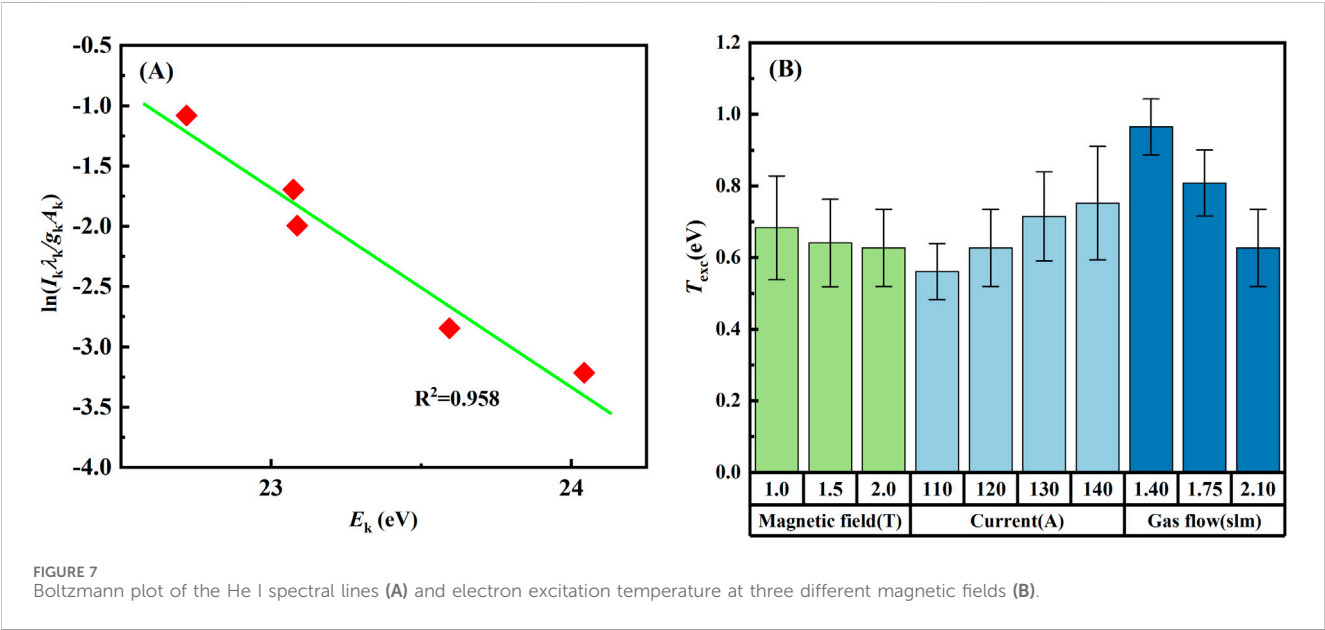
$$\Delta\lambda = \lambda_0^2 \mu_B g_j m_j B / hc$$

where λ_0 is the original wavelength of the spectral line, μ_B is the Bohr magneton, g_j is the Landé g -factor, m_j is the magnetic quantum number, B is the magnetic field strength, h is the Planck constant, and c is the speed of light. From the splitting width in Figure 6, the magnetic fields at the measurement positions for C1 and C2 can be approximately calculated as 1.78 T and 1.26 T, respectively, in close agreement with the actual magnetic field in Figure 2B.

By selecting the spectral lines from the characteristic spectrum listed in Table 2, we can construct the Boltzmann plot depicted in Figure 7A, in which the variation in electron excitation temperature

TABLE 2 Selected he i spectral lines and their parameters.

Wavelength (nm)	Lower level	Upper level	E_k (eV)	A_{ki} (s^{-1})	g_k
402.62	2^3P_2	5^3D_1	24.04	$1.16e+07$	7
471.31	2^3P_2	4^3S_1	23.59	$5.29e+06$	3
501.57	2^1S_0	3^1P_1	23.09	$1.34e+07$	3
667.82	2^1P_1	3^1D_2	23.07	$6.37e+07$	5
706.52	2^3P_2	3^3S_1	22.72	$1.55e+07$	3



can be determined. Figure 7B shows the excitation temperatures calculated using the Boltzmann slope method for different magnetic fields (with a discharge current of 120 A), as well as various discharge currents and gas flow rates (at C1). It can be observed that excitation temperatures do not exceed 1 eV, significantly differing from the actual electron temperature and indicating non-equilibrium plasmas and insufficient collisions [15, 48]. In this region, near the plasma source exit, where both electron temperature and density are high, collisional ionization dominates. The collisional ionization process mainly involves high-energy electrons, and their reduction in number and insufficient collisions likely lead to non-Maxwellian distribution characterized by a lack of high-energy electrons. This could be the reason for the lower excitation temperature.

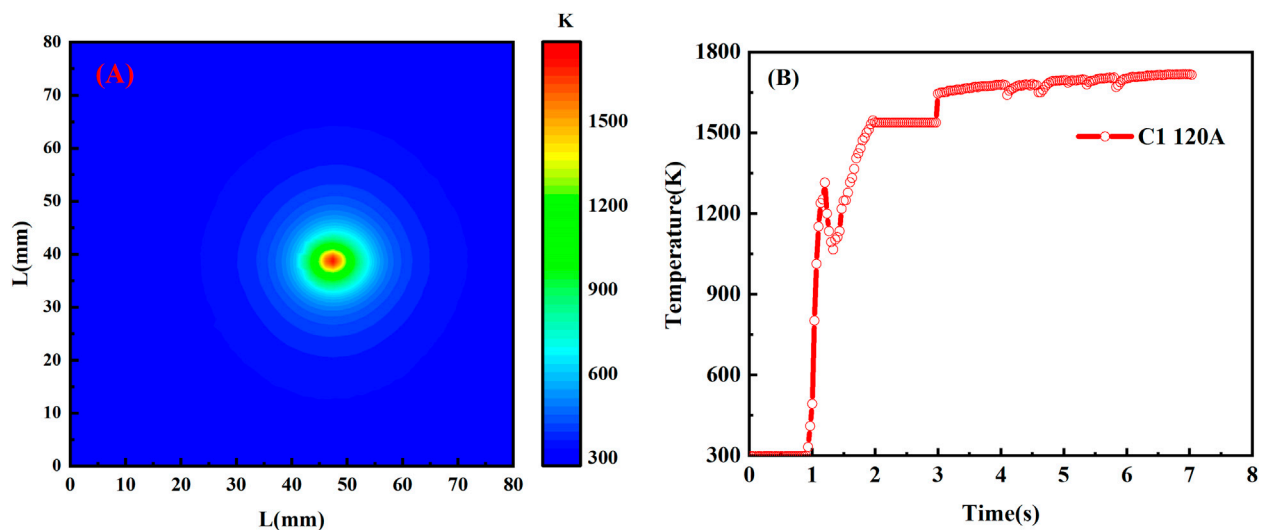


FIGURE 9
At C1 with discharge current of 120 A and gas flow rate of 1slm, (A) at approximately the fifth second, the synthesized surface temperature distribution with a maximum temperature >1700 K; (B) the temperature variation vs. time at the center point of the beam.

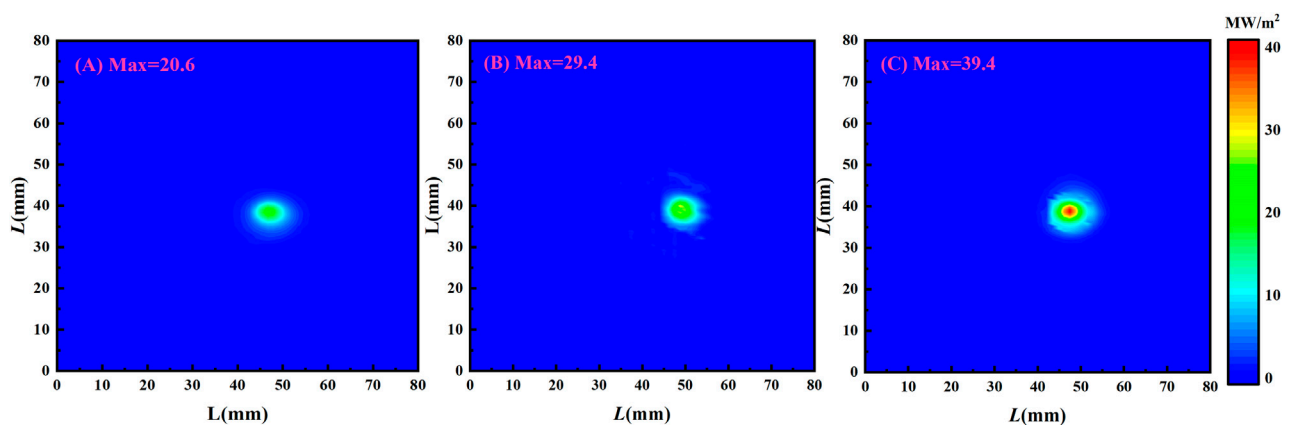


FIGURE 10
Heat flux spots at C1 (A), C2 (B), and C3 (C), respectively, with discharge current of 120 A and a gas flow rate of 1.4 slm at C1.

As shown in Figure 7B, the electron excitation temperature shows a slight downward trend as the magnetic field increases but generally remains stable overall. Thomson scattering measurements on the Pilot-PSI and Magnum-PSI device indicated that electron temperature and density rise with a stronger magnetic field, leading to an increased ionization rate [22, 49]. Consequently, more high-energy electrons are consumed in the ionization process, leading to a slight decrease in electron excitation temperature, which remains significantly lower than the overall electron temperature.

The electron excitation temperature shows a slight upward trend as the discharge current increases, depicted in Figure 7B. The increase in the discharge current leads to a rise in both electron temperature and density [50], increasing the frequency of collisional excitation processes, to induce a modest rise in the electron

excitation temperature. However, since most high-energy electrons are still primarily involved in the ionization process, the increase in excitation temperature is relatively limited. Additionally, the increase in discharge current enhances the collision frequency between electrons and other particles and potentially facilitates energy redistribution among electrons, to increase a faster participation of higher energy electrons in excitation processes. Nevertheless, since most higher energy electrons are still consumed in the ionization process, the rise in excitation temperature remains modest.

As indicated in Figure 7B, the electron excitation temperature noticeably drops with the increase in gas flow. An increase in the gas flow rate raises not only the electron temperature and density of the beam but also the density of heavy particles, leading to a higher

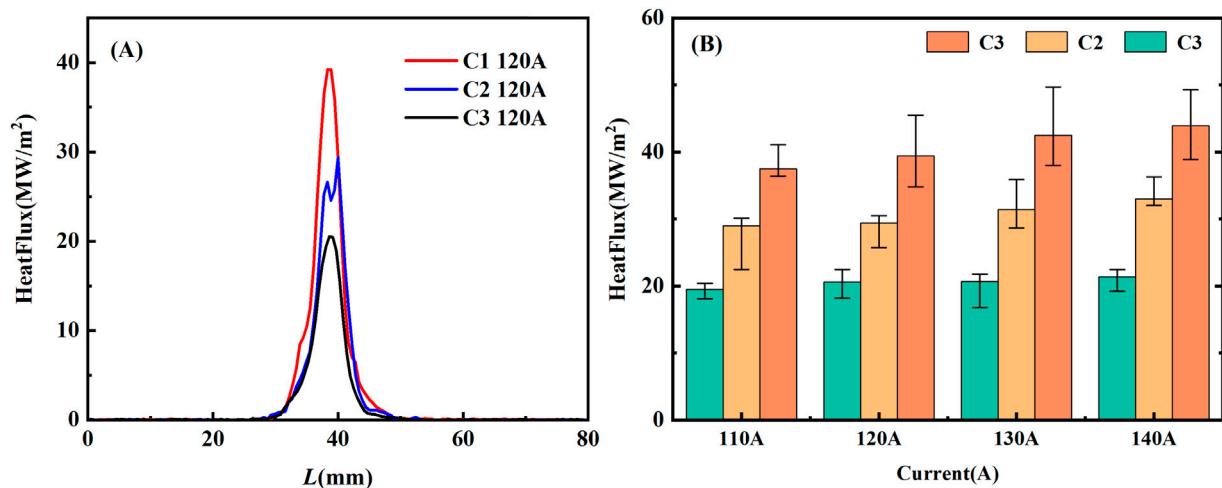


FIGURE 11 (A) The distribution of steady-state heat flux along the vertical direction in Figure 10 and (B) the steady-state heat flux values at different magnetic fields and discharge currents.

collision frequency between electrons and heavy particles. As shown in Figure 3, the number of excited-state atoms rises sharply, resulting in depletion of higher energy electrons and thereby lowering the excitation temperature.

3.2 Heat flux measurement by infrared camera

Infrared camera images captured during the discharge process are shown in Figure 8. The region marked Px1 is the PBFS of the graphite block, reconstructed into a square with a side length of 80 mm in subsequent data processing. Due to limitations of the camera acquisition range, the heating process beyond the selected range cannot be measured in a single run. Therefore, the acquisition is divided into two stages: the first stage measures temperatures in the 0°C–650°C range, and the second in the 300°C–2000°C range. Figure 8 shows real-time images of the two-step temperature measurement. The data above 500°C by the second acquisition are overlaid on the first acquisition data to create a composite temperature profile.

The heat flux is predicted by analyzing the surface heat flux based on the three-dimensional (3D) heat conduction equation to compute the temperature variations within the graphite block, given by the following formula [51]:

$$\frac{\partial T(x, y, z, t)}{\partial t} = \frac{k}{\rho c_p} \left[\frac{\partial^2 T(x, y, z, t)}{\partial x^2} + \frac{\partial^2 T(x, y, z, t)}{\partial y^2} + \frac{\partial^2 T(x, y, z, t)}{\partial z^2} \right]$$

where k is the thermal diffusivity, ρ is the mass density, and c_p is the specific heat capacity.

The PBFS is set at $z = 0$ plane, while the non-PBFSs follow the adiabatic boundary condition of

$$\left. \frac{\partial T(x, y, z, t)}{\partial x} \right|_{x=0, x=L} = \left. \frac{\partial T(x, y, z, t)}{\partial y} \right|_{y=0, y=L} = \left. \frac{\partial T(x, y, z, t)}{\partial z} \right|_{z=L} = 0$$

Heat flux can then be determined by

$$q = -k \left. \frac{\partial T(x, y, z, t)}{\partial z} \right|_{z=0}$$

To enhance the computational efficiency of solving the three-dimensional heat conduction equation, an alternating direction implicit (ADI) algorithm is employed to reduce each step's complexity and significantly improve the computing speed and efficiency. Furthermore, the ADI algorithm has high accuracy and is suitable for various practical applications in 3D heat conduction. Also, the implemented code is rigorously validated by COMSOL and ANSYS results, ensuring its reliability and precision.

Figure 9A depicts the temperature distribution on the graphite strike face (PBFS), measured by the infrared thermography approximately at the fifth second after the discharge onset, with discharge current of 120 A at C1. The temperature profile exhibits a Lorentzian distribution, with the core temperature reaching a significantly high value. Figure 9B presents the temporal evolution of the core temperature. Notably, at less than 1/3 s from the onset, the core temperature rapidly escalates to >1,000°C. After such a rapid rise, there is a slight decrease in temperature, succeeded by another rise. The cause of this temperature fluctuation may be surface modifications or damage caused by the high heat flux, which fundamentally alters the initial graphite surface morphology.

The two-dimensional (2D) and radial distributions of the beam heat flux with discharge current of 120 A and a conservative gas flow rate of 1.4 slm at three distinct magnetic field conditions (C1, C2, C3) are shown in Figure 10. The heat flux can easily exceed 20 MW/m². With the increase in magnetic field strength, a significant enhancement in heat flux is observed, reaching up to 40 MW/m² at C1. Figure 11A presents the 2D beam heat flux profile distribution, which exhibits a quasi-Gaussian shape with no substantial variations across different conditions. The full width at half maximum (FWHM) remains approximately 4 mm,

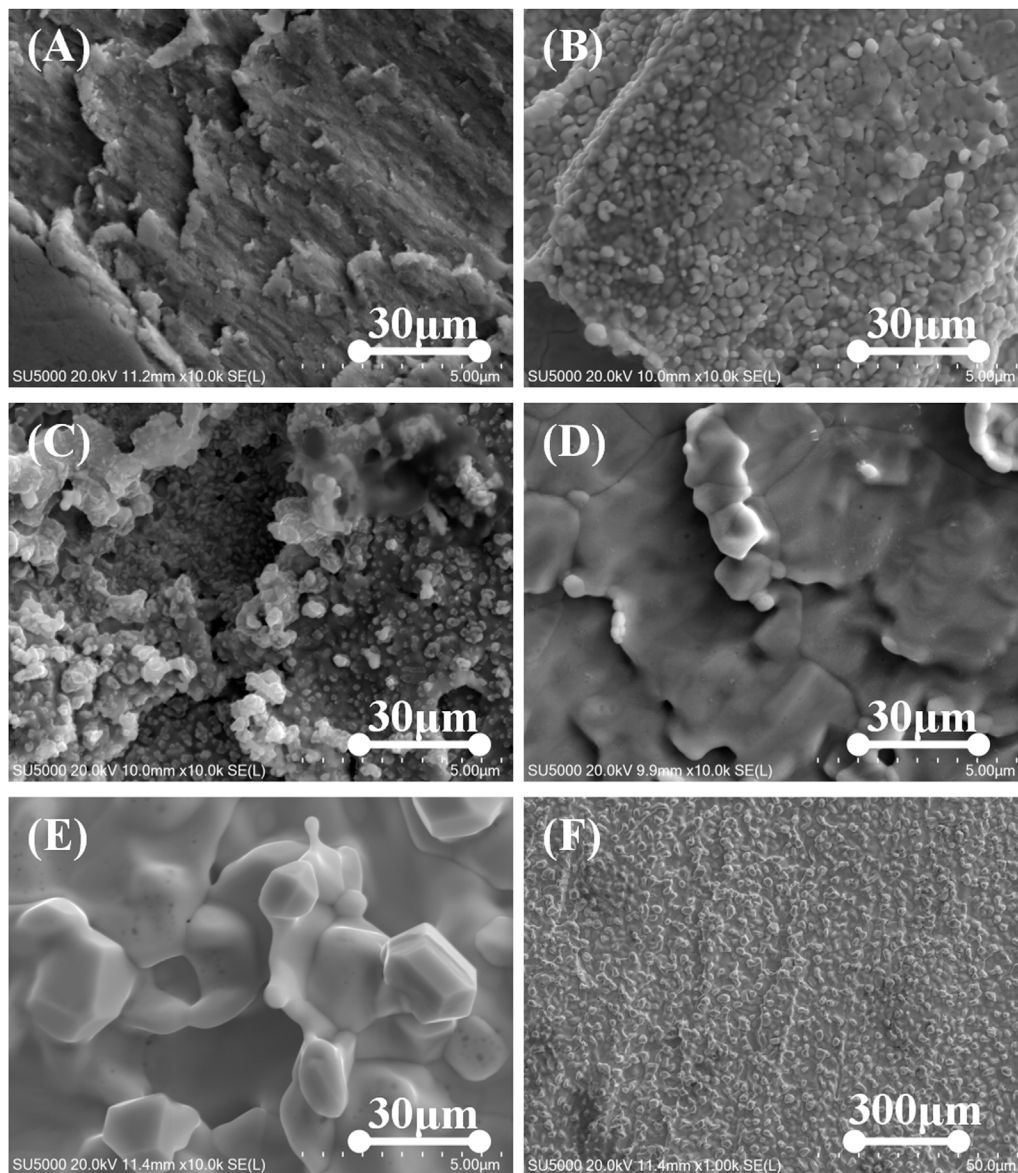


FIGURE 12
SEM images of W samples under different irradiation durations without bias, with the measurement moments at (A) 0 s, (B) 30 s, (C) 60 s, (D) 120 s, and (E, F) 240 s.

consistent with the size of the plasma source exit. [Figure 11B](#) presents the steady-state heat flux at different field and current conditions. The steady-state heat load easily exceeds 20 MW/m^2 , with the beam demonstrating good stability. At higher magnetic fields, the heat flux density curve shows fluctuations during the initial stage and then gradually reaches a steady state. It may be attributed to the rapid changes in surface temperature and physical alterations in surface morphology, leading to variations in temperature measurements. However, the overall trend is clear: stronger magnetic fields and higher currents result in greater heat flux.

It should be noted that, due to the angle between the plasma beam and PBFS of the graphite block, along with the relatively low gas flow rate, the current heat flux represents a conservative estimate

of the device's capabilities, while the actual heat flux achievable by HIT-PSI could be higher. As the magnetic field increases, the power of the plasma source accordingly rises, too, which has been confirmed in our device and other experiments [22, 25, 42]. This enables more power to be coupled into the plasma beam, leading to an increase in the electron temperature and density. Additionally, the strong magnetic field provides better confinement of the plasma, reducing radial diffusion and increasing plasma density. Ultimately, this effect significantly enhances the heat flux of the helium beam at a strong magnetic field.

When the beam reaches Window 2, at a transmission distance of 120 cm, it undergoes significant attenuation. At C3, the beam is almost invisible to the naked eye. In the parameter regime of our experiments, where electron and ion temperatures are

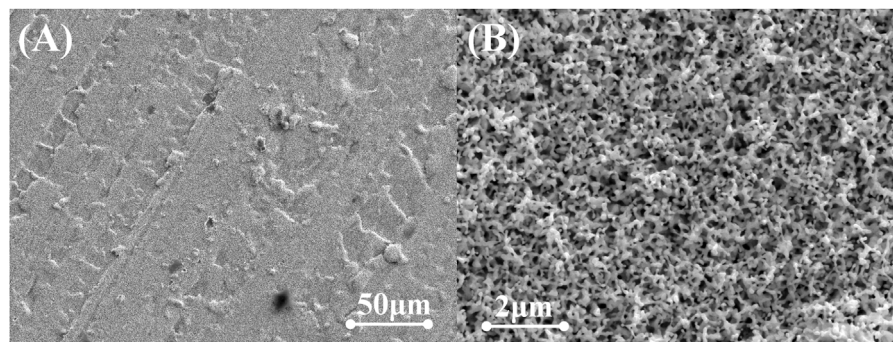


FIGURE 13
SEM images of W sample with -80 V bias after 30 s of irradiation.

approximately below 5 eV [52] and based on elastic collision parameters [53, 54], the collision rates of ions and electrons with atoms in He discharges are estimated in the ranges of 10^6 Hz and 10^7 Hz respectively. The characteristic axial propagation period of the beam is approximately 10^{-3} to 10^{-4} s, accordingly. Such features indicate that during the beam transmission, both electrons and ions undergo numerous collisions with background neutral helium atoms, resulting in significant energy transfer to the background and rapid energy loss from the beam. At the sufficiently high confining magnetic field in HIT-PSI, the impact of radial diffusion of the beam heat flux is far less significant than that of collision effects. To further increase the heat flux, the most effective way is to reduce the background gas pressure.

3.3 Initial experiment of he plasma beam irradiation on tungsten

The irradiation results without an applied bias are shown in Figure 12. The surface irregularity in the non-irradiated sample shown in Figure 12A is due to the polishing process, with noticeable cutting marks. The tungsten surface after 30 s of irradiation shows signs of melting. As the irradiation goes on, noticeable uneven coral-like structures on the surface are shown in Figure 12C after 60 s, and then cracks appear in Figure 12D after 120 s. Further tracing the irradiation to 240 s, the surface exhibits a granular texture in Figures 12E, F. Larger scale SEM images reveal extensive areas of granules in the micron scale, a sign of recrystallization.

The irradiation results with an applied bias of -80 V are shown in Figure 13. After just 30 s of irradiation, the tungsten sample's surface has formed a distinct "fuzzy" structure. Typically, the formation of such a structure is considered to require a helium particle flow reaching 10^{25} m^{-2} [55, 56]. This indicates that the particle flux capability of HIT-PSI has reached a significantly high level. We will gradually improve the measurement of critical parameters for irradiation, such as sample temperature and particle flow, to achieve more precise and systematic experiments that comprehensively simulate the service environment for divertor materials and components under high heat flux and high particle flow irradiation conditions. This will provide experimental data to support the development of new methods and approaches for

enhancing the service conditions of divertor target materials in fusion research facilities.

4 Conclusion

The emission spectra and heat flux characteristics of the He plasma beam are measured at different high magnetic field conditions, and preliminary irradiation experiments on pure tungsten samples are carried out. This study reveals that the heat flux capacity of HIT-PSI can exceed 40 MW/m^2 , far surpassing the initial design target and effectively simulating the extreme heat flux conditions expected in the divertor region of future fusion reactors.

Additionally, the emission spectrum of helium at high magnetic field conditions exhibits a consistent pattern, but the overall spectral intensity significantly rises as the gas flow increases. Preliminary irradiation experiments demonstrate that HIT-PSI can serve as an excellent platform for testing the performance of plasma-facing materials and components in extreme irradiation environments and providing valuable insights for future research and materials development.

Data availability statement

The raw data supporting the conclusions of this article will be made available by the authors, without undue reservation.

Author contributions

TH: Conceptualization, Data curation, Formal Analysis, Investigation, Methodology, Project administration, Validation, Visualization, Writing—original draft, Writing—review and editing. QN: Conceptualization, Data curation, Formal Analysis, Funding acquisition, Investigation, Methodology, Project administration, Resources, Supervision, Validation, Visualization, Writing—review and editing. TJ: Data curation, Investigation, Writing—original draft. CC: Data curation, Investigation, Writing—original draft. YL: Data curation, Investigation, Writing—original draft. JG: Data curation,

Formal Analysis, Investigation, Methodology, Validation, Writing–review and editing. LC: Data curation, Formal Analysis, Investigation, Methodology, Validation, Writing–review and editing. XZ: Data curation, Investigation, Writing–original draft. XW: Conceptualization, Data curation, Formal Analysis, Funding acquisition, Investigation, Methodology, Project administration, Resources, Supervision, Validation, Writing–review and editing.

Funding

The author(s) declare that financial support was received for the research, authorship, and/or publication of this article. This work is supported by the National Natural Science Foundation of China No.12105067.

References

- Merola M, Loesser D, Martin A, Chappuis P, Mitteau R, Komarov V, et al. ITER plasma-facing components. *Fusion Eng Des* (2010) 85:2312–22. doi:10.1016/j.fusengdes.2010.09.013
- Luo GN, Zhang XD, Yao DM, Gong XZ, Chen JL, Yang ZS, et al. Overview of plasma-facing materials and components for EAST. *Physica Scripta* (2007) T128:1–5. doi:10.1088/0031-8949/2007/t128/001
- Linke J, Du J, Loewenhoff T, Pintsuk G, Spilker B, Steudel I, et al. Challenges for plasma-facing components in nuclear fusion. *Matter Radiat Extremes* (2019) 4:5. doi:10.1063/1.5090100
- Luo G-N, Liu G, Li Q, Qin S, Wang W, Shi Y, et al. Overview of decade-long development of plasma-facing components at ASIPP. *Nucl Fusion* (2017) 57(6):065001. doi:10.1088/1741-4326/aa6502
- Herrmann A. Overview on stationary and transient divertor heat loads. *Plasma Phys controlled fusion* (2002) 44(6):883–903. doi:10.1088/0741-3335/44/6/318
- Linke J. High heat flux performance of plasma facing materials and components under service conditions in future fusion reactors. *Fusion Sci Technol* (2006) 49(2T):455–64. doi:10.13182/fst06-a1144
- Holtkamp N. ITER Project Team. An overview of the ITER project. *Fusion Eng Des* (2007) 82(5–14):427–34. doi:10.1016/j.fusengdes.2007.03.029
- Zhuang G, Li GQ, Li J, Wan Y, Liu Y, Wang X, et al. Progress of the CFETR design. *Nucl Fusion* (2019) 59(11):112010. doi:10.1088/1741-4326/ab0e27
- Hirai T, Barabash V, Escourbiac F, Durocher A, Ferrand L, Komarov V, et al. ITER divertor materials and manufacturing challenges. *Fusion Eng Des* (2017) 125:250–5. doi:10.1016/j.fusengdes.2017.07.009
- Pitts RA, Bonnin X, Escourbiac F, Frerichs H, Gunn J, Hirai T, et al. Physics basis for the first ITER tungsten divertor. *Nucl Mater Energy* (2019) 20:100696. doi:10.1016/j.nme.2019.100696
- Uccello A, Bin W, Bruschi A, Causa F, Cremona A, De Angeli M, et al. Linear plasma device GyM for plasma-material interaction studies. *Front Phys* (2023) 11:1108175. doi:10.3389/fphy.2023.1108175
- Nishijima D, Wenzel U, Ohsumi K, Ohno N, Uesugi Y, Takamura S. Characteristics of detached plasmas associated with electron-ion and molecular assisted recombinations in NAGDIS-II. *Plasma Phys Control Fusion* (2002) 44(5):597–610. doi:10.1088/0741-3335/44/5/307
- Kreter A, Brandt C, Huber A, Kraus S, Möller S, Reinhart M, et al. Linear plasma device PSI-2 for plasma-material interaction studies. *Fusion Sci Technol* (2015) 68(1):8–14. doi:10.13182/fst14-906
- Unterberg B, Jaspers R, Koch R, Massaut V, Rapp J, Reiter D, et al. New linear plasma devices in the trilateral euegio cluster for an integrated approach to plasma surface interactions in fusion reactors. *Fusion Eng Des* (2011) 86(9–11):1797–800. doi:10.1016/j.fusengdes.2011.03.082
- Kakati M, Sarmah T, Aomao N, Sabavath G, Dihingia P, Rahman M, et al. Design, development and recent experiments of the CIRCLE-PSI device. *Nucl Fusion* (2019) 59(11):112008. doi:10.1088/1741-4326/ab0248
- Nakashima Y, Takeda H, Ichimura K, Hosoi K, Oki K, Sakamoto M, et al. Progress of divertor simulation research toward the realization of detached plasma using a large tandem mirror device. *J Nucl Mater* (2015) 463:537–40. doi:10.1016/j.jnucmat.2014.12.063
- Zhou HS, Yuan XG, Li B, Liu HD, Luo GN, Chen JL, et al. A new high flux plasma source testing platform for the CRAFT project. *J Fusion Energy* (2020) 39:355–60. doi:10.1007/s10894-020-00277-y
- Sun C, Sang C, Ye H, Wang Q, Liu H, Wang Z, et al. The design of multiple plasma simulation linear device. *Fusion Eng Des* (2021) 162:112074. doi:10.1016/j.fusengdes.2020.112074
- Yin H, Wang J, Guo W, Cheng L, Yuan Y, Lu G. Recent studies of tungsten-based plasma-facing materials in the linear plasma device STEP. *Tungsten* (2019) 1(2):132–40. doi:10.1007/s42864-019-00004-x
- Sakamoto R, Elodie B, Arkadi K, Celine M. Impact of helium and hydrogen plasma exposure on surface damage and erosion of tungsten. *Nucl Fusion* (2024) 64(3):036008. doi:10.1088/1741-4326/ad1fab
- De Groot B, Al RS, Engeln R, Goedheer W, Kruijt O, Meiden H, et al. Extreme hydrogen plasma fluxes at Pilot-PSI enter the ITER divertor regime. *Fusion Eng Des* (2007) 82(15–24):1861–5. doi:10.1016/j.fusengdes.2007.07.052
- Van Rooij GJ, Van der Meiden HJ, Koppers WR, Shumack AE, Vijvers WAJ, Westerhout J, et al. Thomson scattering at pilot-PSI and magnum-PSI. *Plasma Phys Controlled Fusion* (2009) 51(12):124037. doi:10.1088/0741-3335/51/12/124037
- Van Eck HJN, Koppers WR, Van Rooij GJ, Goedheer W, de Groot B, Smeets P, et al. Pre-design of Magnum-PSI: a new plasma-wall interaction experiment. *Fusion Eng Des* (2007) 82(15–24):1878–83. doi:10.1016/j.fusengdes.2007.03.004
- Scholten J, Van Emmichoven PZ, Van Eck HJN, Smeets PHM, De Temmerman GC, Brons S, et al. Operational status of the Magnum-PSI linear plasma device. *Fusion Eng Des* (2013) 88(9–10):1785–8. doi:10.1016/j.fusengdes.2013.05.063
- Van Eck HJN, Abrams T, Van Den Berg MA, Brons S, van Eden G, Jaworski M, et al. Operational characteristics of the high flux plasma generator Magnum-PSI. *Fusion Eng Des* (2014) 89(9–10):2150–4. doi:10.1016/j.fusengdes.2014.04.054
- Van Eck HJN, Akkermans GRA, van der Westen SA, Aussems D, van Berkel M, Brons S, et al. High-fluence and high-flux performance characteristics of the superconducting Magnum-PSI linear plasma facility. *Fusion Eng Des* (2019) 142:26–32. doi:10.1016/j.fusengdes.2019.04.020
- Lau C, Biewer TM, Bigelow TS, Caneses J, Caughman J, Goulding R, et al. Physical and technical basis of Materials Plasma Exposure Experiment from modeling and Proto-MPEX results. *Nucl Fusion* (2023) 63(5):056009. doi:10.1088/1741-4326/acc2d1
- Rapp J, Lumsdaine A, Aaron A, Biewer TM, Bigelow TS, Boyd T, et al. Final design of the material plasma exposure experiment. *Fusion Sci Technology* (2023) 79(8):1113–23. doi:10.1080/15361055.2023.2168443
- Huang T, Nie Q, Wang M, Xu F, Wang X. Conceptual design of a compact divertor heat load simulation device: HIT-PSI. *Appl Sci* (2022) 12(20):10501. doi:10.3390/app122010501
- De Groot B, Ahmad Z, Dahiya R, Engeln R, Goedheer W, Lopes Cardozo N, et al. Magnum-psi, a new linear plasma generator for plasma-surface interaction studies in ITER relevant conditions. *Fusion Eng Des* (2003) 66:413–7. doi:10.1016/s0920-3796(03)00174-1
- Hirooka Y. *Plasma-materials interactions and edge-plasma physics research*. Los Angeles, CA, USA: California University (1991). No. UCLA-PPG-1380.
- Vijvers WAJ, Al RS, Cardozo NL, Goedheer WJ, de Groot B, Kleyn AW, et al. Transport of high fluxes of hydrogen plasma in a linear plasma generator. In: *XXVIII international conference on phenomena in ionised gases (ICPIG 2007) 15–20 July 2007, Prague, Czech republic. Proceedings*. Prague, Czech Republic: Institute of Physics (2007). p. 1793–6.
- Tanaka H, Hayashi Y, Kajita S, van der Meiden HJ, Yoshikawa M, Vernimmen JWM, et al. Cross-field transport in detached helium plasmas in Magnum-PSI. *Plasma Phys Controlled Fusion* (2020) 62(11):115021. doi:10.1088/1361-6587/abb88f

Conflict of interest

The authors declare that the research was conducted in the absence of any commercial or financial relationships that could be construed as a potential conflict of interest.

Publisher's note

All claims expressed in this article are solely those of the authors and do not necessarily represent those of their affiliated organizations, or those of the publisher, the editors and the reviewers. Any product that may be evaluated in this article, or claim that may be made by its manufacturer, is not guaranteed or endorsed by the publisher.

34. Kaveeva E, Rozhansky V, Senichenkov I, Sytova E, Veselova I, Voskoboinikov S, et al. SOLPS-ITER modelling of ITER edge plasma with drifts and currents. *Nucl Fusion* (2020) 60(4):046019. doi:10.1088/1741-4326/ab73c1
35. ITER Physics Expert Group on Confinement and Transport, et al. *Chapter 2: Plasma confinement and transport Nucl Fusion* (1999) 39:2175. doi:10.1088/0029-5515/39/12/302
36. Rapp J, Lumsdaine A, Beers CJ, Biewer TM, Bigelow TS, Caneses JF, et al. Latest results from Proto-MPEX and the future plans for MPEX. *Fusion Sci Technology* (2019) 75(7):654–63. doi:10.1080/15361055.2019.1610315
37. Pitts RA, Carpentier S, Escourbiac F, Hirai T, Komarov V, Kukushkin A, et al. Physics basis and design of the ITER plasma-facing components. *J Nucl Mater* (2011) 415(1):S957–64. doi:10.1016/j.jnucmat.2011.01.114
38. Pitts RA, Bardin S, Bazylev B, van den Berg M, Bunting P, Carpentier-Chouchana S, et al. Physics conclusions in support of ITER W divertor monoblock shaping. *Nucl Mater Energy* (2017) 12:60–74. doi:10.1016/j.nme.2017.03.005
39. Ohno N. Plasma detachment in linear devices. *Plasma physics and controlled fusion. Plasma Phys Controlled Fusion* (2017) 59.3:034007. doi:10.1088/1361-6587/aa5394
40. Ohno N, Seki M, Ohshima H, Tanaka H, Kajita S, Hayashi Y, et al. Investigation of recombination front region in detached plasmas in a linear divertor plasma simulator. *Nucl Mater Energy* (2019) 19:458–62. doi:10.1016/j.nme.2019.03.010
41. Yong W, Cong LI, Jielin SHI, Wu X, Ding H. Measurement of electron density and electron temperature of a cascaded arc plasma using laser Thomson scattering compared to an optical emission spectroscopic approach. *Plasma Sci Technology* (2017) 19(11):115403. doi:10.1088/2058-6272/aa861d
42. Xiaochun MA, Cao X, Lei HAN, Zhang Z, Wei J, Gou F. Characterization of high flux magnetized helium plasma in SCU-PSI linear device. *Plasma Sci Technology* (2018) 20(2):025104. doi:10.1088/2058-6272/aa936e
43. Kajita S, Nishijima D, Fujii K, Akkermans G, van der Meiden H. Application of multiple regression for sensitivity analysis of helium line emissions to the electron density and temperature in Magnum-PSI. *Plasma Phys Controlled Fusion* (2021) 63(5):055018. doi:10.1088/1361-6587/abf36e
44. Kajita S, Iwai S, Tanaka H, Nishijima D, Fujii K, van der Meiden H, et al. Use of machine learning for a helium line intensity ratio method in Magnum-PSI. *Nucl Mater Energy* (2022) 33:101281. doi:10.1016/j.nme.2022.101281
45. De Temmerman G, Daniels J, Bystrov K, van den Berg M, Zielinski J. Melt-layer motion and droplet ejection under divertor-relevant plasma conditions. *Nucl Fusion* (2013) 53(2):023008. doi:10.1088/0029-5515/53/2/023008
46. Ješko K, van der Meiden HJ, Gunn JP, Vernimmen J, De Temmerman G. Plasma pressure and particle loss studies in the Pilot-PSI high flux linear plasma generator. *Nucl Mater Energy* (2017) 12:1088–93. doi:10.1016/j.nme.2017.03.025
47. Heckmann PH, Träbert E. *Introduction to the spectroscopy of atoms*. North-Holland Personal Library (1989).
48. Hayashi Y, Ješko K, Van Der Meiden HJ, Vernimmen J, Morgan T, Ohno N, et al. Plasma detachment study of high density helium plasmas in the Pilot-PSI device. *Nucl Fusion* (2016) 56(12):126006. doi:10.1088/0029-5515/56/12/126006
49. Goedheer WJ, van Rooij GJ, Veremiyenko V, Ahmad Z, Barth CJ, Brezinsek S, et al. Effect of magnetic field strength on pilot-psi plasma beam fluxes probed by thomson scattering and spectroscopy. *High Temperature Mater Process An Int Q High-Techonology Plasma Process* (2004) 8(4):627–33. doi:10.1615/hightempmatproc.v8.i4.120
50. Wang Y, Zhou H, Li X, Liu H, Zhu Y, Luo G. Characterization of cascaded arc He plasma in a compact linear plasma device using voltammetry and optical emission spectroscopy. *Physica Scripta* (2024) 99(6):065604. doi:10.1088/1402-4896/ad4290
51. Gao JM, Li W, Xia ZW, Pan YD, Lu J, Yi P, et al. Reconstruction of heat flux profile on the HL-2A divertor plate with a three-dimensional analysis model. *Chin Phys B* (2013) 22(1):015202. doi:10.1088/1674-1056/22/1/015202
52. Van der Meiden HJ. Collective Thomson scattering for ion temperature and velocity measurements on Magnum-PSI: a feasibility study. *Plasma Phys Controlled Fusion* (2010) 52(4):045009. doi:10.1088/0741-3335/52/4/045009
53. Barata JAS, Conde CAN. Elastic He+ on He collision cross-sections and Monte Carlo calculation of the transport coefficients of He+ ions in gaseous helium. *Nucl Instr Methods Phys Res Section A: Acc Spectrometers, Detectors Associated Equipment* (2010) 619(1-3):21–3. doi:10.1016/j.nima.2009.10.070
54. Available from: <https://fr.lxcat.net>
55. Tanyeli I, Marot L, Mathys D, van de Sanden MCM, De Temmerman G. Surface modification of metals induced by high fluxes of low energy helium ions. In: *Proc. 22nd int. Symp. On plasma chemistry antwerp, Belgium* (2009).
56. Kajita S, Sakaguchi W, Ohno N, Yoshida N, Saeki T. Formation process of tungsten nanostructure by the exposure to helium plasma under fusion relevant plasma conditions. *Nucl Fusion* (2009) 49(9):095005. doi:10.1088/0029-5515/49/9/095005

Frontiers in Physics

Investigates complex questions in physics to understand the nature of the physical world

Addresses the biggest questions in physics, from macro to micro, and from theoretical to experimental and applied physics.

Discover the latest Research Topics

[See more →](#)

Frontiers

Avenue du Tribunal-Fédéral 34
1005 Lausanne, Switzerland
frontiersin.org

Contact us

+41 (0)21 510 17 00
frontiersin.org/about/contact

